Improvement of Activated Charcoal-Ammonia Adsorption Heat Pumping/Refrigeration Cycles.

Investigation of Porosity and Heat/Mass Transfer Characteristics.

by

Lynne Turner

A thesis submitted for the degree of

Doctor of Philosophy

of the

University of Warwick

JULY 1992

Table of Contents

Acknowledgments

ABSTRACT

Reported in this thesis are the results of a combined theoretical and experimental study into improvements to the solid adsorption refrigeration or heat pumping cycle using the ammonia-activated charcoal pair. The three areas which have been examined are the cycle thermodynamics, the porosity characteristics of ammonia-charcoal pairs and the heat transfer through an ammonia granular charcoal packed bed.

It was found through the use of advanced thermodynamic cycles utilizing multiple beds that the coefficient of performance of a refrigerator could be increased by $\approx 250\%$ and the coefficient of amplification of a heat pump could be increased by $\approx 110\%$. The coefficients of performance and amplification may also be increased to a lesser degree by judicious choice of the charcoal porosity characteristics.

A survey of charcoal porosity characteristics revealed that the useful energy per cycle could be doubled by the correct choice of charcoal.

The thermal conductivity of an ammonia granular charcoal bed was measured using a novel piece of apparatus. From the results it was decided for all practical purposes that the bed conductivity may be considered constant and equal to 0.165 W/m K.

The power output of the cycle was found from modelling the dynamic desorption of a reactor using a one-dimensional finite difference model set in radial coordinates. The cycle simulations revealed that ideally the reactor should be constructed from solid charcoal shapes manufactured in such a way as to incorporate paths of enhanced conductance and be integral with the containing vessel wall.

1. INTRODUCTION

The main disadvantage of the ammonia-charcoal adsorption refrigerator or heat pump as it stands is that it is not economically viable. This research investigates ways of reducing both the running costs and capital costs of the system.

The running costs are governed by the coefficient of performance of the cycle and to a smaller extent by the charcoal porosity characteristics. Methods of improving the COP by the use of advanced thermodynamic cycles or optimization of the operating conditions are examined in Section 2 of this work.

The cost of the plant is too high mainly due to the size of the reactor necessitated by the very low power output per unit volume of ammonia charcoal bed. For example, in order to power a standard size larder refrigerator, the volume of the reactor would need to be approximately 3-4 litres. This would cost between £12 to £16 at today's prices for the charcoal alone. Add to this the cost of a pressure safe containing reactor vessel and the cost of a suitable heating system such as gas burners and it can be seen that this system is more cumbersome and expensive than a standard vapour compression system.

The cost of the plant may be reduced either by improving the charcoal porosity characteristics or by improving the heat transfer through the bed. The porosity characteristics are investigated in Section 3 and the heat transfer is investigated in Sections 4-6.

Finally Section 7 presents an finite difference model which simulates an idealized dynamic desorption cycle. This is used to determine the power output of different types of reactors. From the results of these simulations, recommendations are made as to how and to what extent the power output of the system may be improved.

2. ADSORPTION CYCLES

Introduction.

As outlined in the main introduction, one of the three ways in which the overall performance of the adsorption refrigerator or heat pump can be improved is through modification of the thermodynamic cycle. This Section investigates the dependency of the cycle efficiencies on the properties of the adsorbent and on the operating temperatures through the use of predictive modelling. It also reviews and discusses work carried out by other authors into modelling, experiment and advancement of the system using multiple beds and double effect cascades. Generally the cycle thermodynamics has been well investigated and the system design has reached the stage where the cycle efficiency approaches its thermodynamic ideal. The steady state modelling using the 208C-ammonia pair produced here will be combined in Section 7 with a heat transfer model to produce an overall dynamic working cycle.

2.1 Adsorption.

Adsorption is the process in which the molecular species of one substance becomes attached to the surface of another resulting in an increase in concentration of the substance at the interface. Substances may be adsorbed on the surface of a solid from either a liquid or gaseous phase. The solid is known as the adsorbent, and the liquid or gas as the adsorbate.

There are essentially two types of adsorption and these are known as chemisorption and physical or Van der Waals' adsorption. In the case of chemisorption, the adsorbate and adsorbent undergo a chemical reaction when they come into contact with each other. This results in strong bonding between the substances which requires a relatively high energy input to break. In the case of physical adsorption, the adsorbate is attracted to the adsorbent by polar forces resulting in a comparatively weak bond. The latter of the two is more commonly used in heat pumping and refrigeration applications for the following reasons.

(i) It has a low value of the heat of adsorption/desorption (comparable to the latent heat of the adsorbate).

(ii) The adsorption is readily reversible.

(iii) Most pairs of solids and gases (or liquids) will undergo a certain amount of adsorption.

The adsorptive capacity of a substance depends largely on its structure. The set of materials known as microporous adsorbents are of most use in refrigeration and heat pumping cycles due to their large adsorptive capacity. The very highly porous structure of these materials allows in some cases adsorption of more than 50% of its own mass.

Adsorbent/Adsorbate Pairs.

As previously mentioned most adsorbent/adsorbate pairs will undergo a certain amount of adsorption. The amount of refrigerant which can be desorbed from the adsobent for a certain temperature lift directly affects the efficiency of the machine. It is therefore important that the choice of the adsorbent/refrigerant pair is made with the knowledge of the application for which it is intended.

The basic requirements of a refrigerant are:-

(i) A high latent heat to minimize the mass of adsorbent needed thus minimizing the sensible heat requirement of the adsorbent.

(ii) The condensing pressure at the anticipated condensing temperature should be as low as possible reducing the risks associated with high pressure systems.

(iii) The evaporating pressure at the anticipated evaporating temperature should be slightly above atmosphere. This means that the system is always running on positive pressure and if a leak should occur it would be outward. Such an occurrence would not not necessarily render the system useless as would probably be the case if the evaporating pressure were subatmospheric.

(iv) Non toxic, non flammable and inexpensive.

(v) That it be chemically stable e.g no breakdown at high temperatures.

(vi) Non polluting.

Basic requirements of the adsorbent are:-

(i) That it be able to desorb a large amount of refrigerant over a given temperature lift, thus reducing the energy wasted in its own heating and cooling.

(ii) That it is stable with the refrigerant used.

(iii) That it has a low specific heat.

(iv) That it has good heat transfer properties.

(v) That is inexpensive and readily available.

The three most extensive studies found to date have been carried out by Critoph and Vogel [1], and Critoph and Turner [2] in which they examine zeolites and charcoal with a wide range of organic refrigerants, and then activated charcoal with ammonia and methanol. Meunier [3] in a report for the EEC examines different types of zeolites with water and methanol. The US Department of Energy in a report on zeolites for use in refrigeration [4] review its behaviour with organic refrigerants, chlorides, amines as well

as ammonia, sulphur dioxide, carbon dioxide and methane.

By far the most widely used adsorbent/adsorbate pairs for refrigeration, heat pumping and air conditioning are activated charcoal-ammonia, activated charcoal-methanol and zeolite-water. The refrigerants water, methanol and ammonia are used most frequently used because of their high latent heats, 2258 kJ/kg, 1102 kJ/kg, 1368 kJ/kg respectively. Water is suitable for heat pumping and air conditioning only. Methanol has an upper temperature limit of 120 °C before it begins to break down, and so is only useful for air conditioning and refrigeration. Ammonia however may be satisfactorily employed in all three applications. Both of the adsorbents zeolite and activated charcoal are microporous in structure. Of the two, zeolites generally have a higher desorption energy than charcoals and are better suited to high temperature applications. Activated charcoals or carbons are cheaper and are more easily manufactured.

On the basis of the investigations [1-4], the arguments presented above and the lists of requirements, the ammonia activated charcoal pair was selected for use throughout this work.

2.2 Solid Adsorption Refrigeration and Heat Pumping Cycles.

The phenomenon of adsorption becomes of use to us for heat pumping and refrigeration cycles in that it allows us to replace a mechanical compressor and expansion unit with a heat driven adsorbent bed containing a suitable refrigerant. The simple adsorption cycle as applied to refrigeration is intermittent in nature and consists of four processes.

(i) Heating

(ii) Generation

(iii) Cooling

(iv) Adsorption

The generation and adsorption processes follow isobars and the heating and cooling processes follow isosteres (lines of constant concentration). Assuming that the refrigerant and isosteres approximately obey Troutons Law and that they are linear (see Appendix 2a), then they are most conveniently represented on a lnp vs. 1/T diagram. With reference to the pressure, temperature, concentration (p-T-x) diagram shown in figure 2.1, and the schematic diagram of figure 2.2, the system operates in the following way.

FIGURE 2.1
Pressure Temperature Concentration Diagram.
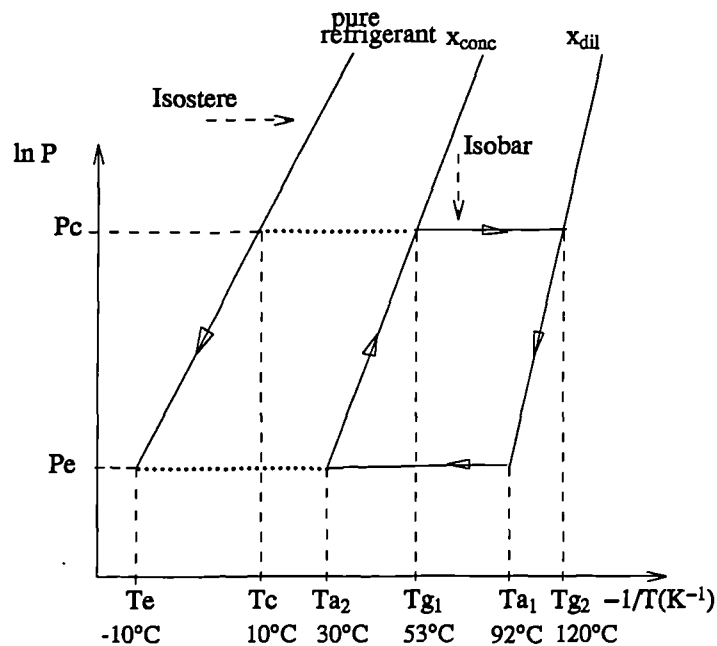
(i) Heating $Ta_2 - Tg_1$

The generator/adsorber starts the cycle containing a rich concentration of refrigerant. With the valve open the bed is heated from its initial temperature of Ta_2 to a temperature Tg_1 following the isostere x_{conc}.

(ii) Generation $T_{g1}-T_{g2}$

At T_{g1} the vapour pressure in the system is equal to the condensing pressure Pc and desorption begins. During generation the temperature of the adsorbent bed rises along the isobar Pc until it retains only a weak concentration of refrigerant x_{dil}. As the refrigerant is desorbed it is cooled to a temperature Tc along the isobar Pc until it condenses in either a water or air cooled condenser. For a heat pump this would form part of the useful energy output.

FIGURE 2.2

Schematic Diagram Of Adsorption Refrigerator.
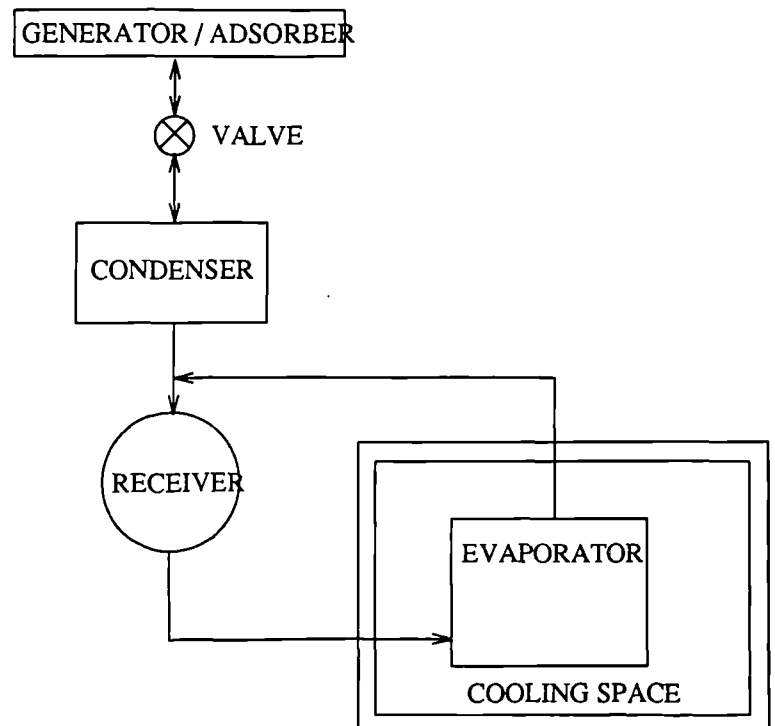
(iii) Cooling $T_{g2}-T_{a1}$

When the maximum cycle temperature is reached and desorption is complete, the valve is closed and the bed is allowed to cool. For a heat pump this heat rejection forms

part of the useful energy. As the bed cools, its pressure reduces until it equals the saturated vapour pressure of the refrigerant at Te.

(iv) Adsorption T_{a1}–T_{a2}

The valve is now opened and pressure difference between the generator and the evaporator causes the refrigerant within the evaporator to boil. Firstly this reduces the bulk temperature of the refrigerant to Te and then causes cooling in the space around the evaporator. For a refrigerating system this is the useful cooling energy. The refrigerant then travels back to the adsorbent bed where it is readsorbed. The heat generated in this process is removed by either air or water cooling. For a heat pump, this is the final portion of the useful energy output. This process continues until the cycle is completed and the system is returned to its original temperature of T_{a2}.

Figure 2.1 shows an idealized adsorption cycle. A real cycle does not have the well defined corner points T_{a2}, T_{g1}, e.t.c, rather the stages (i)-(iv) merge with each other forming a much more curved process line.

The valve situated between the generator and the condenser shown in figure 2.2 is optional. The system can operate without it, the only difference being a reduction in the machine's efficiency. This occurs because without an isolating valve, as soon as the bed starts to cool it readsorbs some refrigerant causing evaporation to take place at a higher temperature than Te.

The desorption and adsorption times are a function of the overall conductivity of the bed. If the bed is at a temperature T_1 and it readsorbs some refrigerant, the bed temperature increases to $T_1 + \Delta T$ due to the release of the heat of adsorption. The bed must now cool down again to at least T_1 before it can adsorb any more refrigerant. This effect produces rather jagged process lines along the isobars in a real cycle. Ultimately the total cycle time will be determined by the heat transfer properties of the adsorber.

Past and Present Uses of the Solid Adsorption Cycle.

Solid/vapour adsorption refrigeration was first demonstrated by Faraday in 1848 and was first used commercially in the early 1900's as reported by Plank and Kuprianoff [5]. These early machines were successfully manufactured and employed the adsorbent/refrigerant pairs calcium chloride-ammonia and activated charcoal-methanol. Later in the 1920's development of a refrigerator/heat pump unit to simultaneously supply heating and cooling power took place [6,7]. The same company also produced refrigeration units for railroad cars using the adsorbent/ refrigerant pair of silica gel and sulphur dioxide. However with the advent of a ready supply of electricity and the hermetically sealed compressor, interest in the system was temporarily lost.

In the recent search for alternative energy sources, especially the utilization of solar power, investigation into solid adsorption cycles has been restarted. The cycle is ideal particularly for use in developing countries since it is non-mechanical and non-electrical. The intermittent nature of the cycle is also well suited to the diurnal cycle of the sun which led initially to research into solar powered systems.

Successful large scale rigs have been built and tested [8-11]. Pons *et al* [8,9] worked with the carbon/methanol pair to produce a solar powered ice-making machine which yielded an experimental cycle COP of 0.43 and an overall solar COP (coefficient of performance, see Equation(2.1)) of 0.12. This compares with similar experiments using the zeolite 13X/water pair [12] for solar cooling where the quoted cycle COP was 0.33 and the solar COP was about 0.1. Tchernev [10,11] has investigated the zeolite/water pair for air conditioning and refrigeration systems. He quotes an experimentally obtained value of 0.3 for the cycle COP and 0.12-0.15 for the solar COP with regard to the air conditioning application.

In industrialized countries the research has been more directed towards heat pumping or cogeneration of heating and cooling power. In 1986 in Berlin, Jank *et al* [13] built

and tested a full scale heat pump. The system was powered by natural gas and used dual zeolite-water adsorbers to cogenerate heating and cooling. In 1989, Shelton *et al* [14] produced a gas driven, dual bed zeolite-water heat pump. This system attempted to utilize a very efficient method of exchanging heat between the beds and was reported to produce a COA (coefficient of amplification, see Equation (2.2)) of up to ≈ 1.8.

Other than these larger scale projects many small scale test rigs have been built using different adsorbent/adsorbate pairs. These include carbon/methanol [15-18], zeolite/water [19-22], calcium chloride/ammonia,methanol [23,24]. Generally the driving energy is solar power but steam and waste industrial heat have also been used. Quoted cooling cycle COP's are ≈ 0.4 for the C-M pair [18], ≈ 0.35 for the Z-W pair [19,21] and ≈ 0.34 for the $CaCl_2 - NH_3$ pair [23].

Many authors have also analyzed the cycle theoretically to obtain the coefficients of performance [15,17,25-30], and in some cases these have been compared with experimentally obtained data [20].

2.3 Mathematical Models of Single Bed Adsorption Cycles.

In order to assess the performance of a refrigerator or a heat pump we must evaluate the COP (Coefficient of Performance) or COA (Coefficient of Amplification) respectively. These are defined as the fraction of useful heat output gained from the high grade heat input.

For a refrigerator:-

$$COP = \frac{(Q_{ref} - Q_{co})}{(Q_h + Q_g)} \quad - (2.1)$$

and for a heat pump:-

$$COA = \frac{(Qad+Qcond+Qc)}{(Qh+Qg)} \quad \text{— (2.2)}$$

where:-

Qref   Refrigerating Load (kJ)

Qad   Heat energy from Adsorption (kJ)

Qh   Sensible Heating Energy (kJ)

Qg   Heat Energy for Generation (kJ)

Qcond   Condenser Load (kJ)

Qc   Bed Cooling (kJ)

Qco   Refrigerant Cooling (kJ)

The simple cycle consists of seven distinct heating or cooling processes as tabulated above. The following analysis is for a general system and any approximations used are stated along with the equations defining the process and its position on the p-T-x diagram. The refrigerant/adsorbent pair used throughout the whole of the modelling is ammonia/activated charcoal (Sutcliffe Speakman 208C).

(i)   Qh   Sensible Heating
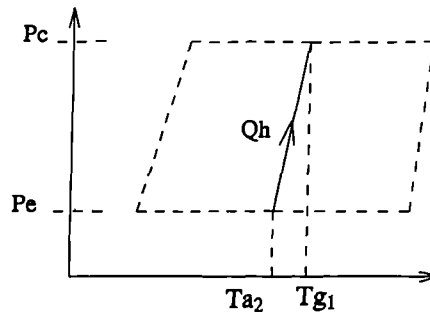
This is the high grade heat energy required to raise the bed pressure from Pe to Pc.

$$Qh = \int_{T=Ta_2}^{T=Tg_1} Cv_{c(T)} \, m_c \, dT + \int_{T=Ta_2}^{T=Tg_1} Cv_{a(T)} \, m_a \, dT \quad \text{— (2.3)}$$

and

$$m_a = x_{conc} \; m_c$$

where:-

m_c	mass of charcoal (kg)
m_a	mass of adsorbed ammonia (kg)
x_{conc}	concentration of ammonia in bed at Ta_2 (kg refrigerant/kg adsorbent)
$Cv_{c(T)}$	Specific heat of charcoal at constant volume (kJ/kg K) (function of temperature)
$Cp_{c(T)}$	Specific heat of charcoal at constant pressure (kJ/kg K) (function of temperature)
$Cv_{a(T)}$	Specific heat at constant volume of adsorbed phase (kJ/kg K) (function of temperature)
Tg_1	Lower generating temperature (K)
Ta_2	Ambient or initial temperature (K)
x	concentration of ammonia (kg/kg)

It is assumed that:-

(a) No desorption takes place until the condensing pressure is reached.

(b) Sensible heating to the ammonia gas contained within the bed volume is negligible.

(c) Heating the bed along an isostere is considered to be a constant volume process.

(d) The specific heat at constant volume $Cv_{c(T)}$ of the charcoal is equal to the specific heat at constant pressure $Cp_{c(T)}$.

The specific heat of several different types of charcoal was measured at National Physical Laboratory on a scanning differential calorimeter. For the charcoal 208C the specific heat was found to vary linearly with temperature, see Appendix 2b.

$$Cp_c = 0.175 + 2.245 \times 10^{-3} T \quad — (2.4)$$

where:-

T   Temperature of bed (K)

The specific heat at constant volume of the adsorbed phase, Cv_a is assumed to be constant over the temperature range used. The data was found from Refs [38,39].

$$Cv_a = 2.8 \text{ kJ/kg K}$$

The concentration x_{conc} is found from an equation known as the Dubinin -Ashtikov equation, see Ref [3] from Section 3.2, which describes the volume filling of micro-porous adsorbents. The equation is modified to suit our purposes and makes the assumption that the density of the adsorbed phase is constant over the temperature range.

$$x = x_0 \exp\left(-K_2 \left(\frac{T-T_{sat}}{T_{sat}}\right)^n\right) \quad — (2.5)$$

where:-

x concentration of ammonia adsorbed in

       bed at temp T and pressure p (kg/kg)

x_0 saturation concentration (kg/kg)

K_2 experimentally determined constant dependent

       on adsorbent/adsorbate properties

T   bed temperature (K)

T_{sat} saturation temperature at bed pressure p (K)

n   Power index of temperature ratio

Using equations (2.3), (2.4) and (2.5) Qh may be found for a unit mass of charcoal.

$$Qh = (2.8\, x_{conc} + 0.175)\,(Tg_1 - Ta_2) + 1.1225 \times 10^{-3}\,(Tg_1{}^2 - Ta_2{}^2) \quad\text{—— (2.6)}$$

(ii) Qg Heat of Generation
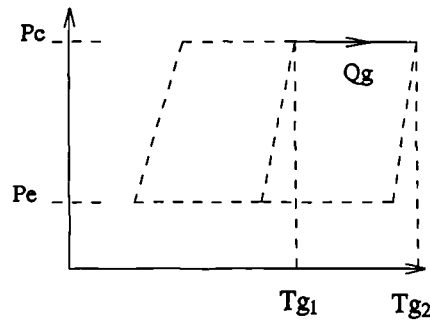
This is the high grade heat required to desorb ammonia from the bed between the upper and lower generating temperatures. It also includes the sensible heating to the charcoal and the remaining mass of adsorbed ammonia.

$$Qg = \int_{T=Tg_1}^{T=Tg_1} m_c\, Cp_{c(T)}\, dT + \int_{T=Tg1}^{T=Tg2} m_c\, x\, Cp_{a(T)}\, dT + \sum_{T=Tg1}^{T=Tg2} H\, \Delta x\, m_c \quad\text{—— (2.7)}$$

where:-

$Cp_{a(T)}$	specific heat at constant pressure (function of temperature) kJ/kg K
H	Heat of desorption (kJ/kg)
Δx	Concentration change (kg refrigerant/kg adsorbent)
Tg_2	Upper generating temperature (K)

It is assumed that:-

(a) Desorption takes place along an isobar.

(b) As soon as ammonia is desorbed from the bed it enters the condenser, ie. no cooling of the takes place within the bed itself.

The specific heat at constant pressure of the adsorbed phase is assumed to be constant over the temperature range. The data can be found from Refs [38,39].

$$Cp_a = 4.9 \text{ kJ/kg K}$$

The heat of desorption H can be found from the Clausius Clapeyron equation, see Appendix 2c.

$$\frac{d}{dT}(\ln p) = \frac{H}{T^2 R} \quad\text{— (2.8)}$$

where:-

p   bed pressure (Bar)

R   gas constant for ammonia (0.488 kJ/kg K)

By plotting the pressure p against its corresponding saturation temperature for pure ammonia, see App 2d, we obtain the linear relationship given in equation (2.9).

$$\ln p = \frac{-2823.4}{T_{sat}} + 11.749 = \frac{-A}{T_{sat}} + B \quad\text{— (2.9)}$$

Rearranging equation (2.5) gives us an expression for $1/T_{sat}$.

$$\frac{1}{T_{sat}} = \frac{1}{T}(1 + (\frac{\ln x - \ln x_0}{-K_2})^{1/n}) \quad\text{— (2.10)}$$

By substituting equation (2.10) into equation (2.9) we obtain an expression for ln p which may be substituted into equation (2.8) to give.

$$\frac{H}{T^2 R} = \frac{d}{dT}(\frac{-A}{T}((\frac{\ln x - \ln x_0}{-K_2})^{1/n} + 1) + B)$$

$$\frac{A}{T^2}((\frac{\ln x - \ln x_0}{-K_2})^{1/n} + 1) = \frac{H}{T^2 R}$$

$$H = R \times A ((\frac{\ln x - \ln x_0}{-K_2})^{1/n} + 1)$$

Substituting equation (2.10) into the above gives.

$$H = R \times A \left(\frac{T}{T_{sat}} \right)$$

$$H = 0.488 \times 2823.4 \left(\frac{T}{T_{sat}} \right) \quad \text{--- (2.11)}$$

The heat of adsorption and the concentration are found every degree K between the upper and lower generating temperatures and are then summed to find the total.

Using equations (2.4), (2.5), (2.7) and (2.11) the generating energy can now be found per unit mass of charcoal.

$$Qg = \left(0.175 + 4.9 \left(\frac{x_{conc} + x_{dil}}{2} \right) \right) (Tg_2 - Tg_1) + 1.1225 \times 10^{-3} (Tg_2^2 - Tg_1^2) + \sum_{T=Tg_1}^{T=Tg_2} H \, \Delta x \quad \text{--- (2.12)}$$

where:-

x_{dil} concentration of adsorbed ammonia at upper generating temperature (kg refrigerant/kg adsorbent)

(iii) Qc Cooling (Bed)
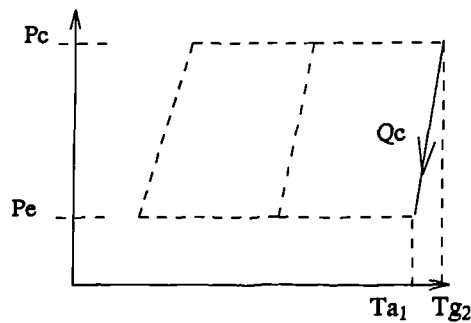
This is heat energy which needs to be rejected from the bed in order to reduce the system pressure back to its original value of Pe.

$$Qc = \int_{T=Ta_1}^{T=Tg_2} m_c \, Cp_{c(T)} \, dT + \int_{T=Ta_1}^{T=Tg_2} m_c \, x_{dil} \, Cv_{a(T)} \, dT \quad \text{--- (2.13)}$$

where:-

Ta_1 adsorption temperature (K)

It is assumed that

(a) No adsorption takes place until the evaporating pressure is reached.

(b) Sensible cooling of the ammonia gas contained within the bed volume is considered negligible.

(c) Cooling the bed along an isostere is considered to be a constant volume process.

As with Qh, $Cv_{a(T)}$ is assumed to be constant over the temperature range, so Qc for unit mass of charcoal is

$$Qc = (0.175 + x_{dil}\ 2.8) (Tg_2 - Ta_1) + 1.1225 \times 10^{-3} (Tg_2^2 - Ta_1^2) \quad \text{---(2.14)}$$

(iv)   Qad   Heat of Adsorption
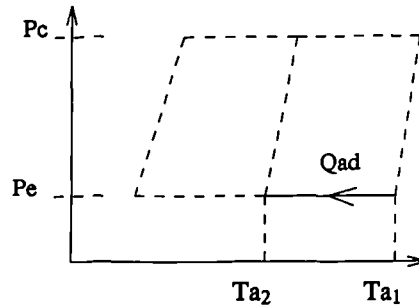
This is the heat energy rejected from the bed as the gaseous ammonia is readsorbed. It is also the heat loss required for sensible cooling of the charcoal and adsorbed ammonia between the adsorption temperature Ta_1 and the ambient temperature Ta_2. Finally, as the ammonia gas is reintroduced to the bed it is at a lower temperature and therefore has a cooling effect on the charcoal.

$$Qad = \int_{T=Ta_2}^{T=Ta_1} m_c\ Cp_c\ dT + \int_{T=Ta_2}^{T=Ta_1} m_a\ Cp_{a(T)}\ dT + \sum_{T=Ta_2}^{T=Ta_1} H\Delta x - \int_{T=Ta_2}^{T=Ta_1} Cp_{ag(T)}\ m_c\ \Delta x\ d(T - Te) \quad \text{---(2.15)}$$

where:-

$Cp_{ag(T)}$ specific heat at constant pressure of

ammonia gas(function of temperature) (kJ/kg K)

Tc   evaporating temperature (K)

It is assumed that :-

(a) Adsorption along an isobar is a constant pressure process.

(b) Saturated vapour only leaves the evaporator i.e no superheating of the refrigerant takes place.

As with Qg, the specific heat at constant pressure of the adsorbed phase is assumed to be constant over the pressure range. The heat of adsorption and concentration are found every degree K from equations (2.11) and (2.5) respectively and summed between Ta₁ and Ta₂ to find the total. The specific heat of the ammonia gas is also assumed to be constant over the temperature range, see Appendix 2e.

$$Cp_{ag(T)} = 2.5 \text{ kJ/kg K}$$

Qad may found per unit mass of charcoal.

$$Qad = (0.175 + 4.9 (x_{conc} - x_{dil}))(Ta_1 - Ta_2) + 1.1225 \times 10^{-3} (Ta_1^2 - Ta_2^2)$$

$$+ \sum_{T=Ta_2}^{T=Ta_1} H \, \Delta x \; - 2.5 (x_{conc} - x_{dil})(\frac{Ta_1 + Ta_2}{2} - Te) \quad — (2.16)$$

For a refrigerating system it is sensible to use the cold ammonia gas leaving the evaporator at Te to part cool the bed. For a heat pump it would make more sense to heat the gas leaving the evaporator to Ta₂ before introducing it to the bed. In this case equation (2.16) would become:-

$$Qad = (0.175 + 4.9 (x_{conc} - x_{dil}))(Ta_1 - Ta_2) + 1.1225 \times 10^{-3} (Ta_1^2 - Ta_2^2)$$

$$+ \sum_{T=Ta_2}^{T=Ta_1} H \, \Delta x \; -2.5 (x_{conc} - x_{dil})(\frac{Ta_1 - Ta_2}{2}) \quad — (2.16b)$$

(v)   Qcond   Condensation Energy
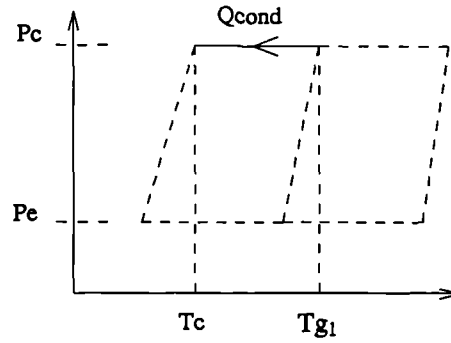
This is the required heat rejection from the system to allow the hot gaseous ammonia to cool and condense to a saturated liquid at pressure Pc.

$$Qcond = \int_{T=Tg_1}^{T=Tg_2} Cp_{ag(T)} \, m_c \, \Delta x \, d(T-Tc) \quad + (x_{conc} - x_{dil}) \, m_c \, Le \quad - (2.17)$$

Le   Latent heat of ammonia (kJ/kg)

Tc   Condensing temperature (K)

The latent heat of ammonia is found from equation (2.11) where $T = T_{sat}$ and $Cp_{ag(T)}$ is assumed constant with temperature. For unit mass of charcoal Qcond becomes.

$$Qcond = 2.8 \, (x_{conc} - x_{dil})(\frac{Tg_2 + Tg_1}{2} - Tc) + (0.488 \times 2823.4)(x_{conc} - x_{dil}) \quad - (2.18)$$

(vi)   Qco   Cooling (refrigerant)
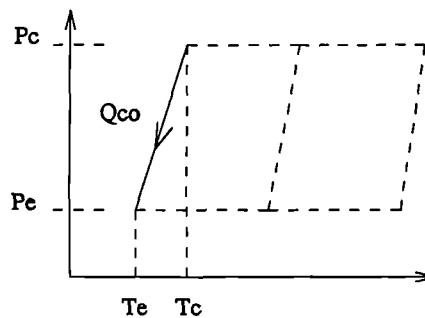
This is the heat lost by the refrigerant as it cools during the pressure reduction from a saturated liquid at Pc to a saturated liquid at Pe. The cooling energy is supplied by the

refrigerant itself. When the adsorbent bed cools and the system pressure drops, a certain amount of refrigerant in the evaporator boils taking heat from the remaining refrigerant. This process continues until the system pressure is Pe and the refrigerant bulk temperature is Te.

$$Qco = \int_{T-Te}^{T-Tc} (x_{conc} - x_{dil}) \, m_c \, Cv_{f(T)} \, dT \quad \text{— (2.19)}$$

$Cv_{f(T)}$ specific heat at constant volume of saturated   K

        liquid ammonia (function of temperature)

It is assumed that the cooling of the pure ammonia is a constant volume process.

The specific heat $Cv_{f(T)}$ of saturated liquid ammonia was approximated to a straight line fit, see Appendix 2f.

$$Cv_{f(T)} = -4.1 \times 10^{-3} \, T + 4.083 \quad \text{— (2.20)}$$

Using equations (2.20) and (2.19) an expression for Qco per unit mass of charcoal can be found.

$$Qco = (x_{conc} - x_{dil})(4.1 \times 10^{-3} (Te^2 - Tc^2) + 4.083 (Tc - Te)) \quad \text{— (2.21)}$$

(vii)   Qref   Refrigerating effect
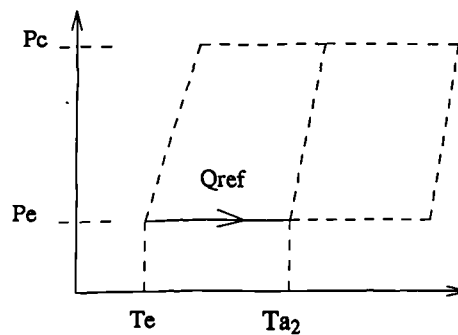
This is the amount of energy required by the system to boil the saturated liquid ammonia, otherwise known as the refrigerating load.

$$Qref = (x_{conc} - x_{dil}) \, Le = (x_{conc} - x_{dil})(0.488 \times 2823.4) \quad \text{— (2.22)}$$

Effect of Carbon Properties on COP.

All activated carbons have different adsorption properties depending on the starting material and the method of activation. The most commonly used equation representing the volume filling of microporous adsorbents is known as the Dubinin-Radushkevich (D-R) equation (2.23), see Section 3.2. For our convenience it has been rewritten in the following form.

$$x = x_0 \exp(-K \left(\frac{T-Tsat}{Tsat} \right)^2) \text{ — (2.23)}$$

The previously mentioned D-A equation is merely an extension of the D-R equation which allows better curve fitting by virtue of having the extra variable n. Equation (2.23) has two variables which are dependent on the charcoal type used. The concentration on saturation x_0 determines the maximum possible uptake of ammonia, and the value K which determines the rate at which ammonia is desorbed with respect to pressure and temperature.

To examine the effect of different charcoal properties on COP we will take a set of typical operating temperatures for refrigerating and vary x_0 and K.

Ta_2	initial temperature	= 300 K	27°C
Tc	condensing temperature	= 300 K	27° C
Te	evaporating temperature	= 263 K	-10°C
Tg_2	upper generating temperature	= 373 K	100°C

Having set four of the operating temperatures, the other two are found using equation (2.11).

for Pc and isostere x_{conc}

$$H = R \times A \left(\frac{Tg_1}{Tc} \right) \text{ — (2.24)}$$

for Pe and isostere x_{conc}

$$H = R \times A \left(\frac{Ta_2}{Te} \right) \qquad - (2.25)$$

equating (2.24) and (2.25) gives

$$Tg_1 = \frac{Ta_2 Tc}{Te} = 342.2 \text{ K}$$

Using a similar procedure for x_{dil} gives

$$Ta_1 = \frac{Ta_2 Tg_2}{Tg_1} = 327.0 \text{ K}$$

From a series of measurements of charcoal data it has been found that realistic ranges for K and x_0 are 4-13 and 0.1-0.55 respectively, see Section 3.3. Other materials have been found to lie outside these ranges and so for completeness a slightly wider range of K and x_0 was used for the calculations. Using equations (2.1), (2.3), (2.7), (2.21) and (2.22) the COP of a cycle was calculated for x_0 varying from 0.15 to 0.75 and for K varying from 1 to 13 and the results are shown in figure 2.3a.

FIGURE 2.3a

Variation of COP with Carbon Properties.
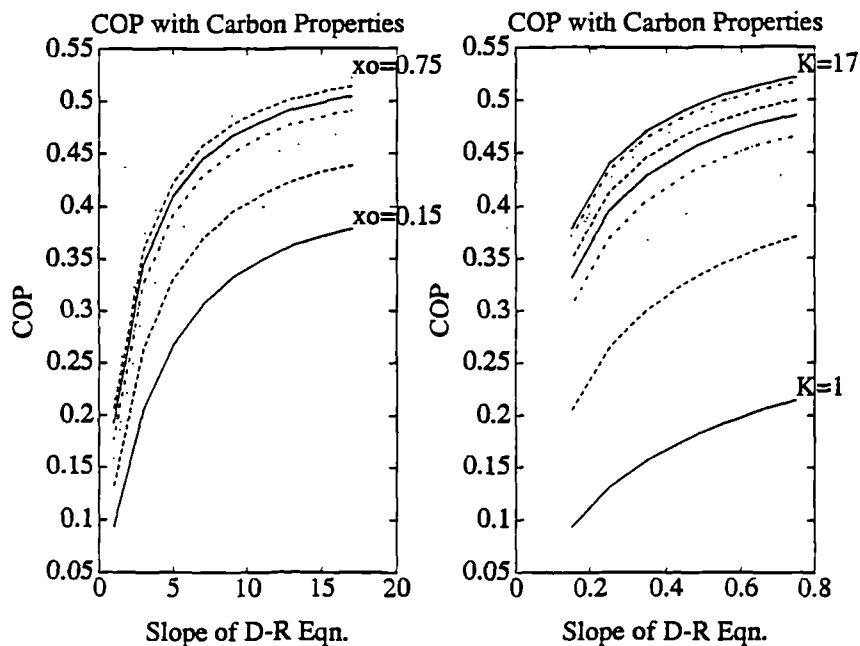
From figure 2.3a it can be seen that the COP increases with increasing values of x_0 and K. This may be explained by considering the COP as being:-

$$COP = \frac{\text{Useful refrigeration energy}}{\text{Sensible heat bed + Desorption Energy}}$$

The refrigeration energy and the desorption energy are both proportional to the concentration change. The sensible heat can be split into two portions. The heat required by the charcoal is constant and the heat requirement of the refrigerant depends on the adsorbed mass. When the concentration change is small, the wasted sensible heat dominates the COP fraction producing a low performance. As the concentration change increases the effect of sensible heat becomes less and less producing higher COPs. As K increases along constant x_0 the graph clearly reflects the exponential nature of the D-R equation in calculating the concentration change. As x_0 increases along constant K the graphs reflect more the linear effect of x_0 in the D-R equation. The graphs also indicate that the COP will at some point tend towards a maximum value. This is because the upper limit of the COP would occur when the concentration change is so large that the sensible heat could be considered negligible.

FIGURE 2.3b

Percentage Increase in COP with Varying Carbon Properties.
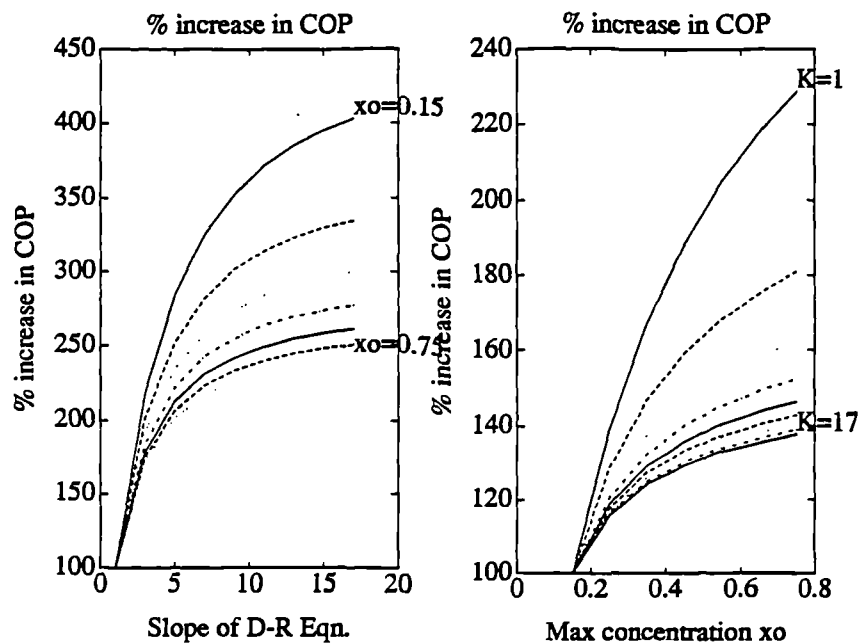
Figure 2.3b shows how the COP increases as a percentage of its starting value along lines of constant K and x_0. It can be seen that increasing K has the greatest effect on improving the COP for all values of x_0 although there are significant gains to be made with the increase of either.

Effect of Carbon Properties on COA.

Using a similar procedure, equations (2.2), (2.6), (2.12), (2.14), (2.16b), (2.18), and a typical set of operating temperatures for a heat pump, the COAs for a range of charcoal properties are obtained. The results are shown in figures 2.4a & 2.4b.

Te	evaporating temperature	= 263 K	-10 °C
Tc	condensing temperature	= 320 K	47 °C
Ta_2	initial temperature	= 320 K	47 °C
Tg_1	generating temperature	= 389 K	116 °C
Tg_2	generating temperature	= 520 K	247 °C
Ta_1	adsorption temperature	= 428 K	155 °C

FIGURE 2.4a

Variation of COA with Carbon Properties.
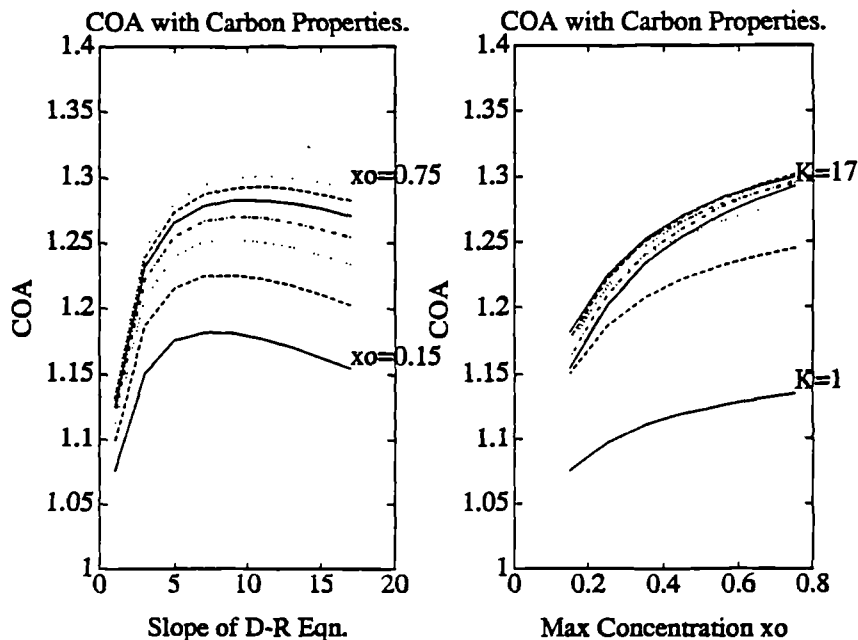
Fig 2.4a, unlike fig 2.3a shows that there is a very definitely a set of charcoal properties that maximize the COA for a particular set of operating temperatures. Again this may be explained by considering the COA as

$$COA = \frac{\text{Sensible Cooling} + \text{Adsorption Energy} + \text{Condensation}}{\text{Sensible Heating} + \text{Desorption Energy}}$$

FIGURE 2.4b

Percentage Increase in COA with Varying Carbon Properties.
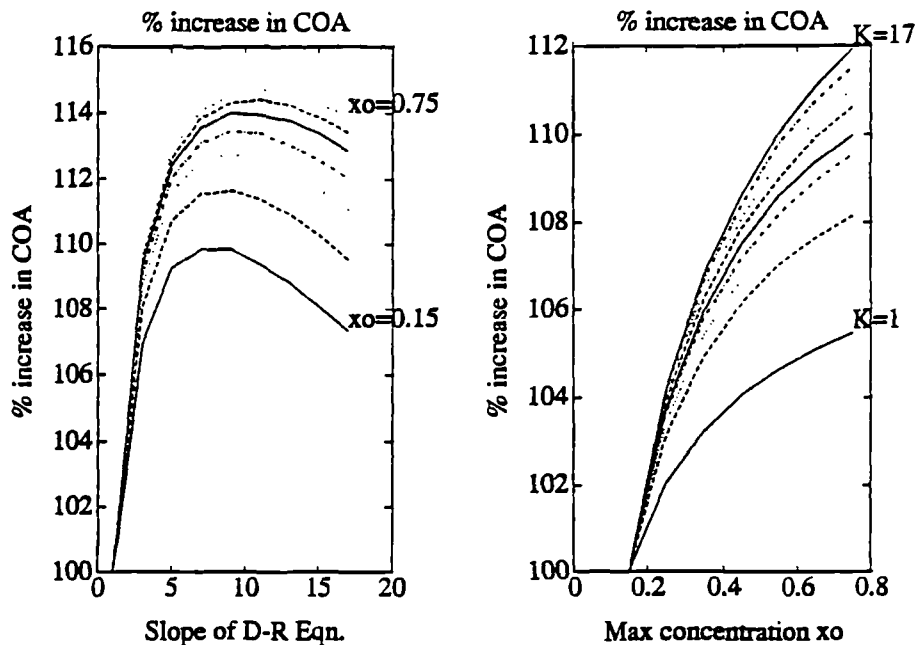
The adsorption, condensation and desorption energies are all proportional to the concentration change (Δx), whereas the sensible heating and cooling are not. An increase Δx will result in more of an increase to the numerator than the denominator and so will produce a higher COA. It may be stated therefore that the COA increases with Δx. Due to the exponential nature of the D-R equation and a higher upper generating temperature, it does not follow that an increase in the value of K will result in an increase of Δx. The peaks in fig 2.4a (left) correspond to the maximum value of Δx for the range of K.

Figure 2.4b shows that the greatest percentage increase in the COA is to be gained when K = 1 or x_0 = 0.15, although these values do not correspond to those maximizing the COA. Generally the COA tends to vary little for the whole range of K and x_0 when T_{g2} is high.

From these results it can be seen that it is possible to choose a charcoal so that its characteristics maximize the performance of a refrigerator or heat pump.

Effect of Operating Temperatures on COP.

The COP is also governed by the temperature limits within which the cycle operates. The four governing temperatures are T_{a2}, T_{g2}, Tc and Te, all of which will be set by the machine and the environment in which it is used. In order to examine the variation of the COP for various cycles, typical limits are chosen for the four controlling temperatures.

(i) T_{a2} = 300 K

(ii) 253 K < Te < 278 K

(iii) 358 K < T_{g2} < 538 K

(iv) 280 K < Tc < 300 K

Since the COP is also dependent on the charcoal characteristics they must be set to a constant value. All of the calculations in this Section use the data for a common charcoal known as 208C. This charcoal is made from coconut shell and is produced by Sutcliffe Speakman. Curve fitting data to the DA equation yielded the following values :-

x_0 = 0.2576 K_2 = 3.655   n = 1.325

The COP was calculated for each set of temperatures and the results are shown in figure 2.5. The effect that each of the operating temperatures has on the COP and the

reasons for it are now discussed in turn.

FIGURE 2.5

Variation of COP with Operating Temperatures.
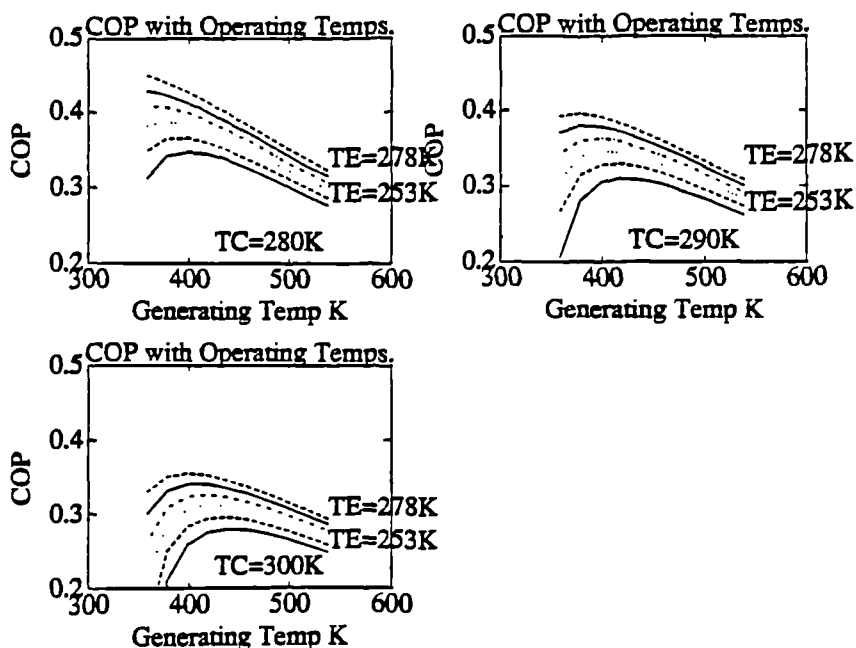
(ii) Effect of Varying Te

As Te increases so does the COP. This is because the value of Te determines on which isostere T_{a2} will fall. From the p-T-x diagram shown in figure 2.6 it can be seen that as Te drops so does the value x_{conc}. Since x_{dil} remains the same over the range of Te then Qref decreases as Te decreases. The sensible heating to the bed therefore becomes a higher proportion of Qg and the COP decreases.

(iii) Effect of Varying T_{g2}

Depending on the values of Tc and Te, the COP has a maximum at some value of T_{g2}. This happens because as T_{g2} increases x_{dil} decreases and so there is a greater concentration change which is proportional to Qref. There reaches a point however where the extra energy needed to heat the adsorber bed negates the increase in desorbed ammonia

FIGURE 2.6
Isostere Grouping at High Concentrations.
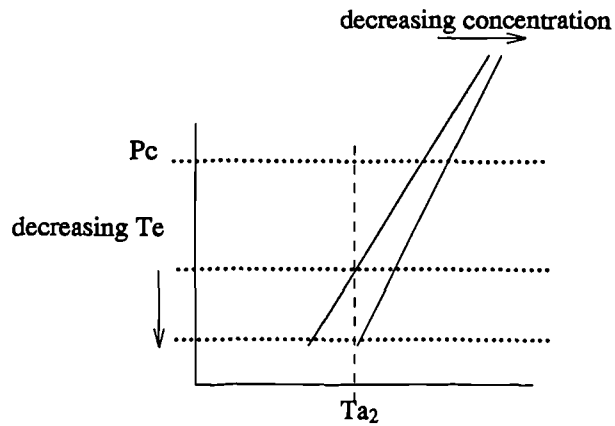
and the COP begins to decrease.

(iv) Effect of Varying Tc

As Tc increases so the COP decreases because there is a higher concentration x_{dil} at Tg_2, see figure 2.7. This means that for the same amount of heat input there is less of a concentration change which means Qref decreases and so does the COP.

FIGURE 2.7
Isostere Grouping at Low Concentrations.
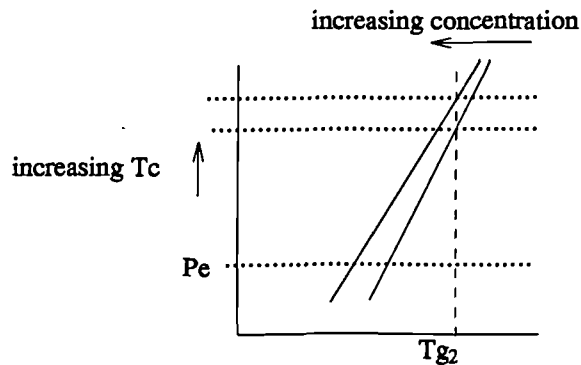
Generally, it can be said that for a certain type of charcoal a maximum value of the COP will occur in the domain bounded by Ta_2, Tg_2, Tc and Te.

Effect of Operating Temperatures on COA.

The COA of a heat pump may be calculated in a similar way using typical operating ranges.

(i) $Ta_2 = 330$ K

(ii) 253 K $< Te < 278$ K

(iii) 438 K $< Tg_2 < 538$ K

(iv) 300 K $< Tc < 330$ K

The main differences in the controlling temperatures between heat pumping and refrigeration are that Tc and Ta_2 are higher for the former.

FIGURE 2.8

Variation of COA with Operating Temperatures.
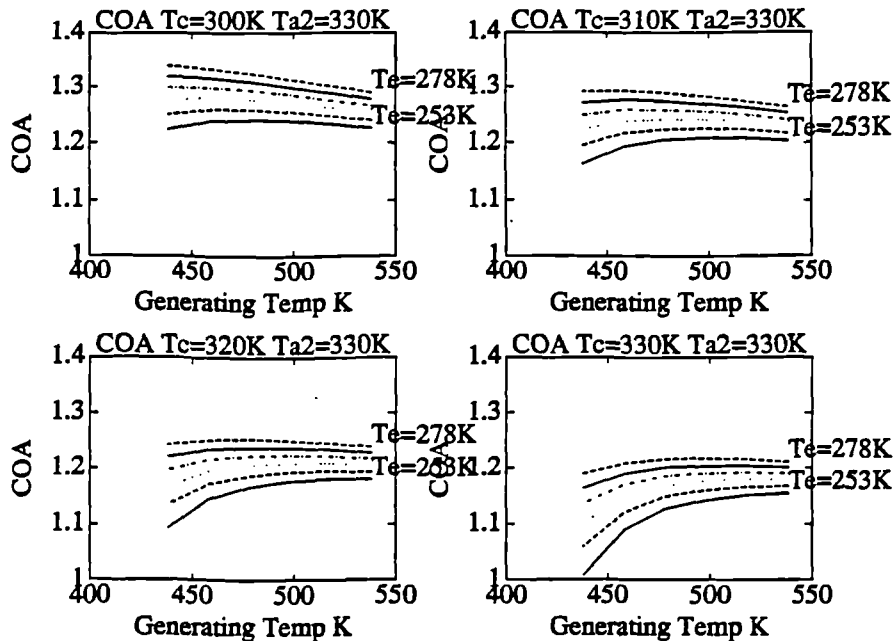
The results of the calculations are shown in figure 2.8 and they can be seen to bear a great similarity to fig 2.5. The explanations of the influence of the cycle temperatures

over the COP may also be applied to the COA.

A likely occurrence in heat pumping is that the condenser and the ambient adsorber temperature are the same. Figure 2.9 looks at the variation in COA as 300 K < Ta_2 = Tc < 330 K. The effect of increasing Ta_2 is to decrease x_{conc} resulting in a loss of performance.

FIGURE 2.9

Variation of COA with Operating Temperatures.
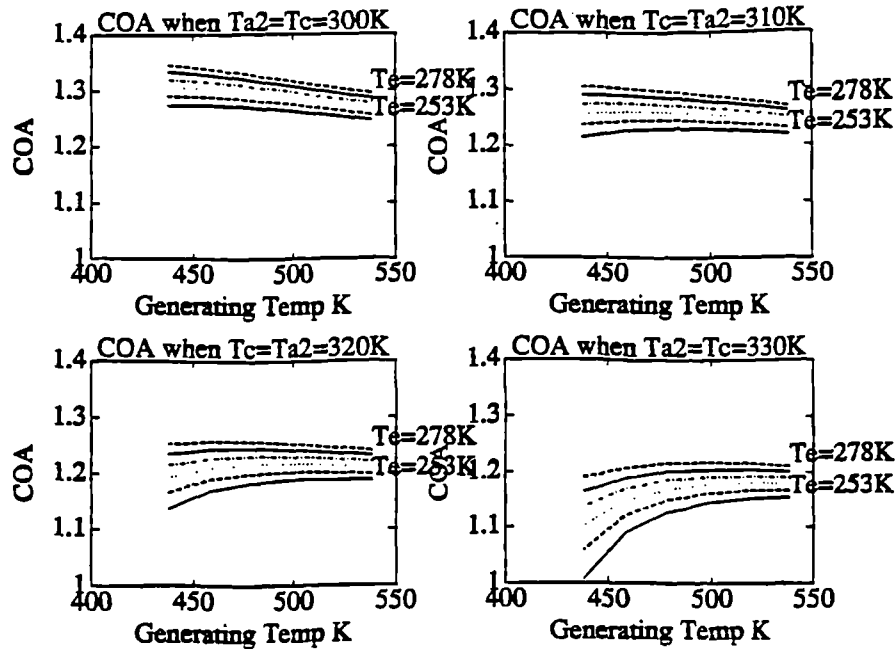
Investigations into the effect of operating temperatures on COP, COA have been carried out by Critoph and Turner [2], Douss and Meunier [31] and Guilleminot et al [32], into carbon-ammonia, carbon-methanol, and zeolite-water pairs respectively. Critoph and Turner examined the performance of heat pumps with varying charcoal properties and cycle temperatures producing results which are similar to those presented here. Douss and Meunier compared experimental values of COP,COA for the carbon-methanol pair. Apart from the use of a different refrigerant Douss and Meunier used equations similar to those derived in Section 2.3. They find good agreement between real and

generated results suggesting that the model may be used accurately for prediction purposes. Guilleminot *et al* examined the zeolite-water pair for use in cooling. The theoretical results show similar trends under the influence of Tc, Te, T_{a2} and T_{g2}. For all variations they obtained a maximum cycle COP of $\approx$ 0.5.

The environment in within which the refrigerator or heat pump works will almost undoubtedly place constraints on its efficiency. Using the model presented in this subsection enables the optimum cycle temperatures to be chosen to maximize the performance.

2.4 Multiple Bed Cycles.

It was soon realized that the performance of the machine could be improved by using two adsorber beds instead of one. These beds would run 180 degrees out of phase so that the heat rejected by one bed as it cooled could be used to heat the other. As the number of beds increases so does the COP, COA. These cycles are generally known as either multiple bed cycles or as cascaded cycles, where the number of cascades is always one less than the number of beds.

Taking the simplest case of two adsorber beds first the cycle works in the following way. Figure 2.10 shows two adsorber beds working within the same temperature limits but 180 ° out of phase. The arrows indicate the direction of the heat flows.

In stage 1, bed 1 is being heated and bed 2 is being cooled. Heat is rejected from bed 2 between the upper generating temperature T_{g2} and some intermediate temperature T_{i2}. This rejected heat heat is used to partially heat bed 1 between T_{a2} and some intermediate temperature T_{i1} where $T_{i2} - T_{i1} = \Delta t$ = temperature difference between beds. The remaining heat lost from bed 2 is rejected from the cycle. The remaining heat requirement to fully heat bed 1 is input from an external source. During stage 2 of the cycle the

roles of beds 1 and 2 are reversed and bed 1 rejects heat to bed 2 as shown.

FIGURE 2.10

Dual Bed Adsorption Cycle.
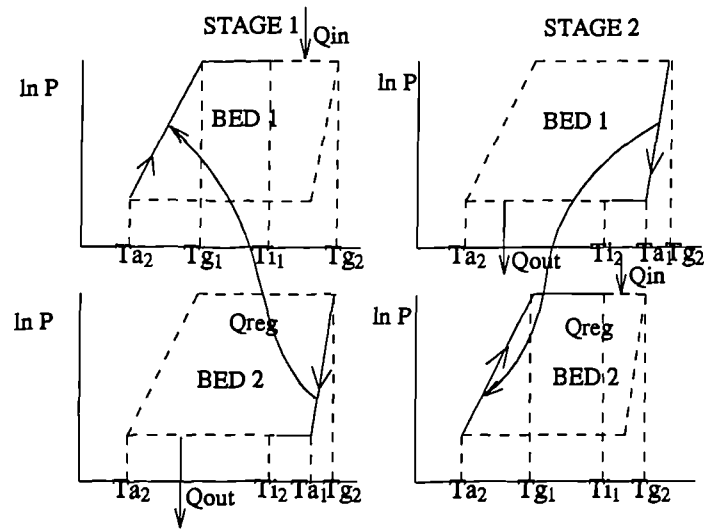
For two beds the COP may be defined as:-

$$COP = \frac{Qref}{Qg + Qh - Qreg} \qquad — (2.26)$$

where:- Qreg = Regenerated Energy (kJ)

Similarly the COA may be defined as:-

$$COA = \frac{Qcond + Qad + Qc - Qreg}{Qg + Qh - Qreg} \qquad — (2.27)$$

Meunier first investigated the theoretical potential of multiple bed cycles in 1985 [33]. He considered the cycle as being reversible except for the energy lost due to the temperature difference necessary between beds to exchange heat. From figure 2.10 it can be seen that to calculate Qreg, the value of Ti_1 and Ti_2 would need to be found. To do this Meunier plotted a graph of dQ/dT vs. T for the whole cycle, see figure 2.11.

FIGURE 2.11

Rate of Change of System Energy with Respect to T
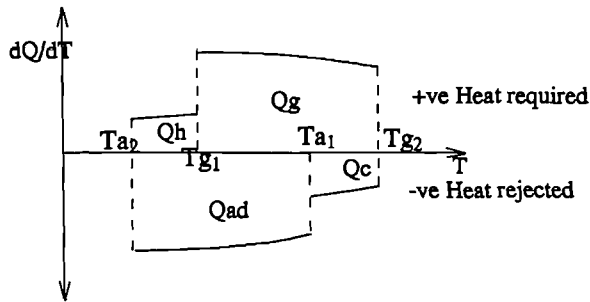
The value dQ/dT is found for every degree K using the equations in Section 2.3. Once the temperature difference between the beds has been established an iterative process is used to match the area under the positive curve between Ta_2 and Ti_1 to the area under the negative curve between Tg_2 and Ti_2, such that

$$\sum_{T=Ta_2}^{T=Ti_1} \frac{dQ}{dT} \Delta T = \sum_{T=Ti_1+\Delta t}^{T=Tg_2} \frac{dQ}{dT} \Delta T \qquad - (2.28)$$

Once this has been accomplished Qreg is automatically known, see figure 2.12.

FIGURE 2.12

Matching of Areas Under Curves to Find Qreg.
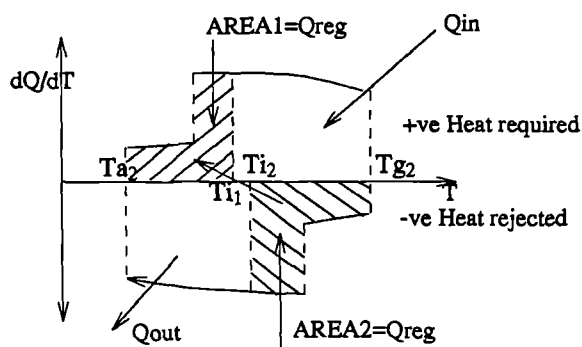
Using the 208C ammonia pair and this technique a similar iterative procedure is used to calculate Qreg for more complex systems. Each time the number of beds is increased by two the number of intermediate temperatures is increased by 1, see figure 2.13.

Using this technique Meunier generated performance figures for different numbers of cascades. These are quoted in the table below, from ref [33].

No. of beds	1	2	4	∞
No. of cascades	0	1	3	∞
COP	0.425	0.684	1.008	1.852
COA	1.420	1.667	1.988	2.964

In the same paper, he then compared the COP's to that of the ideal carnot COP using the same temperature limits, see equation (2.29).

$$COP_{carnot} = \frac{1 - Tc/Tg_2}{Ta_2/Te - 1} \quad - (2.29)$$

He found that the COP of the cycle with an infinite number of cascades and of the intermittent cycle were about 68% and 15% of the ideal carnot COP respectively.

Karagiogas et al [34] and Douss et al [35] continued the work by Meunier. They modelled the two bed adsorber cycle using the zeolite water pair and compared predicted values of COP and COA with experimentally determined ones. The table below summarizes the results obtained by Douss et al in which they get good correlation between test and predictive work.

	single bed		double bed	
	Expt.	Theor.	Expt.	Theor.
COP	0.524	0.490	0.673	0.730
COA	1.386	1.380	1.560	1.560

FIGURE 2.13

Multiple Bed Heat Exchange

4 BEDS

dQ/dT

Qin

+ve Heat required

Ta₂   1   3   Tg₂

T

-ve Heat rejected

Qout

AREA1=AREA2
AREA3=AREA4
Qreg=AREA1+AREA3

8 BEDS

dQ/dT

Qin

+ve Heat required

Ta₂   1 3 5 7   Tg₂

T

-ve Heat rejected

Qout

AREA1=AREA2
AREA3=AREA4
AREA5=AREA6
AREA7=AREA8

Qreg=AREA1+AREA3+AREA5+AREA7

Infinite beds

dQ/dT

Qin

+ve Heat required

Ta₂   Tg₂

T

Qreg

-ve Heat rejected

Qout
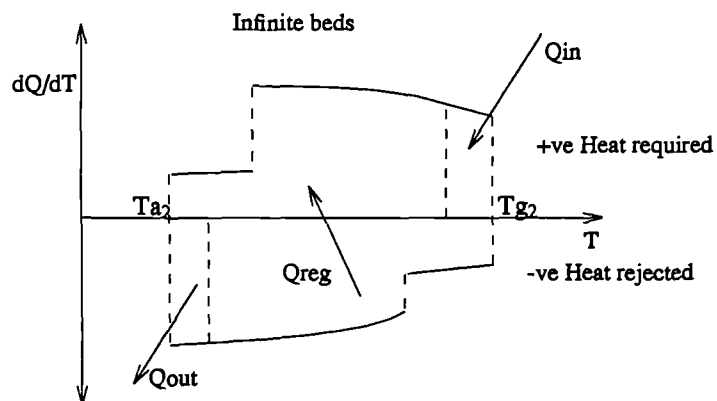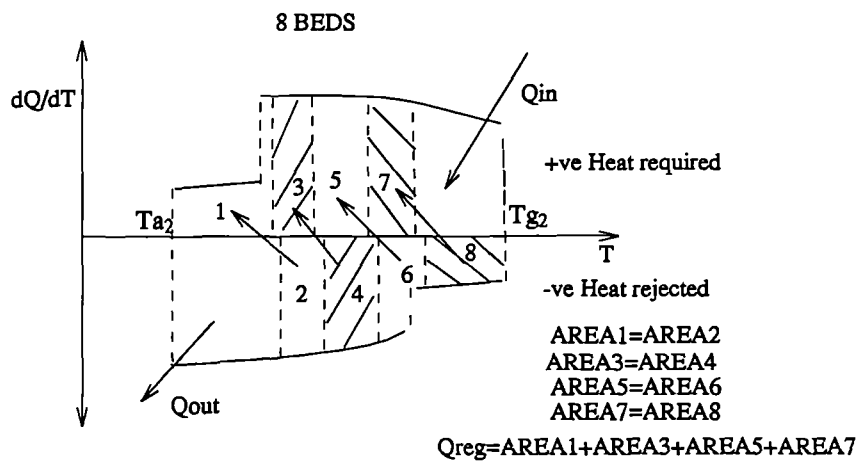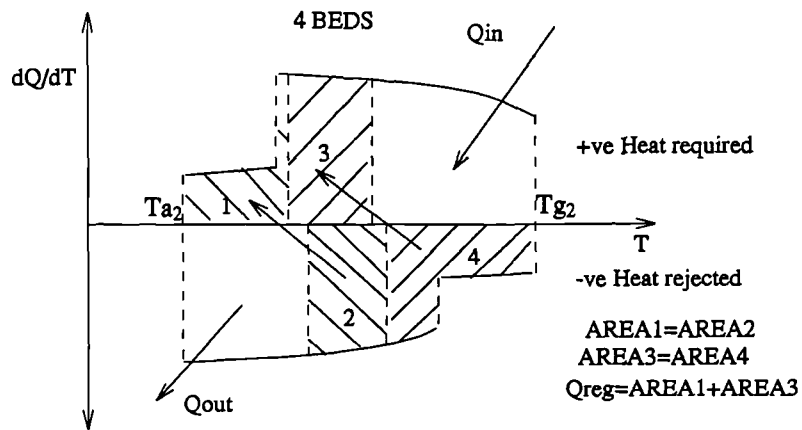
Critoph and Turner [2] used the ammonia charcoal pair for their heat pump cascade modelling. For a four bed adsorber with 80% heat exchange efficiency and ΔT of 10°C they quote a COA of 1.60 for a low upper generating temperature and a COA of 1.80 for a high generating temperature.

Two major problems existed with multiple bed adsorbers as they stood. The first of these was cost. Each extra cascade requires a bed plus adsorbent, pipework, controlled switching valves plus heat exchangers. Once more *than two beds were used the cost* would become prohibitive. The second problem was poor efficiency of the heat exchange due to the mismatch of temperatures between the heating and cooling beds. In 1989, Shelton *et al* [14] reported a system which tackled both of these problems. The system differed from previous attempts in that no mismatch of temperature occurred during heat regeneration. This was achieved by designing the bed such that it had a very high temperature gradient along its length. The bed may then be considered as consisting of a series of small adsorbers able to exchange heat independently of each other. Two such beds run 180° out of phase with each other such that a small section of bed 1 passes heat to a small section of bed 2 via heat exchanger fluid whilst the remainder of the beds stay at their original temperatures, see figure 2.14.

FIGURE 2.14

Method of Heat Transfer for Thermal Wave System
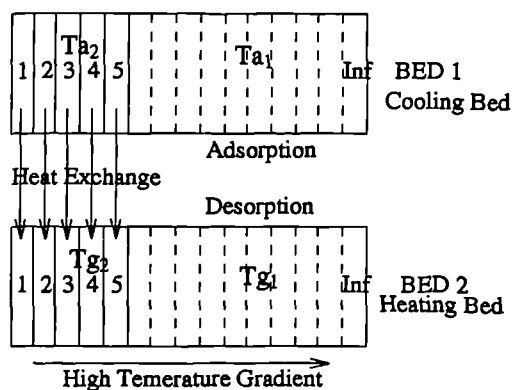
This results in what has been described as a thermal wave moving through both beds, see figure 2.15.

FIGURE 2.15

Temperature Profiles Showing Thermal Wave
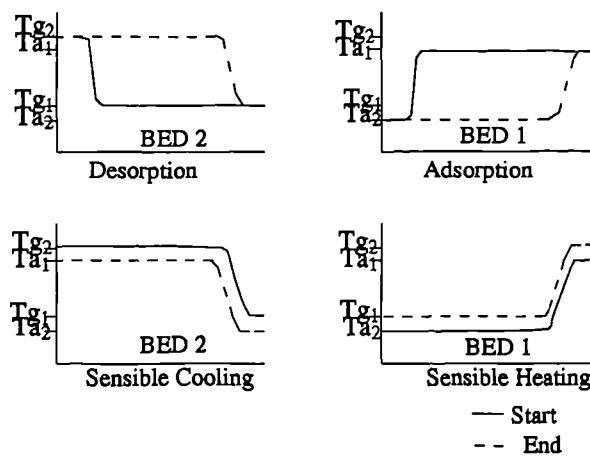
When adsorption and desorption are complete the direction of the heat exchanger fluid is reversed and the beds swap roles.

Shelton *et al* theoretically analyzed the concept with finite difference techniques using a square wave moving through a zeolite ammonia bed. They report a possible COA of over 2.5 dependent upon operating conditions. They conclude that the improved efficiency of this type of system makes the adsorption heat pump a viable contender for commercial use.

The thermal wave idea is comparable to the ideally regenerative cycle discussed by Critoph and Turner [2]. This system consists of two adsorbers running 180 ° out of phase such that all of the available heat during adsorption is transferred to the desorbing bed. In that case Qreg is found simply by plotting a graph similar to that shown in figure 2.11 and finding the area bounded by the adsorption curve when it is superimposed onto the desorption curve, see figure 2.16.

FIGURE 2.16

Ideally Regenerative Cycle.
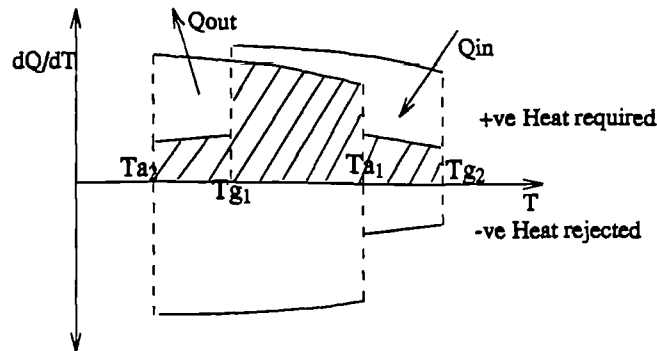
Figure 2.17 shows the some possible obtainable performances using this type of system when the temperature difference ΔT is 10°C. These values are not as high as those reported by some workers and higher than those reported by others. The difference may be due to the different properties of the adsorbent used, the operating conditions or the inclusion of a heat exchange efficiency.

FIGURE 2.17

Performance of Ideally Regenerative Cycles.
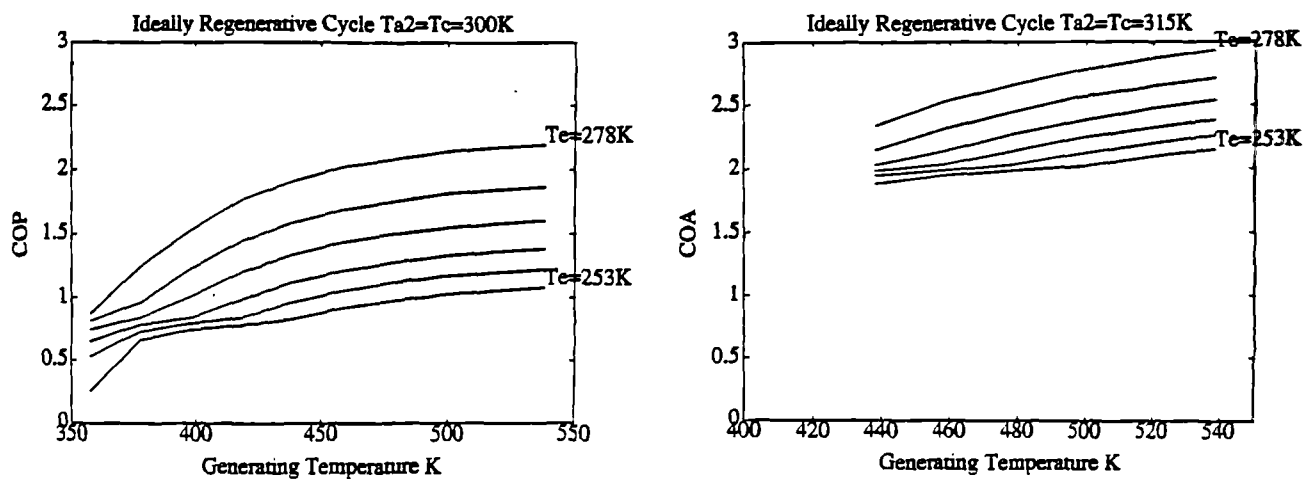
Modelling of Multiple bed Cycles.

The performance of ammonia charcoal multiple bed cycles may be evaluated using the equations in Section 2.3 and the technique described in Section 2.4.

Figure 2.18 shows the variation of COP over a range of operating temperatures with an increasing number of regenerative beds.

FIGURE 2.18

Variation of COP with Increasing Regeneration.

COP Te=253K   Tc=Ta2=300K

COP Te=278K Tc=Ta2=300K
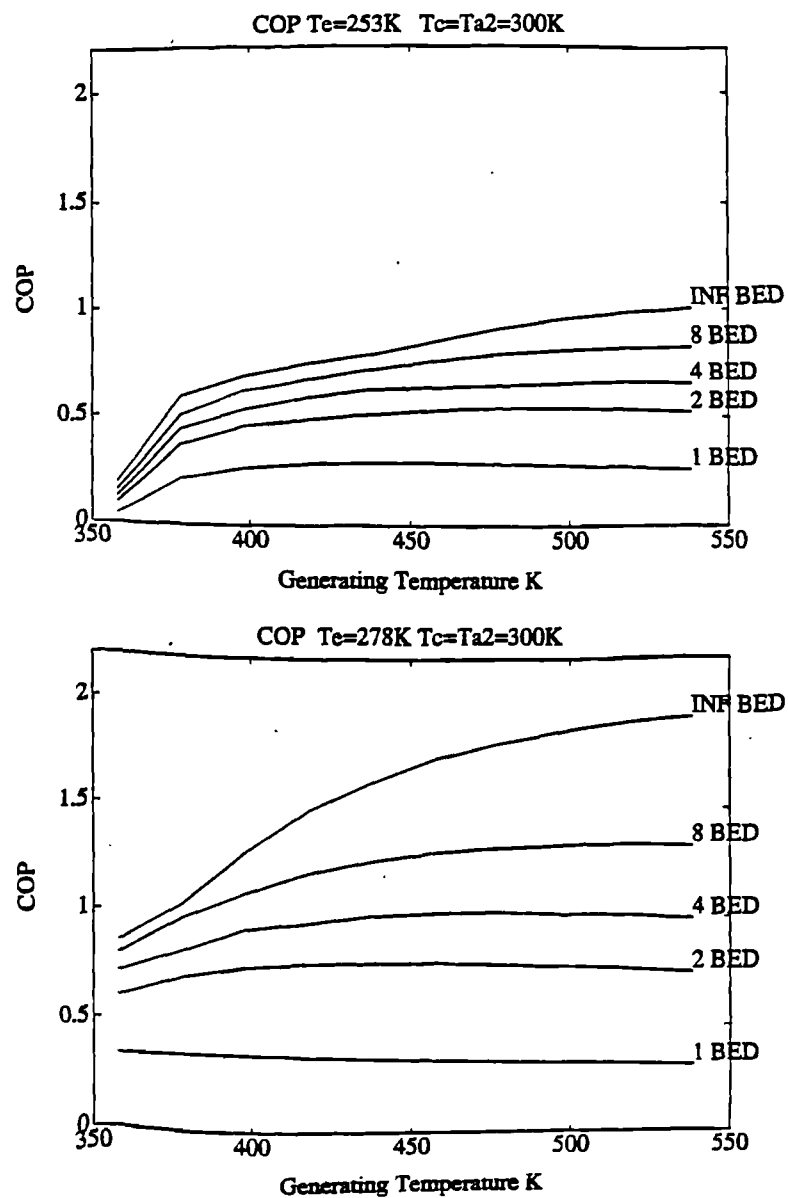
The temperature difference between the beds is taken in all cases to be 10°C. It can be seen from figure 2.18 that as the number of cascades increases, not only does the COP increase but the optimum operating temperatures change. Increasing the upper generating temperature results in improved COP which is not the case for a single bed system. This occurs simply because the energy used in sensible heating of the bed is now being regenerated rather than wasted.

Figure 2.19 shows the percentage increase in COP of multiple beds over single beds for various operating temperatures when $Ta_2 = Tc = 27°C$. It can be seen that the infinite cascade adsorber offers improvements of up to 600% under certain operating conditions. The more beds the system uses, the greater the cost of manufacture. The more realistic two bed adsorber offers improvements of ≈ 75-100% for most conditions.

FIGURE 2.19

Percentage Increase in COP with Increasing Regeneration
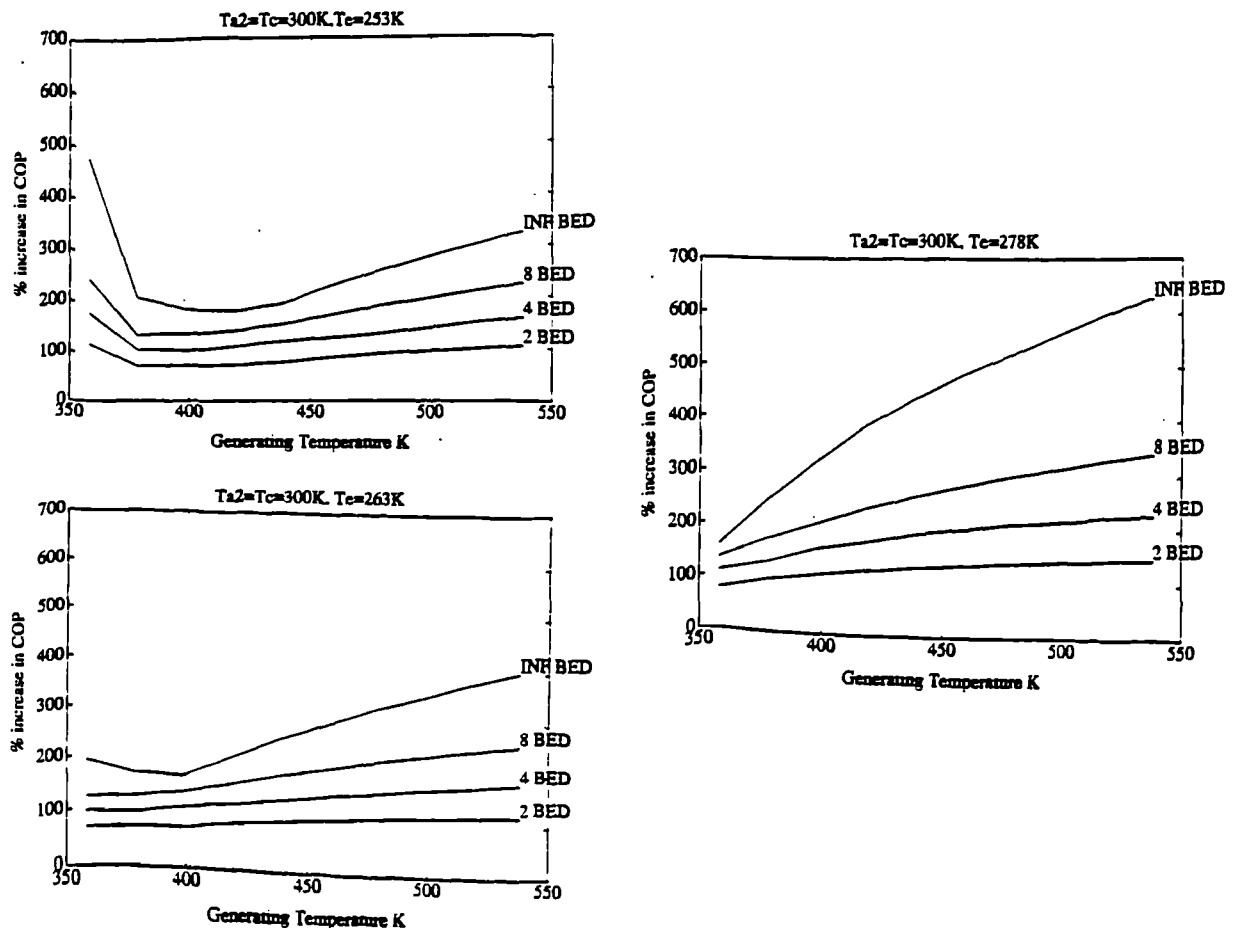
Similar cycle modelling was performed for a cascaded heat pump with Ta_2 = Tc set at 47°C. The resulting plots are shown in figures 2.20 and 2.21.

FIGURE 2.20

Increase in COA with Increasing Regeneration

COA Te=253K Ta2=Tc=320K

COA Te=278K Ta2=Tc=320K
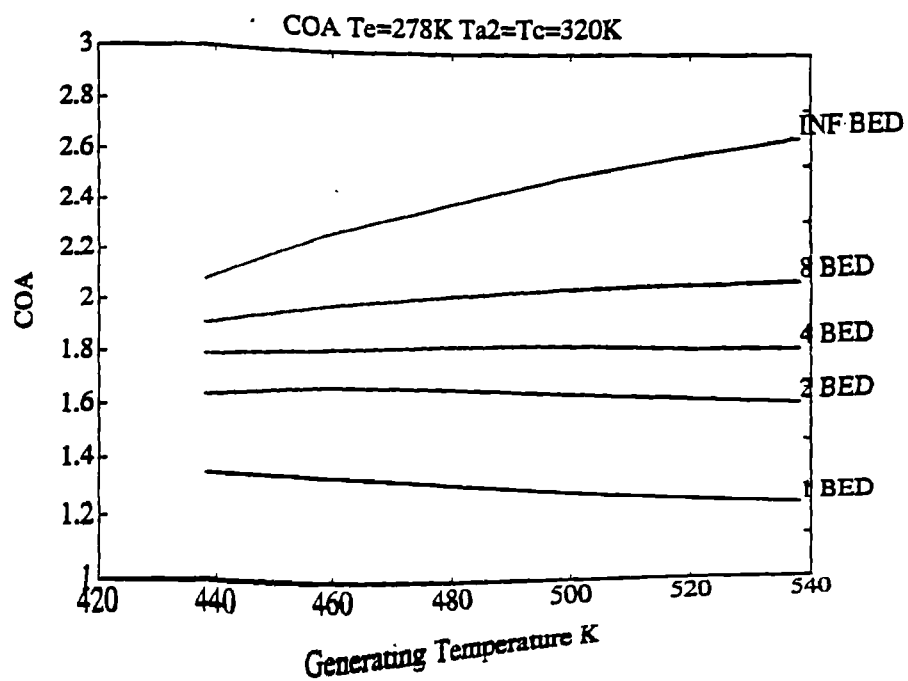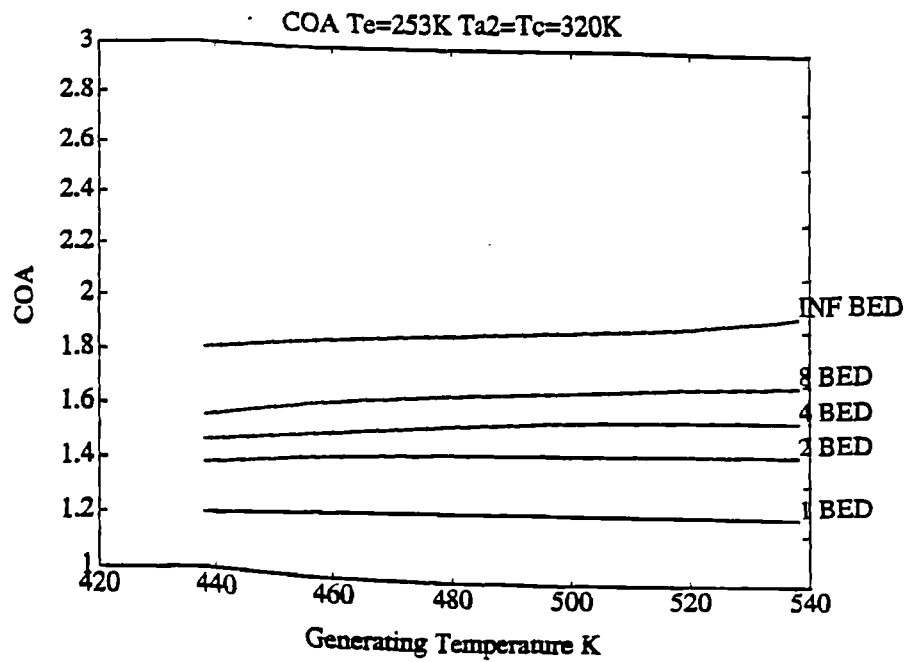
FIGURE 2.21

Percentage Increase in COA with Increasing Regeneration
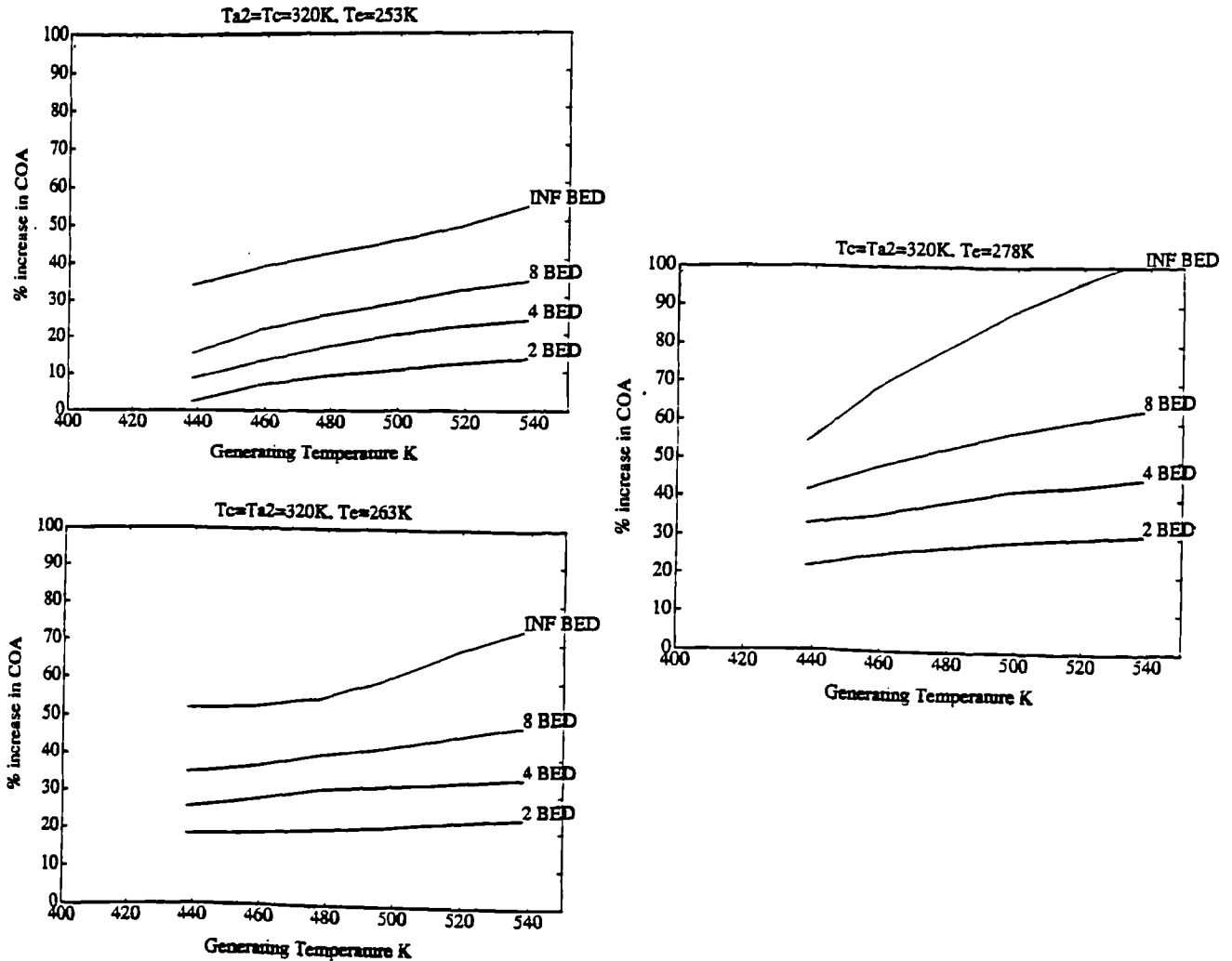
Figure 2.20 shows the COA to have similar trends to the COP and its behaviour is explained by similar reasoning. Figure 2.21, however shows that the COA does not display the kind of improvement as seen with the COP. This is explained with reference to equation (2.27) from which it can be seen that although Qreg decreases the denominator thus increasing the COA, it also decreases the numerator which decreases the COA. The improvement gained through increasing the number of cascades lies between 5% and 100% for most operating conditions.

2.5 Double Effect Cascades.

Double effect cascades present an even better solution to heat management within the adsorbers. In this type of cycle the heat rejected from a bed running with high operating temperatures is used to power a bed running at a lower set of operating temperatures.

Meunier [36] reports theoretical investigation of the double effect cycle using a high temperature zeolite-water bed to drive a low temperature carbon-methanol bed. He presents four case studies for the cogeneration of heating and cooling which are summarized in the table below.

	Hot water 70°C	Steam 120°C	Refrigeration	Hot water 70°C
	Chilled water 2°C	Chilled water 2°C	-10°C	Refrigeration -10°C
COA	1.1	1.35	X	0.9
COP	1.15	0.45	0.85	0.65

He concludes that although cogeneration of hot and cold water or of cold water and steam appear attractive possibilities, it seems difficult to obtain a high COP for low temperature refrigeration.

Critoph and Turner [2] model the ammonia-charcoal pair, see figure 2.22, and quote a COA of 1.81 which compares to COA of ≈2.2 for an ideally regenerative cycle running within the same temperature limits. This type of cycle however has the disadvantage of lowering the charcoal's useful energy output per cycle as compared to that of a standard dual bed system.

Meunier and Douss [37] present results gained from a small scale, 8kW heat source, experimental unit using two zeolite-water beds rejecting heat to one carbon-methanol bed. This three adsorber cascade produced a COP equal to 1.

Apart from the advantages in improvement of efficiencies gained by using double effect cascades, they are ideally suited to situations where waste heat is available and

heating and cooling power is required.

FIGURE 2.22

Double Effect Cascade
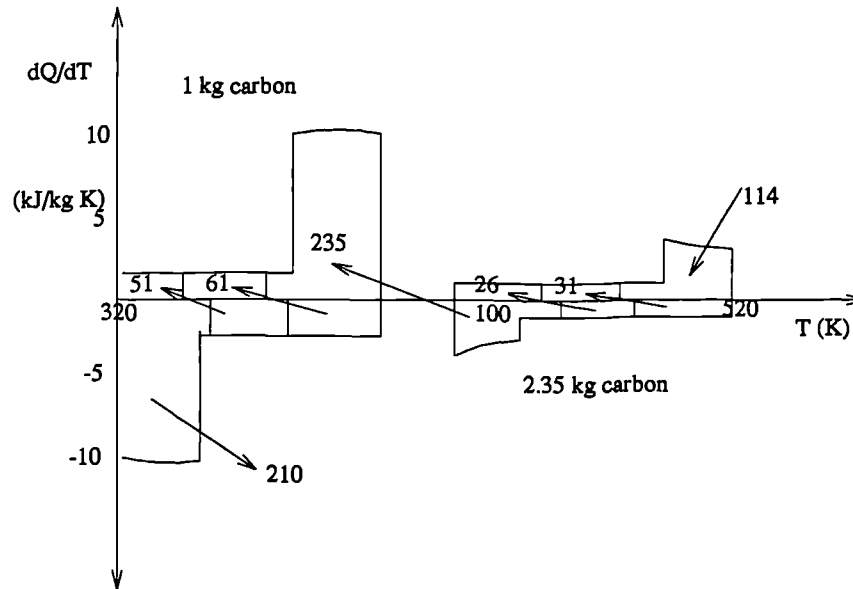
2.6 Conclusions.

The performance of an adsorption heat pump or refrigerator can be bettered by changing the carbon properties. The COP shows the greatest improvement over the properties range and the COA shows the existence of optimum carbon characteristics.

The COP or COA is very sensitive to operating temperatures. Variation of T_{a2} and T_e has a larger effect than T_c or T_{g2} because the isosteres are more closely packed at the concentrated end of the p-T-x diagram. For the temperature ranges surveyed an intermittent single bed adsorber using the charcoal 208C and ammonia pair produces a maximum COP≈ 0.46 and a COA≈ 1.35.

A distinct improvement in performance is obtained by using a multiple bed adsorber. In this type of system two or more adsorbers operate such that heat rejected

from one is regenerated by heating another. It has been shown that if all the heat during the cooling phase is regenerated then a COP≈ 2.0 and a COA ≈ 2.9 are attainable within the temperature limits used. The cost of this infinitely cascaded system would be high, although the thermal wave proposal of Shelton *et al* appears to partially solve this problem. However, for refrigeration significant improvements to COP can be made by use of the relatively simple dual bed system.

Further improvements to the heat management within the cycle can be made by using a double effect cascade. This improves the performance beyond that of an ideally regenerative cycle. The system is highly useful in situations where waste heat is available and cogeneration of heating and cooling power is required.

Overall, the adsorption cycle has been very well investigated in theory, experiment and practical application by many different workers. The sophistication of the cycle has grown such that the a thermal wave type system approaches its thermodynamic ideal in performance.

References

1. Critoph R.E, Vogel R
"Possible Adsorption Pairs for Use in Solar Cooling" International Journal of Ambient Energy, Vol 7, No. 4, 1986, pp183-190

2. Critoph R.E, Turner H.L
"Performance of Ammonia/Activated Carbon and Ammonia/Zeolite Heat Pump Adsorption Cycles." Proceedings Conference. Pompe a Chaleur Chiminique De Haut Performance. Perpignan. 1988 (Publ. Lavoisier.) pp 202-211

3. Meunier F
"Etude des Couples Adsorbant Solide-Refrigerant Liquide." Commision des Communautes Europeennes. Report No. EUR 7708FR

4. Collier Engineering Services.
"Determination of Properties of Zeolite/Refrigerant combinations for Solar Refrigeration Systems." United States Energy Department. Ref No. DE-AC03-838F11919

5. Plank R, Kuprianoff J

"Die Kleinkaltemaschine." Springer-Verlag, Berlin/Gottingen/Heidlberg.(1960)

6. Miller E.B

"The Development of Silica Gel Refrigeration" The American Society of Refrigerating Engineers. Vol 17. No. 4. April 1929

7. Hulse G.E

"Freight Car Refrigeration by an Adsorption System Employing Silica Gel." Refrigerating Engineer. Vol 17. No. 2. Feb 1929.

8. Pons M, Guilleminot J.J

"Design of an Experimental Solar Powered Solid-Adsorption Ice Maker." J.S.E.E., A.S.M.E., Vol 108,Nov 1986. pp 332-337

9. Pons M, Grenier Ph

"Experimental Data on a Solar-Powered Ice Maker using Activated Carbon and Methanol Adsorption Pair." J.S.E.E., A.S.M.E., Vol 109, Sept 1987.pp 303-310

10. Tchernev D.I

"Solar Refrigeration Using Zeolites." Proceedings of the 14th Intersociety Energy Conversion Conference.(14th) Vol 2 ,pp 2070-2073 .(ACS Rep. No.799985)

11. Tchernev D.I

"Solar Air Conditioning and Refrigeration Systems Using Zeolites." Science et Technique du Froid. Vol 3 . 1982 . pp 209-215

12. Grenier Ph, Guilleminot J.J, Mester M, Meunier F, Pons M

"Experimental Results on a Twelve Meter Cubed Solar Powered Cold Store Using the Intermittent Zeolite 13X/water Cycle." Solar World Congress. Vol 8 . Part 1. pp353-358

13. Jank R, Januschkowetz G, Mierke T, Voigt B

"Development of a Zeolite/Water Adsorption Heat Pump for the Simultaneous Supply of Heating and Cooling Power."
Energy: New Frontiers. Vol 3. pp 1324-1327

14. Shelton Sam V, Wepfer William J, Miles Daniel J

"Square Wave Analysis of the Solid-Vapor Adsorption Heat Pump." Heat Recovery Systems & CHP. Vol 9 No. 3. 1989. pp233-247

15. Shridhar K

"Studies on Activated Carbon-Methanol Pairs with Relevance to Ice Making." Msc Report. AIT(Asian Institute of Technology).Aug 1987

16. Excell R.H.B, Bhattacharya S.C, Shridhar K, Upadhyaya Y.R, Wibulswas P

"A Charcoal Methanol Solar Refrigerator." Internal Report AIT

17. Upadhyaya Y.R

"Intermittent Solar Activated Charcoal Methanol Adsorption." Internal Report. AIT 1986.

18. Grenier Ph, Pons M

"Experimental and Theoretical Results on the use of an Activated Carbon CH3OH Intermittent Cycle for the Application to a Solar Powered Ice-Maker." Solar World Congress. Vol 1 1984. pp 500-506

19. Meunier F

"Research and Development Toward New Thermochemical Cycles for Cold Production From Solar Energy Using Solid Adsorbents." Journal of Solar Energy Research. Vol 1, Part 1 . 1983. pp 23-35

20. Bhattacharya M, Roux J.A

"Experimental Investigation of a Refrigerator and Heat Pump Using Natural Zeolite" Proceedings of the 21st Intersociety Energy Conversion Eng Conference. Vol 2. 1986. pp 766-771. ACS. Rep No. 869169

21. Guilleminot J.J, Meunier F

"Experimental Study of a Solar Refrigerator Using the Zeolite 13X/Water Cycle." Revue Generale de Thermique. Vol 20. Pt 239. 1981. pp 825-834

22. Tchernev D.I

"Solar Energy Application of Natural Zeolites." Natural Zeolites, Pergamon Press 1978. pp 479-485

23. Offenhartz P.O'D, Rye T.V, Malsberger R.E, Schwartz D

"Methanol-based Heat Pump for Solar Heating,Cooling and Storage.Phase III" Final Report, Materials Chemistry and Energy Division, Dept of Energy and Environment, Brookhaven National Laboratory.

24. Worsoe-Schmidt P

"Solar Refrigeration for Developing Countries Using a Solid-Adsorption Cycle." International Journal of Ambient Energy. Vol 4. Number 3. July 1983. pp 115-124

25. Guilleminot J.J, Meunier F, Mischler B

"Etude de Cycles Intermittents a Adsorption Solide Pour la Refrigeration Solaire." Revue Phys. Appl. Vol 15 March 1980. pp 441-452

26. Restuccia G, Caccoila G, Quagliata R

"Identification of Zeolites for Heat Transformer,Chemical Heat Pump and Cooling Systems." International Journal of Energy Research. Vol 12 .1988. pp 101-111

27. Critoph R E

"Performance Limitations of Adsorption Cycles For Solar Cooling." Solar Energy. Vol 41. No1. 1988. pp 21-31

28. Passos E, Meunier F, Gianola J.C

"Thermodynamic Performance Improvement of an Intermittent Solar-Powered Refrigeration Cycle Using Adsorption of Methanol on Activated Carbon." Heat Recovery Systems. Vol 6 .No 3 .1986. pp 259-264

29. Meunier F, Mischler B

"Solar Cooling Through Cycles Using Microporous Solid Adsorbents." Sun 2. Vol 1. 1979. pp 676-680

30. Bougard J

"Thermodynamical and Technical Problems in Solar Adsorption Refrigeration." Science et Technique du Froid.Pt 1.1986. pp 676-680

31. Douss N, Meunier F

"Effect of Operating Temperatures on the Coefficient of Performance of Active Charcoal-Methanol Systems." Heat Recovery Systems & CHP. Vol 8. No. 5. 1988 pp383-392

32. Guilleminot J.J, Meunier F, Mischler B

"Etude de Cycles Intermittents a Adsorption Solide Pour la Refrigeration Solaire." Revue Phys Appl. Vol 15.1990 pp 441-452

33.
Meunier F

"Second Law Analysis of a Solid Adsorption Heat Pump Operating on Reversible Cascade Cycles: Application to the Zeolite/Water Pair." Heat Recovery Systems. Vol 5. No.2 1985. pp 133-141

34. Karagiorgas M, Meunier F, Rios J

"Study of Solid-Adsorption Heat Pump Connected with External Heat Reservoirs of Finite Heat Capacity:Case Study of the Zeolite/Water Pair." CEC/British Gas. International Workshop Adsorption Heat Pumps. April 1988. pp264-272

35. Douss Nejib, Meunier Francis E, Lian-Ming Sun

"Predictive Model and Experimental Results for a Two Adsorber Solid Adsorption Heat Pump." Ind.Eng.Chem.Res. Vol 27. No 2. 1988. pp310-316

36. Meunier F

"Theoretical Performances of Solid Adsorbent Cascading Cycles Using the Zeolite/Water and Active Carbon/Methanol Pairs:Four Case Studies." Heat Recovery Systems. Vol 6. No 6. 1986. pp491-498

37. Meunier F, Douss N

"Adsorptive Heat Pumps:Active Carbon/Methanol and Zeolite/Water Pairs." CEC/British Gas. International Workshop Adsorption Heat Pumps. April 1988. pp63-72

38. ASHRAE Handbook

Publ. American Society of Heating, Refrigerating and Air Conditioning Engineers Inc. Atlanta 1982 pp17.105

39. Rivkin S L

"Thermodynamic Properties of Gases" 4th edition Hemisphere 1988 pp69-99

40. ASHRAE Handbook

Publ. American Society of Heating, Refrigerating and Air Conditioning Engineers Inc. Atlanta 1982pp17.35

41. Rogers G.F.C, Mayhew Y.R

"Thermodynamic and Transport Properties of Fluids" Third Edition 1980 Camelot Press Ltd. pp12

3. ACTIVATED CHARCOALS AND THEIR POROSITY CHARACTERISTICS.

Introduction

This section deals with the porosity characteristics of different activated charcoals. A description of the apparatus used to measure the pressure, temperature, concentration (p-T-x) data is presented and a range of currently manufactured charcoals are assessed for use in heat pumping or refrigerating adsorption systems.

The author was unable to find any such similar survey prior to this work since other workers tend to measure only the data relevant to their own particular charcoal. The results shown in Section 3.3 prove that it is possible to double the useful energy output of an adsorption system by choosing the charcoal with the p-T-x characteristics best suited to the system operating temperatures.

Further to this, surface treatments were carried out on selected charcoals with the aim of modifying its surface complexes and consequently its p-T-x characteristics. The results of these experiments, discussed in detail in Section 3.4, proved to be interesting but inconclusive.

3.1 Manufacture and Structure of Activated Charcoals.

Manufacture of Activated Charcoals.

Activated charcoals, also known as active carbons are made by a process of carbonization and activation from starting materials ranging from polymers to wood chips. Almost any organic material may be used, but those most commonly found in commercial manufacture are coal, peat, coconut shell and wood.The product of simple carbonization, or the pyrolisis of the starting material in the exclusion of air, is a virtually inactive charcoal type substance which has a very small internal surface area in the order of m^2/g. Activation is achieved by heating the material to temperatures of 600°C - 1100°C whilst passing steam or carbon dioxide over the charcoal. During this phase layers of carbon atoms are burnt out of the charcoal and the tarry substances blocking the pores are transported away by the activation gas. At the end of this process the material is now an activated charcoal with a highly developed internal porous structure and a large internal surface area in the order of 600 m^2/g - 2000 m^2/g, and it is this feature which makes it an effective adsorbent.

In large scale manufacture the activated charcoal is produced in batches in either rotary, vertical or multiple hearth kilns, and the temperature and rate of activation is used to control the pore size. The whole activation process has been much studied and it has been found that the addition of certain chemicals to the starting material can increase the yield from a batch. Chemical treatment however adds to the cost and the benefits of its usage must weighed against the cost of the final product. The cost of activated charcoal varies depending on the starting material and the expense of processing. The price of 208C, a coconut shell based charcoal produced by Sutcliffe Speakman, is approximately £4 per kg. Other chemically impregnated charcoal using expensive polymers as a starting material can cost anything up to £20 per kg.

The Structure of Activated Charcoals.

Activated charcoal has properties more or less the same as those of graphite. Graphite itself is composed of layer planes formed by carbon atoms ordered into regular hexagons and joined to each other by perpendicular links, see figure 3.1.

FIGURE 3.1

Structure of Graphite
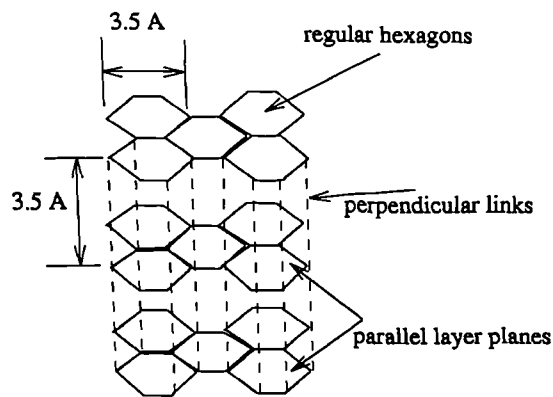
Activated charcoal differs in structure from graphite in that it is far less perfectly ordered. The layers still consist of regular hexagons but they are not orientated with respect to their common perpendicular axis. The angle of one layer plane with respect to another is random and the layers overlap each other irregularly. The section of layer plane is known as the elementary crystallite and their schematic arrangements as found in activated charcoals is shown in figure 3.2.

FIGURE 3.2

Schematic Arrangement of the Elementary Crystallites
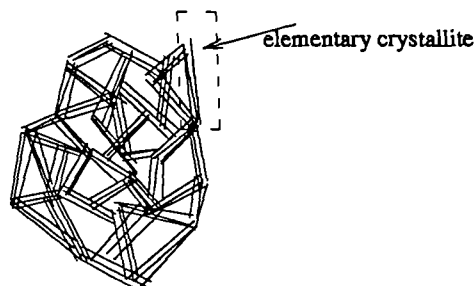
It is the spaces between these elementary crystallites which become cleared during the activation process to form voids known as pores. It is generally believed that pores vary in shape and type. The shape may be ink-bottled (contraction at the pore throat), slit shaped, 'V' shaped or tapered. The four different pore types to be found are shown in figure 3.3.

FIGURE 3.3

Types of Pore
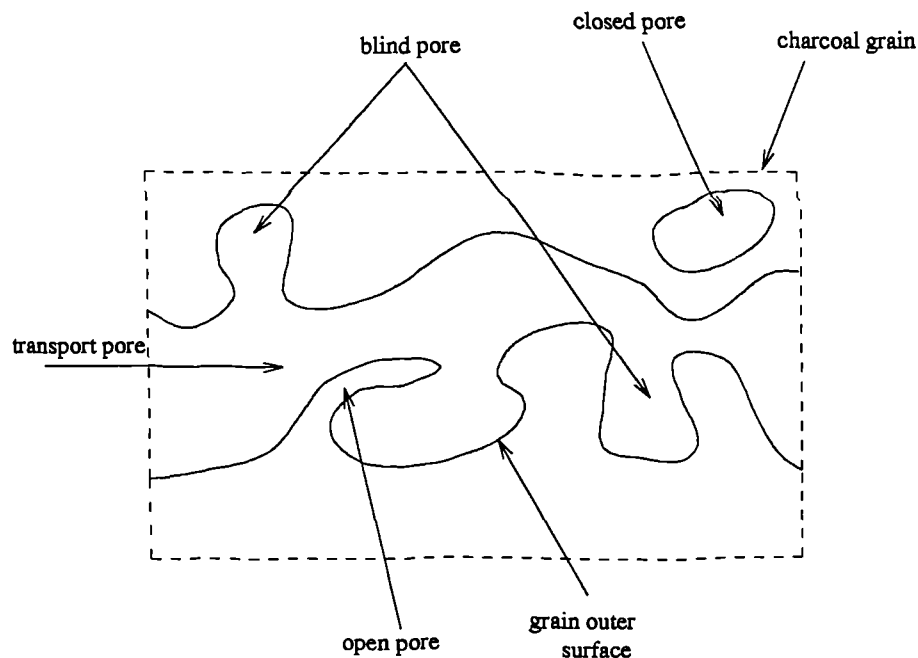
The pores also vary in size and may be classified according to the International Union of Pure and Applied Chemistry (IUPAC) [1] as follows:-

micropores ≤ 2 nm

2nm $\leq$ mesopores ≤ 50 nm

50nm $\leq$ macropores

In short the pore shape size and type is random and varies considerably with the starting materials and the process. Figure 3.4 shows some electron micrographs taken at Warwick University of the charcoal 208C produced by Sutcliffe Speakman from coconut shell.

FIGURE 3.4

Examples of Porosity.
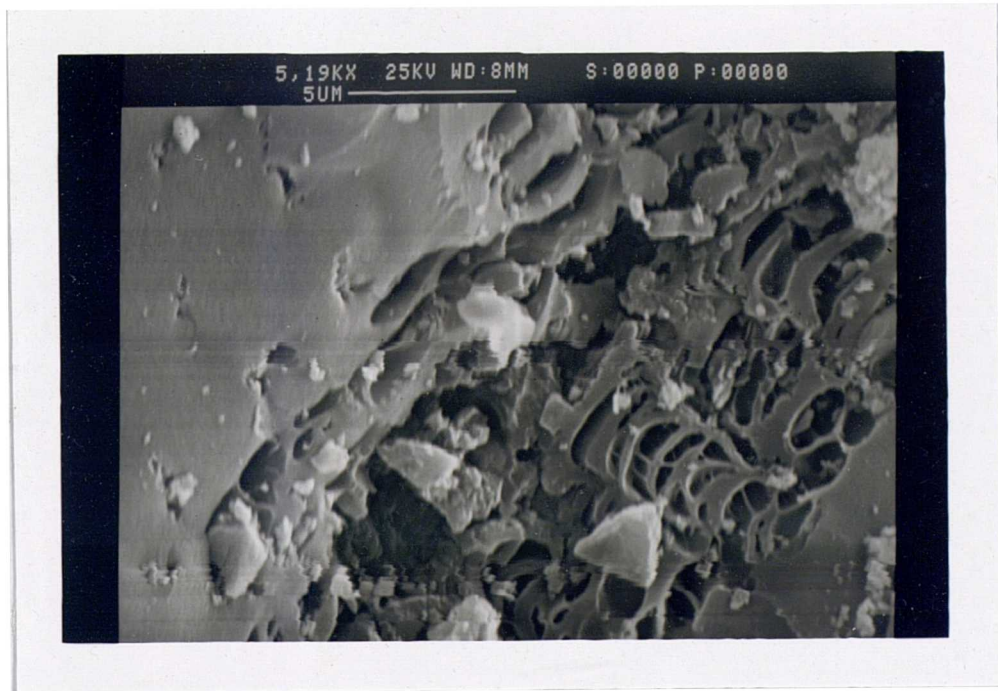
The first photograph shows the structure of mainly macropores and some mesopores. The second photograph shows mesopores and some of the larger micropores in the order of 50nm.

Extensive research has been carried out into all aspects of activated charcoal, their main use being molecular sieves, and for this reason the author refers the reader to refs [2] -[4] if he or she should require any further information.

3.2 Theory of Microporous Adsorbents.

The Process of Physical Adsorption.

The adsorptive properties of activated charcoal are determined by its chemical composition as well as its porosity. In the presence of partially burnt off graphite layers in the crystallites, the arrangement of the electron cloud in the carbon skeleton is changed. As a result residual valencies or unpaired electrons appear and it is the resulting van der Waal's forces which influence the adsorptive characteristics of the charcoal, especially in the case of polar adsorbates such as ammonia and water. It is for this reason that physical adsorption is also known as van der Waal's adsorption.

When activated charcoal comes into contact with a gas, the gas molecules strike the charcoal surface and some remain trapped for a certain time period and in physical adsorption this binding rate is very high.

The gas reaches the outer charcoal surface by means of normal gas diffusion. From there the molecules can proceed to the internal surface of the pore in one of four ways.

(i) convective flow - only present in large pores.

(ii) molecular (Knudsen) diffusion - transport method in small pores.

(iii) surface diffusion - the adsorbed gas molecule makes successive jumps between adsorption centres.

(iv) adsorbate transfer - depends on the width of the pores and the degree to which they are filled with adsorbate.

The equations representing the volume filling of micropores are described in the following section.

The Potential Theory of Adsorption and the Dubinin - Radushkevich Equation.

The surface of a charcoal may be thought of as a plane over which the potential energy varies from point to point. The points of maximum energy are known as adsorption sites or centres. If all of the adsorption sites have the same potential energy then the surface is known as a homogeneous surface. When the surface is covered in centres of varying energy the surface is known as heterogeneous. This heterogeneous surface is most commonly found in activated charcoals.

The potential theory of adsorption is based on the idea that molecules of adsorbed gas are held in a compressed state by the attractive forces acting from the surface to a certain distance into the surrounding space.

For a homogeneous plane surface all points at the same distance from the surface will have the same potential ε_i, and the potential will fall to zero at a point r_{max} away from the surface, see fig 3.5a.

A volume of V_i is enclosed between each equipotential surface and the surface of the charcoal. The maximum enclosed volume is V_0 which represents the total limiting adsorption space of a given surface. The real case, shown in fig 3.5b, is obviously more complex. It is still true to say however that there is a maximum limiting volume between

FIGURE 3.5

Schematic Representation of Force Field at Charcoal Surface.

3.5a Plane Homogeneous Surface   3.5b Real Surface
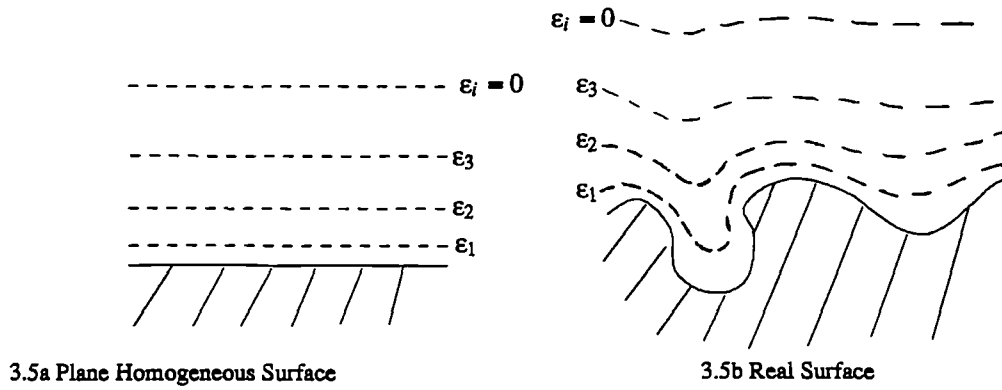
the plane of zero potential and the adsorbent surface. In this case the adsorbate exists in a compressed state, and its density is not constant, being a maximum at the solid surface and a minimum at $\varepsilon_i = 0$. It was proposed by Polanyi [3] that the adsorption potential ε may be represented by the equation for isothermal work of compression, equation (3.1).

$$\varepsilon_i = R\ T\ \ln\frac{p_2}{p_1} \qquad — (3.1)$$

where:-

p_2 is the pressure of the compressed adsorbate on an equipotential surface

p_1 is the pressure of the adsorbate in the gaseous state.

In an extensive study, Dubinin and Radushkevich [5] found the relationship between V and ε to be described by an equation which had the form of a Gaussian distribution, equation (3.2).

$$V = V_0 \exp[-k\ \varepsilon_i{}^2] \qquad — (3.2)$$

where:-

k is a constant, V_0 is the limiting volume for adsorption and V is the volume filled at an equipotential plane.

Substituting equation (3.1) into equation (3.2) gives,

$$V = V_0 \exp[-k \ (R \ T \ \ln\frac{p_2}{p_1})^2] \quad — (3.3)$$

Equation (3.3) is further developed by analysis of the constant k.

It may be proven that k is a function of two other constants β and B, Ref [6], such that

$$k = \frac{B}{\beta^2} \quad — (3.4)$$

where,

B is a function of the carbon microstructure. Its value decreases as the microporosity of the carbon increases.

β is the affinity coefficient which is a function of the adsorbate only, and is approximated by the ratio of the adsorbate volume at T to that of a reference gas, usually benzene at the same temperature. For ammonia β is quoted as 0.28 Ref [7].

Now, p_2 is the saturated vapour pressure of the adsorbate at temperature T and will henceforth be written as p_{SAT}, and the system pressure p_1 will be written as p. Substituting equation (3.4) into equation (3.3) produces the Dubinin-Radushkevich equation (3.5).

$$V = V_0 \exp[-B \ (\frac{RT}{\beta} \ \ln\frac{p_{SAT}}{p})^2] \quad — (3.5)$$

Critoph and Turner [8] found from error analysis on experimental data that the porosity characteristics of a charcoal could be equally well represented by a modified form of the D-R equation (3.6).

$$x = x_0 \exp[-B \ (\frac{R \ T}{\beta} \ \ln\frac{p_{SAT}}{p})^2] \quad — (3.6)$$

x is the adsorbate mass concentration at T and p.

x_0 is the limiting adsorbate mass concentration.

Also, the saturated liquid temperatures and pressures are represented by the straight line equation (3.7).

$$\ln p_{SAT} = A - \frac{C}{T_{SAT}} \qquad - (3.7)$$

where A and C depend on the adsorbate and T_{SAT} is the saturation temperature at system pressure p.

Substituting this into equation (3.6) produces a final version of the D-R equation (3.8), see appendix 3a for proof.

$$x = x_0 \exp[-B \, (\frac{CR}{\beta})^2 (\frac{T}{T_{SAT}} - 1)^2] \quad - (3.8)$$

where C is the slope of the saturation line for a particular refrigerant.

Generally, it is not necessary to know B,C and β individually and these constants are grouped together as a single constant K_1. Therefore equation (3.8) becomes,

$$x = x_0 \exp[-K_1(\frac{T}{T_{SAT}} - 1)^2] \quad - (3.8a)$$

An extension of equation (3.8a) is that of the Dubinin Ashtikov [3] equation (3.9), which employs a variable index n which allows a better fit to the charcoal porosity characteristics.

$$x = x_0 \exp[-K_2(\frac{T}{T_{SAT}} - 1)^n] \quad -(3.9)$$

Equations (3.8a) and (3.9) will be used in the analysis of the results of the porosity tests as described in sections 3.3 and 3.4.

3.3 Porosity Characteristics of Charcoals.

Measurement of p-T-x Data

In order to calculate cycle efficiencies as discussed in section 2 we must measure the porosity characteristics of the adsorbent. At a certain pressure and temperature the adsorbent will contain a certain mass of refrigerant. This is generally known as p-T-x data and it can be measured using the equipment shown in figure 3.6.

FIGURE 3.6
p-T-x Data Measurement Apparatus
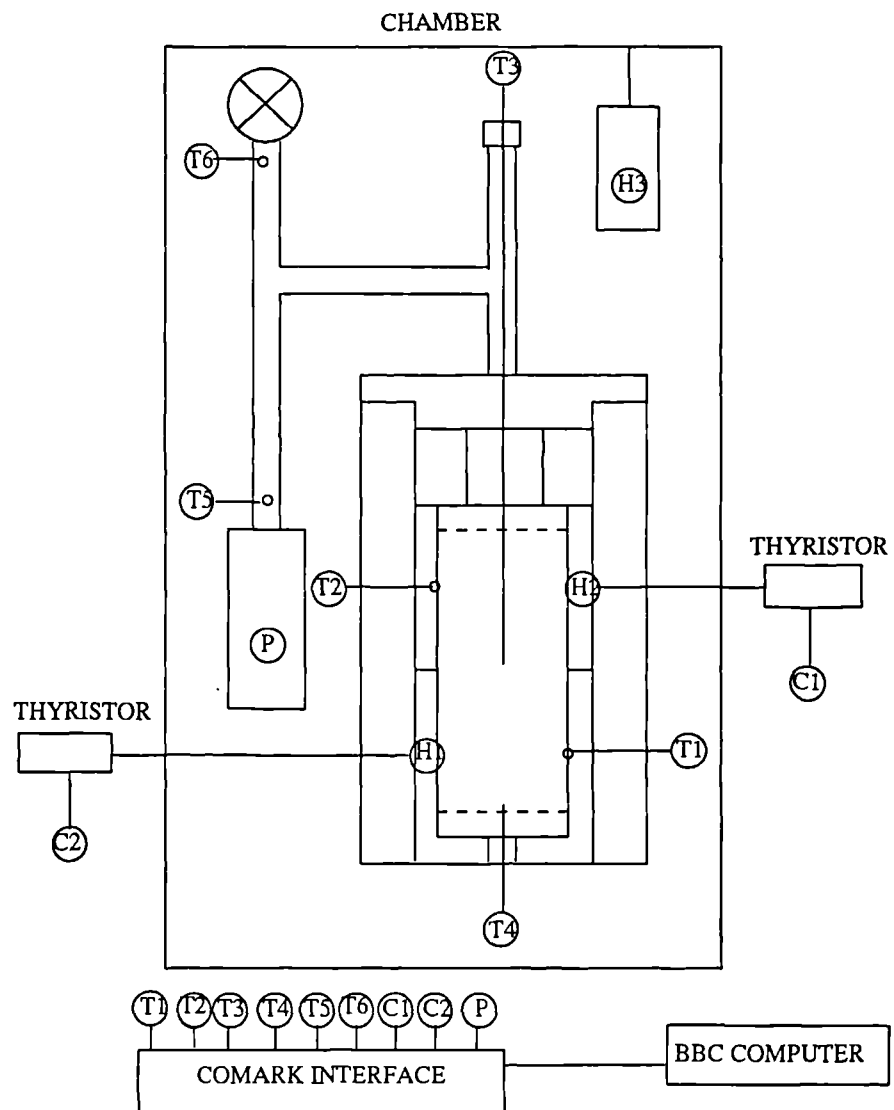
The apparatus consists of an electrically heated stainless steel pressure vessel 25 mm O.D. x 150 mm long. The heating is by means of two band heaters H1 and H2. The vessel temperature under each heater is measured by bare ended thermocouples T1,T2 and transferred to the BBC computer via a Comark Compuface interface. A PID control algorithm written within the computer is used to modulate the heaters via the interface and thyristor controllers, maintaining T1 and T2 at the required temperature. The temperature is measured by two stainless steel sheathed thermocouple probes positioned at the centre T3 and at the end T4 of the sample. The sample is spaced about 10 mm from the ends of the vessel by a stainless steel gauze to avoid any possible cold spots. The pressure P in the system is measured by a Druck PDCR 921 0-40 bar strain gauge pressure transducer via the interface. The entire apparatus is contained within a chamber heated by H3 to ensure that condensation does not take place at any cold spots. Pipe work temperatures T5 and T6 are continuously monitored to ensure they are above saturation temperature.

Experimental Method

Test Method

(i) All samples are degassed at 250 ° for 24 hrs under a vacuum of 0.2 Torr and then stored in an inert gas.

(ii) The empty vessel is evacuated and weighed.

(iii) The sample is transferred to the vessel under an inert atmosphere and the vessel is re-evacuated.

(iv) The mass of the sample and vessel is recorded and the mass of the sample calculated.

(v) The vessel is charged with ammonia, evacuated, recharged and re-evacuated.

(vi) The vessel is charged with ammonia and weighed. The mass of ammonia is calculated.

(vii) The vessel is placed in its insulating jacket and connected to the power supplies and control systems.

(viii) The controlling program takes the vessel through a series of set temperatures. When both the carbon end centre temperatures T3, T4 are within 1°C of the vessel temperature T1, T2 readings of pressure and temperatures are taken and the concentration calculated from knowledge of ammonia properties, vessel and pipework volumes and temperatures.

(ix) On the completion of a "nominal isostere" the vessel is reweighed to ensure that no leakage has occurred. A certain amount of ammonia is then released from the vessel, and the vessel reweighed to determine the new mass of ammonia.

(x) The whole process from (vii) is repeated until five nominal isosteres are obtained.

When concentrations are calculated it is assumed that a volume occupied by the ammonia gas is the difference between the vessel plus pipework volume and the volume already occupied by the mass of the sample charcoal based on its apparent density. The mass of the gaseous ammonia is calculated from the system pressure and the vessel and pipework temperatures.

The volume and density data required to calculate the ammonia concentration is derived as follows:-

Vessel and Pipework Volume

was found by weighing the apparatus both evacuated and full of a refrigerant at a known pressure and temperature. It was calculated to be 57.85 cc ±0.2 cc.

Pipework Volume

This was calculated as 17.33 cc from the known length and diameter of the pipework.

Apparent Charcoal Density

A weighed and degassed sample of charcoal is immersed in water until adsorption is complete. The sample is then dried in warm air until all surface water has evaporated and only adsorbed water remains in the sample. The sample is placed in a measuring cylinder which is then topped up with a known volume of water. The total volume of sample plus water is measured and the difference between this and the known top up volume will allow us to calculate the void volume likely to be filled with gaseous ammonia during test. The apparent density is defined by equation below.

$$\text{apparent density} = \frac{\text{dry charcoal mass}}{\text{charcoal} + \text{micropore volume}}$$

Error Analysis

The maximum instrumentation errors are :-

pressure   ± 0.02 bar (manufacturers data and calibration)

mass of vessel   ± 10 mg (manufacturers data)

temperature   ± 2°C (Maximum possible error in mean sample temperature.

                  The individual sensors are correct to ± 0.5°C)

This maximum error in the saturation temperature T_{SAT} occurs when the pressure is at its maximum possible value of 30 bar.

T_{SAT} ± 0.04°C ± 0.0001%

The maximum error in $\frac{1}{T}$ occurs when T is at its minimum 30°C.

$\frac{1}{T}$ $\pm 1.4 \times 10^{-5} \text{K}^{-1}$ $\pm 0.7\%$

Given a nominal dry charcoal sample mass of 15g and conditions of maximum pressure and minimum temperature and concentration, and assuming an error of $\pm$ 10mg in both the measurement of the charcoal mass and total mass measurement at the start of an isostere test, the worst error in the calculated ammonia concentration x is $\pm$ 0.53%.

Test programme

The porosity characteristics of 12 types of activated charcoal and 1 type of zeolite (for comparison) were found. Three different samples of 208C were tested in order to assess how great the variation could be between individual batches. The charcoals were chosen to include a range of starting materials and activation processes. The charcoal names, manufacturers and types are listed in Table 3.1, and figure 3.7 overleaf shows the physical form of a small sample of each.

Some of the samples were tested on a different piece of test apparatus which worked on exactly the same principles as already described but with upper temperature and pressure limits of 120°C and 20 Bar respectively. The pressure and temperature range was not as large because originally the data was collected for modelling refrigeration systems only.

Using the test method detailed, the p-T-x data for five isosteres was recorded for each of the 15 samples listed in Table 3.1. This data was then fitted to both the D-R and D-A equations (3.8a) and (3.9) respectively in order to identify the important variables x_0 and K_1 or K_2 and n. Fitting was achieved by specially written MATLAB software which minimizes the sum of the squares of the error between the real data and that generated

from the D-R or D-A equations. The variables are listed along with the fitting error for each charcoal and the pressure and temperature limits within which the equations are valid in Tables 3.2.

TABLE 3.1

Details of Activated Charcoals Tested

Charcoal Name	Manufacturer	Starting Material	Activation Process	Physical Form
208C	Sutcliffe Speakman	coconut shell	steam	grain
BPL	Chemviron	coal	N.A.	grain
SC11	Chemviron	coconut shell	N.A.	grain
AS12	Degussa	coal	N.A.	grain
AX21	Anderson	N.A.	N.A.	soot
AX31	Anderson	AX21+binder	N.A.	grain
CC200	Carbon cloth Co.	woven polymer	N.A.	cloth
CC250	Carbon cloth Co.	woven polymer	N.A.	cloth
CC700	Carbon cloth Co.	woven polymer	N.A.	cloth
Zeolite 13X	Laporte	clay+binder	Natural	sphere
Preformed Carbon	Warwick University	compressed cellulose powder	Nitrogen + Zinc chloride leaching agent	disc
BC	Barnaby Cheney	coconut shell	N.A.	grain
CP/13	Sutcliffe Speakman	cocnut shell	N.A.	grain

FIGURE 3.7

Samples of Activated Charcoals

BPL 4*10

SC 11 4*10

208C

AC35

AS12

WS IV

CC250

ZEOLITE 13X

BC

AX31

AX21

PREFORMED DISC
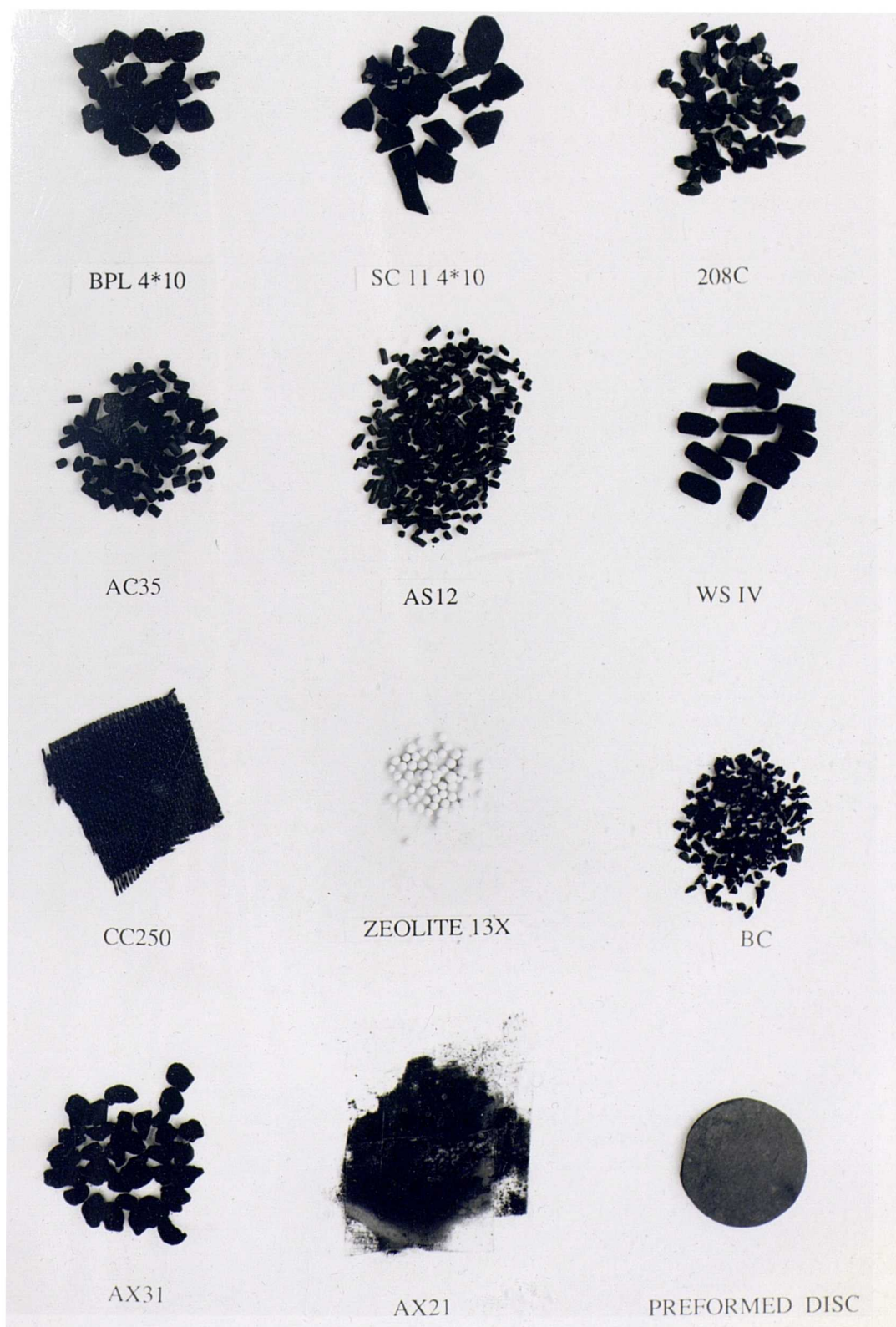
TABLE 3.2

Fit to D-R and D-A Equations

Charcoal	D-R Eqn			D-A Eqn				limits
	K_1	x_{01}	%SEE	K_2	x_{02}	n	%SEE	
208C1	10.758	0.249	0.418	8.572	0.252	1.832	0.345	a
208C2	5.985	0.234	1.854	4.058	0.246	1.498	1.055	b
208C3	6.398	0.216	0.902	4.321	0.240	1.464	0.640	b
BPL	10.062	0.204	2.672	5.674	0.277	1.281	2.506	a
SC11	9.495	0.254	2.435	6.936	0.283	1.312	2.396	a
AS12	10.060	0.317	2.700	10.226	0.318	1.990	2.606	b
AX21	8.866	0.555	2.480	6.095	0.605	1.607	2.405	a
AX31	12.294	0.451	1.792	12.416	0.465	1.900	1.702	a
CC200	7.984	0.282	1.651	4.611	0.304	1.468	0.623	a
CC250	8.395	0.295	2.282	5.569	0.315	1.602	2.091	a
CC700	7.677	0.261	2.080	5.230	0.275	1.637	1.804	a
13X	1.411	0.159	1.720					a
SS13	10.000	0.195	3.040	8.834	0.243	1.756	1.560	b
disc	4.600	0.138	0.194					a
BC	6.470	0.282	2.806	6.747	0.273	2.060	2.705	b

limit a --- 1 bar $\leq p \leq$ 20 bar, $30°C \leq T \leq 120°C$

limit b --- 1 bar $\leq p \leq$ 30 bar, $30°C \leq T \leq 250°C$

and the standard error of estimate (SEE) is defined as

$$SEE = \sqrt{\sum_{i=1}^{i=j} \frac{(x_i - x'_i)^2}{j-2}}$$

where

x_i = real value of concentration

x'_i = value of concentration generated from DR or DA equation

j = number of data points

The D-R equation only is fitted to the data for the preformed discs and for the zeolite. This was because the low porosity characteristics of these materials made it difficult to gather enough data to fit the less constrained D-A equation.

From Table 3.2 it can be seen that the values of x_0 and K vary quite considerably from charcoal to charcoal. From the investigation carried out in section 2.3 it is already known that the values of x_0, K do not have much effect on the COP or the COA. In this discussion we will consider the effect of these variables on the useful energy output of the cycle. The value x_0 is the maximum possible ammonia concentration obtainable within the charcoal, and K is the rate at which ammonia will be desorbed with respect to pressure and temperature. The charcoals which perform best will be those with the larger values of K and x_0. Looking at the columns of figures in Table 3.2 it is difficult to decide which of the charcoals is the best suited to a particular adsorption system.

In order to assess the performance of an adsorbent the idea of a figure of merit (FOM) is introduced. The FOM is the concentration change Δx of an adsorbent when working between set operating pressures and temperatures. The FOM is directly related to the useful energy of the cycle and the larger Δx the better the adsorbent. The FOM is calculated from either the D-A or D-R equation for each of the adsorbents for both refrigerating or heat pumping applications, see Table 3.3.

For a refrigerator the operating limits are:-

$$. T_{a2} = T_c = 30°C$$

$$T_e = -10°C$$

$$T_{g2} = 120°C$$

and for a heat pump the operating limits are:-

$$T_{a2} = T_c = 50°C$$
$$T_e = 5°C$$
$$T_{g2} = 250°C$$

The charcoals tested over the range defined by limits b only are used to calculate FOM's for a heat pump.

TABLE 3.3

FOM's For Refrigerator or Heat Pump.

REFRIGERATOR			
Charcoal	x_{conc} %	x_{dil} %	FOM=Δx
208C1	20.5	10.0	10.5
208C2	20.2	13.2	7.0
208C3	19.2	11.5	7.7
BPL	18.1	8.3	9.8
SC11	17.4	6.9	10.5
AS12	26.5	12.8	13.7
AX21	47.8	25.4	22.4
AX31	35.7	13.5	22.2
CC200	24.0	14.0	10.0
CC250	25.4	14.2	11.2
CC700	22.7	13.4	9.3
13X	15.5	14.0	1.5
SS13	18.9	8.5	10.4
DISC	12.7	9.2	3.5
BC	24.6	15.7	8.9

HEAT PUMP			
Charcoal	x_{conc} %	x_{dil} %	FOM=Δx
208C2	18.9	3.4	15.5
208C3	17.8	2.8	15.0
SS13	16.9	0.5	16.4
BC	23.3	2.2	21.1
AS12	24.2	0.6	23.6

Looking at Table 3.3 it can be seen that by far the best FOM's are obtained by the AX21 and AX31 charcoals. These materials are produced in a totally different way to any of the others. Instead of steam or CO_2 activation the charcoals are prepared by exfoliation in the presence of potassium hydroxide, the process was patented by Wennerberg et al [9]. The end result is a charcoal which has an exceedingly large internal surface area $\approx$ 3000 m^2/g and a large pore volume $\approx$ 1.6 cc/g.

The cost of this charcoal however is in the region of £30 per kg as compared to £4 per kg for 208C and therefore the ratio of FOM to cost per kg for AX21 is only half that of 208C. The bulk density of AX21 is half that of 208C, so an adsorber built for the AX21 would only be two thirds of the size of one built for 208C. It becomes obvious that the FOM alone does not necessarily point out the most economical charcoal and it would be up to the designer to weigh up the cost against the required useful energy and then decide for him or herself which charcoal to use.

In our case the charcoal 208C has been chosen for the thermal conductivity measurements, the COP-COA and the dynamic adsorption cycle modelling because of its low cost, easy availability and ease of handling.

3.4 The Total Isostere Plot

Figure 3.8 overleaf shows a plot of the DA equation fitted to nominal isostere data taken for the batch of 208C used in the thermal conductivity experiments in section 6.

It can clearly be seen that not all the points lie on the curve defined by the DA equation. At conditions near to saturation deviations may occur due to capillary condensation taking place in the macropores, and at the low concentration end deviations may occur due to small amounts of chemisorption. In general it can be seen that each nominal isostere displays a different fit to the DA equation. With this in mind, it was decided that a

FIGURE 3.8

OVERALL DA FIT TO 208C
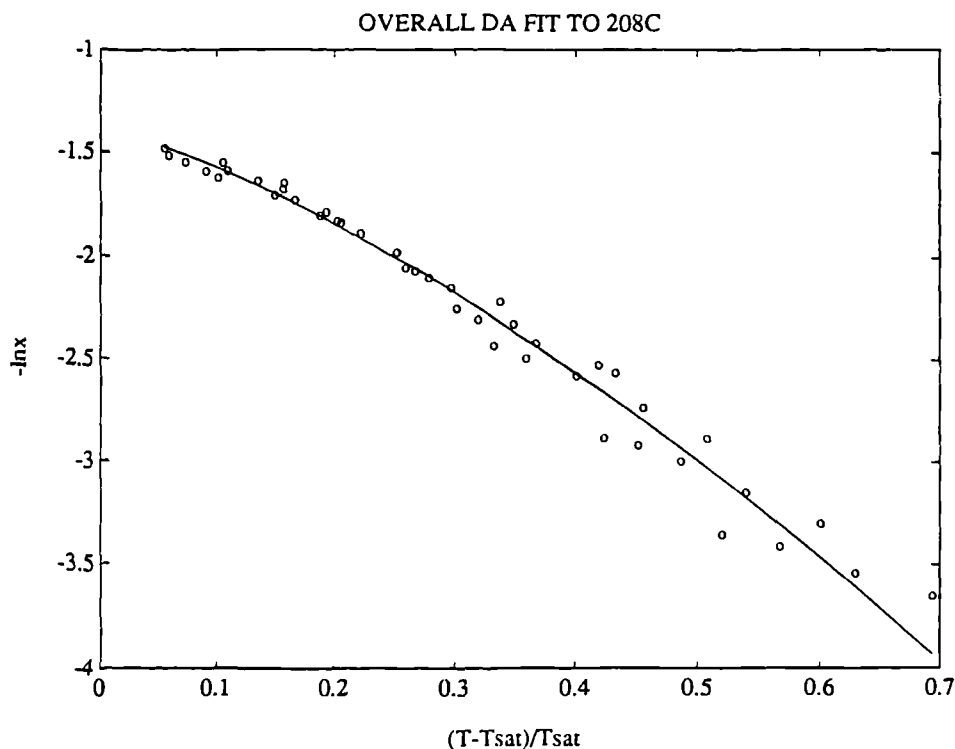
total isostere was needed which reflected the real form and grouping of the isosteres. This was achieved by means of fitting smooth curves through the data points for each isostere. The method of fitting proposed by Turner [10] is outlined below.

(a) A cubic is fitted to plots of T_{SAT} vs. $\frac{1}{T}$ and T_{SAT} vs. conc for each nominal isostere, see figure 3.9 overleaf.

(b) Isobar data is the extracted from the cubic fits of fig 3.9 at interval of 5 K in T_{SAT}. Cubics are then fitted to a plot of conc vs. $\frac{1}{T}$ for each isobar, see figure 3.10.

(c) We now have a set of data containing $\frac{1}{T}$, x, T_{SAT} for 11 isobars covering the ordinary working temperature and pressure range. This information is the used to generate a total isostere plot as shown in figure 3.11 overleaf.

FIGURE 3.9

Cubic Fits for 208C Data.
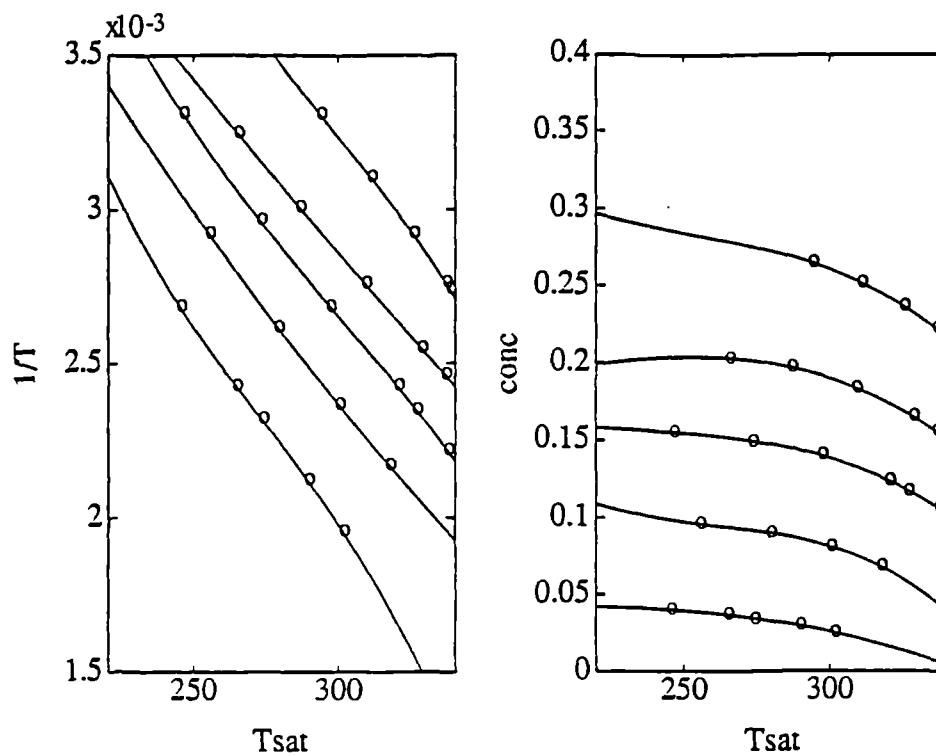
FIGURE 3.10

Cubic fit to Isobar Data for 208C.
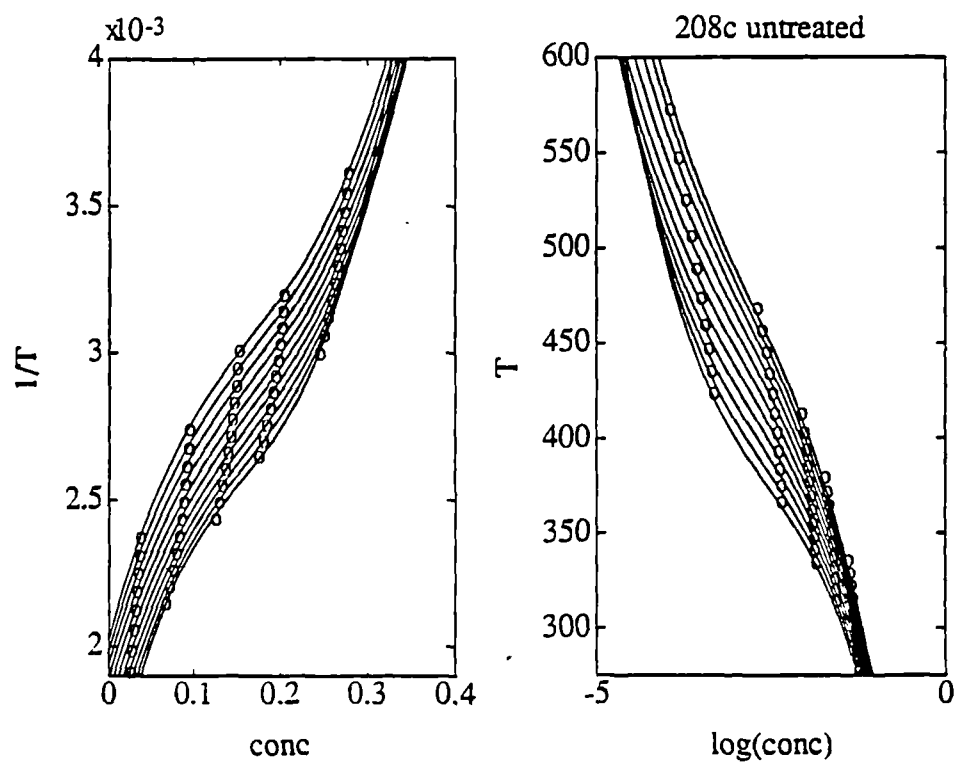
FIGURE 3.11

Total Isostere Plot for 208C.
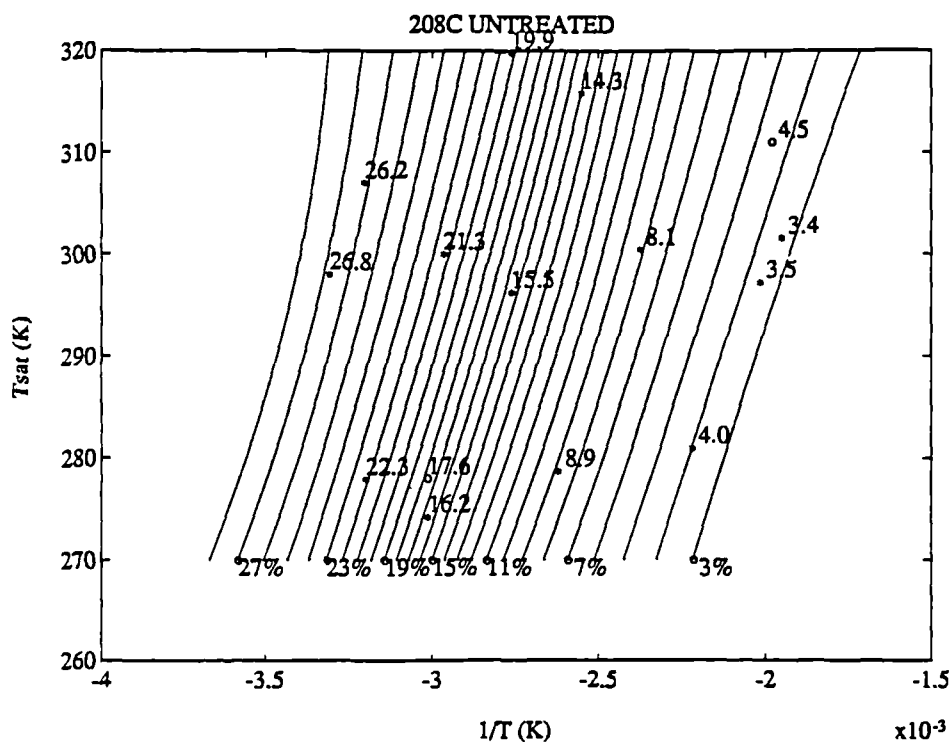
The concentration of each isostere is given at the lower pressure limit T_{SAT} = 270 K, the real data points are shown by the symbol '*' and the strong and weak concentrations used to calculate the FOM for the stated working conditions are shown by the symbol 'o'.

The grouping of the isosteres in figure 3.11 is certainly interesting since if the charcoal truly behaved as defined by the theoretically derived DR equation then the isosteres would become progressively closer spaced as the concentration increased to its maximum obtainable value. It can be seen from figure 3.11 that the isosteres tend to form a closely spaced bunch in the mid concentration range and tend to be spaced further apart at both the high and low ends of the concentration range. This behaviour corresponds to that predicted by the DA equation. It is thought that the closely spaced isosteres

correspond to certain dominant pore size or desorption energy.

The concentration limits of the 208C sample working within the set temperature and pressure ranges of a heat pump are shown in fig 3.11 by the symbol 'o'. It can be seen that if it were possible to shift all of the isosteres along the temperature axis to the right, then because of their bunching more isosteres would be shifted into the high concentration limit than would be shifted out of the low concentration limit and thus the FOM would be higher. Section 3.5 investigates possible methods of achieving this.

3.5 Surface modifications to charcoals.

A set of experiments was carried out to find out if the positioning of the isosteres could be altered as a result of surface treatments to the charcoal. The rationale for this work may be summarized as follows. Ammonia is a polar molecule and it is known that polar adsorbates interact strongly with the polar chemical complexes present on the surface of the charcoal, these are the adsorption sites or centres as already mentioned in section 3.2. The commonest surface groups are those containing oxygen, although there are others containing nitrogen, halons and sulphur. Oxygen-containing groups present on the surface of the charcoal exhibit a wide range of functionality, including acidic, basic and neutral functional groups. Experiments conducted by Puri [11], suggest that the ammonia reacts strongly with the acidic oxygen complexes as one would intuitively expect. Since it is not known what complexes are present on a particular charcoal, two different types of surface treatments were tried on three different types of charcoals.

The extent to which the oxygen-containing complexes are present may by altered by either thermal treatment or by chemical treatment. Puri[11] showed that heating charcoals to 500°C under vacuum almost completely removed the acidic surface functional groups. Conversely heating the charcoal to 400°C in the presence of oxygen increased

the acidic surface functional groups. Finally Puri[12] recommends the use of the oxidizing agent hydrogen peroxide as a wet chemical treatment to increase the number of oxygen-containing surface groups.

The three charcoals chosen for the experiment were:-

(a) Barnaby Cheney (BC) - This is a high pore volume granular coconut shell charcoal.

(b) Sutcliffe Speakman 208C - This is medium pore volume granular coconut shell charcoal.

(c) Degusorb AS12 - This is a coal based extruded charcoal with a high pore volume. It is expected that AS12 will behave differently to the BC and 208C because of its different starting material.

Figures 3.12 and 3.13 show the total isostere plots for untreated AS12 and BC respectively, these may be compared with fig 3.11.

FIGURE 3.12

AS12 UNTREATED

FIGURE 3.13

BARNABY CHENEY UNTREATED
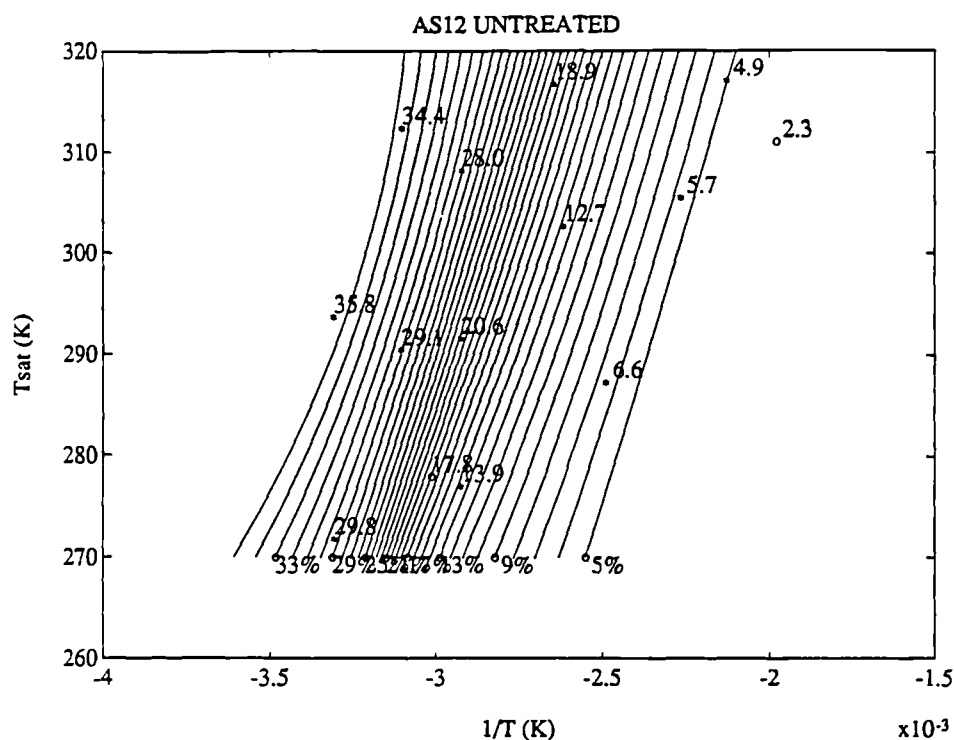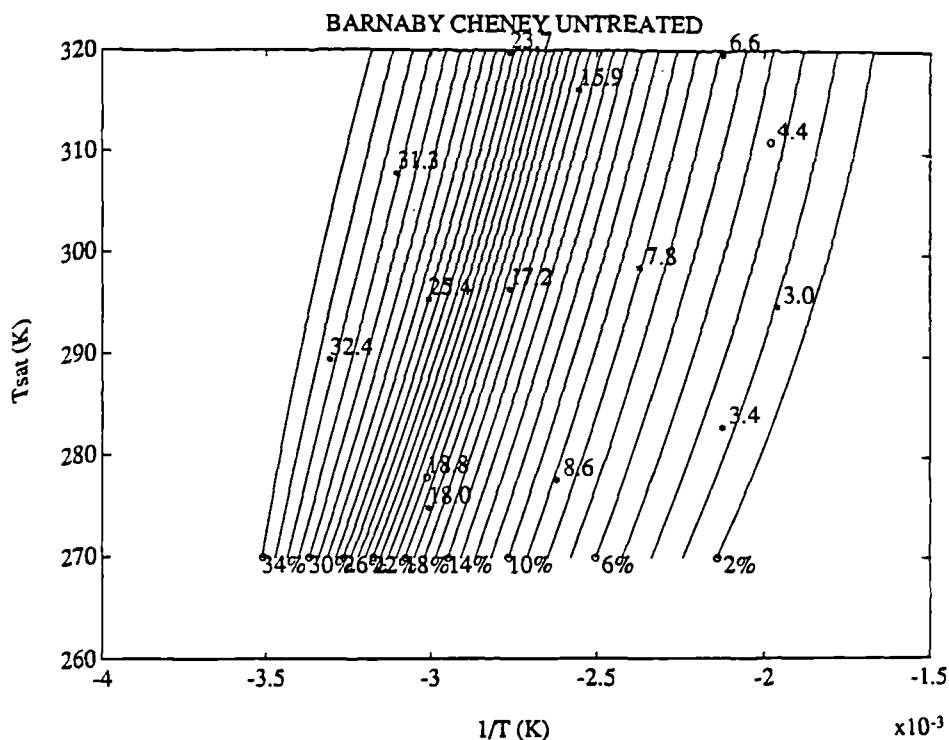
Comparison of these plots clearly shows the high pore volumes of the AS12 and the BC. It is also seen that the isosteres are much more closely bunched together for the AS12 and BC, this perhaps reflects the presence of a more uniform pore size which would cause a large concentration change over as relatively small temperature change.

Treatments (i) - (iii) were carried out on all three charcoals, treatment (iv) was carried out on the AS12 charcoal only and treatment (v) was carried out on the BC charcoal only.

(i) Charcoals were tested in their as received or untreated condition, see plots 3.11-3.13.

(ii) Charcoals were heated to 400°C in a stream of argon for 4 hours to try and strip the surface of its oxygen-containing complexes.

(iii) Charcoals were heated to 400°C in a stream of air for 1 hour to try and increase the presence of oxygen-containing complexes.

(vi) Heating to 400°C in a stream of air for 4hrs to add surface oxygen complexes.

(v) Chemical addition of oxygen groups.

This treatment was optimized by Puri[12]. The charcoal is immersed in a 3M solution of H_2O_2 and agitated for 48hrs at room temperature.(100ml per 1g of charcoal)

Table 3.4 below shows the results of these experiments in terms of an improvement to the FOM over the charcoal as tested in its untreated condition.

TABLE 3.4

Results of Surface Treatments to Charcoals.

	$x_{conc}\%$	$x_{weak}\%$	FOM=$\Delta x\%$	improvement in FOM
BC Untreated	18.8	4.4	14.4	
BC Air Treated	19.6	4.5	15.1	+0.7
BC Argon Treated	18.7	3.5	15.2	+0.8
BC Peroxide Treated	20.0	2.5	17.5	+3.1
208C Untreated	17.6	4.5	13.1	
208C Air Treated	17.6	3.8	13.8	+0.7
208C Argon Treated	16.4	4.0	12.4	-0.7
AS12 Untreated	17.8	2.3	15.5	
AS12 Air Treated	14.3	1.4	12.9	-2.6
AS12 Argon Treated	17.3	3.7	13.6	-1.9
AS12 Air 4 hrs	18.3	4.1	14.2	-1.3

Discussion of the Results.

The basis of the surface treatment experiments is that increasing the presence of surface oxides will leads to increased uptake of ammonia during adsorption. According to this argument there should be a reduction of ammonia uptake after treatment with argon and an increase after either air or peroxide treatment.

Considering the argon treatment first, the broad expectations of decreased uptake of ammonia compared to the untreated carbons are confirmed at both the strong and weak concentration limits for the BC and 208C charcoals. In the case of the AS12 charcoal there is an expected reduction in ammonia uptake at the concentrated end, but an increase at the dilute end. Thus for the argon experiments the expected treatment effect is borne out in 5 out of the 6 cases.

The situation is not so clear cut for the air treatment. Increases in ammonia uptake are found at both ends of the working range for BC, but a decrease in ammonia uptake is found at both ends of the range for 208C and AS12. The drastic reduction in adsorptive capacity of AS12 after air treatment is particularly interesting. The most probable reason for the variable response to air treatment lies in the difficulty of controlling the reaction. Air treatment involves not only formation of surface groups, but gasification of the charcoal. The gasification process is highly exothermic and liable to overheating and runaway effects which will inevitably alter the micropore structure of the charcoal. The gasification reaction can be accelerated by the presence of catalytic impurities in the mineral matter content of each individual charcoal. The different effects on the charcoals may therefore be influenced by their different mineral matter contents reflecting their different origins.

Wet chemical treatment of BC by hydrogen peroxide produced the greatest increase in ammonia uptake at the concentrated condition and decreased uptake at the dilute condition thus improving the FOM by some 21.5% over untreated charcoal. This result may reflect the much larger degree of control one has over this type of oxidizing treatment.

Generally it very difficult to predict what effect a certain treatment will have on an individual charcoal due to the many surface groups present and the unique nature of the charcoal starting material.

3.6 Conclusions.

The DR and DA equations may be used with reasonable accuracy to model the ammonia concentration with respect to pressure and temperature. Using the best fit DR and DA equation constants, the useful energy of any adsorption heat-pumping or refrigerating cycle can be maximized by choosing a charcoal which has a high concentration change between the upper and lower working limits.

Of the range of charcoals tested, AX21 and AX31 had the highest FOMs for both a heat pump and a refrigerator, and could increase the useful energy of the cycle by some 2-3 times over the base case of the 208C. However, when the ratio of FOM to cost for the AX21/31 was compared to that of the 208C, it was found that the AX21/31 proved to be more costly.

The novel method developed for producing a total isostere plot from the nominal isostere data for any charcoal revealed that the isostere spacing was very different for different types of charcoal and that the isosteres formed a closely spaced bunch in the concentration region of 50%-75% of the maximum obtainable ammonia concentration.

It was realized that if the isostere bunch could be shifted to the right on the temperature axis it was very possible that an increase the FOM would result. To achieve this the surface complexes on the charcoals were modified using both chemical and thermal treatments. The most successful result of these modifications was that gained from wet chemical treatment of the charcoal using the oxidizing agent hydrogen peroxide. In the case of the Barnaby Cheney charcoal this increased the FOM by 21.5% over the untreated case.

Overall, it was found that the effect of modification of the surface complexes was difficult to predict and it was thought that this was due to lack of controllability of the thermal treatments and the unique nature of the charcoal starting material.

The useful energy of the cycle will increase not only if the FOM is increased but if the cycle time is decreased. Since the FOM can only be increased to 2-3 times (at the

expense of cost) over the 208C base case, it is concluded at this stage that cheaper and

greater improvements are likely to come from decreasing the cycle time by increasing the

thermal conductivity of the bed.

References

1. Sing KSW Everett DH Haul RAW Moscou L Pierotti RA Rouquereol J Siem-
ieniewska T

"Reporting Phyisorption Data for Gas/Solid systems with Special References to the
Determination of Surface Area and Porosity." Pure and Applied Chemistry, Vol 57,
1985, pp603-619

2. Gregg SJ Sing KSW

"Adsorption Surface Area and Porosity." Academic Press. London. 1982.

3. Smisak M Cerny S

"Active Carbon." Elsevier, New York 1970.

4. McEnaney B Mays TJ

"Short Course. Introduction to Carbon Science. Porosity in Carbons and Graphites."
Course Notes of Seminar held at Newcastle Upon Tyne University. 12th-16th Sept 1988.

5. Dubinin MM Raduskevich LV

"Equation of the Characteristic Curve of Activated Charcoal" Doklady Akad Nauk
S.S.S.R Vol 55. 1947. pp327-329

6. Smisak M Cerny S

"Active Carbon." Elsevier, New York 1970. pp118-119

7. Critoph RE

"Performance Limitations of Adsorption Cycles for Solar Cooling." Solar Energy. Vol 41
No.1, 1988 pp21-31

8. Critoph RE Turner LH

"Performance of Ammonia-Activated Carbon and Ammonia-Zeolite Heat Pump Adsorp-
tion Cycles." Proceedings of Conference. Pompe A Chaleur Chiminique De Haut Perfor-
mance. Perpignan. (publ. Lavoisier) 1988. pp202-211.

9. Wennerberg A O'Grady T
US Patent #4,082,694

10. Turner LH

"Improvement of Activated Charcoal-Ammonia Adsorption Heat-Pumping /Refrigeration Cycles. Investigation of Porosity and Heat/Mass Transfer Characteristics." 3rd International Workshop on Research Activities on Advanced Heat Pumps. Graz 1990. pp 325-334

11. Puri BR

"Surface Complexes on Carbons." Chemistry and Physics of Carbon. Vol 6 PL Walker Jnr, Marcel Dekker, New York, 1970. pp 191-282

12. Puri BR

"Chemisorbed Oxygen Evolved As Carbon Dioxide and Its Influence on Surface Reactivity of Carbons." Carbon, Vol 4, 1966, pp391-400.

4. THEORY OF HEAT TRANSFER IN PACKED GRANULAR BEDS.

Introduction

In order to theoretically determine the effective conductivity of an ammonia activated charcoal adsorber we encounter the problem of how to model a randomly packed granular bed. This is a problem which occurs quite frequently in engineering practice, and as a consequence considerable effort has been invested in developing suitable models. This section presents a review of model development and how heat transfer through the bed may be represented by a one dimensional model. Part 3 of this section is devoted to explanation of the Zehner-Bauer model. This model is very important since it is the most widely applicable to randomly packed bed systems. The equations defining the mechanisms of heat transfer are listed and derived. The Zehner-Bauer model will be used in Section 6 where it modified to include the adsorbed phase and in Section 7 where it is used in the dynamic adsorption cycle modelling.

4.1 Modelling of Packed Granular Beds.

The difficulty in modelling packed beds arises not from the fundamental theory governing the heat transfer but from the need to know the shape, size, conductivity and exact location of each grain together with any interaction between them. Since the measuring of such detailed information is virtually impossible, simplifying assumptions have to be made. In the past two different approaches to the problem have been pursued.

1.Fourier's Law Models.

This type of model utilizes an idealized geometry for which the temperature field may be solved. Knowing the temperature field the effective thermal conductivity may be found using the Fourier-Biot law.

This model received considerable attention during the early days of model development, but its usefulness is limited since there exists only a few configurations for which there are closed form solutions for the Fourier equation. It was soon realized that a more general model was needed and so the Ohm's law model was developed.

2. Ohm's Law Model

In this type of model simple repetitive units are assumed to be representative of the randomly packed system. The problem is further simplified by assuming one dimensional heat transfer. An equivalent electrical network is then constructed and the overall conductivity can be found from the overall thermal resistance of the unit.

Simple Ohm's Law Models

Figure 4.1 overleaf shows a simple cell for an Ohm's law model. The solid and gas volume fractions of the packed bed are retained for the unit cell. The shaded volume represents the solid fraction and the porosity (gas fraction) of the bed is denoted by ψ, where:-

$$\psi = \frac{\text{pore volume}}{\text{unit volume}} \qquad - (4.1)$$

and

$$1 - \psi = \frac{\text{solid volume}}{\text{unit volume}} \qquad - (4.2)$$

FIGURE 4.1
Simple Unit Cell
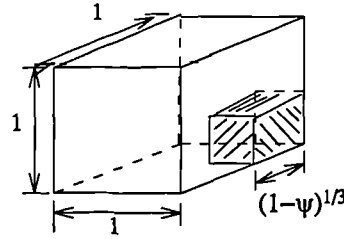
Making the assumption of one dimensional heat transfer presents two options, each of which results in an equivalent thermal resistance network. It may either be assumed that the heat flux is uniform in the direction of the heat transfer or that the isotherms are straight and parallel. The resulting resistance networks for these two assumptions are shown in figures 4.2a & 4.2b respectively.

The thermal resistance R_{th} is found from:-

$$R_{th} = \frac{z}{\lambda_* A} \qquad — (4.3)$$

where:-

z   conduction length parallel to heat flow (m)

A   Area perpendicular to heat flow (m²)

λ_* phase conductivity (W/m K)

λ conductivity of gas phase (W/m K)

λ_s conductivity of solid or granular phase (W/m K)

It is important to note that these two solutions form the boundaries to the real solution. This is because making the assumption of parallel and linear heat flux lines is the same as that of infinite lateral resistance. Similarly, making the assumption of parallel isotherms is the equivalent of zero lateral resistance. In reality the packed bed will have a

FIGURE 4.2

Equivalent Thermal Resistance Networks

$$\frac{(1-(1-\psi)^{1/3})}{\lambda(1-\psi)^{2/3}} \qquad \frac{(1-\psi)^{1/3}}{\lambda_s(1-\psi)^{2/3}}$$

$$\frac{1}{\lambda(1-(1-\psi)^{2/3})}$$
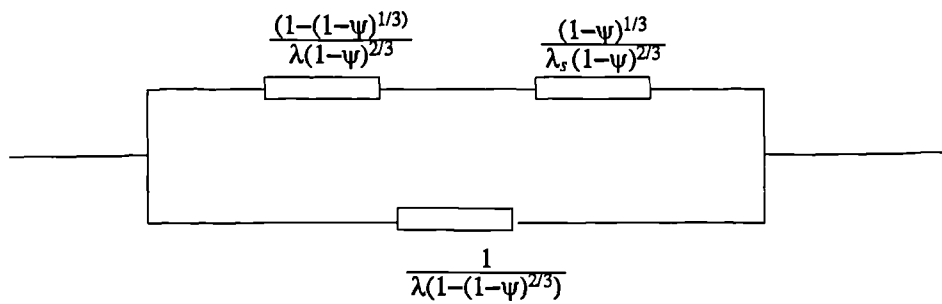
a) Parallel heat flux lines

$$\frac{1}{\lambda_s(1-\psi)^{1/3}}$$

$$\frac{(1-(1-\psi)^{1/3})}{\lambda}$$

$$\frac{(1-\psi)^{1/3}}{\lambda(1-(1-\psi)^{2/3})}$$
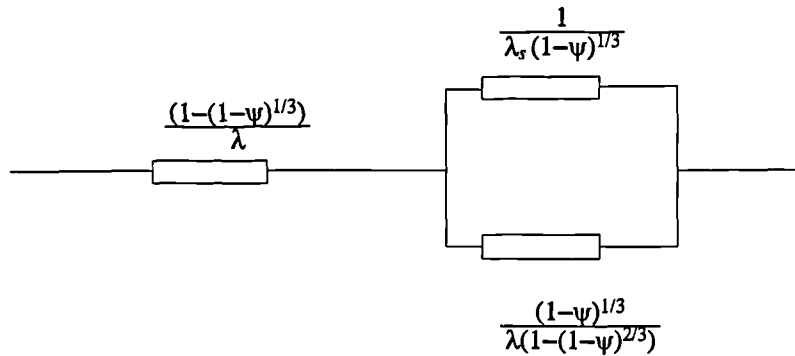
b) Straight and parallel isotherms

finite resistance which obviously lies between these two values. Crane et al [1] have measured the the overall bed conductivity of some 170 solid-fluid packed bed pairs. They compare the measured values with those predicted using the uniform heat flux and parallel isotherm models. The results of their findings are sketched in figure 4.3.

For values of $\frac{\lambda_s}{\lambda} < 10$ either bounding equation gives reasonably accurate results.

FIGURE 4.3

Comparison of Bounding Conductivities

with Experimental Data for Varying Porosity. Ref [1]

Comparison of bounding conductivities with experimental data for a porosity of 0.31.

Comparison of bounding conductivities with experimental data for a porosity of 0.43.

Comparison of bounding conductivities with experimental data for a porosity of 0.58.
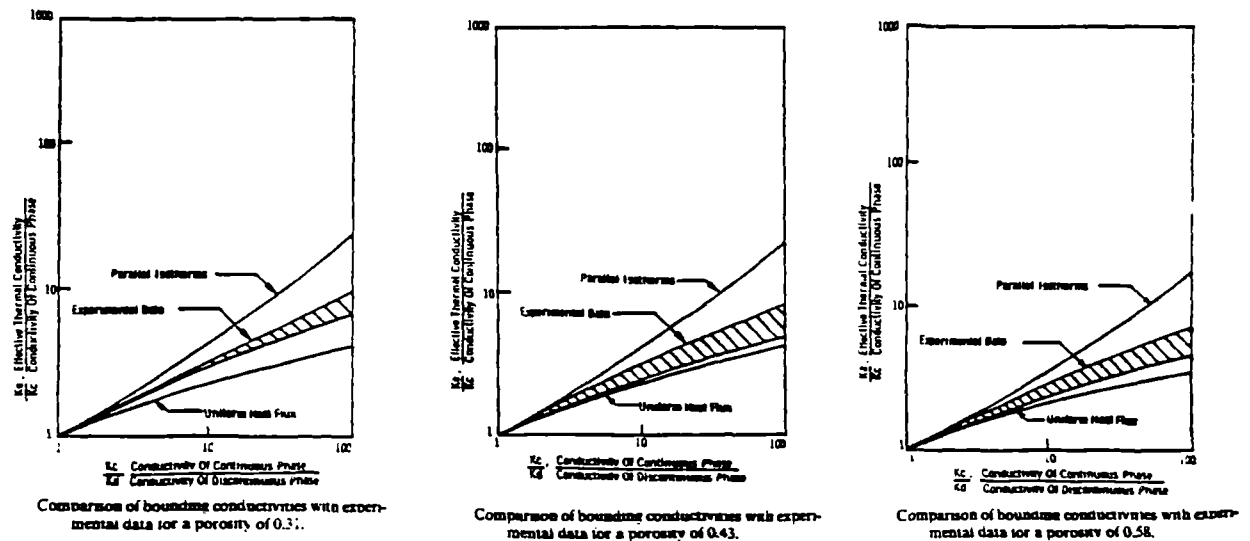
When $\frac{\lambda_7}{\lambda}$ = 100 both solutions deviate significantly from experimental data.

From experiments detailed in Section 5.2, the intergranular void volume ψ was found to be 0.478 for the packed granular bed on which the thermal conductivity bed measurements were made. This value lies closest to to the middle graph of those shown in figure 4.3. This clearly shows that the uniform heat flux model will more accurately predict the overall bed conductivity.

Crane concludes that the limitations placed on the Ohm's Law models may be attributed to two principle causes:

1) Unrealistic Geometric Assumptions: The model utilizes a highly idealized particle shape and particle array which differs significantly from a randomly packed bed with random particle shape and size.

2) Unrealistic Heat Flow Assumptions: The assumption of one dimensional heat transfer is not justified for system with widely different phase conductivities, see fig 4.3.

In order to extend the range and accuracy of Ohm's Law models the above mentioned problems must be tackled.

Model Development

As previously mentioned, the original models of packed beds required a detailed knowledge of the particle size, shape and packing geometry, along with the conductivity of both phases. The temperature distribution throughout the bed may then be calculated by using Fourier's Law and a numerical relaxation technique. Deissler and Boegli [2] present such a model using a cubic lattice packing of regular spheres to simulate packed beds of metallic powders with a mean particle diameter of ≈ 0.1mm. The work presents a carpet plot of isotherms and finds good agreement between experimental and theoretically predicted overall conductivity. Wakao and Kato [3] present work using the same modelling and analysis technique but with larger particle diameters. They conclude that the correlation obtained between theoretical and experimental results is fairly good.

The main disadvantages of Fourier models apart from those already mentioned are the computational requirement and the lack of evidence of applicability of the model with a varied particle size and shape.

One of the earliest Ohm's Law models was presented by Schumann and Voss [4] as far back as 1934. This work used a rectangular hyperbola to generate the shape of the unit cell, see fig 4.4a. Making the assumption of parallel and uniform heat flux lines, Schumann and Voss obtained very good agreement between real and calculated data on a bed of uniform size steel shot. When they further experimented with different size grains of coal and quartz, the error in the correlation was much larger and tended in most cases to 60%.

FIGURE 4.4

Ohm's Law Unit Cell Shapes

hyperbola

solid

solid

gas

a) Schumann & Voss

solid

gas

b) Yagi & Kunii

isotherms

solid

gas

c) Woodside

solid

gas

d)Kunii & Smith
   Schlunder
   Hayashi

gas

solid

e) Zehner
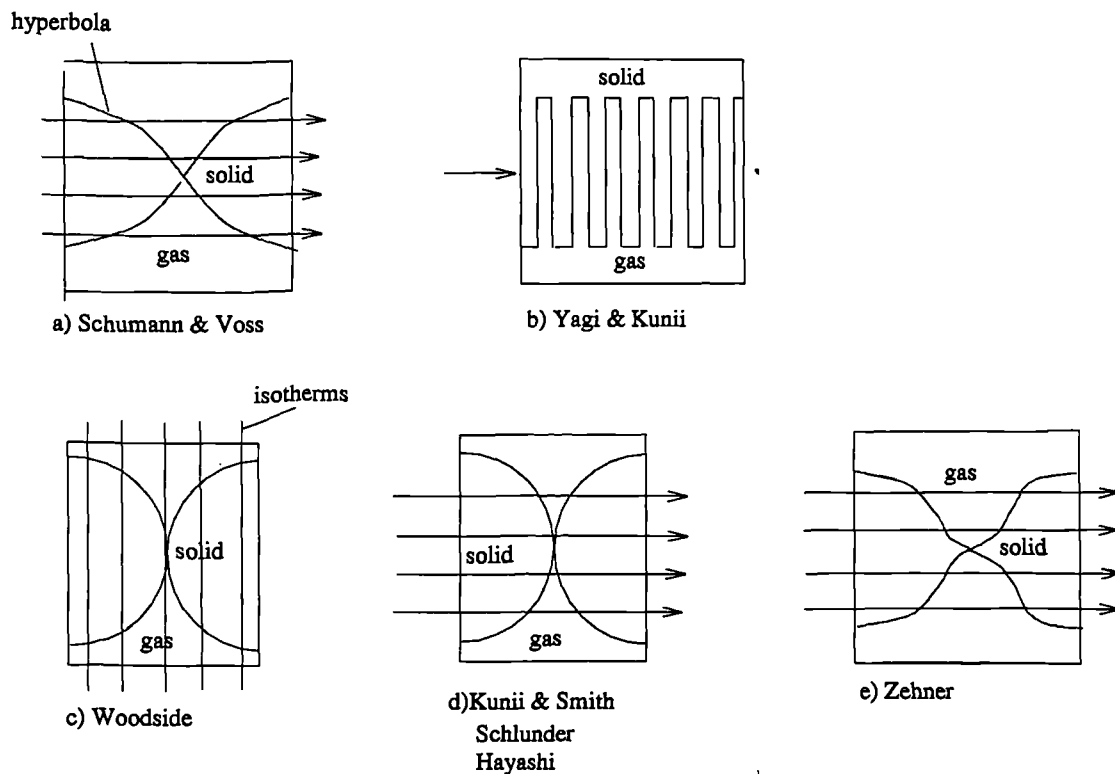
Yagii and Kunii [5] present a very different geometry for their unit cell, see fig 4.4b. They calculate the effective conductivity of the cell by finding its overall heat transfer coefficient. They obtain good correlation between real and calculated values for different particle shape, size, material and fluid phase.

In 1958 Woodside [6] proposed a unit cell based on the solid sphere to represent the grain and isotherms perpendicular to the direction of heat flow, see fig 4.4c. He states however that this type of model is only really valid when the ratio of the solid to gas conductivity is close to unity, and the larger the ratio, the larger the error introduced.

The most popular model found is that of a solid sphere unit cell with parallel isotherms as presented by at least three different authors [7], [8], [9], see fig 4.4d. These models are easy to use and formulae for prediction of the overall effective conductivity of the bed are put forward. Most of the experimental work in these pieces of literature is again carried out on uniform, regular shaped particles rather than random systems.

To compensate for unrealistic heat flow assumptions and unrealistic particle and array geometries, Zehner [10] introduced a variable contour particle shape and assumed parallel heat flux lines, see fig 4.4e. This work, later extended by Bauer [11], is the most extensive and complete of its kind to be found to date.

4.2 Mechanisms of Heat Transfer in Stagnant Packed Beds.

Figure 4.5 below shows a section of a randomly packed bed with a non-uniform particle shape and size. The void space or pore space between the particles is filled with a gas. There are six identified mechanisms of heat transfer through the bed assuming convection is negligible.

FIGURE 4.5

Mechanisms of Heat Transfer Through a

Granular Packed Bed
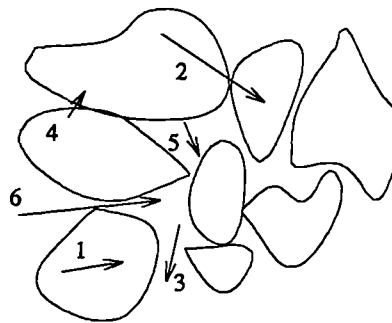
where:-

1. Conduction through grain.

2. Conduction from grain to grain through a point or area contact.

3. Conduction through the gas phase.

4. Conduction through the gas phase near the points of grain contact.

5. Radiant heat transfer from grain to grain surface.

6. Radiant heat transfer from void to void.

For any of the models discussed in the previous section, see fig 4.4, the heat transfer always takes place through three distinct material phases. These are:-

(i) a solid conduction path

(ii) a gas-solid in series path or the mixed bed region

(iii) a gas path or pore region

Each of these employs several of the mechanisms demonstrated in figure 4.5.

material phase	mechanism number
grain	1 2
mixed	1 3 4 5
gas	3 4 6

Making the assumption of parallel heat flux lines will result in the three phases working in parallel with each other as shown in the network below.

FIGURE 4.6

Resistance Network Showing the Three Material Phases

SOLID
solid conduction

MIXED   gas conduction

solid conduction

solid-solid radiation

gas conduction

GAS

void-void radiation
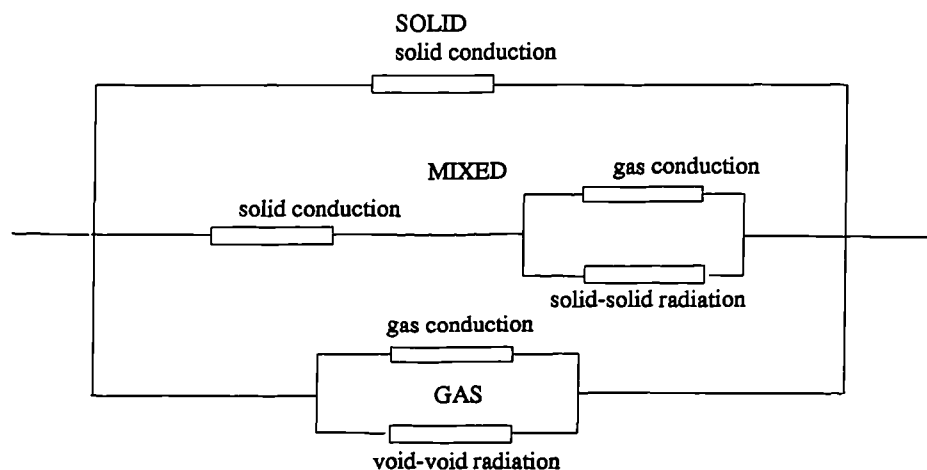
Mechanisms 1-3,5,6 are straightforward conduction or radiation, but mechanism 4 requires some further explanation. When heat is conducted through the gas phase near the points of grain contact its conductivity is reduced. This effect is known as the Knudsen or Smolowski effect and occurs when the mean free path of the gas molecule becomes comparable in size to the space in which it is moving. This effect and the derivation of governing equations are discussed in App 4b. The reduction in conductivity will be more apparent for low pressure adsorption systems such as those using methanol or water but at this stage it will still be included in our calculations.

From equation (4.3) it can be seen that the magnitude of the thermal resistance will depend on the conduction length and area as well as conductivity. The values z and A will vary with unit cell geometry. Since the Zehner-Bauer model is the most extensively applicable to packed beds, the equations for mechanisms 1-6 will be derived for the this model only.

4.3 The Zehner Bauer Model

This section is devoted to explanation of the Zehner-Bauer (ZB) model and to derivation of all the equations defining the model and mechanisms of heat transfer. The ZB model has been analyzed to this extent because after modification to include the adsorbed phase, see Section 6, it is used in modelling the dynamic adsorption cycle in Section 7.

The cross section of the unit cell proposed by ZB is shown in figure 4.7, ref[11]. It consists of a solid central core, a mixed bed region and an outer annulus of fluid. It has unit height, volume and CSA. The shape of the solid particle is generated using equation 4.4 shown overleaf.

FIGURE 4.7
The Zehner-Bauer Model
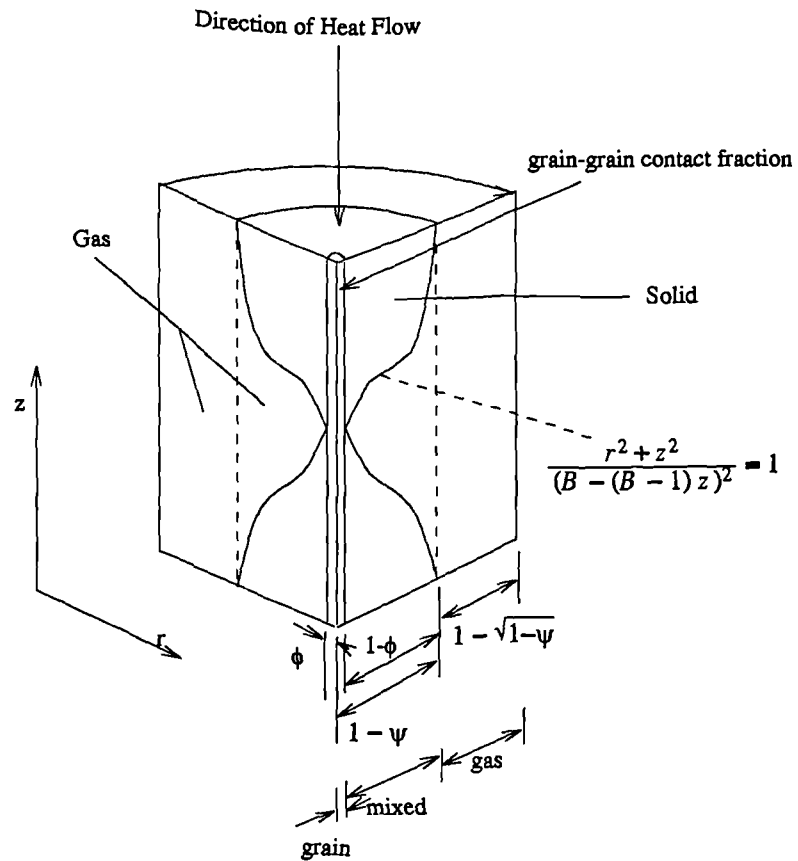
* note that the dimensions shown are relative areas

$$r^2 + \frac{z^2}{(B-(B-1)z)^2} = 1 \qquad \text{—(4.4)}$$

where:-

B   Deformation Factor

z,r   cylindrical coordinates

Equation (4.4) has the following bounding geometries:-

a) When B = 0, $r^2 = 0$ -- z axis

b) When B = 1, $r^2 + z^2 = 1$ -- sphere

c) When B → ∞, $r^2 = 1$ -- cylinder

The deformation factor B allows the model to have a variable contour defining the particle shape. It is by virtue of the extra degree of freedom that the Z.B model generally produces a superior fit to experimental results. This is because the errors introduced into the equation by assuming uniform geometry and parallel heat flux may be minimized by distorting the particle geometry to fit the result. Following from this it is important to realize that the ZB unit cell particle shape is not necessarily similar to that of the real particle.

Looking again at figure 4.7 it can be seen that we have three distinct regions of heat transfer. The outer annulus contains only a fluid phase and has a relative area of $1-\sqrt{1-\psi}$. The central cylinder has a relative area of $\sqrt{1-\psi}$ and can itself be split into two distinct volumes. The central core represents a grain conduction path and has a relative area of ϕ. The remainder of the cylinder is what is known as the mixed bed region and it consists of grain and fluid phases in series. The annulus has a relative area of $1-\phi$.

The first important difference between the ZB model and other Ohm's law models is the derivation of the relative area of the fluid phase annulus. Zehner states [10] that in a fictitious case where the conductivity of the granular phase approaches zero, the heat transfer and mass transfer equations are analogous and may both be represented by Laplace's equation. If the particles are impermeable to both heat and mass transfer, and the boundary conditions are the same for both situations then it is true to say that:-

$$\lim_{\frac{\lambda_s}{\lambda} \to 0} \frac{\lambda_{so}}{\lambda} = \frac{\delta_{so}}{\delta} \qquad -(4.5)$$

where:-

λ_{so} overall bed conductivity (W /m K)

λ fluid conductivity (W /m K)

δ_{so} effective diffusion coefficient of bed (m^2/s)

(with no flow)

δ effective diffusion coefficient of fluid phase (m^2/s)

Figure 4.8 below [10] shows the collated data of several authors' experimental measurements of the ratio of effective bed to effective fluid diffusion coefficient as a function of the bed porosity ψ. The measurements were made on stagnant packed beds of many different particle shapes including cylinders, sand, salts, Raschig rings and powders. From these results it can be seen that the particle shape has very little influence and that the empirically derived relationship shown in equation (4.6) describes the curve with sufficient accuracy.

FIGURE 4.8

Ratio of Bed to Fluid Diffusion Coefficient vs. Bed Porosity
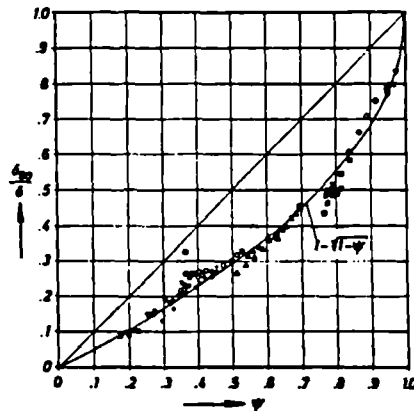
Abhängigkeit effektiver Diffusionskoeffizienten von der Porosität nach Experimenten von:

O Kugeln und Sand, + Carborund, ☐ Salz, △ Erdreich, ■ Porzellanerde, ◇ Cellulose-acetat (⊕ Cellit), ▽ Stahlwolle, ◆ Keramikperlen;

● Kugeln, ▲ Raschigringe;

✕ Kugeln und Sand.

Ausgleichskurve nach Gleichung (25)

$$\frac{\delta_{so}}{\delta} = 1 - \sqrt{1-\psi} \qquad —(4.6)$$

Applying equation (4.3) and the assumption of parallel heat flux lines to the ZB unit cell in the case where $\lambda_s \to 0$ and $z = 1$ leads to equation (4.7).

$$\frac{1}{\lambda_{so} A_1} = \frac{1}{\lambda A_2} \qquad —(4.7)$$

where:-

A_1 unit area of cell $= 1$ m^2

A_2 relative area of fluid phase conduction path m^2

thus,

$$\frac{\lambda_{so}}{\lambda} = \frac{A_2}{A_1} = A_2 \qquad —(4.8)$$

Combining equations (4.5) and (4.6) gives:-

$$\frac{\lambda_{so}}{\lambda} = 1 - \sqrt{1-\psi} \qquad —(4.9)$$

therefore the relative surface area of the fluid phase annulus A_2 must equal $1 - \sqrt{1-\psi}$.

This concludes definition of the important aspects of the ZB geometry. Following from this are the equations defining the heat transfer mechanisms. According to [11] the overall bed conductivity may be defined as :-

$$\frac{\lambda_{so}}{\lambda} = 1-\sqrt{1-\psi}\left[\frac{\psi}{(\psi-1)+\frac{\lambda}{\lambda_D}} + \psi\frac{\lambda_R}{\lambda}\right] + \sqrt{1-\psi}\,\phi\frac{\lambda_s}{\lambda} + \sqrt{1-\psi}\,(1-\phi)\frac{\lambda_{so^*}}{\lambda} \qquad —(4.10)$$

λ_D	Knudsen conductivity	W/m K
λ_R	Radiation Conductivity	W/m K
λ_{so^*}	Effective mixed bed conductivity	W/m K
λ_s	grain conductivity	W/m K
ϕ	grain contact area	m^2

The first group on the right hand side of equation (4.10) defines conduction through the fluid phase of the unit cell. The second group defines conduction through the central granular phase, and the third defines heat transfer through the mixed bed region.

Further to equation (4.10), λ_{so*} is defined as :-

$$\frac{\lambda_{so*}}{\lambda} = \frac{2}{p}\left(\frac{B(\frac{\lambda_s}{\lambda}+\frac{\lambda_R}{\lambda}-1)\frac{\lambda}{\lambda_D}\frac{\lambda}{\lambda_s}}{p^2} \times \ln\left[\frac{(\frac{\lambda_s}{\lambda}+\frac{\lambda_R}{\lambda})\frac{\lambda}{\lambda_D}}{B(1+(\frac{\lambda}{\lambda_D}-1)(\frac{\lambda_s}{\lambda}+\frac{\lambda_R}{\lambda}))}\right]\right.$$

$$\left. -\frac{B-1}{p}\frac{\lambda}{\lambda_D}+\frac{B+1}{2B}(\frac{\lambda_R}{\lambda}\frac{\lambda}{\lambda_D}-B(1+(\frac{\lambda}{\lambda_D}-1)\frac{\lambda_R}{\lambda}))\right)$$

and

$$p = [1+(\frac{\lambda_R}{\lambda}-B\frac{\lambda_D}{\lambda})\frac{\lambda}{\lambda_s}]\frac{\lambda}{\lambda_D}-B(\frac{\lambda_D}{\lambda}-1)\times(1+\frac{\lambda_R}{\lambda}\frac{\lambda}{\lambda_s}) \qquad — (4.12)$$

Equations (4.10) -(4.12) are complicated and require detailed explanation. Firstly, we will deal with the definitions of λ_R and λ_D and then with equation (4.10) and finally with the definition of λ_{so*} and equations (4.11) and (4.12).

The Equivalent Conductivity due to Radiation λ_R

The equation used to represent λ_R, shown in its non-dimensionalized form in equation (4.13), was originally proposed by Damkohler [12].

$$\frac{\lambda_R}{\lambda} = \frac{0.04Cs}{(\frac{2}{\varepsilon}-1)\lambda}(\frac{T}{100})^3 x_R \qquad — (4.13)$$

where:-

Cs   Modified Stephan Boltzmann constant = 5.67 (W/m^2K^4)

ε Emissivity of the solid surface

T   Temperature of the surface (K)

x_R Effective radiation length characteristic of the particle packing (m)

From Appendix 4a it can be seen that equation (4.13) is that of radiant heat exchange between two parallel grey plates. This equation will be slightly modified at a later stage of the ZB model to account for the non-parallel nature of the pore shape and for a different characteristic dimension.

The Equivalent Conductivity due to Knudsen Effect λ_D.

In the gaps between the grains where the mean free path of the gas molecule is comparable or larger to the space in which it is trying to move, the conductivity of the gas is reduced. In this situation the heat is not transferred from gas to the grain surface by convection but as a result of molecular bombardment of the surface. This regime is known as free molecular flow and must be analyzed apart from conventional continuum fluid mechanics.

The equivalent gas conductivity between particles due to the Knudsen or Smolowski effect is defined by equation (4.14).

$$\frac{\lambda}{\lambda_D} = 1 + \frac{2\sigma}{x_D}(\frac{2}{\gamma} - 1) \quad - (4.14)$$

where:-

σ mean free path length of gas molecule (m)

γ accommodation coefficient

x_D effective gas path length characteristic (m)

        of the particle packing

The mean free path of any gas may be found from equation (4.15).

$$\sigma = \sigma_0 \frac{T P_0}{T_0 P} \quad - (4.15)$$

where:-

P Gas pressure (N/m^2)

P_0 Reference pressure = 1.01×10^5(N/m^2)

T_0 Reference Temperature = 273.15 (K)

σ_0 Mean free molecular path at P_0 and T_0 (m)

The value of σ_0 may be found from reference books or from the gas molecule diameter using equation (4.16).

$$\sigma_o = \frac{8.4 \times 10^{-27}}{\eta^2} \qquad - (4.16)$$

η gas molecule diameter   m

The derivation of equation (4.14) may be found in App 4b.

Thermal Resistance Network of ZB Unit Cell. Equation (4.10)

Equation (4.10) is derived from the equivalent thermal resistance network for the ZB unit cell assuming uniform heat flux. In this network, shown in figure 4.9, the resistances from bottom to top represent the fluid, mixed and granular phases respectively.

FIGURE 4.9

Resistance Network Showing the Three Material Phases
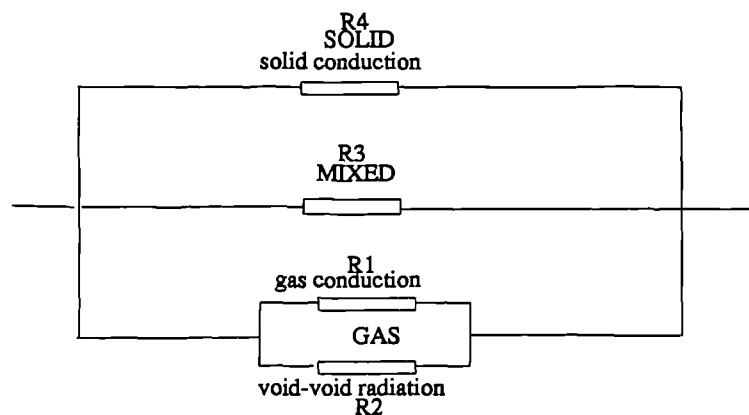
The fluid Phases R1 & R2.

The thermal resistance R1 is that due to conduction through the gas, see equation (4.14). Equation (4.14) however is based on a characteristic dimension of the particle x_D and represents conduction between particles. To represent conduction in the pore the equation must be based on a characteristic dimension of the pore, in this case its depth.

Therefore equation (4.14) becomes:-

$$\frac{\lambda}{\lambda_{D1}} = 1 + \frac{2\sigma}{x_D} \frac{x_D}{s} (\frac{2}{\gamma} - 1) \qquad\text{— (4.17)}$$

where:-

s   pore depth   m

λ_{D1} Gas conductivity in pore   W/m K

The ratio of pore depth to particle diameter can be approximated by the porosity ratio ψ, see Appendix 4c.

$$\frac{s}{x_D} = \psi \qquad\qquad\text{— (4.18)}$$

Combining equations (4.17) and (4.18) gives us the conductivity of the gas in the pore.

$$\frac{\lambda}{\lambda_{D1}} = 1 + \frac{2\sigma}{x_D} \frac{1}{\psi} (\frac{2}{\gamma} - 1)$$

But from equation (4.14)

$$\psi \frac{\lambda}{\lambda_{D1}} = \psi + \frac{\lambda}{\lambda_D} - 1$$

so,

$$\lambda_{D1} = \frac{\psi \lambda}{(\psi - 1) + \frac{\lambda}{\lambda_D}} \qquad\text{— (4.19)}$$

therefore,

$$R1 = \frac{1}{\left(1 - \sqrt{1-\psi}\right)\lambda_{D1}} = \frac{1}{(1-\sqrt{1-\psi})\left(\dfrac{\psi\lambda}{\psi-1+\dfrac{\lambda}{\lambda_D}}\right)} \qquad - (4.20)$$

The thermal resistance R2 is that due to radiation heat transfer through the pore space, see equation (4.13). Again equation (4.13) is based on the particle dimension x_R and must be altered such that it is based on the pore depth s.

$$\frac{\lambda_{R1}}{\lambda} = \frac{0.04Cs}{(\frac{2}{\epsilon}-1)\lambda}(\frac{T}{100})^3 x_R \frac{s}{x_R} = \lambda_R \psi \qquad - (4.21)$$

and

$$R2 = \frac{1}{\left(1 - \sqrt{1-\psi}\right)\lambda_R \psi} \qquad - (4.22)$$

The Mixed Bed Phase R3.

$$R3 = \frac{1}{\sqrt{1-\psi}\,\left(1-\phi\right)\lambda_{so*}} \qquad - (4.23)$$

The Grain Solid Phase R4.

$$R4 = \frac{1}{\sqrt{1-\psi}\,\left(\phi\lambda_s\right)} \qquad - (4.24)$$

The total thermal resistance of the network R_{tot} may be expressed as:-

$$\frac{1}{R_{tot}} = \frac{1}{R1} + \frac{1}{R2} + \frac{1}{R3} + \frac{1}{R4} = \lambda_{so}$$

therefore

$$\frac{\lambda_{so}}{\lambda} = (1-\sqrt{1-\psi})\left(\frac{\psi}{(\psi-1)+\dfrac{\lambda}{\lambda_D}} + \psi\frac{\lambda_R}{\lambda}\right) + \sqrt{1-\psi}\,\,\phi\frac{\lambda_s}{\lambda} + \sqrt{1-\psi}\,(1-\phi)\frac{\lambda_{so*}}{\lambda} \qquad - (4.10)$$

The Mixed Bed Conductivity λ_{so*} & Equations (4.11) & (4.12).

The overall conductivity of the mixed phase region is found by summing the parallel resistances of each small annulus element in the region r = 0 to r = 1, see figure 4.10.

FIGURE 4.10

Resistance Element in the Mixed Phase Region

Annulus Area $= 2\pi r.dr$
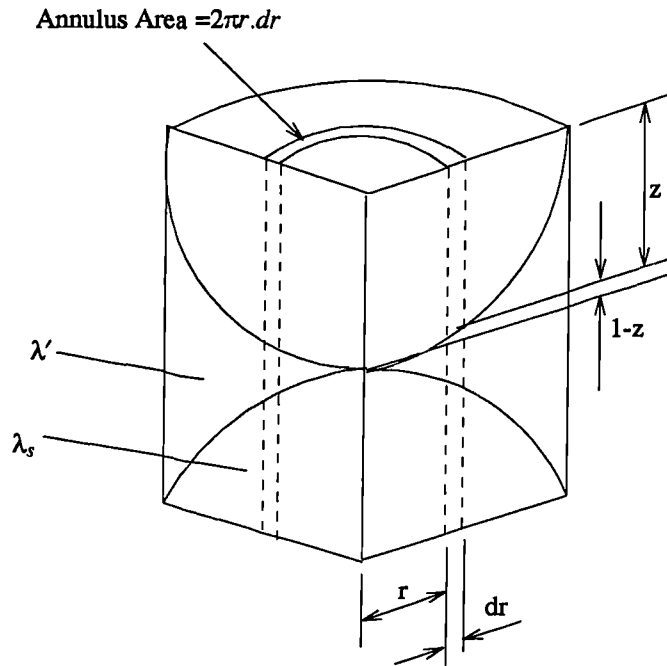
Integrating over the mixed phase region gives:-

$$\frac{\lambda_{so*}}{\lambda} = \frac{1}{\pi} \int_{r=0}^{r=1} \frac{\lambda_{so**[z,r]}}{\lambda} 2\pi r.dr \qquad \text{— (4.25)}$$

where $\lambda_{so**[z,r]}$ is the conductivity of an element at radius r.

Looking at a particular element at radius r we can see that we have a grain conduction length of z and a gas conduction length of 1-z.

The thermal resistance of this element may be written as :-

$$R_{so**} = \frac{1}{\lambda_{so**}} = \frac{1-z}{\lambda'} + \frac{z}{\lambda_s} \qquad - (4.26)$$

R_{so**} Thermal resistance of element (K/W)

λ' Thermal conductivity of gas region (W/m K)

Equation (4.26) may be rewritten,

$$\frac{\lambda_{so**}}{\lambda} = \frac{1}{(1-z)\frac{\lambda}{\lambda'} + \frac{\lambda}{\lambda_s}z} \qquad - (4.26a)$$

The parameter λ' is the effective conductivity of the fluid region due to radiation and gas conductivity with Knudsen effect in parallel, and may be defined as,

$$\frac{\lambda'}{\lambda} = \frac{1}{1 + \frac{(\frac{\lambda}{\lambda_D} - 1)}{(1-z)}} + (\frac{1-z}{z})\frac{\lambda_R}{\lambda} \qquad - (4.27)$$

The full derivation of λ' may be found in Appendix 4d.

Since λ_{so**} is defined in terms of z we now wish to find an expression relating r.dr and z.dz so that we can integrate equation (4.25) with respect to z. This relationship is found from equation (4.4) defining the particle geometry.

$$r^2 + \frac{z^2}{(B - (B-1)z)^2} = 1 \qquad - (4.4)$$

Rearranging and differentiating gives,

$$r.dr = \frac{-Bz}{(B - (B-1)z)^3}.dz \qquad - (4.28)$$

See Appendix 4e for a full derivation of (4.28).

Substituting equations (4.28), (4.27) and (4.26a) into the integral (4.25) gives us :-

$$\frac{\lambda_{so*}}{\lambda} = -2B \int_{z=1}^{z=0} \frac{z(1 - \frac{\lambda_R}{\lambda}) + \frac{\lambda_R}{\lambda}\frac{\lambda}{\lambda_D}}{z((\frac{\lambda}{\lambda_s} - \frac{\lambda_R}{\lambda}\frac{\lambda}{\lambda_s} - 1) + (1 + \frac{\lambda_R}{\lambda}\frac{\lambda}{\lambda_s})\frac{\lambda}{\lambda_D})(B - (B-1)z)^3}.dz \qquad - (4.29)$$

Again see Appendix 4f for full working.

To integrate equation (4.29) the expression inside the square brackets is split into partial fractions.

$$\frac{z(1-\frac{\lambda_R}{\lambda})+\frac{\lambda_R}{\lambda}\frac{\lambda}{\lambda_D}}{z((\frac{\lambda}{\lambda_s}-\frac{\lambda_R}{\lambda}\frac{\lambda}{\lambda_s}-1)+(1+\frac{\lambda_R}{\lambda}\frac{\lambda}{\lambda_s})\frac{\lambda}{\lambda_D})(B-(B-1)z)^3} = \frac{S}{z((\frac{\lambda}{\lambda_s}-\frac{\lambda_R}{\lambda}\frac{\lambda}{\lambda_s}-1)+(1+\frac{\lambda_R}{\lambda}\frac{\lambda}{\lambda_s})\frac{\lambda}{\lambda_D})}$$

$$+ \frac{T}{(B-(B-1)z)^3} + \frac{U}{(B-(B-1)z)^2} + \frac{V}{(B-(B-1)z)} \qquad \text{---(4.30)}$$

Integrating the right hand side of equation (4.30) with respect to z between the limits of

z = 1 and z = 0 gives:-

$$\frac{\lambda_{so*}}{\lambda} = -2B\left((\frac{S}{\frac{\lambda}{\lambda_s}-\frac{\lambda_R}{\lambda}\frac{\lambda}{\lambda_s}-1})\ln(\frac{NB}{M}) - \frac{V}{B-1}(\ln B) - \frac{T}{2}\frac{(1+B)}{B^2} - \frac{U}{B}\right) \qquad \text{---(4.31)}$$

where:-

$$N = (1+\frac{\lambda}{\lambda_s}\frac{\lambda_R}{\lambda})\frac{\lambda}{\lambda_D} \qquad \text{---(4.32)}$$

$$M = B\left(\frac{\lambda}{\lambda_s}+(\frac{\lambda}{\lambda_D}-1)(1+\frac{\lambda}{\lambda_s}\frac{\lambda_R}{\lambda})\right) \qquad \text{---(4.33)}$$

and the partial fractions S, T, U and V are found to be :-

$$S = \frac{\frac{\lambda}{\lambda_D}(M-BN)^2}{B^2(N-M)^3} \qquad \text{---(4.34)}$$

$$T = \frac{\frac{\lambda_s}{\lambda}\left(1-(N-M)-(B-1)(\frac{\lambda}{\lambda_D}-1)\right)}{(M-N)} \qquad \text{---(4.35)}$$

$$U = -\frac{\frac{\lambda}{\lambda_D}(B-1)}{(N-M)^2} \qquad \text{---(4.36)}$$

$$V = \frac{\frac{\lambda}{\lambda_D}(B-1)(M-BN)}{B(N-M)^3} \qquad \text{---(4.37)}$$

Substituting (4.34)-(4.37) into (4.31) gives:-

$$\frac{\lambda_{so^*}}{\lambda} = \frac{2}{(N-M)}\left(\frac{N-\frac{\lambda}{\lambda_s}\frac{\lambda}{\lambda_D}}{(N-M)^2}\ B\ \ln\frac{N}{M} + \frac{\frac{\lambda}{\lambda_D}(M-BN)}{(N-M)^2}(\ln B)\right.$$

$$\left. + \frac{1+B}{2B}\frac{\lambda_s}{\lambda}(1-(N-M)-(B-1)(\frac{\lambda}{\lambda_D}-1)) - \frac{\lambda}{\lambda_D}\frac{(B-1)}{(N-M)}\right) \qquad\text{— (4.38)}$$

now,

$$N - M = [1 + \frac{\lambda}{\lambda_s}(\frac{\lambda_R}{\lambda} - B\frac{\lambda_D}{\lambda})]\frac{\lambda}{\lambda_D} - B(\frac{\lambda}{\lambda_D}-1)\times(1+\frac{\lambda_R}{\lambda}\frac{\lambda}{\lambda_s}) = p \qquad\text{— (4.39)}$$

Substituting (4.39), (4.32) and (4.33) into (4.38) and rearranging gives us equation (4.11) defining the mixed bed conductivity in terms of B, ϕ, λ, λ_D, λ_R, λ_s and ψ.

$$\frac{\lambda_{so^*}}{\lambda} = \frac{2}{p}\left(\frac{B(\frac{\lambda_s}{\lambda}+\frac{\lambda_R}{\lambda}-1)\frac{\lambda}{\lambda_D}\frac{\lambda}{\lambda_s}}{p^2}\times\ln[\frac{(\frac{\lambda_s}{\lambda}+\frac{\lambda_R}{\lambda})\frac{\lambda}{\lambda_D}}{B(1+(\frac{\lambda}{\lambda_D}-1)(\frac{\lambda_s}{\lambda}+\frac{\lambda_R}{\lambda}))}]\right.$$

$$\left. -\frac{B-1}{p}\frac{\lambda}{\lambda_D} + \frac{B+1}{2B}(\frac{\lambda_R}{\lambda}\frac{\lambda}{\lambda_D}-B(1+(\frac{\lambda}{\lambda_D}-1)\frac{\lambda_R}{\lambda}))\right)$$

Appendix 4g gives full workings from equation (4.29) to equation (4.11).

References

1. **Crane RA Vachon RI**
"A Prediction of the Bounds on the Effective Thermal Conductivity of Granular Materials. " Int J of Heat & Mass Transfer. Vol 20 1977 pp 711-722

2. **Deissler RG Boegli JS**
"An Investigation of Effective Thermal Conductivities of Powders in Various Gases " Trans A.S.M.E Vol 8. 1958. pp 1417-1425

3. **Wakao N Kato K**
"Effective Thermal Conductivity of Packed Beds." J of Chem Eng of Japan. Vol 2. No. 1 1969. pp 24-33

4. **Schumann TE Voss V**
"Heat Flow Through Granulated Materials " Fuel. Vol 13. 1934. pp 249-256

5. Yagi S   Kunii D

"Studies of Effective Thermal Conductivities of Packed Beds. " A I Ch E Journal. Vol 3. 1957. pp 373-381

6. Woodside W

"Calculation of the Thermal Conductivity of Porous Media "Canadian Journal of Physics. Vol 36. 1958. pp 815-822

7. Kunii D   Smith JM

"Heat Transfer Characteristics of Porous Rocks" A I Ch E Journal. Vol 6. No. 1. 1960. pp 71-78

8. Schlunder EU

"Heat Transfer In Packed Beds" Warme und Soffubertragung. Bd 1. 1968. pp 153-158

9. Hayashi s   Kubota K   Masaki H et al

" A Theoretical Model for the Estimation of the Effective Thermal Conductivity of a Packed Bed of Fine Particles. " The Chemical Engineering Journal. Vol 35. 1987. pp 51-60

10. Zehner P

"Experimentelle und theoretische Bestimmung der effektiven Warmeleitfahrigekeit Durchstromter Kugelschuttungen bei massigen und hohen Temperaturen." Dissertation for Dipl Ing. 1972. University of Karlsruhe

11. Bauer R

" Effektive radiale Warmleitfahigekeit Gasdurchstromter Schuttungen mit Partikeln unterschiedlicher Form und Grossenverteilung. " VDI Forschungsh. 582

12. Damkohler G

from paper by Euken and Jacob . Der Chemie Ingenieur. Vol 3. no. 1 , 1937

13. Eckert ERG   Gross JF

" Introduction to Heat and Mass transfer " Mc Graw Hill. pp 249-251

14. Gradsteyn IS   Ryzhik G

" Tables of Integrals, Series and Products. " Academic Press. 1980. pp 58-59.

15. Flood E Alison

"The Solid-Gas Interface " Edward Arnold (Publishers) Ltd. 1967. pp 831-841

5. THERMAL CONDUCTIVITY MEASUREMENT OF AN AMMONIA-GRANULAR CHARCOAL BED.

Introduction

The piece of equipment described in this section has been specifically designed to measure the overall thermal conductivity of a packed granular bed in the presence of the adsorbate ammonia at high pressure and temperature. This test equipment is unique and previous to this work the author has been unable to find any reports of measurement of the conductivity of high pressure adsorbers and the problems associated with it.

All of the documented thermal conductivity apparatus using a steady state measurement technique are similar in nature. They consist of a cylindrical vessel with a central core heater. The annular space between the inner and outer walls is packed with the test material. The temperature across the bed is measured at a set power output and hence the overall bed conductivity can be calculated.

The measurement of overall bed conductivity of low pressure systems has been well investigated. Fritsch et al [1] present a piece of apparatus to measure the thermal conductivity of packed granular bed at atmospheric pressure under steady state conditions. They suggest the use of guard heaters to restrict longitudinal heat losses from the test section, see Section 5.1. Gurgel et al [2] measured the conductivity of an activated charcoal-methanol adsorber under steady state conditions at low pressures and temperatures. Using the same piece of equipment as ref [2], Sahnoune et al [3] measured the conductivity of a zeolite-water adsorber at low pressures and temperatures. Lui *etal* [4] measured the conductivity of solid zeolite blocks using a transient technique.

This section describes each component of the apparatus in detail. The main problem associated with measuring the thermal conductivity of a high pressure adsorber is that of heating the very large thermal mass of a pressure vessel whilst accurately maintaining the low heating power required by the test section. With this in mind the equipment was designed with several sets of heaters, each with a power range and resolution suited to its particular task.

The remainder of this section is devoted to a description of the test programme and the method of analysis of results to obtain the overall bed conductivity λ_{so}.

5.1 Thermal Conductivity Test Apparatus

The equipment consists of a pressure vessel which contains the granular charcoal and is heated by three sets of heaters which are computer controlled via thyristors. The adsorbate pressure is controlled by the use of a liquid adsorbate reservoir submerged in a temperature controlled oil bath. Since this piece of equipment is unique, a full description of the design and function of each component is presented below.

The Pressure Vessel

The pressure vessel has been designed to work in a pressure range of 0 to 30 bar, and a temperature range of 40°C to 200°C. A higher upper temperature is desirable but the limit was imposed by the silicone rubber material used in the o'-ring seal. The materials used in the vessel must be compatible with the gases air, helium, neon, argon and ammonia. The vessel is constructed from stainless steel 316L and consists of two concentric tubes which are joined at one end by a welded annulus plate, and at the other by a welded flange and bolted on end plate, see figure 5.1.

FIGURE 5.1

Assembly Drawing of Vessel
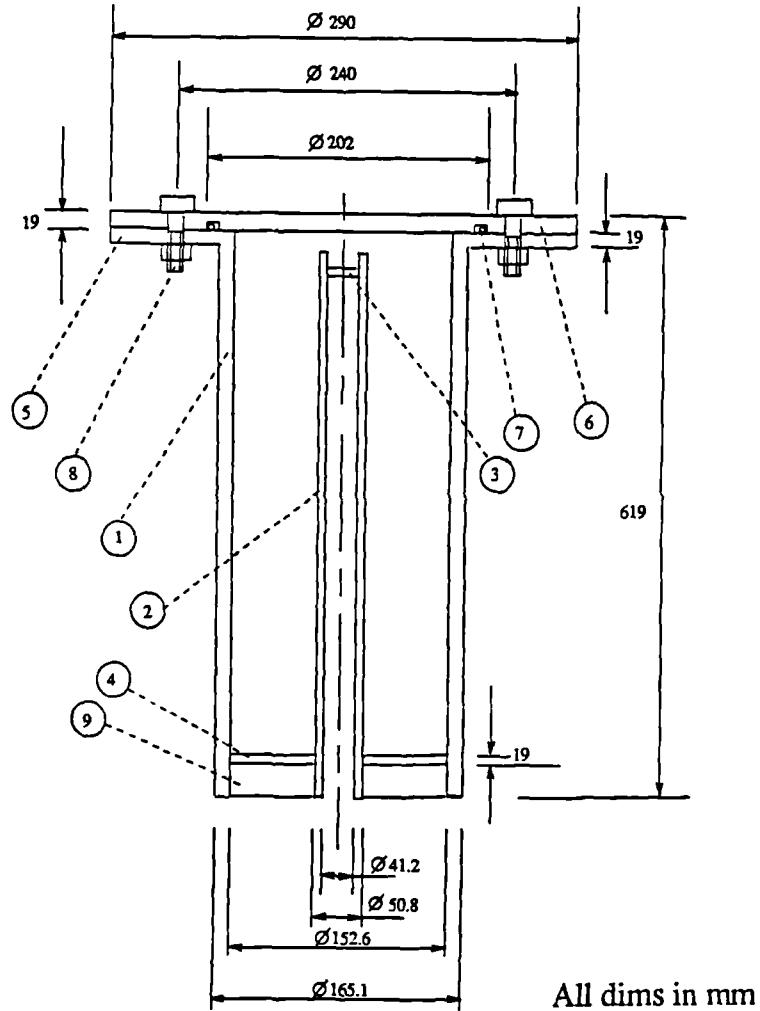
All dims in mm

Part No.	Description	Material
1	Outer Tube	Stainless Steel 316L
2	Inner Tube	Stainless Steel 316L
3	Small End Plate	Stainless Steel 316L
4	Annulus	Stainless Steel 316L
5	Flange	Stainless Steel 316L
6	Large End Plate	Stainless Steel 316L
7	'O' Ring Seal	Silicone
8	High Tensile Cap Head nut and bolt M14	High Tensile Steel
9	Webbing	Stainless Steel 316L

The annular cavity between the two tubes creates the space into which the granular charcoal is packed. To add extra strength to the vessel three radial webs were added at the sealed end, shown as part 9 in fig 5.1. The bolted end is fastened with high tensile steel M14 nuts and bolts and is made pressure tight by a silicone rubber o'-ring seal. Silicone was the only material found to be non-porous to ammonia gas at 200°C. The only disadvantage of using silicone is that its maximum working temperature is 200°C and at about 220°C the rubber softens and sticks to the metal surrounding it.

The radial sizing of the vessel was determined by two main criteria. The first was that the vessel should be strong enough with respect to the working pressure and temperature. The second was that the bed thermocouples should be far enough apart not to form a path of enhanced conductance, see bed thermocouples sub-section. The distancing of the bed thermocouples determined that the radial bed length should be not less than 50mm. Finite difference modelling using an approximate bed conductivity determined the vessel height, see heaters sub-section below. The thickness of the material used in the tubes and plates was determined by the ultimate tensile strength of the material and the working pressure. Appendix 5a contains all the relevant stress calculations. The vessel operates with a safety factor of 3 at 30 bar and 200°C. Before use the vessel was hydraulically pressure tested and found to be leak tight at 80 bar.

Bed heaters

There are a total of eight separately controlled heaters on the outer walls of the pressure vessel. Three heaters form the inner heater set and another three form the outer set. An additional two heaters are placed on the end plates to aid the initial heating up.

The inner and outer heaters also form three sets of longitudinal heaters, the dimensions of which are shown in figure 5.2. The upper, middle and lower sections each have an inner and outer heater working as a pair. The upper and lower pairs act as guard

heaters to maintain a temperature profile across the bed such that there is no longitudinal heat transfer. The middle set of heaters controls the test section on which all measure- ments are made.

FIGURE 5.2

Dimensions of Heated Sections

UPPER SECTION

MIDDLE SECTION

LOWER SECTION

205

325

575

All dims in mm
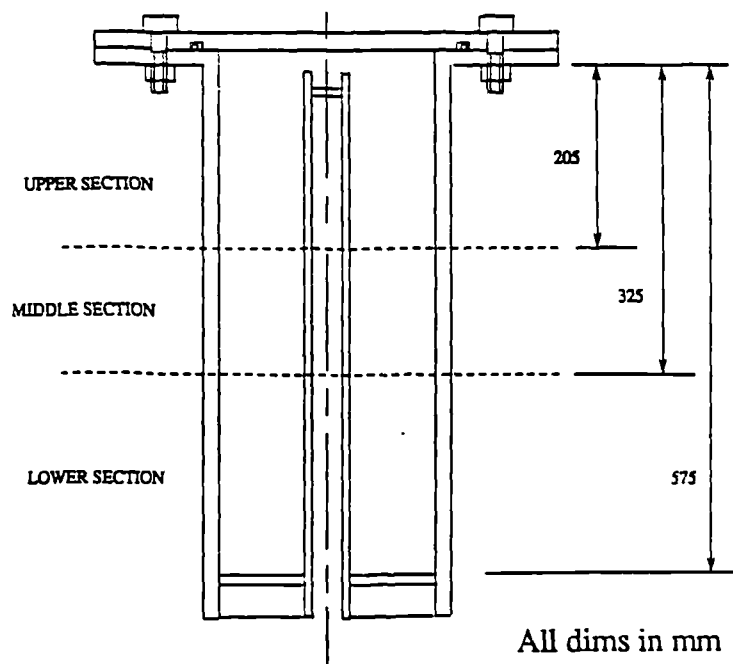
The Inner Heaters

The three inner sets of heaters are separately temperature controlled and powered by a low voltage dc amplifier, the input signal to which is sent via a Comark interface by software with a built in three term temperature controller. A scheme of the equipment is shown in figure 5.3 below.

The heaters are made from high resistance heating wire known as hecnum or eureka wire, wrapped tightly and uniformly at 2mm intervals around a core made from glass

FIGURE 5.3
Power Control Circuit For Inner Heaters
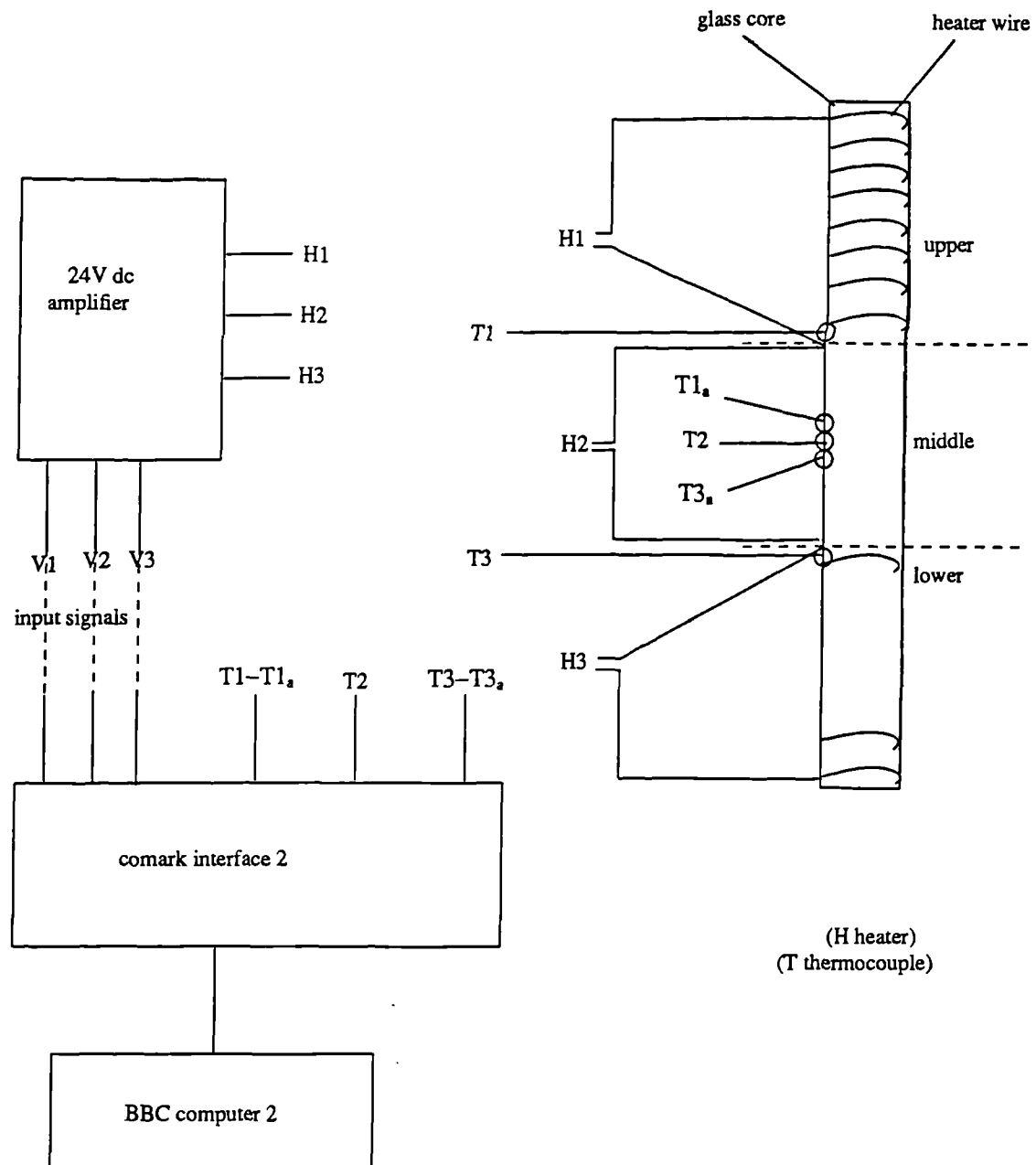
tubing. The wire has a resistance of 7Ω /m and was coated in fibreglass sleeving to avoid any electrical problems.

To connect each heater to its power supply, a single strand copper wire was silver soldered to the hecnum wire at the end of each heater section. The copper wire was then fed through a hole drilled in the glass tube wall and down through the centre of the tube

and out to a connecting block. This was done to avoid any unwanted extra heating as would be the case if the heater wire were continued through to the connecting block.

The bare ended thermocouples were positioned as shown in figure 5.4 between the heater wire and the glass tube.

FIGURE 5.4
Section Through Inner Heater

section length upper = 195 mm
section legth middle = 120 mm
section length lower = 195 mm
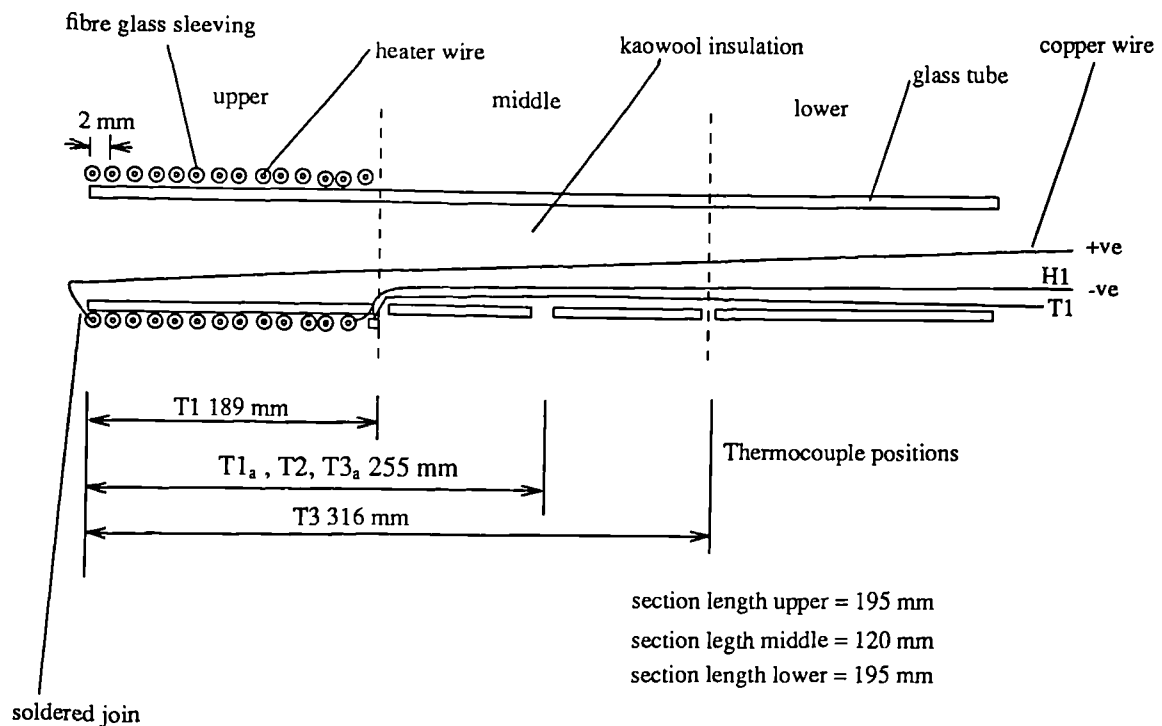
Only the thermocouple junction is present on the tube surface and the remainder of the wire is passed through a hole and down the centre of the tube. The thermocouples $T1_a$, $T2$ and $T3_a$ all read the temperature at the centre line of the middle section. $T2$ is an absolute reading whereas $T1_a$ and $T3_a$ are wired back to back with $T1$ and $T3$ respectively so that they are measuring a temperature difference. This was done to improve the accuracy of the temperature control on the outer upper and lower sections.

To avoid any unwanted convection taking place through the centre of the tube, it was filled with an insulating wool.

After the heaters were wound and the thermocouples positioned, the tube is inserted into the pressure vessel center tube, part 2 in figure 5.1, with which it forms a push fit.

The Outer Heaters

The outer heaters are separately temperature controlled and powered by mains voltage passed through chopping thyristors. The 0 - 5 V input signal to the thysistors is sent via a Comark interface by software with a built in three term temperature controller. The equipment is shown in figure 5.5 below.

FIGURE 5.5
Power Control Circuit for Outer Heaters
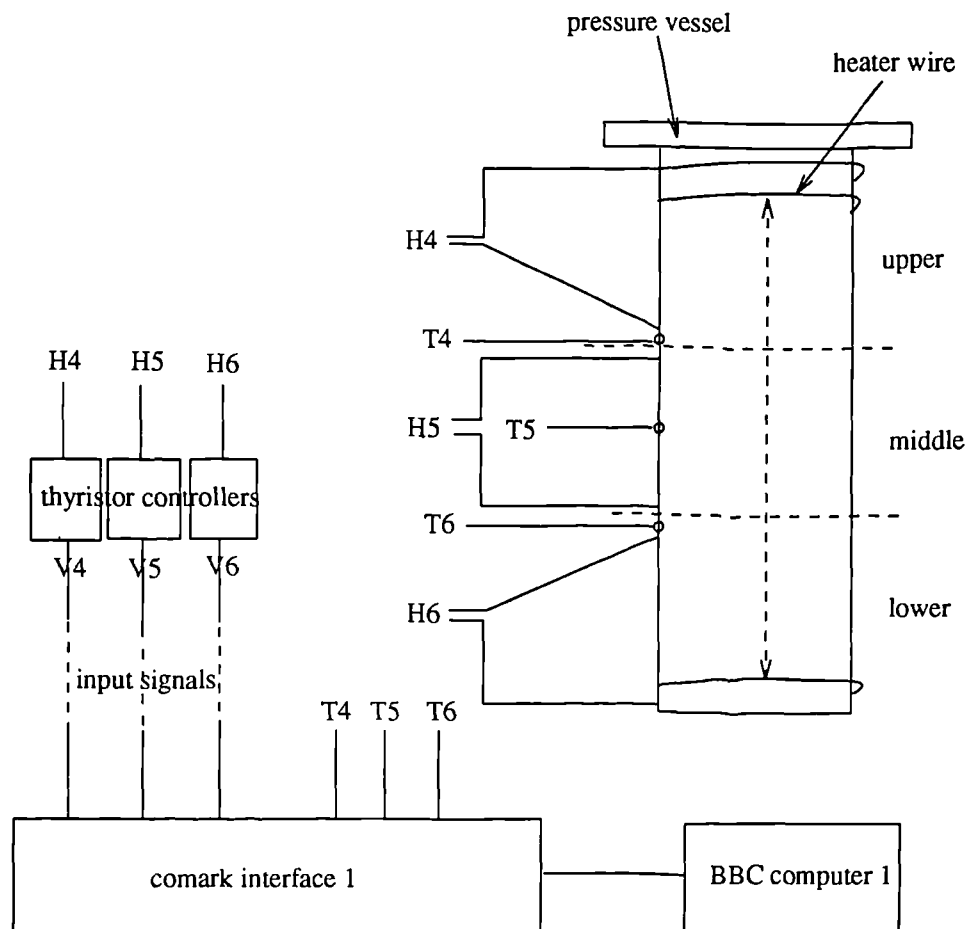
The heater wire used for the outer heaters is the same as that used for the inner heaters and again it is insulated by glass fibre sleeving. The connections from the heater wire to the power supply are made with copper wire. The heater wire is wound at a pitch of 2 mm around the outer wall of the pressure vessel and the sections have the dimensions shown in figure 5.2.

The bare ended thermocouples T4, T5 and T6 are positioned to correspond longitudinally with T1, T2 and T3 respectively. They are fixed to the surface of the pressure vessel with a thermosetting putty, after which the heater wire is wound over them. The purpose of the outer heaters is twofold. Firstly they assure that there is no longitudinal heat transfer between the upper, middle and lower sections and secondly they provide the necessary heating power to raise the vessel and its contents to the required temperature level.

For tests where the temperature exceeds 90°C, an insulting cylindrical jacket made from ceramic fibre was placed around the vessel. For tests where the temperature is less than 90°C it was found that a thin layer of kaowool insulation was sufficient.

End Heaters

The vessel is heated at either end by temperature controlled circular heaters, see figure 5.6. The function of these heaters is to aid in the initial heating up of the vessel and to maintain the end plates at the required temperature level. It was found that without the end plate heaters, longitudinal heat losses occurred due to too large a temperature difference between the upper and lower sections and the ends of the vessel.

The bolted end plate was insulated with discs of the ceramic fibre material and the lower end plate was insulated by packing the cavities between the webbing with kaowool.

FIGURE 5.6

End Plate Heaters
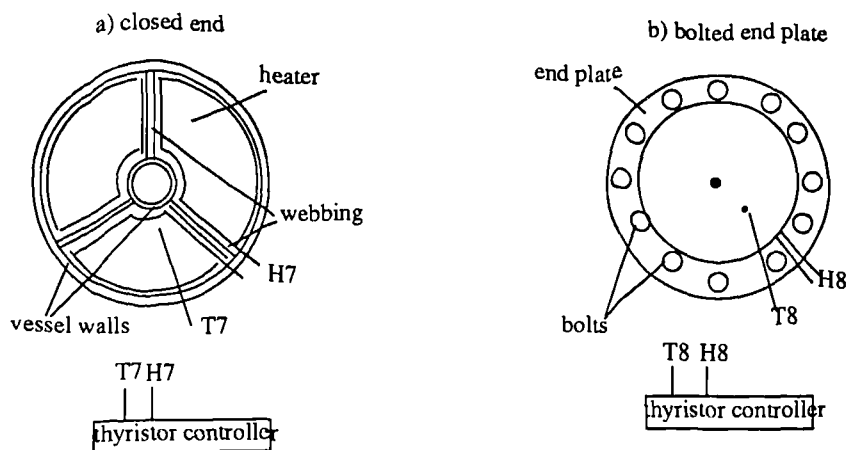
Bed Thermocouples

The temperature profile across the bed was measured using seven stainless steel sheathed K-type probe thermocouples which have a diameter of 1 mm. It was found by the use of a finite difference model, that the distance between the probe centres should not be less than 12mm to ensure that the thermocouples themselves did not provide a path of enhanced conductance, see appendix 5b. Figure 5.7 overleaf shows the positions of each of the seven thermocouples and their fittings.

Thermocouples TB4 and TB5 are positioned 1mm inside the outer and inner bed walls respectively. TB2, TC1 and TC2 are all positioned half between the inner and outer bed radii. TC1 and TC2 are used as a means of checking the accuracy of the thermocouple positioning and it was found that the three thermocouples all read to within 0.5°C of each other. Thermocouples TB1 and TB3 are placed at a quarter and threequarters of the way between the inner and outer radii respectively. The thermocouples are 300 mm long and measure the temperature at the longitudinal centre of the middle section. The probes are designed for use at 250°C and are connected to a Comark interface by PTFE

FIGURE 5.7
End Plate Showing Positions of Thermocouples
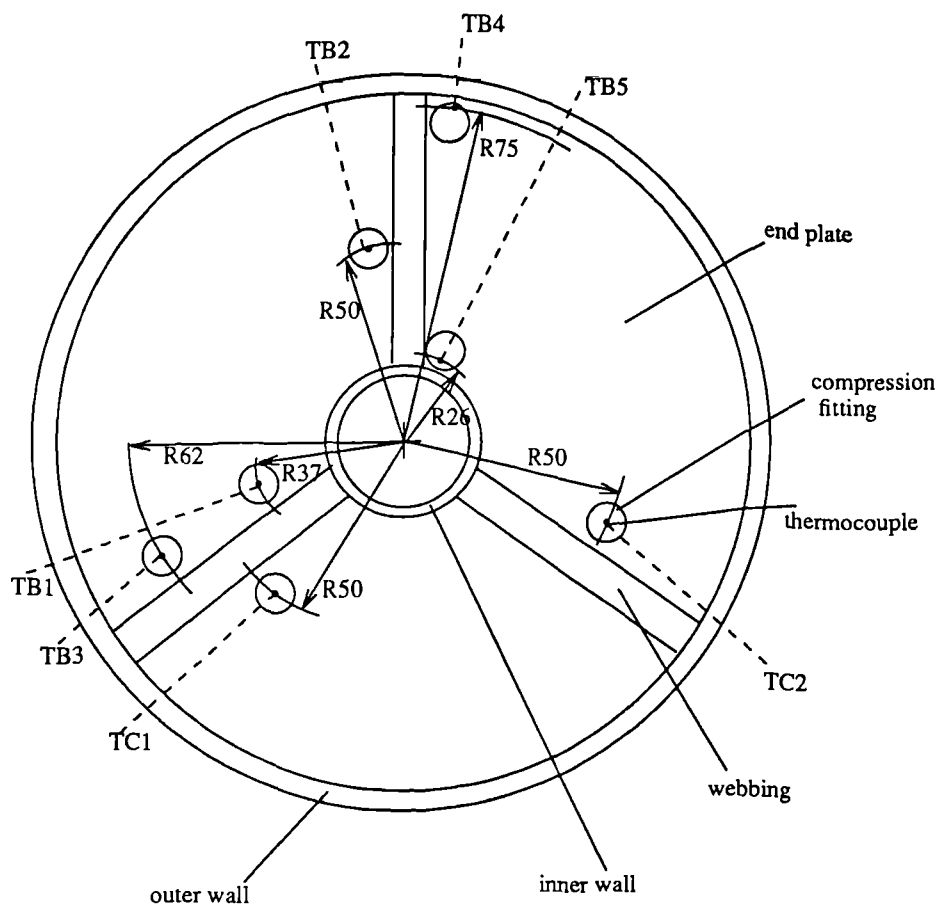
insulated K-type thermocouple wires. Figure 5.7 shows the positions of the compression fittings in the lower end plate. The thermocouple probe is threaded through the centre of the fitting which is then tightened to form a pressure tight seal.

Pressure Measurement

The gas pressure in the vessel is measured using a 0-30 bar strain gauge pressure transducer made by Druck, see figure 5.8.

The body of the transducer is made from stainless steel and the diaphragm from Hastelloy. The transducer requires a 10 V power supply and the output signal is

FIGURE 5.8

Pressure Measurement
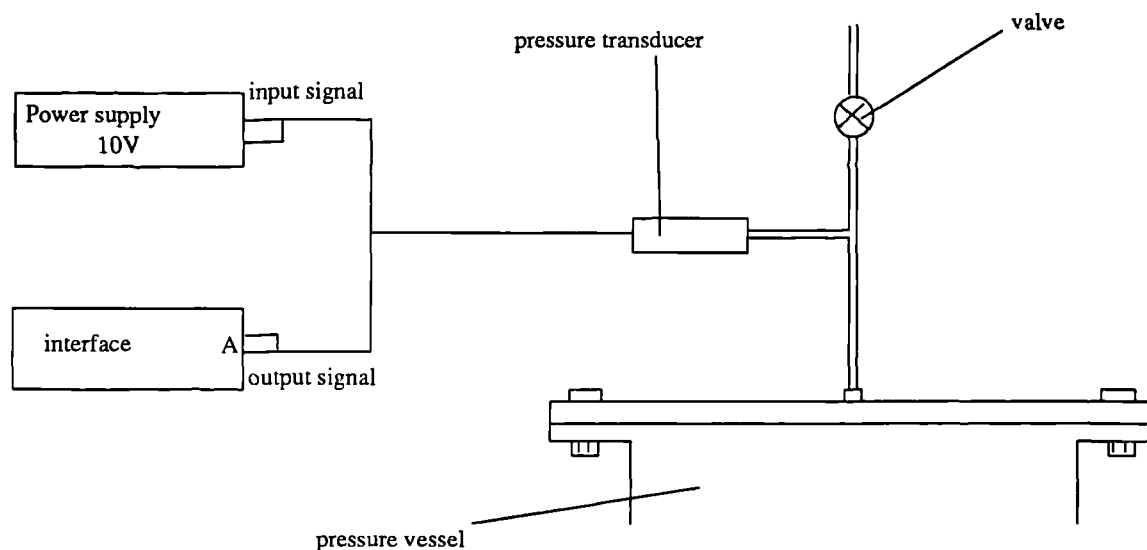
measured in mV by a Comark interface . The transducer is initially calibrated using a dead weight tester, see appendix 5c. A graph of mV output versus pressure in bar was found to by linear and fitted the equation :-

$$P = 0.1985 \times A + 0.1116 \qquad\qquad -(5.1)$$

where:-

P   pressure   bar

A   transducer output signal   mV

Ammonia Reservoir

When carrying out the conductivity tests with the adsorbable ammonia gas it is vital that a constant pressure and thus a constant concentration is maintained in the pressure vessel. The easiest way to accomplish this is to connect the pressure vessel to a reservoir

of liquid ammonia submerged in a temperature controlled oil bath, see figure 5.9.

FIGURE 5.9

Liquid Ammonia Reservoir
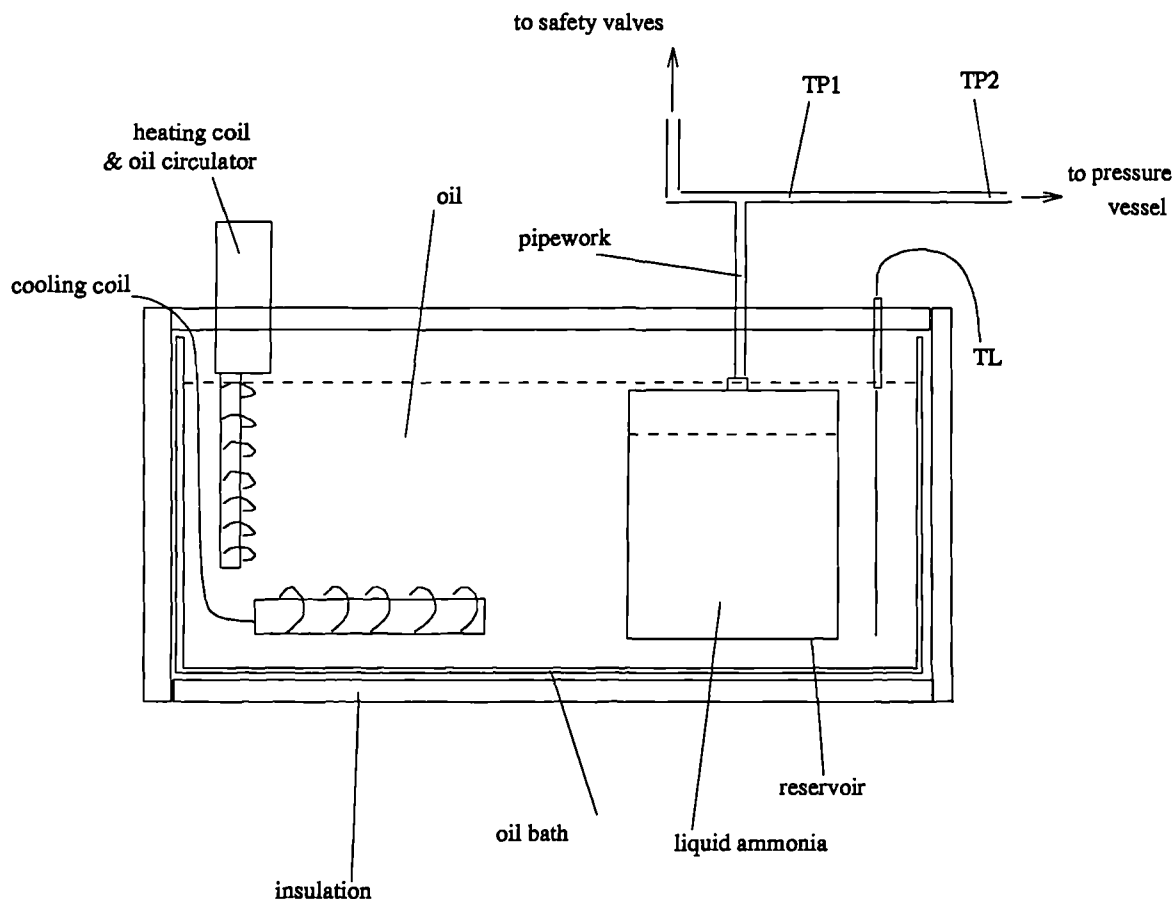
To control the oil bath temperature accurately a heating and cooling coil are used together and operate continuously.

The reservoir itself was designed to hold 1.6 litres of saturated liquid ammonia. It was constructed from a stainless steel cylinder and before use was hydraulically pressure tested to 80 bar and found to be leak tight. Appendix 5a contains all the relevant stress calculations and drawings. The pipework connections from the pressure vessel to the reservoir were made from 1/4" stainless steel tubing and Swagelok fittings. The temperature of the pipework was kept above the saturation temperature of the ammonia gas by the use of a heating tape wrapped around the pipework and covered by insulation. The

temperature of the pipework was measured in two places using bare ended thermocouples which were logged through Comark 2. The oil temperature was measured using a probe thermocouple dipped into the oil near the reservoir and logged through Comark 2.

For tests involving high ammonia pressures it was found to be necessary to insulate the oil bath to maintain a constant and uniform temperature.

Interfaces

The Comark interfaces shown in figures 5.3 & 5.5 are identical and are separately connected to independently working BBC computers by RS232C connections. Each Compuface has eight thermocouple channels, four analogue input channels and four analogue output channels. The channels are connected as shown in figures 5.10a & 5.10b.

FIGURE 5.10a
Comark Interface 1
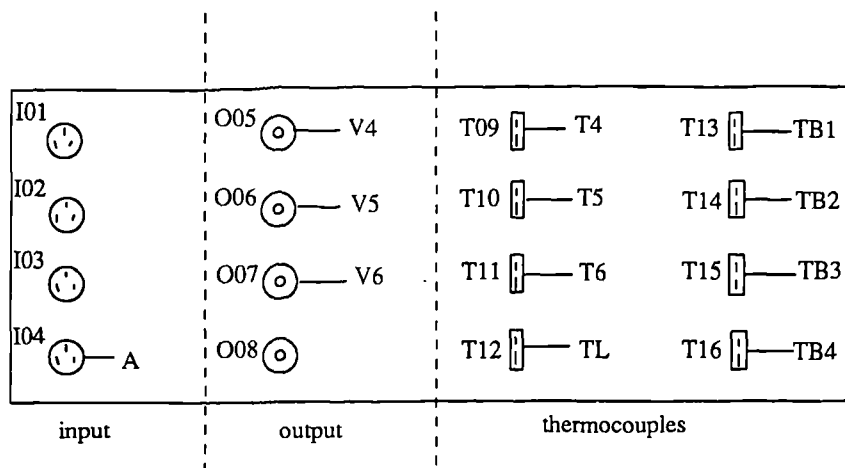
On Comark 2 the thermocouple channels T09 and T11 have been programmed to read as analogue input channels since they are reading a voltage from back-to-back thermocouples.

FIGURE 5.10b

Comark Interface 2

I01 ⊙	O05 ⊙—— V1	T09 ▯—T1$_a$-T1	T13 ▯——TB5
I02 ⊙	O06 ⊙—— V2	T10 ▯——T2	T14 ▯——TP2
I03 ⊙	O07 ⊙—— V3	T11 ▯——T3$_a$-T3	T15 ▯——TC1
I04 ⊙	O08 ⊙	T12 ▯——TP1	T16 ▯——TC2
input	output	thermocouples	
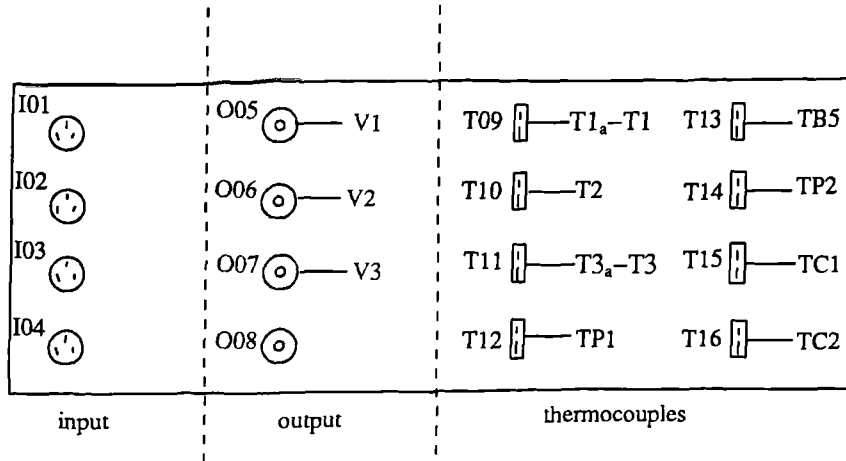
Software

The inputs and the outputs to the Comark interfaces are controlled by software written for BBC computers with RS232C connectors. The readings to and from all of the connected comark channels are read every second and displayed on monitors. Every hour the readings are sent to printers to provide a hard copy.

As well as collecting the incoming information from the interfaces, the software calculates the outgoing voltage signals V1-V3 to the amplifiers via comark 2 for the inner heaters, and the output voltage signals V4-V6 to the outer heaters via thyristor controllers and comark 1. The control signal sent to each heater is based on the difference between the current heater temperature and the required heater temperature and uses the following algorithm :-

$$E1_{(t-1)} = E1_{(t)}$$

$$E1_{(t)} = T_0 - T_n$$

$$ESUM = ESUM + E1_{(t)}$$

$$V = ESUM \times C1 + E1_{(t)} \times C2 - (E1_{(t-1)} - E1_{(t)}) \times C3$$

T_0	required heater temperature
T_n	current heater temperature
$E 1_{(t)}$	required heater temp - current heater temp
$E 1_{(t-1)}$	previous reading of $E 1_{(t)}$
ESUM	total sum of $E 1_{(t)}$ over time t
V	ouput signal voltage
C1	summing term constant
C2	proportional term constant
C3	differentiating term constant

The constants C1,C2 and C3 have to be found by trial and error using the equipment. They were found to be :-

outer heaters:- C1 = 0.001 , C2 = 0.151 , C3 = 0.0765

inner heaters:- C1 = 0.001 , C2 = 0.350 , C3 = 0.150

When the programs are set running, the user has only to answer the prompted question of required heater temperature and the program then runs until it is manually stopped. The printouts below show a sample of the hard copies obtained from both programs.

Outer heaters

T4	T5	T6	TB4	TB1	TB2	TB3	P
TARGET	TUPPER	TMIDDLE	TLOWER	TWALLO	1/4R	1/2R	3/4R	-PRESS
230.000	230.000	229.800	230.000	229.900	238.500	234.900	232.000	1.521
TARGET	TUPPER	TMIDDLE	TLOWER	TWALLO	1/4R	1/2R	3/4R	PRESS
230.000	230.000	229.900	230.000	229.800	238.500	234.900	232.100	1.521
TARGET	TUPPER	TMIDDLE	TLOWER	TWALLO	1/4R	1/2R	3/4R	-PRESS
230.000	229.900	230.200	230.000	229.900	238.400	234.900	232.000	1.521

Inner heaters

$T1_a-T1$	T2	$T3_a-T3$	TB5	TC1	TC2	V2
TARGET	TUPPER	TMIDDLE	TLOWER	TWALI	1/2R	1/2R	VOLT
250.000	0.000	250.000	0.000	242.400	234.700	234.600	18.498
TARGET	TUPPER	TMIDDLE	TLOWER	TWALI	1/2R	1/2R	VOLT
250.000	0.000	250.000	0.000	242.400	234.700	234.600	18.494
TARGET	TUPPER	TMIDDLE	TLOWER	TWALI	1/2R	1/2R	VOLT
250.000	0.000	250.000	0.000	242.400	234.700	234.600	18.509

The only control voltage recorded on hard copy is that sent to the inner middle heater which is given as an average over the previous hour.

Evacuation Equipment and Gas Supplies

Prior to testing, the charcoal sealed within the pressure vessel must be prepared by degassing. This involves heating the charcoal to 200°C and keeping the vessel under vacuum. This process removes any unwanted adsorbed gases from the micropores and in effect "cleans" the charcoal ready for use. In the first instance, a rotary vacuum pump was used to degas the charcoal under a vacuum of 0.1 Torr for 24 hrs. This removes the bulk of unwanted gases from the vessel. A diffusion pump was then used to complete the degassing process for a further 24 hrs at a vacuum of 10^{-4} Torr. The charcoal was afterwards stored in its degassed state by flooding the vessel with the inert gas argon. The equipment is shown in figure 5.11 overleaf.

All pipework and connections are made from 1/4" stainless steel components. The valves used to isolate the gas supplies or the vacuum are Swagelok stainless steel bellows type valves capable of holding a vacuum of 10^{-4} Torr.

FIGURE 5.11
Evacuation Equipment and Gas Supplies
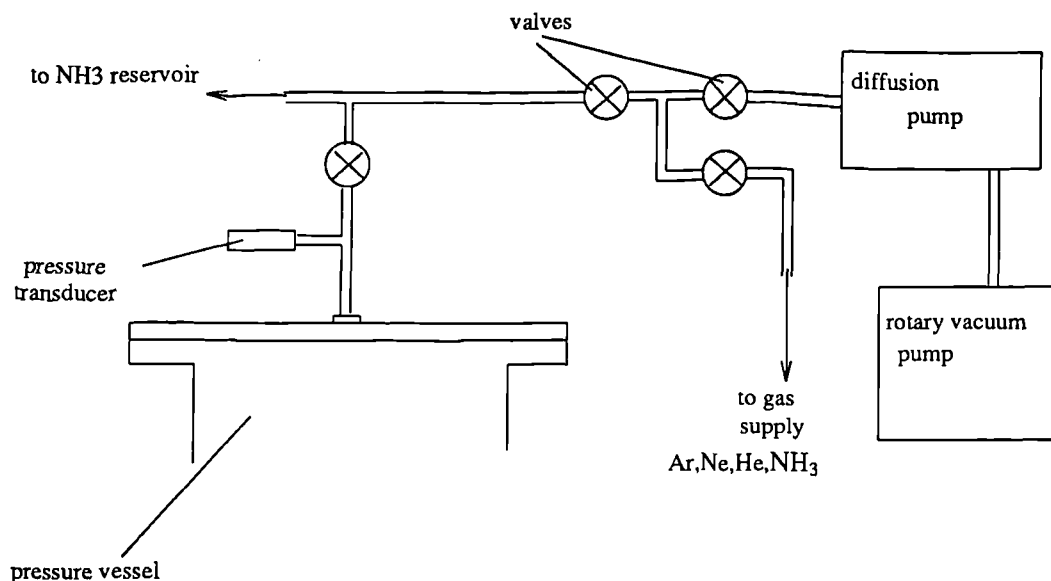
The evacuation equipment was also used for the set of tests conducted under vacuum during which the pumps were left running continuously.

Safety Measures

As it can be imagined, dealing with 30 bar of 200°C anhydrous ammonia could lead to a potentially dangerous situation unless suitable safety precautions are taken. The safety measures listed below cover every possible eventuality which could be caused by equipment failure.

Pressure Cut-out Switch

The mains supply to the outer heaters is wired through a pressure cut-out switch set to 30 bar. In the event of the pressure in either the vessel or the reservoir rising above 30 bar the power to the outer heaters is switched off.

Pressure Relief Valve

Also connected to the pressure vessel and the reservoir is a pressure relief valve set to 30 bar. In the case of the adsorbable gas ammonia, it is possible that desorption would continue and the pressure rise even after the power to the outer heaters is cut. At 30 bar the pressure relief valve opens and exhausts the unwanted gas to outside.

Thermal Fuse

A thermal fuse is stuck to the outer wall of the pressure vessel and is wired through the power supply to the outer heaters. The fuse burns out at $\approx$ 220°C so that in the case of overheating the heaters will be quickly switched off.

Software

Safety is built into the software so that if the pressure exceeds 30 bar or the temperature exceeds 220°C the control signals V4,V5 and V6 are immediately set to zero.

Earthing

An earth strap is taken from the vessel to the power supply of the main heaters.

Extractor Fan

An extractor fan is in continuous operation in case of any ammonia leakage.

Remote Control

As a final safety measure the computers, monitors and printers are in a separate room to the test equipment so that tests may be started and monitored remotely. It is not therefore necessary for anyone to be in the same room as the vessel when it is at high pressure.

5.2 Test Procedures

Packing the Bed and Alignment of Thermocouples.

The bed thermocouples TB1-TB5,TC1 and TC2 are correctly positioned with the aid of the alignment plate shown in figure 5.12.

FIGURE 5.12
Bed Thermocouple Alignment Plate
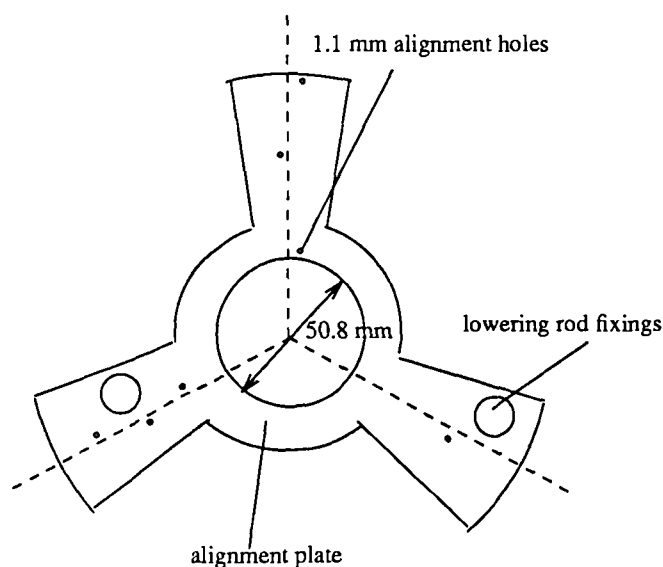
The plate is fixed to two lowering rods by the fixing shown on the drawing and is lowered to the bottom of the vessel. The thermocouples are then threaded through the compression fitting in the end plate of the vessel and through the corresponding hole in the alignment plate. Once all seven thermocouples have been threaded in this way, the compression fittings are tightened to secure the base position of the probe and packing of the charcoal may now begin. The granulated charcoal is dropped into the vessel and spread underneath the plate by patting it gently. This packs the charcoal around the thermocouples. The alignment plate is then raised a few centimeters and another layer of charcoal is added. This process continues until the end of the probes is reached at which point the alignment plate is carefully removed and charcoal is packed to the top of the vessel. This method of thermocouple alignment was found to work very well because

during packing the thermocouples are continually constrained to their correct radii. It was found that when the alignment plate was finally removed that the thermocouples did not spring out of position.

Evacuation of the Charcoal

Before any testing commences the charcoal must be degassed. As it stands, the charcoal contains an appreciable amount of water vapour in the micropores which it has adsorbed from the air around it. There is also air and water vapour present in the inter-granular void space which needs to be removed. Degassing is accomplished by heating the vessel to 200°C for 48 hrs whilst subjecting the charcoal to a vacuum. The vacuum supplied is 0.1 Torr for the first 24 hrs and 10^{-4} Torr for the final 24 hrs. For an initial period of 3-4 hrs the vessel is heated with the isolation valve open to atmosphere. This allows most of the water to escape as steam before using the vacuum equipment.

This thorough degassing process only needs to be carried out once, unless it is suspected that the vessel is not pressure tight and air has leaked into it. After degassing and between tests the charcoal is stored under the non-adsorbable gas argon.

Measurement of Void Volumes

The total Void Volume

This value is measured to find the ratio of total void volume to total volume. The total void volume includes the interparticle void plus the micro, meso and macropore volume. This value will be used in the modelling undertaken in Section 6. This test is carried out using the equipment shown in figure 5.13.

FIGURE 5.13
Apparatus for Finding Total Void Volume

isolating valves

pressure transducer
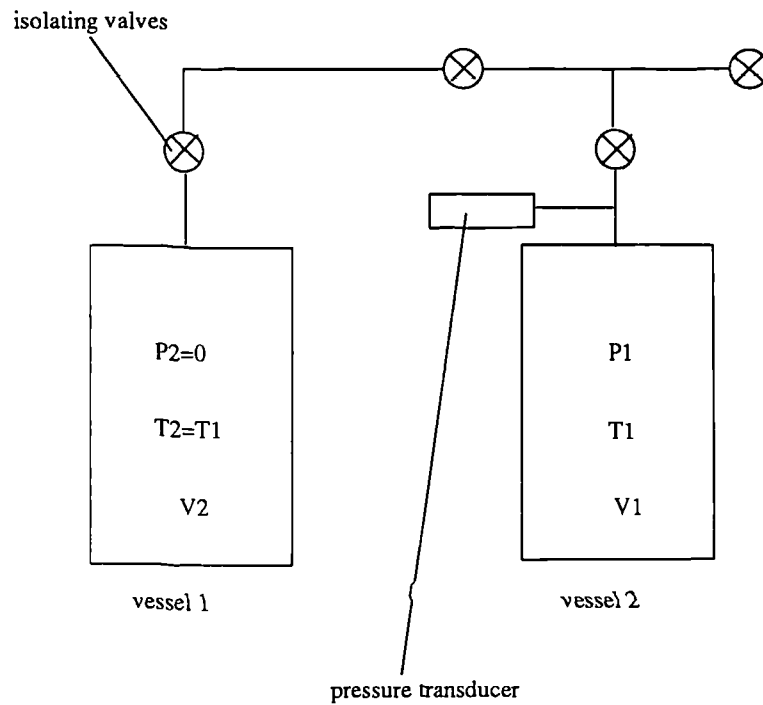
The pressure vessel V1 is filled with helium gas to a known pressure P1. This is connected to a second vessel V2 which has been evacuated. The isolating valve between the two vessels is opened and pressure is allowed to equalize to Pf. Both of the vessels are at a known temperature and so the void volume in the pressure vessel Vv can be calculated.

$$\frac{P1\,Vv}{T1} = \frac{Pf\,(Vv + V2)}{T1}$$

$$Vv = \frac{Pf\ V2}{P1 - Pf}$$

From which

$$\frac{\text{void volume}}{\text{total volume}} = 0.77$$

The Intergranular Void Volume

This is the value ψ in the ZB model and is the ratio of the interparticle void volume to the total void volume. This value is found by the following method.

A sample of charcoal is soaked in water so that all the macro, meso and micropores are full. The surplus water is then drained off and the charcoal grains are dried by blowing air over them. The charcoal is then packed into a measuring beaker which is large enough to ensure that packing distortion at the beaker's edge is negligible. The charcoal is packed to a level marker of a predetermined volume and the mass of the beaker and contents is weighed. Water is then added up to the level marker and the beaker is weighed again. The difference between the two readings enables us to calculate the intergranular void volume. ψ was found to be,

$$\psi = \frac{\text{intergranular void volume}}{\text{total volume}} = 0.478$$

Procedure for Measuring Bed Conductivity

The conductivity tests may be split into three categories, each of which has a slightly different test procedure.

(i) Vacuum.

The charcoal in the vessel is roughed down to a vacuum of 0.1 Torr using a rotary vacuum pump, after which a diffusion pump further reduces the vacuum to 4×10^{-5} Torr. The diffusion and rotary pump operate continuously during the tests.

(ii) Non-adsorbable Gases. Ne He Ar

The vessel is evacuated and filled with the required gas to the correct pressure. The gas bottle is left connected to the vessel and the pressure is maintained through a regulating valve.

(iii) Adsorbable Gases. NH₃

The vessel is evacuated and filled with ammonia from a supply bottle, this takes some time because the heat generated during adsorption needs to be allowed to dissipate before more adsorption can take place. The reservoir is also evacuated and filled with liquid ammonia. The connecting valve between the vessel and the reservoir is then opened and the pressure allowed to equalize. The desired test pressure is set using the temperature control on the reservoir.

After the vessel has been charged with the correct gas or evacuated the test follows the procedure outlined below.

(a) The inner heater control temperature is set via BBC 2.

(b) The outer heater control temperature is set via BBC 1.

(c) The vessel and its contents are left to reach a steady temperature state. This may take some 48 hrs.

(d) It is judged that the vessel has reached a steady state when the voltage output to the inner middle heater does not vary by more than ±0.01V for a continuous 15 hrs.

(e) When the test is finished both sets of heaters are switched off.

(f) Before the vessel has cooled the resistance of the heaters H2 is measured so that its power output can be calculated.

(g) The linearity of the amplifiers controlling H1, H2 and H3 is checked using a set input signal and measuring the output signal.

Test Programme

A total of 19 sets of tests were carried out using either vacuum, adsorbable or non-adsorbable gases. Each of the tests was designed to highlight a specific mechanism of heat transfer within the bed.

(i) vacuum tests

When the bed is under vacuum, heat can only be transferred by grain to grain radiation or by solid conduction though point contact of the grains. It is important that the vacuum is low enough so that there is definitely no gas conduction taking place. This may be found using the equation defining Knudsen conductivity, ref[5].

$$\lambda_D = \frac{\lambda}{1 + \frac{2T\sigma_0 P_0}{x_D T_0 P}(\frac{2}{\gamma} - 1)} \qquad — (5.2)$$

Also from ref[5] for air,

$$\frac{P_0}{T_0}\sigma_{0air} = 2.27 \times 10^{-5}\frac{T}{P} \qquad — (5.3)$$

substituting equation (5.3) into equation (5.2) gives,

$$\lambda_D = \frac{\lambda}{1 + \frac{2 \times 2.27 \times 10^{-5}T}{x_D P}(\frac{2}{\gamma} - 1)} \qquad — (5.4)$$

The conductivity due to Knudsen effect will be at its largest when T is at its smallest and P and x_D are at their largest. The maximum value for x_D is estimated at approximately 10 mm and the minimum value for T is 313 K. The accommodation coefficient is estimated at 0.8 from ref [5]. The conductivity of air at 313 K is 0.02624 W/m K.

So equation (5.4) becomes,

$$\lambda_D = \frac{0.02624}{1 + \frac{2.131}{P}} \qquad — (5.5)$$

The pressure therefore determines the apparent conductivity of the air. The conductivity of the bed under vacuum is estimated at 0.1 W/m K, therefore we shall place a limit on λ_D of 0.001 W/m K.

$$\lambda_D \leq 0.001 \leq \frac{0.02646}{1 + \frac{2.131}{P}}$$

therefore

$$P \leq 0.084\text{Pa} \leq 6\times10^{-4} \text{ Torr}$$

The pressure for these tests must always be less than 6×10^{-4} Torr for the gas conduction to be negligible. Four vacuum tests were conducted over a temperature range of 313 K to 473 K. The change in overall conductivity is due solely to the increase in radiation heat transfer. It is assumed that over this relatively narrow temperature band the conductivity of the charcoal grain remains constant.

(ii) Tests with Non-adsorbable Gases

The overall conductivity of the bed was measured with three different non-adsorbable gases, helium, argon and neon. Conduction in the presence of these gases is due to all the mechanisms outlined in the ZB model outlined in section 4.2. Because the gas is not adsorbed it can be stated that the grain conductivity λ_s remains constant. The variation of gas conductivity with temperature is found from ref [6].

(a) Helium Tests.

In total six helium tests were carried out. The first test was carried out at 30 bar and 513 K and the second at 3.7 bar and 513 K. The difference in the bed conductivity of these two tests indicates the extent of any Knudsen effect. Depending on how great this is a similar test could be carried out with argon. The lower pressure limit of 3.7 bar is calculated using equation (5.2) such that the mean free path of the helium is equal to the maximum mean free path of ammonia in its working pressure and temperature range. The remainder of the helium tests are carried out over a temperature span of 313 K to 513 K at 3.7 bar.

(b) Argon and Neon Tests.

Three argon and one neon test are conducted over a temperature range of 313 K to 483 K at pressures of 1.24 bar and 2.5 bar respectively. The test pressures are calculated using equation (5.2) to give the required mean free path length. An additional test of

argon at 30 bar was included in the initial test programme.

(iii) Adsorbable Gas.

Five sets of tests were carried out using ammonia gas. The object of these tests is to establish the variation of the grain conductivity with different concentrations of adsorbed ammonia. To this end all of the tests were conducted at the same temperature with the concentration being controlled by the pressure.

The table below summarizes the provisional test programme.

TABLE 5.1

Test Programme

Test No.	Gas	Mean Bed Temp (K)	Pressure (Pa)
1	Helium	513	30×10^5
2	Helium	513	3.7×10^5
3	Helium	438	3.7×10^5
4	Helium	383	3.7×10^5
5	Argon	383	1.24×10^5
6	Argon	428	1.24×10^5
7	Argon	483	1.24×10^5
7a	Argon	483	30×10^5 (provisional test)
8	Vacuum	473	4×10^{-3}
9	Vacuum	423	4×10^{-3}
10	Vacuum	373	4×10^{-3}
11	Helium	383	3.7×10^5 (repeatability test)
Outer insulation removed for lower temperature tests.			
12	Ammonia	313	1.56×10^5
13	Ammonia	313	4.24×10^5
14	Ammonia	313	5.79×10^5
15	Ammonia	313	7.00×10^5
16	Ammonia	313	11.3×10^5
17	Vacuum	313	4×10^{-3}
18	Neon	313	2.5×10^5
19	Helium	313	3.7×10^5

Error Analysis

The results of the experiments shown in section 5.3 are analyzed using equation (5.6) defining one dimensional radial heat transfer.

$$Q = \frac{2\pi L \, \lambda_{so} \Delta T}{\ln(\frac{r_0}{r_i})} \quad - (5.6)$$

where:-

Q   power output to inner middle heater (W)

λ_{so} bed conductivity (W/m K)

L   axial length of test section (m)

ΔT radial temperature difference across bed (K)

r_0 outer radius (m)

r_i inner radius (m)

Rearranging equation (5.6) to find the bed conductivity gives,

$$\lambda_{so} = \frac{Q \ln(\frac{r_0}{r_i})}{2\pi L \, \Delta T} \quad - (5.6a)$$

The power output Q is found from equation (5.7) below.

$$Q = \frac{V^2}{R} \quad - (5.7)$$

where:-

V   voltage to inner heater   V

R   resistance of inner heater Ω

The table overleaf lists the accuracy of measurement of the above parameters.

parameter	accuracy	% accuracy
r_0	±0.5 mm	±0.7%
r_i	±0.5 mm	±2.0%
L	±1mm	±0.8%
ΔT	±0.2 °C	±1.0%
V		±0.05%**
R		±1.0%*

* accuracy of multimeter

** includes accuracy of comark analogue output channel, amplifier and multimeter.

The accuracy of the power output measurement is ±2.0 %, and the accuracy of the overall bed conductivity is ±6.1 %.

One further source of inaccuracy in the results must be combated. Longitudinal power leakage between the middle and upper and middle and lower sections occurs due to the possibility of the thermocouples T1-T6 being placed on either hot or cold spots. This problem is overcome by making two measurements of an overall bed conductivity, with different temperature differences across the bed but with all the other conditions being held the same. Plotting Q against ΔT and finding the intercept with the Q axis when ΔT = 0 gives us the power leakage for each test. Initial experiments showed us that the results of a test using four temperature differences fell on a straight line of a plot of Q against ΔT as expected. It was decided henceforth that only two tests would be necessary to gain the axial power loss.

5.3 Results and Treatment of Data

This section summarizes the results of the experiments described in 5.1 and 5.2 and describes the treatment of the data to extract the overall bed conductivity λ_{so} and the heat transfer coefficient between the vessel wall and the charcoal bed.

Overall Thermal Conductivity of Bed.

Table 5.2 overleaf shows the results gained from the 19 sets of tests carried out. The values are the averages taken over the steady state period of fifteen hours. As it can be seen, test 7a was not carried out since after initial analysis and comparison of tests 1 and 2 it was found not to be necessary.

Table 5.3 shows the results of plotting the temperature difference across the bed ΔT against the power output Q to the test section. The constant c found from the linear fit is the steady state power loss at zero temperature difference and must therefore be subtracted from Q to give the corrected power output Q_{corr}.

$$Q = a \Delta T + c$$

$$Q_{corr} = Q - c$$

Of the mechanisms of heat transfer involved in tests 1-19, the solid conductivity is constant, the gas conductivity is linear with respect to temperature, and the radiation conductivity is cubic with respect to temperature. For all of the tests the maximum temperature difference across the bed is 27°C and in most cases is considerably less 5°C. It is therefore unlikely that the cubic influence of the radiation will be noticeable over such a small temperature range. In addition to this the maximum mean temperature of the tests

TABLE 5.2

Results of conductivity tests.

Test No.	TB4 75mm °C	TB3 64mm °C	TB2 51mm °C	TB1 38mm °C	TB5 27mm °C	ΔT °C	V V	Q W
1	230.9 237.0	232.7 237.6	235.5 238.2	238.6 238.8	242.1 239.6	11.2 2.6	18.097 9.749	5.914 1.713
2	230.8 237.2	232.7 237.7	235.5 238.4	234.4 238.8	241.9 239.8	11.6 2.6	17.680 9.270	5.622 1.543
3	156.6 162.8	158.7 163.2	161.6 163.8	165.1 164.4	169.1 165.3	12.4 2.5	16.882 8.798	5.135 1.387
4	101.0 107.1	103.1 107.5	106.1 108.1	109.7 108.9	113.5 109.6	12.6 2.6	15.680 8.341	4.414 1.245
5	100.9 107.1	103.2 107.6	106.4 108.3	110.2 109.1	113.9 109.8	12.9 2.7	10.200 5.643	1.860 0.570
6	146.4 152.7	148.7 153.1	151.9 153.8	155.7 154.4	159.6 155.3	13.1 2.6	10.966 6.067	2.151 0.662
7	201.6 207.7	203.7 208.1	206.7 208.7	210.4 209.2	214.3 210.1	12.7 2.3	12.001 6.645	2.563 0.791
8	183.6 197.8	188.1 198.2	194.5 198.7	202.2 199.3	209.5 200.2	25.8 2.4	11.425 5.135	2.335 0.473
9	133.3 147.6	138.0 148.0	144.6 148.6	152.5 149.4	159.7 150.3	26.4 2.7	10.000 4.530	1.795 0.367
10	82.9 97.1	87.5 97.6	94.2 98.3	102.2 99.2	109.2 99.9	26.3 2.8	8.866 3.853	1.404 0.266
11	100.9 107.0	103.0 107.4	106.0 108.1	109.7 108.9	113.4 109.6	12.5 2.6	15.865 8.242	4.518 1.270
12	34.0 37.6	35.6 38.1	37.9 39.0	40.7 40.0	43.5 40.8	9.5 3.3	8.350 6.170	1.243 0.476
13	32.9 37.3	34.8 37.9	37.6 38.8	40.9 40.0	44.0 40.7	11.0 3.4	9.091 5.365	1.468 0.511
14	34.0 37.5	35.6 38.2	37.9 39.0	40.6 40.0	43.6 40.9	9.6 3.4	8.499 5.254	1.283 0.491
15	37.6 34.0	38.2 35.6	39.0 37.9	40.0 40.7	40.9 43.7	3.3 9.7	5.318 8.637	0.503 1.321
16	33.9 37.5	35.5 38.1	37.9 38.9	40.4 40.0	43.6 40.8	9.7 3.3	8.955 5.488	1.424 0.536
17	37.5 31.6	38.1 33.8	39.0 37.1	40.0 41.3	40.8 44.8	3.3 13.2	2.834 5.263	0.143 0.494
18	37.5 34.6	38.1 36.0	38.9 38.0	40.0 40.4	40.9 43.0	3.4 8.4	5.875 8.944	0.615 1.426
19	37.5 35.6	38.1 36.7	38.9 38.3	39.9 40.2	40.7 42.1	3.2 6.5	7.233 10.078	0.933 1.811

TABLE 5.3

Correction to Power Output

Test No	ΔT °C	Q W	a W/°C	c W	Q_{corr} W
1	11.2	5.914	0.4885	0.443	5.426
	2.6	1.713	"	"	1.270
2	11.1	5.622	0.4833	0.277	5.345
	2.6	1.543	"	"	1.266
3	12.4	5.135	0.3775	0.443	4.692
	2.5	1.387	"	"	0.944
4	12.6	4.414	0.3172	0.433	3.981
	2.6	1.245	"	"	0.812
5	12.9	1.860	0.1263	0.225	1.635
	2.7	0.570	"	"	0.345
6	13.1	2.151	0.1410	0.298	1.853
	2.6	0.662	"	"	0.364
7	12.7	2.563	0.1710	0.396	2.167
	2.3	0.791	"	"	0.395
8	25.8	2.335	0.0794	0.285	2.050
	2.4	0.473	"	"	0.188
9	26.4	1.795	0.0604	0.203	1.592
	2.7	0.367	"	"	0.164
10	26.3	1.404	0.0485	0.128	1.276
	2.8	0.266	"	"	0.138
11	12.5	4.518	0.3281	0.417	4.101
	2.6	1.270	"	"	0.853
12	9.5	1.243	0.1213	0.081	1.162
	3.3	0.476	"	"	0.395
13	11.0	1.468	0.1249	0.090	1.378
	3.4	0.511	"	"	0.421
14	9.6	1.283	0.1267	0.065	1.218
	3.4	0.491	"	"	0.426
15	3.3	0.503	0.1283	0.079	0.424
	9.7	1.321	"	"	1.242
16	9.7	1.424	0.1403	0.067	1.357
	3.3	0.536	"	"	0.469
17	3.3	0.143	0.0352	0.027	0.116
	13.2	0.494	"	"	0.467
18	3.4	0.615	0.1619	0.071	0.544
	8.4	1.426	"	"	1.355
19	3.2	0.933	0.2693	0.063	0.870
	6.5	1.811	"	"	1.748

is 210°C which is relatively low and it is probable that the linear nature of the gas con-
ductivity will dominate the overall conductivity.

The differential form of equation (5.6) may be written as:-

$$Q = -2\pi r L \lambda_{so} \frac{dT}{dr}$$

which when integrated gives,

$$\ln r = \frac{-2\pi}{Q} L \lambda_{so} T + C \qquad - (5.8)$$

where C is the constant of integration.

So if we have one dimensional radial conduction where λ_{so} may be considered con-
stant for a particular test, a plot of T against ln r will reveal a straight line. This process
was carried out for each test and in every case the results formed an almost perfect
straight line, some examples of which are shown in figure 5.14a-d. Using a curve fitting
program the equation of the line representing the data was found for every test.

From equation (5.8) it can be seen that the overall bed conductivity λ_{so} may now be
found from equating the gradient m of the straight line fit to $\frac{-2\pi L \lambda_{so}}{Q}$.

Rearranging gives,

$$\lambda_{so} = \frac{-mQ}{2\pi L} \qquad - (5.9)$$

The results of the curve fits and their corresponding standard estimate of error are tabu-
lated along with the derived conductivities in Table 5.4 on page 140 overleaf.

FIGURE 5.14a

Plot of Bed Temperature vs. ln radius
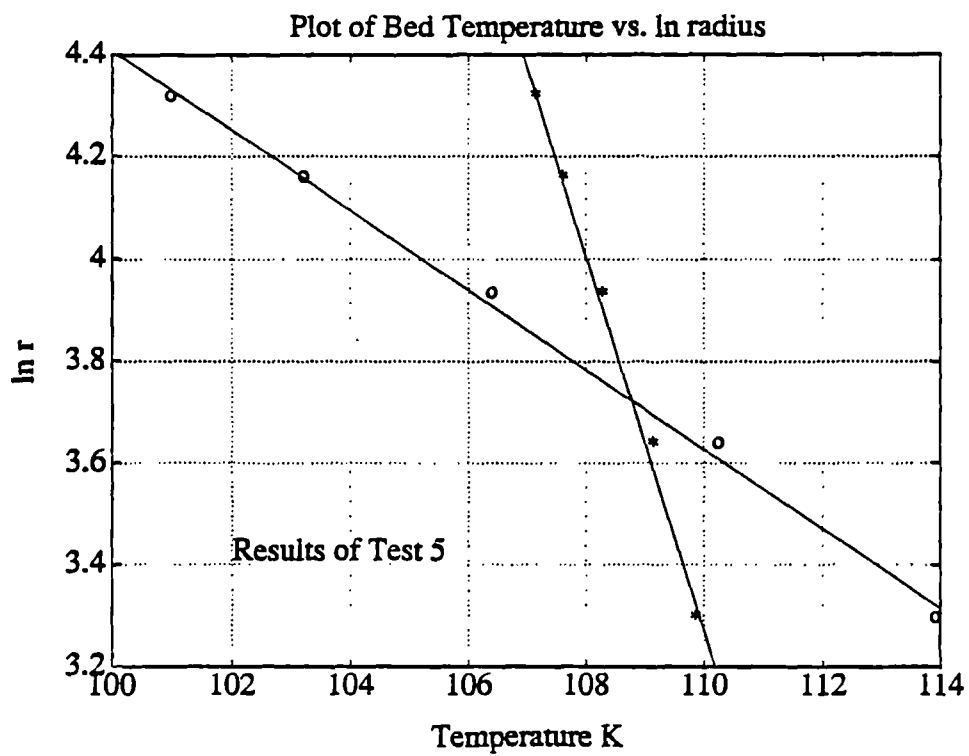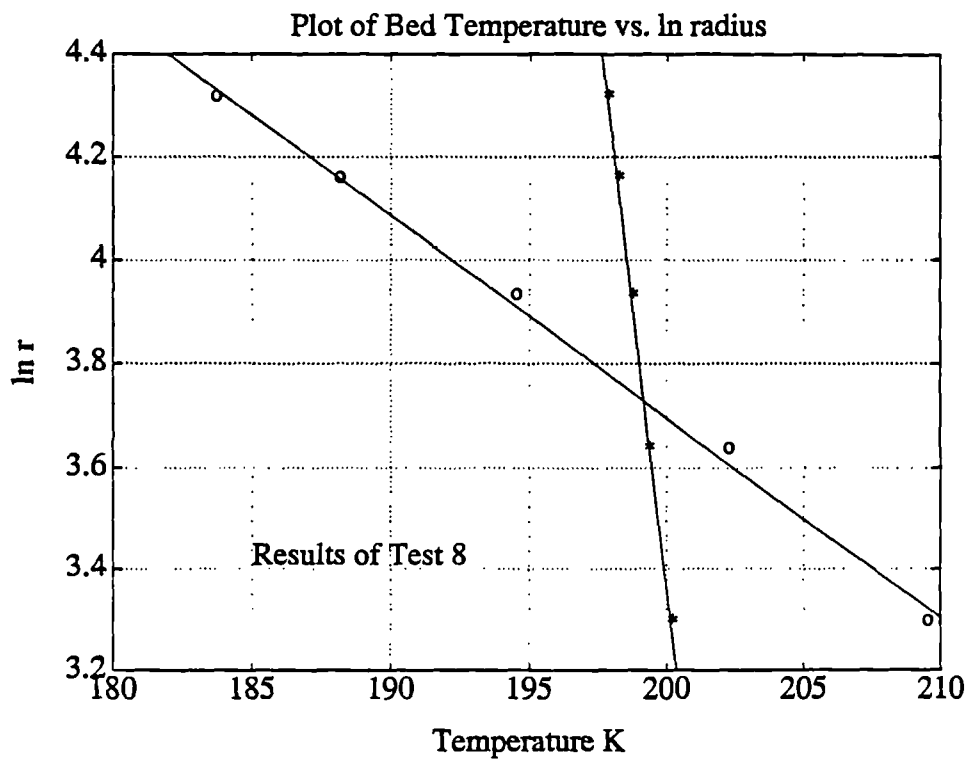
Results of Test 1

FIGURE 5.14b

Plot of Bed Temperature vs. ln radius

Results of Test 5

FIGURE 5.14c

Plot of Bed Temperature vs. ln radius

Results of Test 8

FIGURE 5.14d

Plot of Bed Temperature vs. ln radius

Results of Test 13
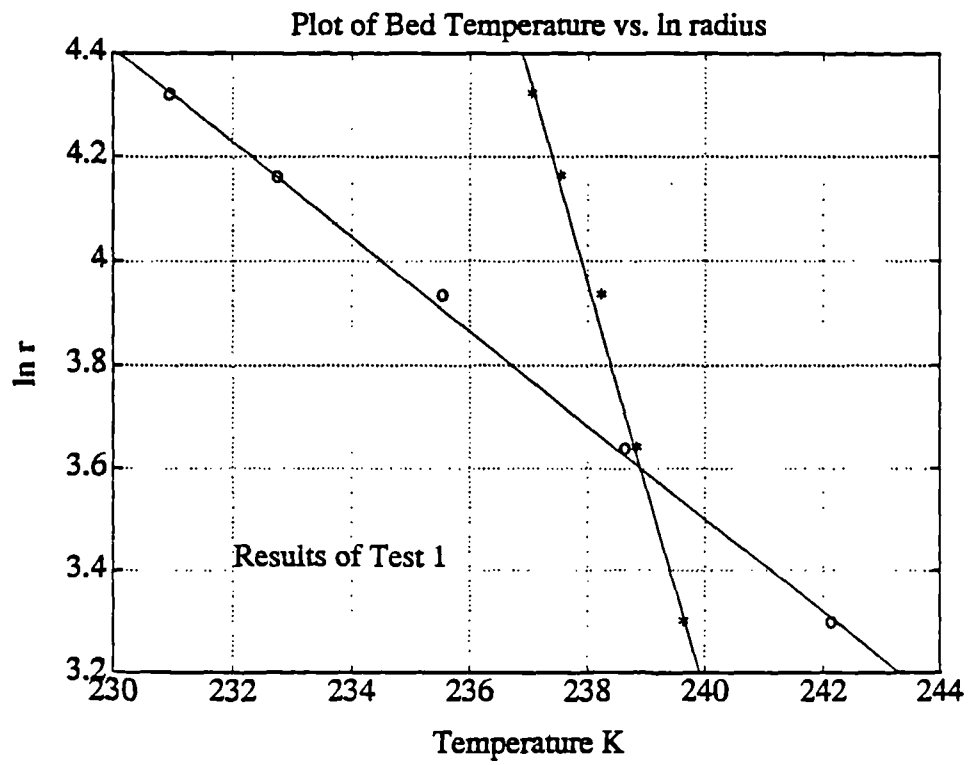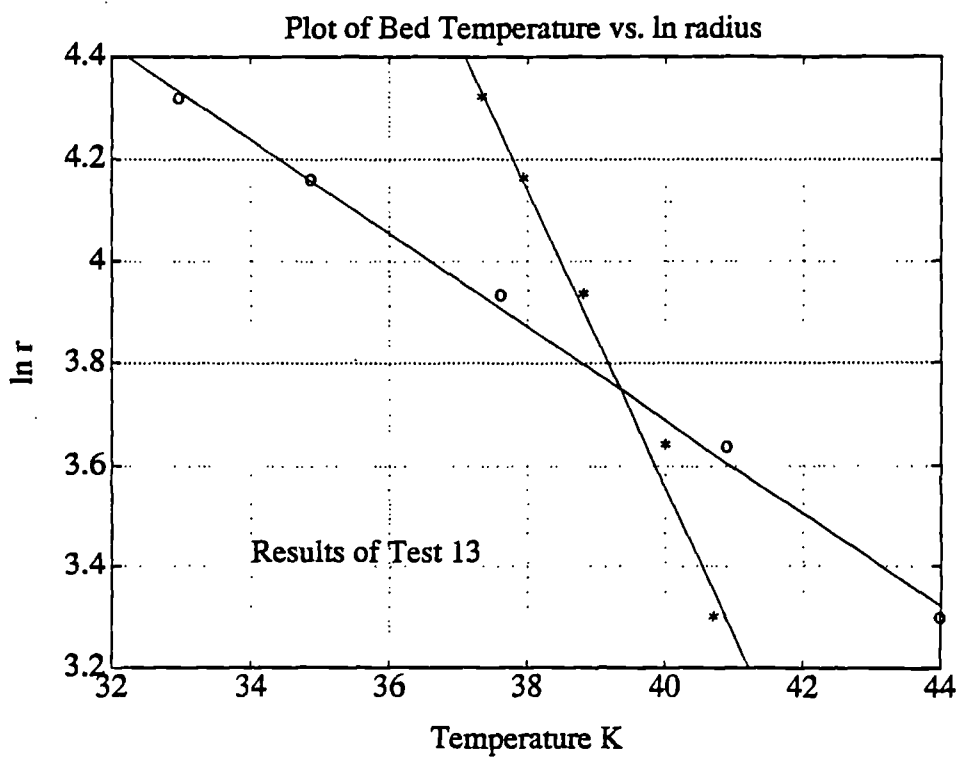
TABLE 5.4

Results of Straight Line Least Square Fits.

Test No.	Test Type	Mean charcoal Temp K	m	C	%SEE	λ_{so} W/m K
1	Helium "	510.4 "	-0.0909 -0.3960	25.3 98.2	0.29 0.13	0.660 0.667
2	Helium "	510.5 "	-0.0925 -0.4001	25.6 99.2	0.31 0.18	0.656 0.672
3	Helium "	436.5 "	-0.0822 -0.4159	17.2 72.0	0.29 0.13	0.512 0.521
4	Helium "	380.8 "	-0.0811 -0.3918	12.5 46.3	0.77 0.24	0.428 0.422
5	Argon "	381.0 "	-0.0782 -0.3673	12.2 43.7	1.14 0.30	0.170 0.168
6	Argon "	426.5 "	-0.0774 -0.3976	15.7 65.1	0.70 0.11	0.190 0.192
7	Argon "	481.5 "	-0.0804 -0.4481	20.5 97.4	0.34 0.06	0.231 0.235
8	Vacuum "	470.8 "	-0.0391 -0.4358	11.5 90.5	1.26 0.06	0.106 0.109
9	Vacuum "	420.8 "	-0.0383 -0.3770	9.5 60.0	2.07 0.07	0.081 0.082
10	Vacuum "	370.3 "	-0.0383 -0.3533	7.5 38.6	3.30 0.43	0.065 0.065
11	Helium "	380.8 "	-0.0812 -0.3855	12.5 45.6	0.77 0.31	0.442 0.436
12	Ammonia "	312.1 "	-0.1071 -0.3058	8.0 15.8	1.94 1.23	0.165 0.160
13	Ammonia "	311.7 "	-0.0917 -0.2905	7.4 15.2	2.83 1.60	0.168 0.162
14	Ammonia "	312.0 "	-0.1061 -0.3003	7.9 15.6	1.52 1.47	0.172 0.170
15	Ammonia "	312.1 "	-0.3044 -0.1053	15.8 7.9	1.08 1.41	0.171 0.174
16	Ammonia "	312.0 "	-0.1062 -0.2998	7.9 15.6	1.05 1.20	0.191 0.186
17	Vacuum "	312.7 "	-0.3035 -0.0758	15.7 6.7	1.41 3.90	0.047 0.047
18	Neon "	312.0 "	-0.2972 -0.1218	15.4 8.5	0.93 1.24	0.214 0.219
19	Helium "	312.0 "	-0.3106 -0.1566	16.0 9.9	0.98 1.03	0.358 0.363

SEE - Standard Estimate of Error

Vessel Wall to Bed Heat Transfer Coefficient

A heat transfer coefficient exists between the vessel and the charcoal bed due to a distortion of the grain packing at the wall. The magnitude of the heat transfer coefficient will depend to a large extent upon the radius of the container wall. The larger the radius, the less the packing distortion and the greater the number of grains touching the vessel wall. This can be seen from the photograph, shown in figure 5.15, of a 1:1 sample of the packed granular bed which has been cast in resin, sectioned and polished. The white and grey areas are intergranular pores and the black areas are charcoal grains.

FIGURE 5.15

Photograph of Grain Packing
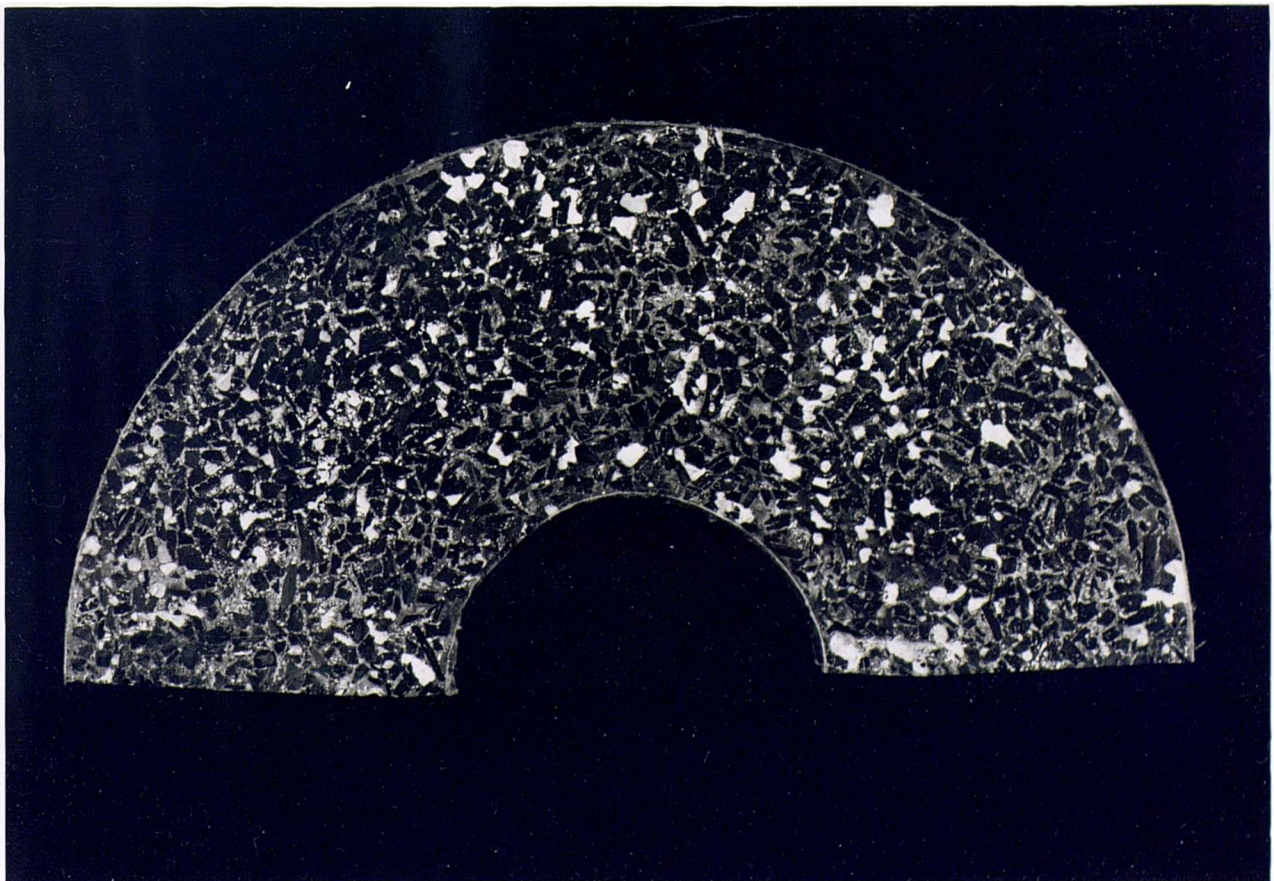
It can clearly be seen that a greater number grains touch the outer wall per unit area than do the inner. The heat transfer coefficient will also depend on the radiation heat transfer coefficient, which varies cubically with respect to temperature, and on the gap between the grain and the wall. Finally the heat transfer coefficient will also depend on the gas conductivity.

In theory the heat transfer coefficient can be found from a plot of log r vs. T,see figure 5.16.

FIGURE 5.16

Method for Finding Bed to Wall Heat Transfer Coefficient.

Plot to Find the Wall to Bed Heat Transfer Coefficient
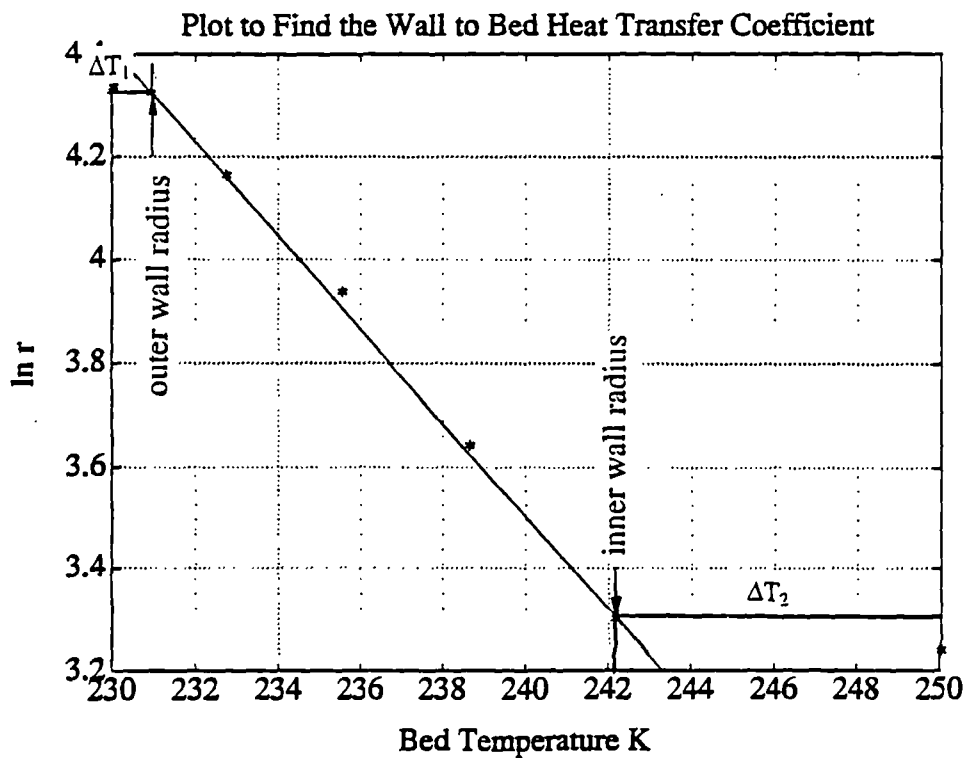
The straight line fit through the set of data points is extrapolated to the inner and outer wall radii. The difference between this wall temperature and heater controlling temperature is shown as ΔT_1 and ΔT_2. The heat transfer coefficient for the inner and outer walls may be found from equations (5.10a) and (5.10b) respectively.

$$h_1 = \frac{Q}{\Delta T_1 A_1} \qquad - (5.10a)$$

$$h_2 = \frac{Q}{\Delta T_2 A_2} \qquad - (5.10b)$$

where A_1 and A_2 are the inner and outer wall areas and h_1 and h_2 are the inner and outer heat transfer coefficients.

Unfortunately, the test results from tests 1-19 include a heat transfer coefficient from the heater to the vessel wall and it is not possible to extract either h_1 or h_2 from them. It is also probable that the thermocouples controlling the heater temperatures are positioned in either hot or cold spots, in which case ΔT_1 and ΔT_2 cannot be measured accurately.

It is possible however to estimate a value for h by assuming an average gap between the wall and charcoal of 1mm to 2mm. Depending on the gas used in the bed it is estimated that h ranges between 10 W/m²K and 150 W/m²K.

The results shown in Table 5.4 will be used in Section 6 to find the values of ϕ, λ_s, B, $\frac{x_R}{(\frac{2}{\varepsilon}-1)}$ which produce a best fit to the ZB model equations.

References

1. Fritsch CA Prettyman PE .
"Measurements of the Thermal Conductivity of Granular Carbon and the Thermal Contact Resistance at the Container Wall". (Bell Telephone Lab Inc, Whippany N.J), Nat Bur Standards US, Special Publication No. 302, 1967, pp 695-702.

2. Gurgel JM Grenier Ph
"Mesure de la Conductivite´ Thermique du Charbon Actif AC-35 en Presence de Gaz" The Chemical Engineering Journal, Vol 44, 1990 pp 34-50.

3. Sahnoune H Grenier Ph
"Mesure de la Conductivite´ Thermique d'une Zeolithe" The Chemical Engineering Journal, Vol 40 1989 pp 45-54.

4. Liu ZY Cacciola G Restuccia G Giordano N

"Fast Simple and Accurate Measurement of Zeolite Thermal Conductivity" Zeolites 1990 Vol 10 pp565-570

5. Holman JP

"Heat Transfer" Sixth Edition McGraw Hill 1986. pp 617

6. Touloukian Liley Saxeria

"Thermal Conductivity of Non-Metallic Liquids and Gases" Thermophysical Properties of Matter. TPRC Series Vol 3 IFIF Plenum New York 1970.

7. Young Warren C

"Roark's Formulas for Stress and Strain" McGraw Hill pp 398-408

8. BS3605

"Seamless and Welded Austenitic Stainless Steel Pipes and Tubes for Pressure Purposes." 1973 pp 54

6. MODELLING OF THERMAL CONDUCTIVITY OF ADSORBENT BEDS.

Introduction

The object of this section is to present a modified version of the ZB model which predicts the overall bed conductivity of an ammonia-activated charcoal adsorber over its complete working range of pressure, temperature and concentration.

Sections 6.1 and 6.2 derive a simplified version of the ZB equations defined in Section 4.3 and fits the results of the thermal conductivity tests to them. The four unknowns in the ZB model are found by minimizing the sum of the squares of the error between the real and predicted data points. The accuracy of the ZB model is determined by predicting the conductivity of a neon and 208C bed and comparing the results to the real data.

The ZB model equations are then modified to include the variable grain conductivity when the adsorbed phase is present. A model of the variable grain conductivity based on the theory of the volume filling of micropores is proposed and found to be accurate to +3.1% -2.5%.

Finally, in Section 6.3, methods of improving the thermal conductivity of an ammonia-activated charcoal adsorber are discussed and an idea for a prototype reactor is presented.

6.1 The Simplified ZB Model Equations.

The results of helium tests 1 and 2 summarized in the table below are highly significant when using the ZB model to represent high pressure adsorbent systems.

Test No.	Mean Bed Temp	Pressure	Overall Bed Conductivity
	K	Bar	W/m K
1	513	30	0.664
2	513	3.7	0.664

Test 1 was carried out under conditions which minimized the mean free path of the gas molecule and test 2 under conditions which maximized it. It can be seen that there is no measured difference in the overall bed conductivity λ_{so}, which implies that the Knudsen effect is negligible at the likely operating pressures and temperatures of an ammonia activated charcoal heat pump or refrigerator. This is not the case with low pressure systems such as methanol- activated charcoal [1] or zeolite water [2]. It is important to note that it may also not be the case with a high pressure system where the interparticle pore size approaches the mean free path length as may be case with a very fine charcoal grain. With the coarse grain of 208C however, the results imply that $\frac{\lambda}{\lambda_D} \to 1$. Applying this simplification to equations (4.10), (4.11) and (4.12) in section 4.3 leads to equations (6.1), (6.2) and (6.3) respectively.

$$\frac{\lambda_{so}}{\lambda} = 1 - \sqrt{1-\psi}\,[\,1 + \psi\,\frac{\lambda_R}{\lambda}\,] + \sqrt{1-\psi}\,(\phi\frac{\lambda_s}{\lambda}) + \sqrt{1-\psi}\,(1-\phi)\frac{\lambda_{so}*}{\lambda} \qquad - (6.1)$$

$$\frac{\lambda_{so}*}{\lambda} = \frac{2}{p}\left(\frac{B\,(\frac{\lambda_s}{\lambda} + \frac{\lambda_R}{\lambda} - 1)\frac{\lambda}{\lambda_s}}{p^2} \times \ln(\frac{\frac{\lambda_s}{\lambda} + \frac{\lambda_R}{\lambda}}{B}) - \frac{B-1}{p} + \frac{B+1}{2B}\frac{\lambda_R}{\lambda}\right) - B \qquad - (6.2)$$

$$p = 1 + (\frac{\lambda_R}{\lambda} - B)\frac{\lambda}{\lambda_s} \qquad - (6.3)$$

The data from all of the tests using Ne, Ar or He can be fitted to equations (6.1), (6.2) and (6.3). In the case of the vacuum tests the ZB model equations can be simplified even further since the gas conductivity $\lambda \to 0$. Applying this to equations (6.1),(6.2) and (6.3) leads to equations (6.4), (6.5) and (6.6).

$$\lambda_{so} = 1 - \sqrt{1-\psi} \ (\psi \ \lambda_R) + \sqrt{1-\psi} \ (\phi \lambda_s + (1-\phi)\lambda_{so*}) \qquad - (6.4)$$

$$\lambda_{so*} = \frac{B+1}{2B}(\frac{\lambda_R}{p}) \quad - (6.5)$$

$$p = 1 + \frac{\lambda_R}{\lambda_s} \qquad - (6.6)$$

Combining (6.5) and (6.6) gives:-

$$\lambda_{so*} = \frac{B+1}{2B}\frac{\lambda_s \lambda_R}{\lambda_s + \lambda_R} \qquad - (6.7)$$

Data from the vacuum tests only is fitted to equations (6.4) and (6.7).

The tests involving ammonia will be dealt with at a later stage since they require special treatment because the grain conductivity λ_s is not constant.

6.2 Fitting the Test Data to the ZB Model Equations.

The data obtained from tests 1-11 and 17-19 are fitted to their specific set of equations, (6.1)-(6.3) or (6.4) & (6.7), in order to find the best fit values of the following four unknowns.

B   defines cell geometry

ϕ relative grain-grain contact area

$\dfrac{x_R}{\frac{2}{\varepsilon}-1}$ effective radiation length and emissivity

λ_s grain conductivity

This is achieved by the use of specially written software run on MATLAB. This program minimizes the sum of the squares of the error between the measured and generated values of overall bed conductivity, see equation (6.8), for each of the above parameters simultaneously.

$$Minimize\ \left(\sum_{n=0}^{n=i}(\lambda_{so}\ measured\ -\lambda_{so}\ generated\ )^2\right)^{1/2} \qquad — (6.8)$$

It can be seen from equations (6.1)-(6.3) that in the case of non-adsorbable gases we need to supply the relevant gas conductivity λ. This data was obtained from Touloukian [3], and plots of gas conductivity vs. temperature revealed adequate straight line fits, see appendix 6a. The equations found to represent the conductivities are shown below.

Helium

$$\lambda_{He} = 3.091{\times}10^{-4}\ T + 0.05652 \qquad — (6.9)$$

Argon

$$\lambda_{Ar} = 4.383{\times}10^{-5}\ T + 0.00443 \qquad — (6.10)$$

Neon

$$\lambda_{Ne} = 9.542{\times}10^{-5}\ T + 0.02002 \qquad — (6.11)$$

Figures 6.1, 6.2 and 6.3 overleaf show plots of the helium, argon and vacuum tests respectively.

FIGURE 6.1

Helium Results Tests 1,2,3,4,19

$$\lambda_{so} = 4.058 \times 10^{-6} T^2 - 1.798 \times 10^{-3} T + 0.5255$$

FIGURE 6.2

Argon Results Tests 5,6,7

$$\lambda_{so} = 2.849 \times 10^{-6} T^2 - 1.813 \times 10^{-3} T + 0.446$$
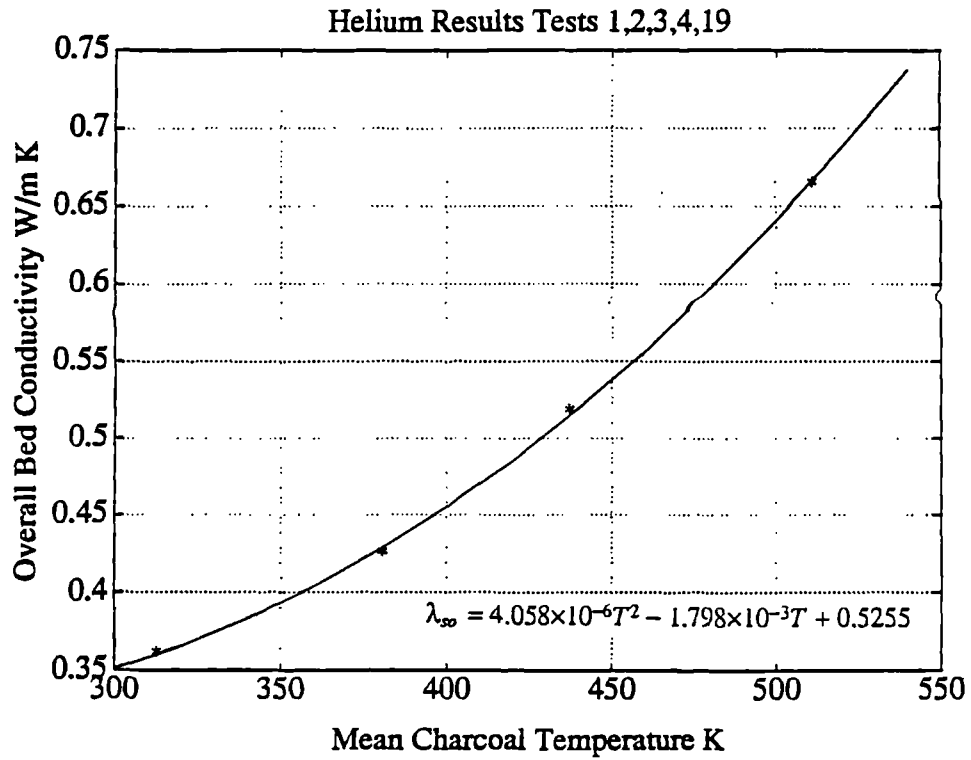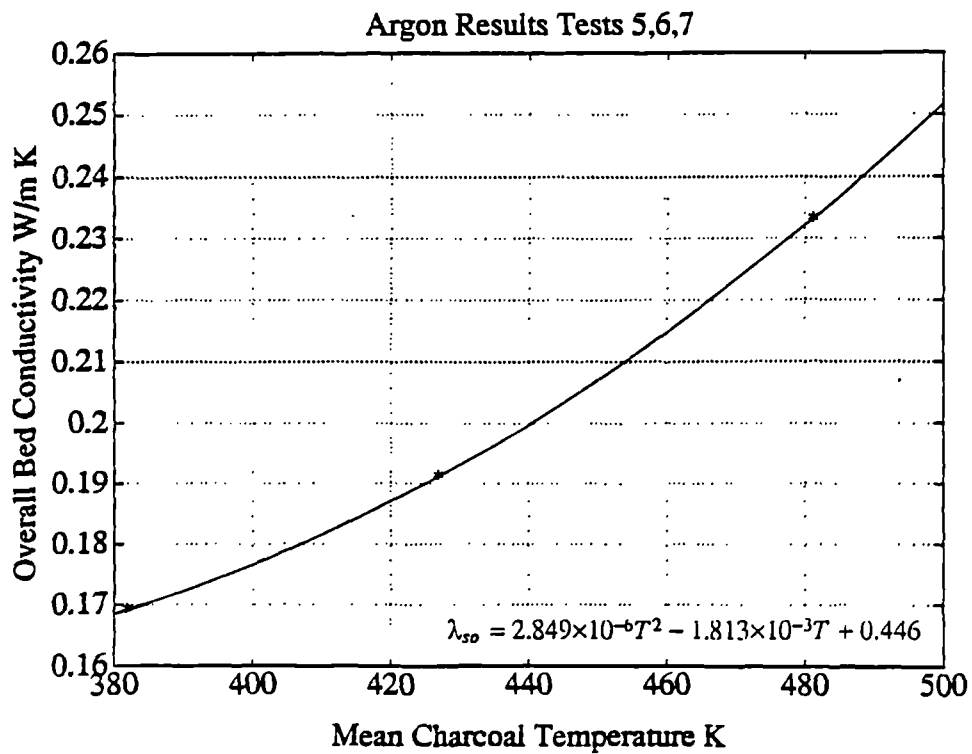
FIGURE 6.3
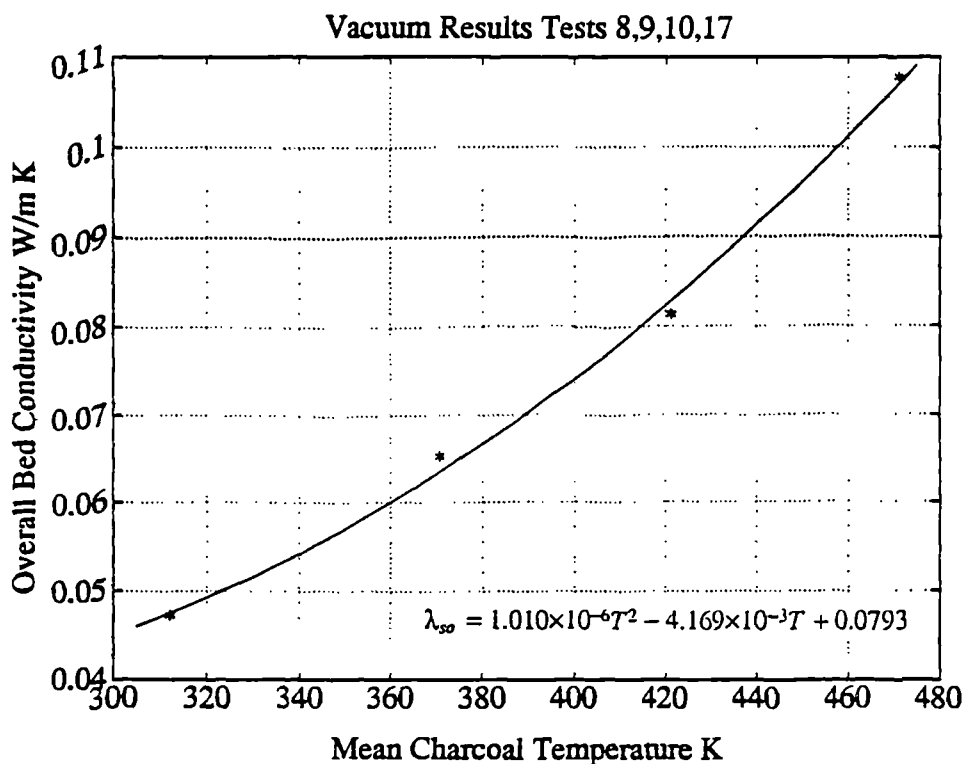
The equations of a quadratic curve fit through the data points are given for each case. It is realized that a quadratic will obviously fit the argon results perfectly since there are only three points. Its use is justified by the fact that quadratics fit the helium and vacuum results and the argon results are going to be of a similar nature. Data points lying between $313 \text{ K} \leq T \leq 473 \text{ K}$ only are used to find the best fit for the four unknowns in the ZB equation. To make sure that the input file contains the same number of data points for each case, any additional points required are generated from the quadratics within the test data temperature range.

The input file is shown overleaf, the asterisk indicates real experimental data.

When the minimization routine has converged to a preset tolerance a screen listing is provided of the real and generated value and the % error between them.

Three different minimization equations are used as listed below Table 6.1.

TABLE 6.1

INPUT FILE

HELIUM		ARGON		VACUUM	
λ_{so}	T	λ_{so}	T	λ_{so}	T
W/m K	K	W/m K	K	W/m K	K
0.583	473	0.169	381.5 *	0.0474	311.7 *
0.517	436.5 *	0.174	393	0.0525	333
0.475	413	0.178	403	0.0580	353
0.460	403	0.183	413	0.0650	370.3 *
0.425	380.1 *	0.191	426.5 *	0.0715	393
0.419	373	0.202	443	0.0794	413
0.396	353	0.209	453	0.0815	420.8 *
0.386	343	0.217	463	0.0882	433
0.377	333	0.226	473	0.0977	453
0.361	312 *	0.233	480.9 *	0.1075	470.8 *

$$\left(\sum_{n=0}^{n=i} (\lambda_{so} \, measured - \lambda_{so} \, generated \;)^2 \right)^{1/2} \qquad - (6.8)$$

$$\sum_{n=0}^{n=i} (\lambda_{so} \, measured \, - \lambda_{so} \, generated \;)^2 \qquad - (6.12)$$

$$\sum_{n=0}^{n=i} (\lambda_{so} \, measured \, - \lambda_{so} \, generated \;)^4 \qquad - (6.13)$$

Equations (6.8),(6.12) and (6.13) progressively weight the ZB model fit to the higher error values. The results of the three fits list the four ZB unknowns, the percentage between the data and the model, the sum of the percentage errors and the mean percentage error. Figures (6.4), (6.5) and (6.6) show graphs of the data real and generated data points for the three fits respectively.

Fit to Equation (6.8)

<div align="center">

ZB Model Unknowns

$\phi = 0.03411$

$B = 1.4796$

$$\frac{x_R}{\frac{2}{\epsilon} - 1} = 0.00292$$

$\lambda_s = 0.8187$

</div>

Table of % Error Between ZB Model and Experimental Data

Helium	Argon	Vacuum
%	%	%
-17.9	0	-1.9
-12.0	0.3	-0.3
-6.5	0.6	0.5
-4.6	0.4	-1.9
0	-0.5	0.9
0.6	-1.7	0.8
3.6	-2.5	2.0
5.2	-3.6	0.4
6.3	-4.7	0
7.6	-6.0	-1.0

<div align="center">

Total Error = 94.5%

Mean error = ±3.2%

FIGURE 6.4

</div>

Comparison of Experimental Data and ZB Model fit

Fit to Equation (6.12)

ZB Model Unknowns

$$\phi = 0.02959$$

$$B = 1.3764$$

$$\frac{x_R}{\frac{2}{\epsilon} - 1} = 0.00293$$

$$\lambda_s = 0.8738$$

Table of % Error Between ZB Model and Experimental Data

Helium	Argon	Vacuum
%	%	%
-15.9	-0.2	-2.9
-10.0	0.2	-0.9
-4.6	0.6	0.4
-2.7	0.6	-1.6
1.9	-0.2	1.7
2.5	-1.2	1.8
5.4	-1.9	3.2
7.0	-3.0	1.8
8.1	-3.9	1.6
9.3	-5.1	0.9

Total Error = 101.1%

Mean error = ±3.4%

FIGURE 6.5

Comparison of Experimental Data and ZB Model Fit.

(.)-Data generated from quadratics
(*)-Data from ZB model
(o)-Experimental data

Fit to Eqn.(6.12)
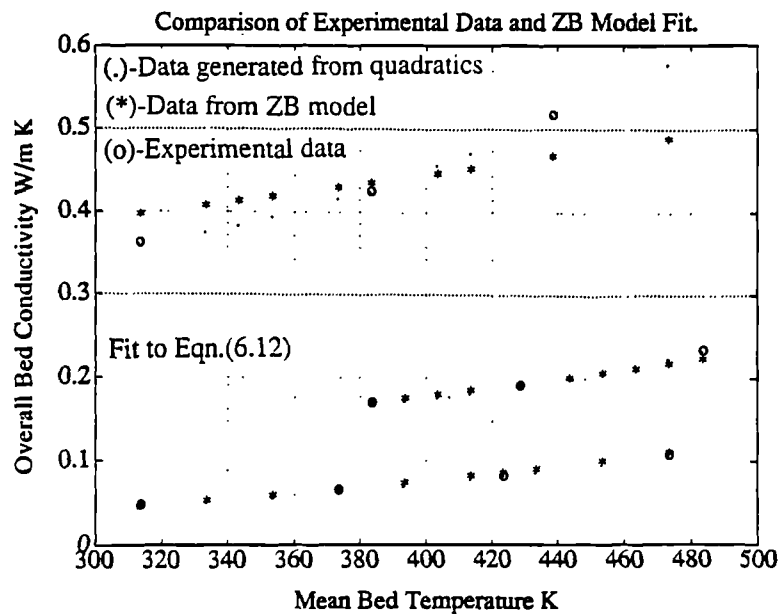
Fit to Equation (6.13)

ZB Model Unknowns

$$\phi = 0.01936$$

$$B = 0.9561$$

$$\frac{x_R}{\frac{2}{\varepsilon} - 1} = 0.00269$$

$$\lambda_s = 1.0685$$
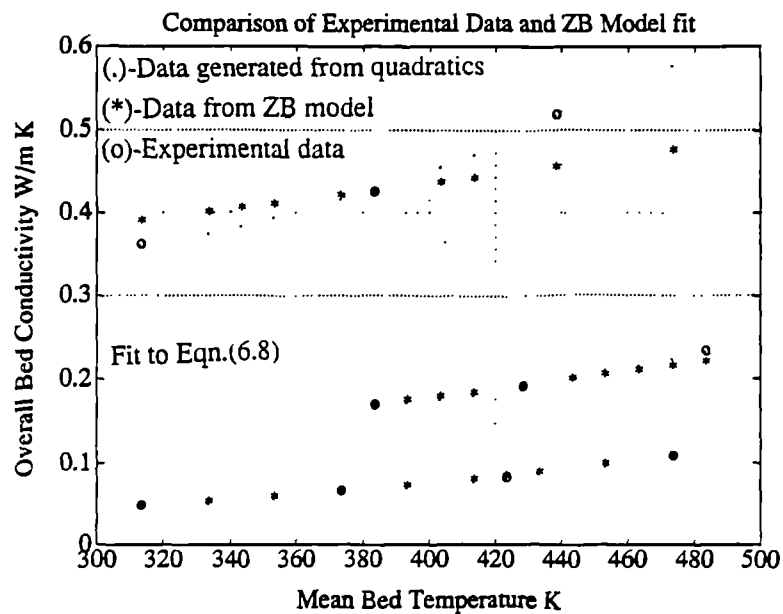
Table of % Error Between ZB Model and Experimental Data

Helium	Argon	Vacuum
%	%	%
-12.5	-5.8	-5.9
-7.2	-4.9	-2.7
-2.2	-4.1	-0.3
-0.5	-4.1	-1.2
3.8	-3.8	3.1
4.1	-4.1	4.1
6.6	-4.4	6.0
7.9	-5.0	4.9
8.8	-5.5	5.5
9.5	-6.3	5.4

Total Error = 149.7%

Mean error = ±5.0%

FIGURE 6.6

Comparison of Experimental Data and ZB Model Fit
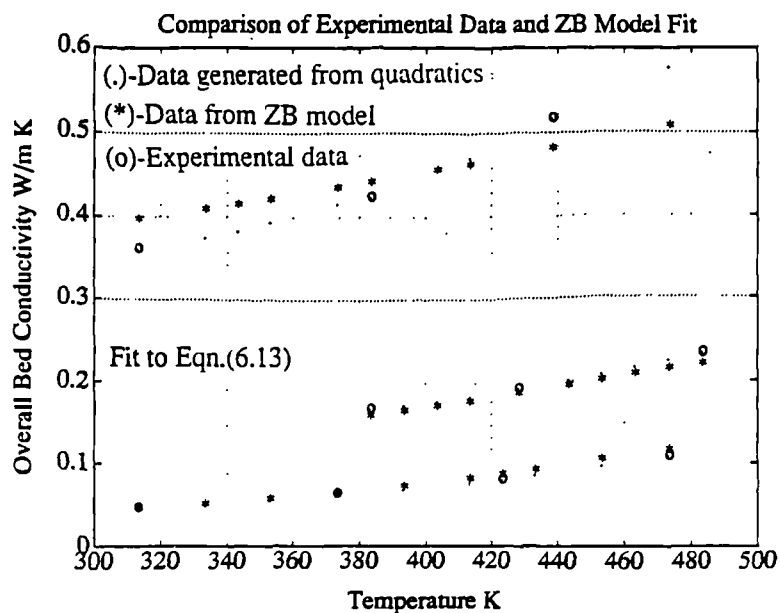
From the results it can be seen that although the fit using equation (6.8) gives the lowest mean percentage error, the results generally are biased to fitting well at lower values of λ_{so}. This means that the vacuum results fit very well but that the helium results do not. Conversely, using equation (6.13) gives a greatly improved fit for the helium results but a poor fit for the vacuum and argon results. The fit using equation (6.12) however, biases the error minimization more to the argon results. In addition to this the gas conductivities of argon and ammonia are similar, and so the set of ZB unknowns produced by this equation will henceforth be used for any modelling.

The results from test using neon (test 18), have deliberately not been used in the ZB model fitting . These results have been reserved to be used as a check on the validity of the model.

The overall bed conductivity of 208C charcoal with neon gas at 313 K was measured to be 0.217 W/m K.

Using equations (6.1)-(6.3) the ZB model predicts the that overall bed conductivity under the same conditions is 0.229 W/m K.

The error in the prediction is 5.6 % which is considered to be acceptable.

Finally it is important to realize the significance of the ZB model unknowns and also to assess whether or not the minimization program has produced sensible values.

Firstly we will look at the two parameters defining the particle geometry, ϕ and B. The relative solid-solid contact area ϕ is low, 0.02959. This is expected since on examining figure 5.15 in Section 5.3, it can be seen that there is very little grain point to point contact. The deformation factor B is 1.3764 which means that the apparent shape of the particle is nearly that of a sphere. This again is reasonable with the knowledge that ψ, the intergranular void ratio is 0.478.

The three parameters ϕ, B, and ψ completely define the particle shape as shown overleaf in figure 6.7. The dimensions are given in areas but the drawing scales the radii.

FIGURE 6.7

Apparent Shape of ZB Unit Cell When B=1.3764, ϕ = 0.02959 and ψ = 0.478.
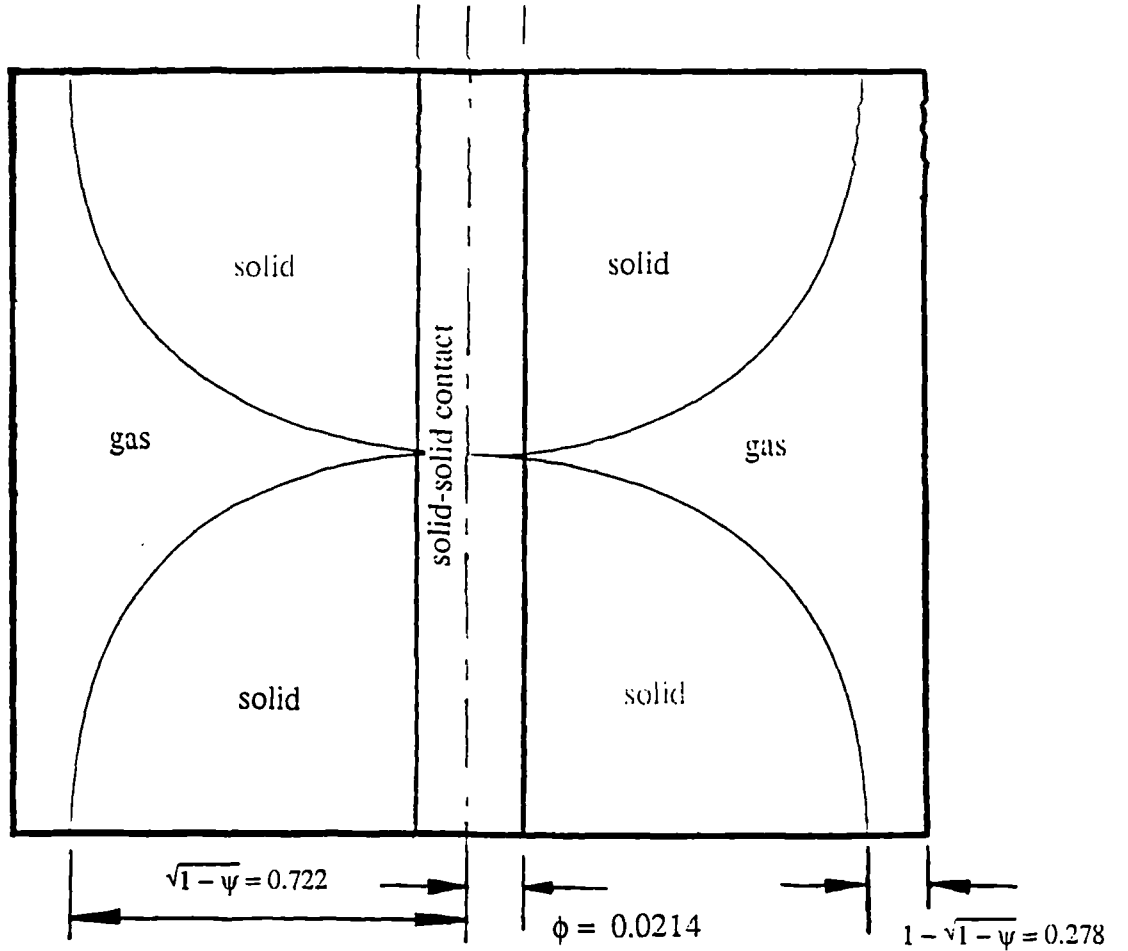
* values given are relative areas

The radiation term $\dfrac{x_R}{\frac{2}{\varepsilon}-1}$ = 0.00293. It is estimated that the emissivity of a black glassy surface is about 0.8 Ref [4]. If this is the case then x_R = 4.395 mm. This term characterizes the effective radiation path length of the particle packing. Again, by looking at figure 5.15 in section 5.3, it can be seen that the size of the gaps between the grains ranges from 0 - 8 mm. Therefore the value found for $\dfrac{x_R}{\frac{2}{\varepsilon}-1}$ by minimization is very rea-

sonable.

Lastly we will deal with the value found for the grain conductivity, λ_s. This is the most important value of those found since it is a real value, (the other three define an apparent geometry). The value of λ_s in this case is 0.8738 W/m K, and this compares very well with other quoted values. Hayashi et al [5], using the model defined in section 4.1 derived a value of 0.651 W/m K for the grain conductivity of an unnamed activated carbon. Gurgel et al [1] derived a value of 0.54 W/m K using the ZB model for the grain conductivity of AC35 which is a coal based extruded activated charcoal.

It is expected that different charcoals will have different conductivities. The grain may be considered to consist of layers of graphite with holes or pores burnt into them. The better the uninterrupted graphite path, the higher the conductivity, or possibly it could be stated that the less porous the material the higher the conductivity.

The grain conductivity will be examined more stringently in section 6.3 since it will not stay constant when the adsorbed phase is present.

6.3 Modified ZB Model to Include the Adsorbed Phase.

Fitting the ZB Model to the Ammonia Results.

When heat transfer takes place in the charcoal bed filled with the adsorbate ammonia, the grain conductivity λ_s will vary depending on the concentration of ammonia held within the micropores of the grain. Henceforth the solid conductivity will use the notation λ_{s*} to represent a variable grain conductivity. The results of the ammonia tests 12-16 are shown in the table overleaf.

Test no.	Mean Bed Temperature	Pressure	Bed Conductivity
	K	Bar	W/m K
12	313	1.56	0.163
13	313	4.24	0.165
14	313	5.79	0.171
15	313	7.00	0.173
16	313	11.30	0.189

The ZB model may be used in its standard form to find the overall bed conductivity as if ammonia gas were a non-adsorbed gas, that is, the micropores are empty. The value found for λ_{so} in this case is 0.164 W/m K.

In order to find the value for λ_{s^*} each test result is run through the error minimization program one at a time, keeping ϕ, ψ, B and $\frac{x_R}{\frac{2}{\varepsilon}-1}$ the same as before. *Because we are* minimizing one result only, we obtain a perfect fit to the results each time. Therefore the result we have just predicted for empty micropores must be processed in the same way so that in each case the generated values of λ_{so} have the same error fit to the real values of λ_{so}.

The only condition which varies throughout tests 12-16 is the pressure. This will vary the mass concentration of ammonia contained within the charcoal micropores. It seems sensible then that in order to modify the ZB model to include the adsorbed phase that the relationship between λ_{s^*} and the concentration x needs to be found.

The concentration may be found from equations (6.14) and (6.15) below.

$$\ln x = \ln x_0 - (0.001 \times K) \times (2755 \, (\frac{T - T_{sat}}{T_{sat}}))^n \qquad — (6.14)$$

$$\ln p = \frac{-2830.4}{T_{sat}} + 11.786 \qquad — (6.15)$$

Equation (6.14) is known as the Dubinin-Ashtikov (DA) equation, and the three constants x_0, K and n define the volume pore filling with respect to pressure and temperature and they are different for each charcoal. Detail of how these constants are obtained is given in Section 3. In the case of activated charcoal 208C equation (6.14) becomes,

$$\ln x = \ln 0.2582 - (0.001 \times 0.1291) \times (2755 \, (\frac{T - T_{sat}}{T_{sat}}))^{1.305}$$

Equation (6.15) is the isostere of pure saturated liquid ammonia, the data source being Ref [6].

The values of ammonia concentration, λ_{so} and λ_{s*} are listed for each test in Table 6.2.

TABLE 6.2

Ammonia Results listing λ_{s*} and x.

Test No.	Mean Bed Temp	Pressure	λ_{so}	% conc	λ_{s*}
	K	Bar	W/m K	kg/kg	W/m K
12	313	1.56	0.163	13.3	0.850
13	313	4.24	0.165	18.8	0.875
14	313	5.79	0.171	20.7	0.963
15	313	7.00	0.173	21.8	0.994
16	313	11.3	0.189	24.5	1.250
predicted	313 .	XXX	0.164	0	0.8625

Figures 6.8 and 6.9 overleaf show graphs of the overall bed conductivity and grain conductivity plotted against ammonia concentration respectively.
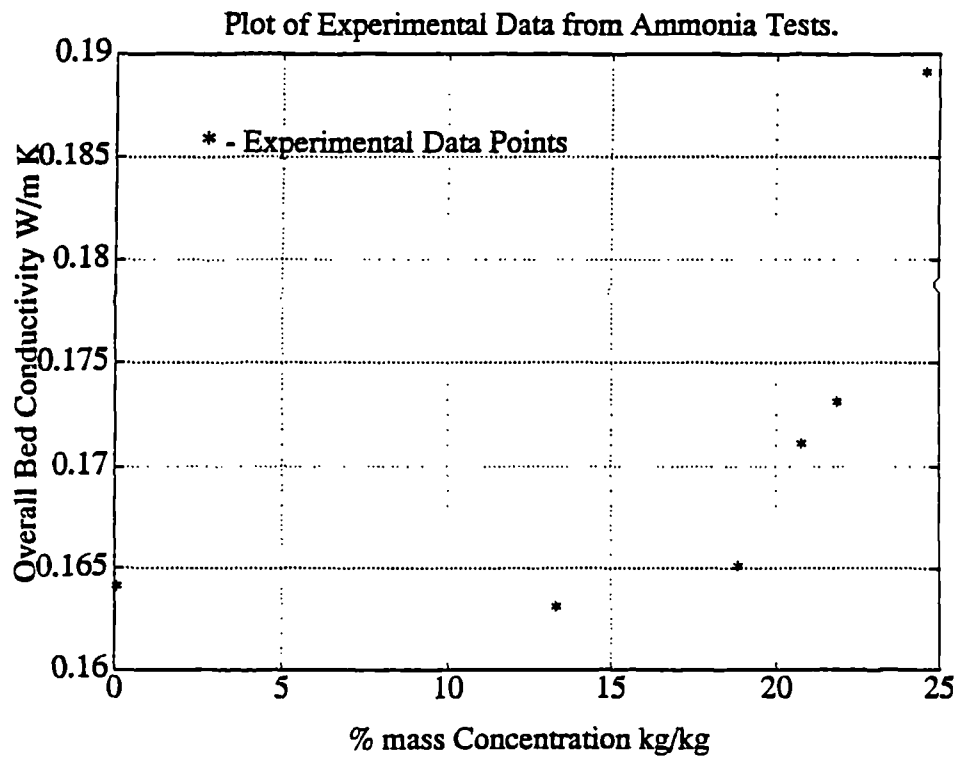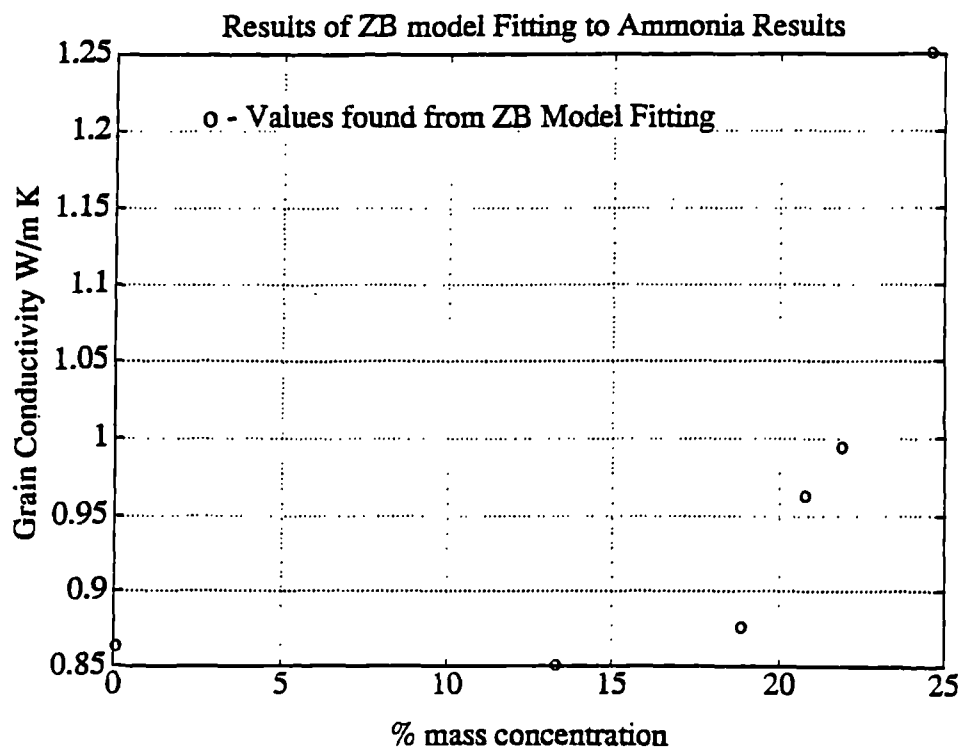
FIGURE 6.8

Plot of Experimental Data from Ammonia Tests.

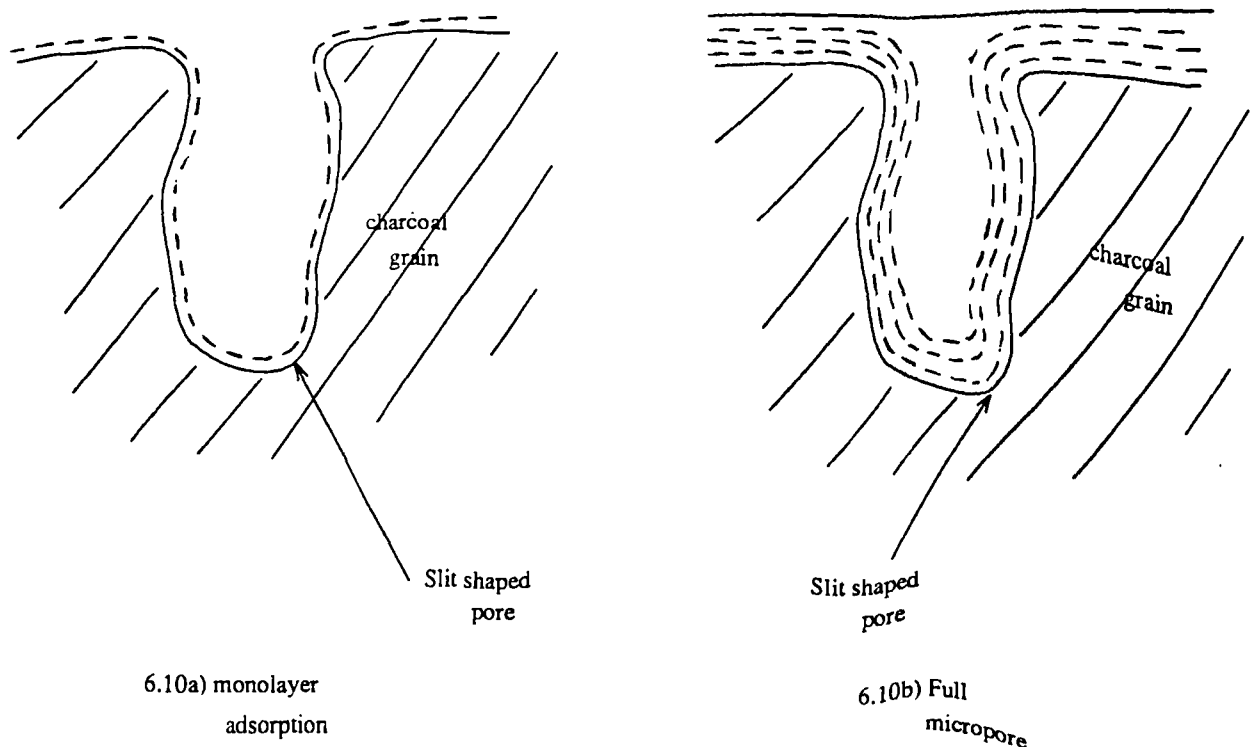FIGURE 6.9

Results of ZB model Fitting to Ammonia Results

Modelling of the Grain Conductivity.

To construct a model representative of the grain, it is important to understand the physical process of adsorption. This topic has already been detailed in Section 3 and may be summarized as follows.

Figure 6.10 below represents a slit shaped micropore present within the charcoal grain. As ammonia is adsorbed it firstly forms a single layer of molecules over the inner surface of the pore, this is known as monolayer adsorption, see figure 6.10a. On increasing the pressure, further layers of adsorbed ammonia build up until until eventually they combine to form a meniscus in the narrowest cross-section of the pore, see fig 10b.

FIGURE 6.10

Physical Process of Micropore Filling

charcoal grain

Slit shaped pore

6.10a) monolayer adsorption

charcoal grain

Slit shaped pore

6.10b) Full micropore

When considering a whole grain, heat may be transferred by two mechanisms only, see figure 6.11. Mechanism 1 is that of solid conduction along an uninterrupted graphite path. Mechanism 2 is that of conduction through the grain and empty, partially or completely filled micropore.

FIGURE 6.11

Mechanisms of Heat transfer Through Grain
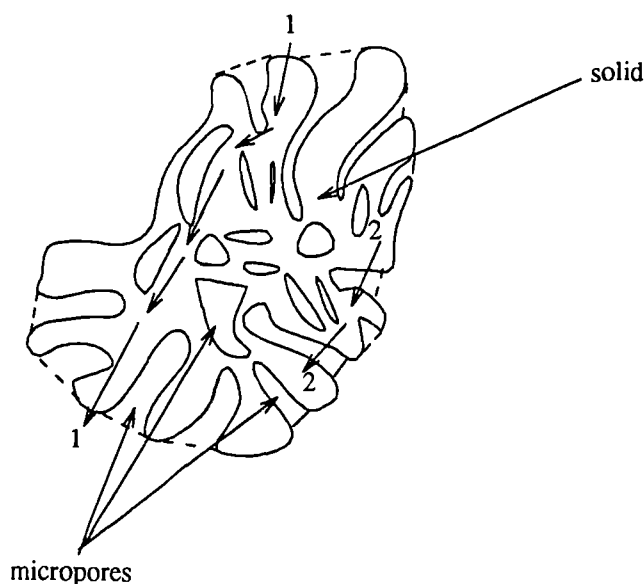
micropores

When the micropore is empty, it can be assumed that its conductivity is negligible in comparison to that of the grain material. This is because the micropores are so small, $2nm \le$ pore width ≤ 50 nm, that radiation heat transfer in W/m K will be of the same order of ten as the pore size in m and gas conduction will be totally dominated by Knudsen effect. This statement is important since it means that heat is transferred by mechanism 1 only when the micropores are empty.

When the micropores are full, heat is transferred by both mechanisms 1 and 2. This would be represented by a solid conduction path in parallel with a solid-adsorbed phase in series. With this in mind, it is proposed that the unit cell shown in figure 6.12a and its

corresponding resistance network shown in figure 6.12b be used in modelling the grain.

FIGURE 6.12

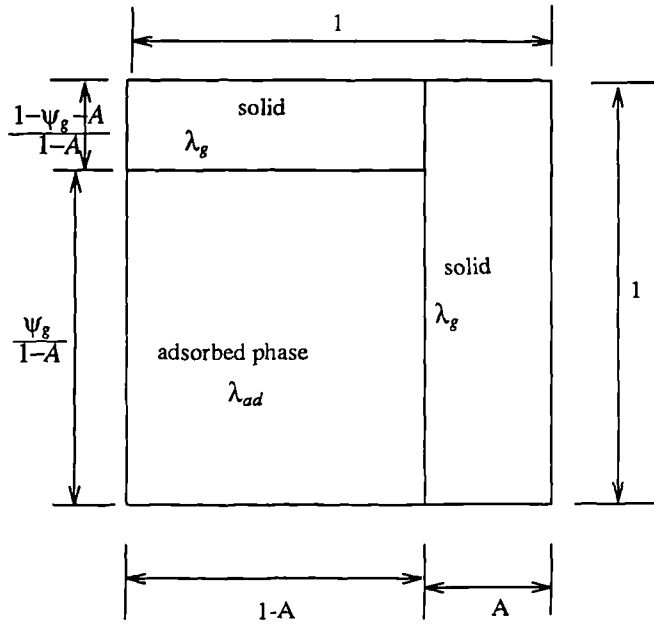fig 6.12a) Unit Cell Representing
Grain
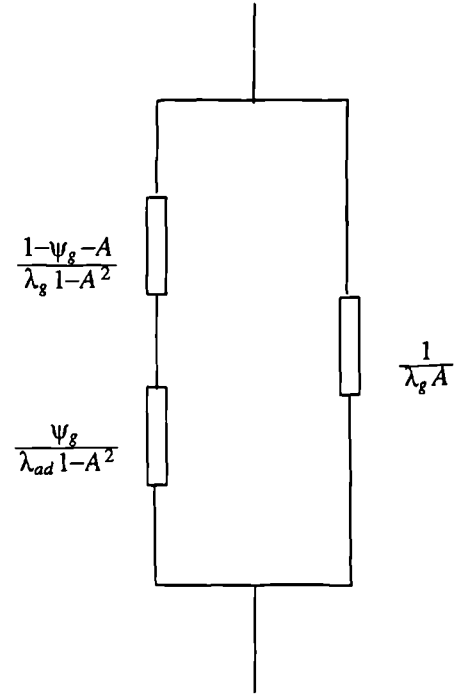
fig 6.12b) Unit Cell Resistance
Network

where:-

$$\psi_g = \frac{\text{micropore volume}}{\text{grain volume}} \quad \text{--- (6.15)}$$

$$1-\psi_g = \frac{\text{solid volume}}{\text{grain volume}} \quad \text{--- (6.16)}$$

A = relative area of solid conduction path

λ_{ad} = adsorbed phase thermal conductivity

λ_g = grain solid thermal conductivity

The relative void volume of the packed bed, including micro, meso and macropores as well as the interparticle void was found from the experiment described in section 5.2 to be 0.77. The interparticle void was found to be 0.478.

This means that the solid volume = 0.23 and the pore volume within the grain only = 0.77-0.478 = 0.292.

This gives a total grain volume of 0.292 + 0.23 = 0.522.

Not all of this void volume however will contain adsorbate,ie the macropores and mesopores. We need to calculate the filled micropore volume for use in the unit cell model.

At 313 K, the density of the adsorbed phase may be assumed to be the same as that of the pure saturated liquid [6]. For ammonia this was given as 582.2 $\frac{kg}{m^3}$, Ref[5]. The bulk density of 208C as given on the manufacturers data sheet is 490 $\frac{kg}{m^3}$. Alternatively 1 m³ of packed bed holds 490 kg of charcoal.

1 kg of packed bed contains a maximum concentration of ammonia of 0.2582 kg and this occupies a volume of 4.435×10^{-4}m³. Therefore 1 m³ of packed bed holds a maximum of 0.217 m³ of adsorbed ammonia.

Total Grain Volume = solid volume + adsorbed phase volume = 0.23 + 0.217 = 0.447 so,

$$\psi_g = \frac{0.217}{0.447} = 0.485 \qquad - (6.19)$$

$$1 - \psi_g = \frac{0.23}{0.447} = 0.515 \qquad - (6.20)$$

The overall grain conductivity λ_{s^*} is found from the overall resistance of the network in fig 6.12b, and is defined by equation (6.21) below.

$$\lambda_{s^*} = \lambda_g A + \frac{\lambda_g \lambda_{ad}(1-A)^2}{(1 - \psi_g - A)\lambda_{ad} + \psi_g \lambda_g} \qquad - (6.21)$$

When the micropores are empty, heat transfer takes place through the solid volume only and equation (6.21) reduces to,

$$\lambda_{s^*} = \lambda_g\, A \qquad — (6.22)$$

Substituting the predicted result from Table 6.2 into equation (6.22) gives,

$$\lambda_g = 0.8625 \qquad — (6.23)$$

Substituting the results of test 16 and into equation (2.21) gives,

$$1.25 = \lambda_g A + \frac{\lambda_g \lambda_{ad}(1-A)^2}{(1-\psi_g-A)\lambda_{ad} + \psi_g \lambda_g} \qquad — (6.24)$$

Substituting equations (6.23), (6.19) and $\lambda_{ad} = 0.449$ W/m K (Ref [3]), into equation (6.24) gives,

$$1.25 = 0.8625 + \frac{\frac{0.8625}{A} \times 0.449\,(1-A)^2}{(0.515-A) \times 0.449 + 0.485 \times \frac{0.8625}{A}}$$

This can be rearranged into a quadratic in A.

$$1.449\,A^2 - 2.231A + 0.582 = 0 \qquad — (6.25)$$

Solving for A gives,

$$A = 1.209 \text{ or } 0.333$$

Since A must be less than 1 then A = 0.333 is the solution we require.

From equation (6.23),

$$\lambda_g = 2.59\text{W/mK}$$

It is nearly impossible to say whether or not the value found for λ_g is correct. The solid grain material consists of highly disordered graphite layers,and the extent of the disorder will determine the conductivity. To confirm λ_g a series of tests would have to be carried out using 208C with 3 or 4 different adsorbates to obtain a range of values for λ_{s^*}.

Using a similar procedure, Gurgel et al [1], quote a value of 1.06 W/m K for λ_s for AC35, so it would seem that comparatively the value found for λ_g is not unreasonable.

Looking at figure 6.13 below it can be seen that thermal conductivity λ_g can be represented as two straight intersecting lines. The results reflect the fact that micropore filling takes place in two stages. Firstly, the layers of adsorbent build up on the inner walls of the pore. This does not affect the thermal conductivity of the grain since there is still an insulating gap in the centre of the pore, see fig 6.10a. This is represented as a horizontal line superimposed on the data points.

FIGURE 6.13

Straight Line Fits to Grain Conductivity
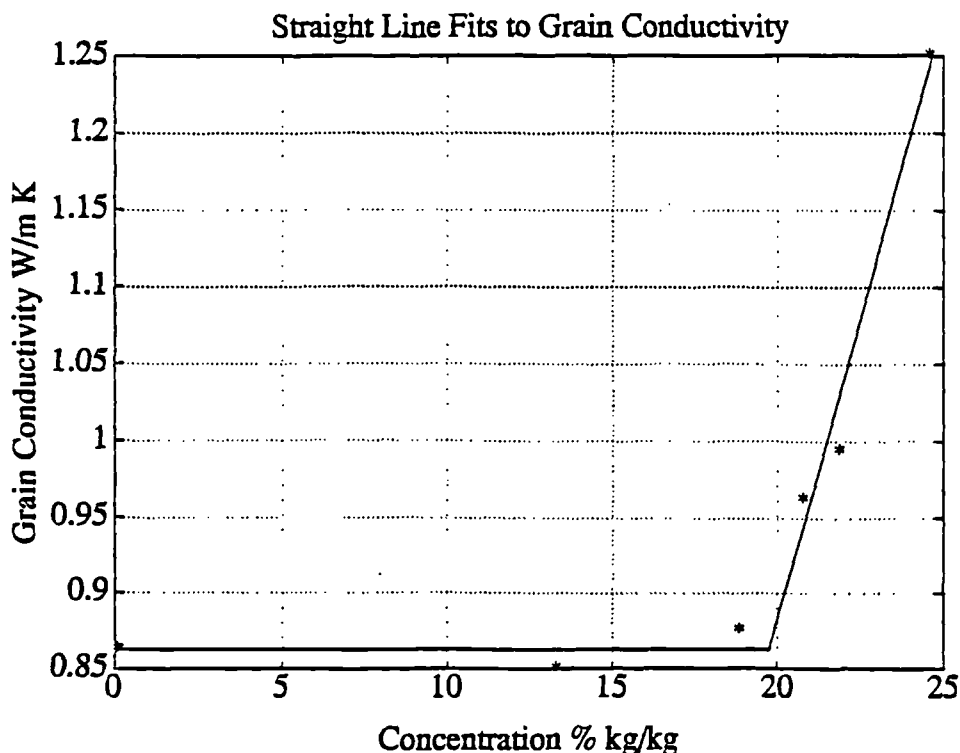
The second phase of pore filling, as shown by fig 6.10b, is the joining together of the adsorbed phase layers to form meniscii in the throats of the pores. This is accompanied by a rise in the grain conductivity due to the establishing of a continuous path along which heat may be transferred. This again is represented as a straight line in figure 6.13.

The equation of this straight line is,

$$\lambda_{s*} = 0.0786x - 0.6885 \qquad — (6.26)$$

The point of intersection of the two straight lines is,

$$\lambda_{s*} = 0.8625 \text{ W/mK}$$

$$x = 19.73 \%$$

This means that the grain conductivity may be completely defined over the concentration range within the stated limits.

When $0\% \leq x \leq 19.73\%$ then $\lambda_{s*} = 0.8625$ W/ m K

When $19.73\% \leq x \leq 25.82\%$ then $\lambda_{s*} = 0.07866x - 0.6885$

Table 6.3 overleaf summarizes the error to the fit between the values found for λ_{s*} using the ZB minimization program (see Table 6.2) and the values of λ_{so} and the those generated by the modified ZB model.

It is difficult to present a model which would be true for any activated charcoal. Gurgel et al [1] do not observe the two phases of pore filling when using AC35. Instead they observe a linear increase in λ_{s*} over the whole concentration range. It is possible that because the conductivity of the adsorbed methanol is about 60% less than that of adsorbed ammonia that λ_{s*} is little affected by adsorption. Sahnoune et al [2] do observe the two phases of pore filling when undertaking conductivity experiments on zeolite NaX and water where $\lambda_{ad} = 0.6$ W/m K.

It is more likely that λ_{s*} reflects the uniformity of the pore size. If there is a wide pore size distribution then there is no marked increase in conductivity as the pores become full as may be the case with AC35. When the pore sizes fall within a narrow band, the point of sudden increase in the conductivity is very definite. This argument is put forward as an explanation of the results found for the charcoal 208C.

TABLE 6.3

Summary of Error Between Real and Generated Data.

Test No.	12	13	14	15	16	
ammonia conc kg/kg	13.3	18.8	20.7	21.8	24.5	0
λ_{s^*} from ZB model W/m K	0.850	0.875	0.963	0.994	1.250	0.8625
λ_{s^*} from grain model W/m K	0.8625	0.8625	0.939	1.025	1.237	0.8625
error in λ_{s^*} % rows(3&4)	1.4	-1.4	-2.5	3.1	1.0	0
λ_{so} measured W/m K	0.163	0.165	0.171	0.173	0.189	0.164
λ_{so} modified ZB W/m K	0.164	0.164	0.169	0.175	0.189	0.164
error in λ_{so} % rows(3&4)	0.6	-0.6	-0.9	1.2	0	0

Since λ_{s^*} is so dependent on the pore size distribution, then without detailed knowledge of the individual charcoal it is impossible to present a general model for the grain. It would not be unreasonable however the use an average value for λ_{so} over the concentration range. The mean value for λ_{so} is 0.1725 W/ m K and this models the conductivity of the packed granular bed including the adsorbed phase with an accuracy of ±7.1 %.

6.4 Possible Improvements to the Overall Bed Conductivity

As can be seen from the previous section the overall bed conductivity of an ammonia charcoal reactor is low 0.17 W/m K. This low conductivity will mean a long cycle time, and this leads to a low power output. This section deals with various methods of increasing the thermal conductivity of the bed.
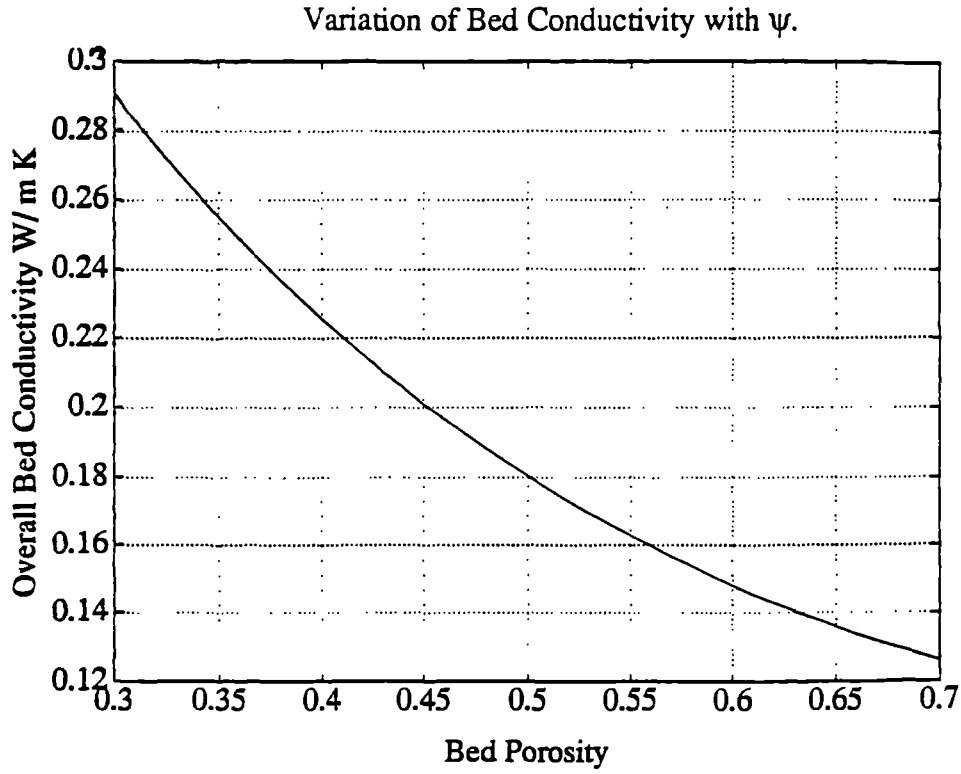
Bimodal Charcoal Mixtures.

A bimodal mixture refers to a mix of large and small grains which when they are packed together reduce the bed porosity ψ. As ψ decreases the more the unit cell volume is filled with solid grain. Using the modified ZB model, it is possible to examine the variation of λ_{so}. As ψ decreases the ZB parameters describing the point to point contact ϕ and the radiation heat transfer will change but not to any great extent, so for this study they will be assumed to be constant. The grain conductivity is taken to be the mean value of a 208C grain containing adsorbed ammonia $\lambda_{s*} = 1\,049$ W/m K. The deformation factor B can be calculated from equation (6.27) below, see appendix 6b for proof.

$$B = 1.25 \left(\frac{1-\psi}{\psi}\right)^{10/9} \qquad — (6.27)$$

Using this and equation (6.1), the variation of λ_{so} is examined between $0.3 \leq \psi \leq 0.7$, see fig 6.14.

Looking at fig 6.14 it can be seen that even at the lower limit of ψ that the conductivity only increases to 0.29 W/ m K. Barcik [7] observed an increase in the thermal conductivity of a granular charcoal bed of 10 % when using bimodal mixtures to increase the packing density. Zehner [8] observed increases in conductivity of between 100 % to 200 % depending on the ratio of λ_s/λ for the same range of ψ as shown in fig 6.14.

FIGURE 6.14

Variation of Bed Conductivity with ψ.

Other Bimodal Mixtures

Another possible way of improving the bed conductivity is to mix grains of high conductivity material in with the charcoal. If we assume that the grains of this material have exactly the same geometry as the charcoal then the ZB model may be used to find the total overall bed conductivity. If the secondary material and the charcoal are mixed in a 50%:50% by volume mix then the resistance network representing the bed is simply a grain of charcoal in series with a grain of secondary material, see figure 6.15.

Summing the thermal resistance network results in equation (6.28).

$$\lambda_{soTOT} = \frac{\lambda_{so}\,\lambda_{soH}}{\lambda_{so} + \lambda_{soH}} \quad - (6.28)$$

where:-

λ_{soTOT} = Overall Bed Conductivity of Mixture (W/m K).

λ_{soH} = Overall Secondary Material Conductivity (W/m K).

λ_{sH} = Solid Conductivity of Grain Material (W/m K).

FIGURE 6.15

Resistance Network Including Secondary Material
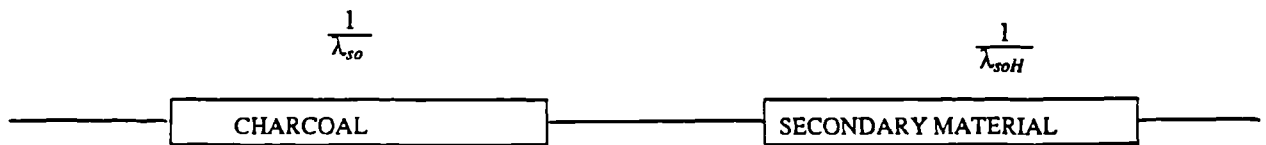
Taking λ_{so} as 0.17 W/m K, the value of λ_{sod} is varied from 10 W/m K to 250 W/ m K (this covers the range of usable metals). The corresponding increase in λ_{soTOT} is shown in figure 6.16 below.

FIGURE 6.16

Variation of Bed Conductivity Including a Secondary Material

Conductivity of Secondary Grain Material W/m K

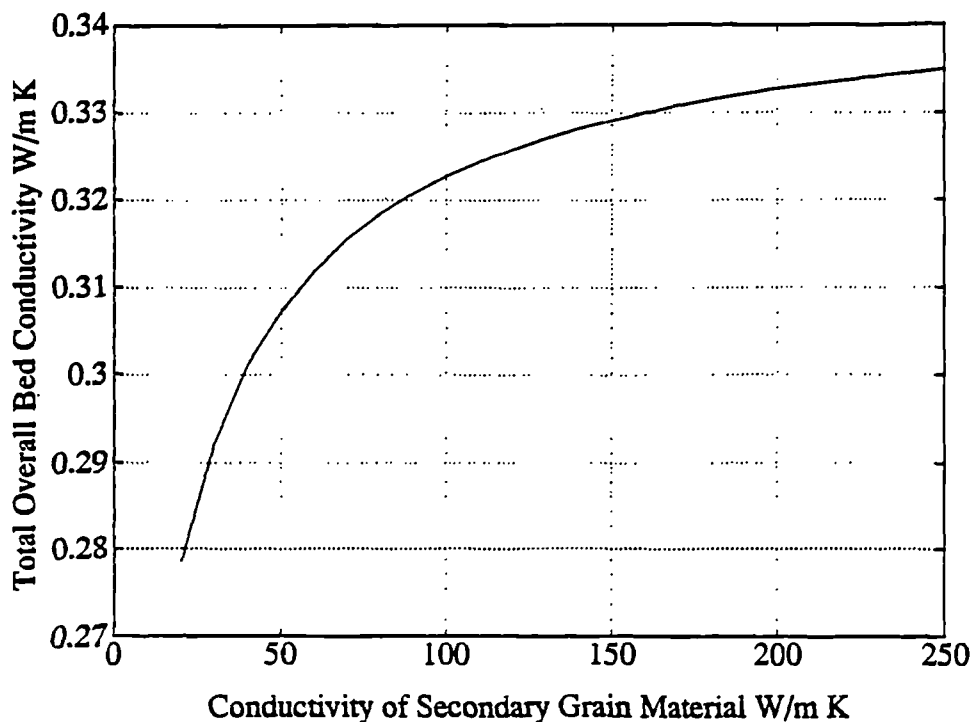Again it can be seen that even when the charcoal is mixed with grains of a very good conductor such as aluminium, the overall bed conductivity is still not significantly improved. The reason for this is that the grains touch each other by point to point contact only or sometimes by line contact, so the area of the solid-solid conduction path is very small. In order to improve the bed conductivity the contact area needs to be significantly increased.

Solid Charcoals

One method of eliminating the high thermal resistance of a point contact is to produce a solid charcoal shape. Figure 6.17 overleaf shows some examples of different solid charcoal shapes made by different workers. The top example was made by the author from a preformed disc of compressed cellulose powder which was then activated. Problems occurred in some of the discs with cracking and warping during activation, and after testing it was also found that the porosity of the disc was very low. These problems can be overcome by experimenting with the activation temperature and rate. Workers at Sutcliffe Speakman have been reported to have produced a solid disc some 6" in diameter for use in methane storage. Problems of cracking were avoided by making the disc in six segments and then bonding them together after activation.

The middle specimen in fig 6.17 was also produced by researchers at Sutcliffe Speakman from an extruded coal based material. Fig 6.17c was produced by workers at CNR-TAE in Sicily from a granular material held together by a pitch binder and then activated. Its porosity characteristics are not known. They have also produced solid zeolite blocks specifically for use in adsorption systems.

In all cases of solids, the wall to bed heat transfer coefficient will virtually be eliminated and the overall bed conductivity will be that of the grain conductivity λ_s. In the case of 208C and ammonia this means that $0.85 \text{ W/m K} \leq \lambda_{so} \leq 1.25 \text{ W/m K}$. Although

FIGURE 6.17

Examples of Solid Charcoal Shapes

PREFORMED DISCS

RODS

SOLID BLOCK
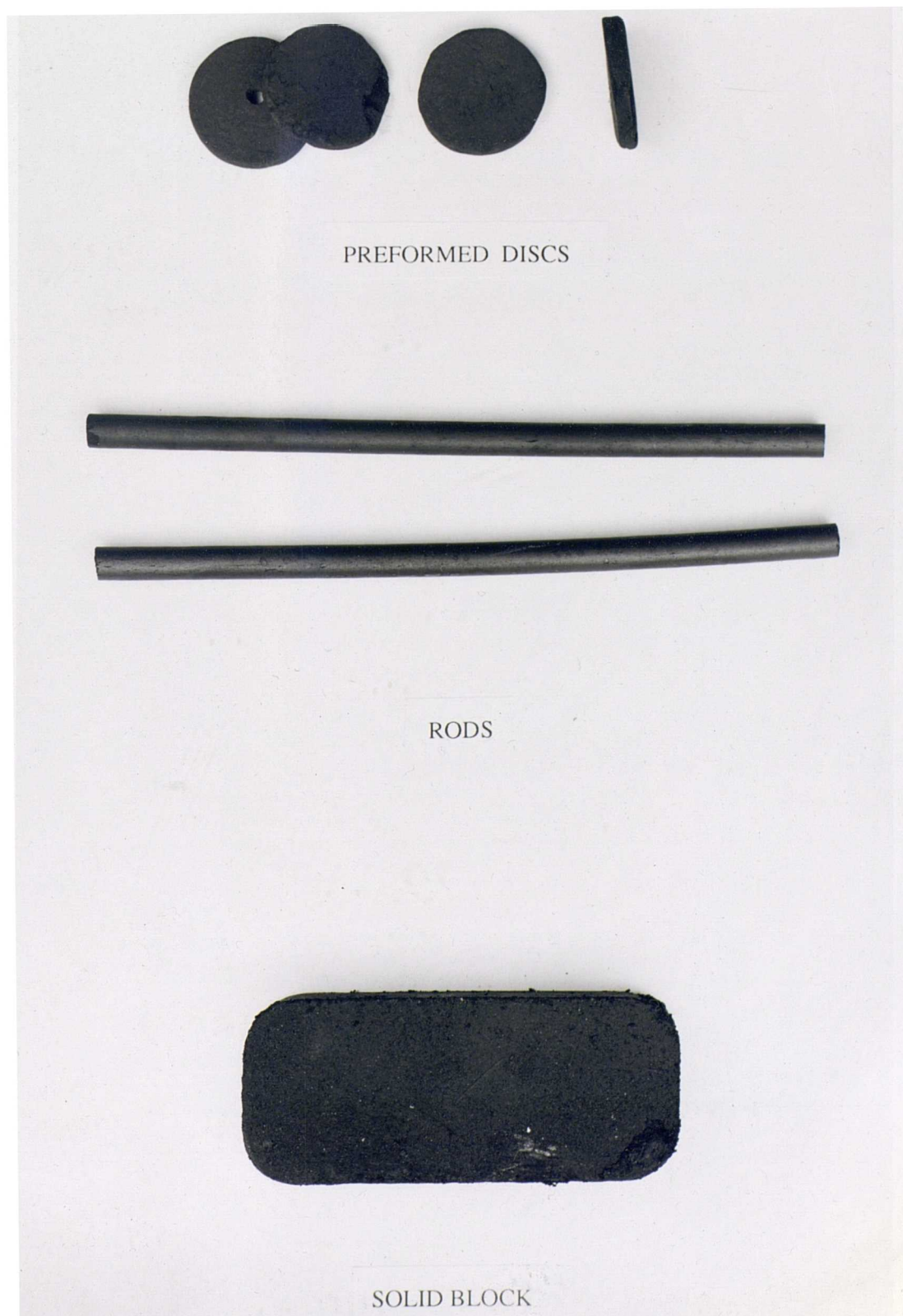
this is an improvement of ten times over the granular bed, the conductivity is still low and other means of increasing it must be found.

Sinters, Foams and Paths of Enhanced Conductance.

Guilleminot et al [9] have measured the thermal conductivity of zeolite pellets in the presence of copper and nickel foams. They found that with the copper metallic foam, the bed conductivity increased by a factor of 1.8 over a packed zeolite bed. The nickel foam was found to give a similar increase even though its conductivity is four times less than that of copper.

Oms [10] measured the bed conductivity of a calcium chloride-ammonia reactor which used graphex 1000 (conductivity = 100 W/m K) to enhance the heat transfer. The bed conductivity was found to range between 1 W/m K - 2 W/m K depending on the packing density.

Another idea which was tried at Warwick University was to mix a sintered metal in with the granular charcoal and to heat it until the mixture had fused together. Initial tests indicate an improvement to the conductivity but no accurate quantative data is available.

Increasing the bed conductivity is no easy task and of all the ideas tried at best it is still only 1 W/m K - 2 W/m K. In light of this it is probably more sensible to think about reducing the bed thickness and presenting a large heat transfer surface to the charcoal rather than trying to increase the conductivity. This would have the same effect of decreasing the cycle time and increasing the power output of a particular system. It is possible that this could be achieved by bonding the solid charcoal disc onto an aluminium disc of the same diameter as shown in figure 6.18.

In this way heat is transferred quickly along the aluminium disc and from there axially into the charcoal, thus the heat transfer does not rely solely on radial conduction through the charcoal.

FIGURE 6.18

Proposed Reactor Disc
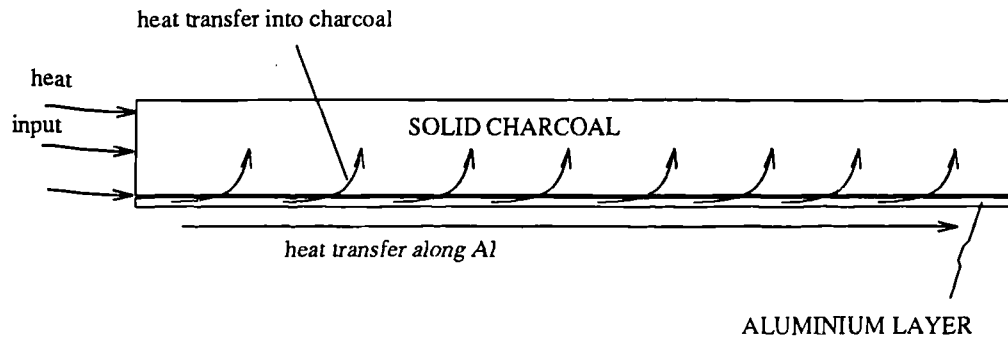
At present the concept depicted in figure 6.18 only exists as an idea and it is not known whether or not the charcoal would adhere to the metal surface. Assuming a good thermal bond could be achieved, it is expected that the difference in the thermal expansion coefficient of the two materials may lead to problems of separation along the bond or cracking of the charcoal brick. Obviously, a prototype would have to be made and tests carried out before it could definitely be put forward as a solution to the low conductivity problem.

6.5 Conclusions

The results of helium tests 1 and 2 shown in Section 6.1 prove that when dealing with coarse grain, high pressure packed granular beds the change in Knudsen effect over the working pressure range is negligible. This leads to much simplified ZB model equations.

When dealing with a packed bed under vacuum, heat is transferred only by way of radiation or by grain to grain conduction and consequently the ZB model equations can be simplified further still.

The four unknowns in the ZB model equations have been found by minimizing the square of the error of the fit between the real and predicted data points. The minimization has been weighted such that a good fit is obtained in the region of conductivity of the bed if it were to contain ammonia gas.

The minimization routine is found to produce very reasonable results for the ZB unknowns. The most useful of these values for modelling is the grain conductivity which was found to be 0.874 W/m K.

Plotting the values of ammonia concentration vs. grain conductivity for the ammonia results produces data points which lie on two straight intersecting lines. This behaviour may be explained by the theory of volume filling of micropores. The model used to define the variable grain conductivity predicts the results to within +3.1% and -2.5%. This model can be much simplified by using

$\lambda_g^* = 0.8625$ W/m K when $0\% \leq x \leq 19.73\%$

$\lambda_g^* = 1.056$ W/m K when $19.73\% \leq x \leq 24.5\%$

This would produce an error of

0% when $0\% \leq x \leq 19.73\%$

$\pm 7.6\%$ when $0\% \leq x \leq 19.73\%$

Generally the overall conductivity of a granular adsorber is low and to make the power output of an adsorption system comparable to that of other systems this parameter needs to be greatly increased. Producing a solid adsorber would increase the conductivity by about 6 times, but this is still not enough. Since this is the limit of what can be achieved with the material, the cycle time of the adsorber needs to be reduced by another means. This could be achieved by presenting the charcoal with a large area for heat exchange, as shown in fig 6.18, rather than by trying to increase the conductivity.

The COP and COA cycle models defined in Section 2 are used along with the modified ZB model equations to produce a dynamic adsorption/desorption cycle in Section 7.

References

1. Gurgel JM Grenier Ph

"Mesure de la Conductivité Thermique du Charbon Actif AC-35 en Presence de Gaz" The Chemical Engineering Journal, Vol 44 1990 pp43-50

2. Sahnoune H Grenier Ph

"Mesure de la Conductivité Thermique d'une Zeolithe." The Chemical Engineering Journal, Vol 40 1989 pp45-54

3. Touloukian Liley Saxeria

"Thermal Conductivity of Non-Metallic Liquids and Gases." from Thermophysical Properties of Matter. TPRC Series Vol 3 pp5,33,60,95,97. IFI Plenum, New York 1970.

4. Touloukian DeWitt

"Thermal Radiative Properties of Non-Metallic Solids." from Thermophysical Properties of Matter. TPRC Series Vol 8 .IFI Plenum, New York 1970.

5. ASHRAE Handbook

Properties of Ammonia pp17.105. Publication of the American Siciety of Heating, Refrigerating and Air Conditioning Enginerrs Inc. Atlanta 1982.

6. Milan Smisek   Slovoj Cerny

"Active Carbon Manufacture, Properties and Applications." Elsevier, New York (1970)

7. Barcik MK

"Effects of Bimodal Particle Mixtures on Density and Thermal Conductivity in A Solid Adsorbent Bed Heat Pump Application." By Private Communication.

8. Zehner P

"Experimentelle und Theoretische Bestimmung der Effektiven Warmeleitfahrigekeit Durchstromter Kugelschuttungen Bei Massigen und Hohen Temperaturen." Dissertation for Dipl Ing. 1972. University of Karlsruhe

9. Guilleminot JJ Gurgel JM

"Heat Transfer Intensification In Adsorbent Bed of Adsorption Thermal Devices." Proceedings of the 12th Annual International Solar Energy Conference. Miami USA. Publ. A.S.M.E. New York 1990. pp 69-74

10. Oms Jean Luc

"Identification des Parameters Thermiques de Lits Poreux Reactifs de Pompe a Chaleur Chimique. Controle de l'advancement de la Reaction par Sonde a Choc Thermique." Thesis presented for Doc Ing of University of Perpignan, 1990.

7. DYNAMIC ADSORPTION HEAT PUMP AND REFRIGERATION CYCLES.

Introduction.

In Section 2 we have examined the COP's and COA's of refrigeration and heat pumping cycles under different operating conditions. In this section, we wish to establish the cycle time and power output of similar cycles, again under varying operating conditions. To achieve this aim, the following section presents a transient heat and mass transfer model of an idealized ammonia-208C adsorber using the conductivity data and model outlined in Section 6.

The adsorber is modelled as a one-dimensional system in radial coordinates, and the method of solution uses the implicit Crank-Nicholson finite difference scheme.

The model is used to simulate desorption within the reactor only. This enables us to find the cycle time and the reactor's power density, expressed as kW/m³ of reactor. The effect of the different governing parameters on power output is examined, and from this conclusions are drawn as to the best possible way of optimizing the cycle.

7.1 Theory of Transient Heat and Mass Transfer in Adsorbent Beds.

Background

The theory of heat and mass transfer in adsorbent beds was until recently studied by

chemical engineers with a view to modelling adsorption in fixed beds. These models have dealt mainly with isothermal diffusion [1]. More recently Ruthven and Lee [2] and Rajniak and Ilavsky [3] have presented theoretical studies of the non-isothermal case. Following from this work, Sun *et al* [4] studied heat and mass transfer within a spherical grain of adsorbent taking into account inhomogeneities of temperature and concentration.

Udell [5] has studied heat and mass transfer in porous media including the effects of capillarity, gravity forces and phase change. In this work he discovered that the heat transfer was increased by several orders of magnitude above that of pure conduction due to an evaporation, convection and condensation phenomenon similar to conventional heat pipe operation. He termed this simply 'the heat pipe effect' and it is relevant to our case.

Work relating to adsorption heat pumps and refrigerators has been carried out by Shelton *et al* [6], and Aittomaki and Harkonen [7] when modelling the thermal wave type system. The most relevant work with respect to the model presented in this section is that of Guilleminot *et al* [8], who used a two dimensional finite difference model to predict the cycle time of a carbon-methanol adsorption cycle and have compared theoretical results to those gained by experiment with good agreement. Since the assumptions made in ref [8] have been proved valid, they will largely form the basis for the heat and mass transfer model presented here.

System Description and Simplifying Assumptions

The system we wish to model is that of heat and mass transfer within a heterogeneous medium. The medium itself consists of the porous material 208C containing adsorbed ammonia within the micropores whilst the mesopores, macropores and inter-granular voids are full of gaseous ammonia.

Three equations govern the behaviour of transient heat and mass transfer within a fixed bed:-

(i) the heat transfer equation

(ii) the mass transfer equation

(iii) the state equation for adsorption

At this stage it is useful to make two simplifying assumptions which apply to beds of high porosity (in the case of 208C, the total void volume $\psi=0.77$, see Section 5.2).

(1) the pressure is uniform throughout the bed

(2) the heterogeneous medium is treated as an equivalent continuous medium.

These two assumptions lead to significant simplifications since the functions become continuous and the system is now governed by the heat transfer and the state equations only. It is these two equations which control the mass transfer by a force similar to the operation of a heat pipe, again identified by Guilleminot et al [8] and shown in more detail in Section 7.4 of this work.

System Equations

The reactor vessel is constructed from stainless steel and is in the form of a long cylinder. The vessel contains 208C charcoal and ammonia.

For the vessel, the equation defining transient heat transfer is

$$\frac{\rho_1 Cp_1}{k_1} \frac{\partial T}{\partial t} = \frac{1}{r} \frac{\partial}{\partial r}(r \frac{\partial T}{\partial r}) \qquad - (7.1)$$

And similarly for the packed bed.

$$(\rho_2 (Cp_2 + Cp_3 x) + m_g Cp_4)\frac{\partial T}{\partial t} = k_2 (\frac{1}{r} \frac{\partial}{\partial r}(r \frac{\partial T}{\partial r})) + H \frac{dm_{ads}}{dt} \qquad - (7.2)$$

where:-

ρ_1	density of stainless steel (kg/m^3)
ρ_2	bulk density of 208C charcoal (kg/m^3)
Cp_1	Specific heat of stainless steel $(J/kg\ K)$
Cp_2	Specific heat of 208C $(J/kg\ K)$
Cp_3	Specific heat of adsorbed ammonia $(J/kg\ K)$
Cp_4	Specific heat of ammonia gas $(J/kg\ K)$
k_1	Thermal conductivity of stainless steel $(W/m\ K)$
k_2	Thermal conductivity of packed bed $(W/m\ K)$
T	temperature (K)
t	time (s)
H	Heat of desorption/adsorption (J/kg)
x	concentration of adsorbed ammonia (kg/kg)
m_g	mass of gaseous ammonia (kg)
m_{ads}	mass of adsorbed ammonia (kg)
r	radius of bed (m)
p	pressure (Pa)

All of the terms in equation (7.1) and (7.2) are known except for $\frac{dm_{ads}}{dt}$, which is the rate of change of adsorbed mass with respect to time.

The adsorbed mass is a function of pressure and temperature and may be expressed as a partial differential equation.

$$dm_{ads} = \frac{\partial m_{ads}}{\partial T}.dT + \frac{\partial m_{ads}}{\partial lnp}.dlnp \qquad —(7.3)$$

Differentiating equation (7.3) with respect to time gives.

$$\frac{dm_{ads}}{dt} = \frac{\partial m_{ads}}{\partial T}.\frac{dT}{dt} + \frac{\partial m_{ads}}{\partial lnp}.\frac{dlnp}{dt} \qquad —(7.4)$$

Equation (7.4) may be rewritten as:

$$\frac{dm_{ads}}{dt} = \frac{\partial m_{ads}}{\partial lnp}.\frac{dlnp}{dt} - \frac{\partial m_{ads}}{\partial lnp}\frac{\partial lnp}{\partial T}.\frac{dT}{dt} \qquad —(7.5)$$

The partial differential $\frac{\partial m_{ads}}{\partial \ln p}$ may be found from the DA equation.

$$m_{ads} = m_0 \exp\left[-K\left(\frac{T}{T_{sat}} - 1\right)^n\right] \quad -(7.6)$$

where:-

m_0 adsorbed mass under saturation conditions (kg)

T_{sat} Saturation temperature (K)

K, n Experimentally determined constants for 208C

Also from the equation defining the relationship of $\ln p$ against $\frac{1}{T_{sat}}$ for pure ammonia,

$$\ln p = \frac{-2823.4}{T_{sat}} + 11.749 \quad -(2.9)$$

or

$$\frac{1}{T_{sat}} = B - \frac{\ln p}{A} \quad -(7.7)$$

Combining (7.6) and (7.7) and differentiating with respect to $\ln p$ gives,

$$\frac{\partial m_{ads}}{\partial \ln p} = \frac{K \, T \, n \, m_0}{A}\left(\frac{T}{T_{sat}} - 1\right)^{n-1} \exp\left[-K\left(\frac{T}{T_{sat}} - 1\right)^n\right] \quad -(7.8)$$

The partial derivative $\frac{\partial \ln p}{\partial T}$ is a form of the Clausius Clapeyron equation.

$$\frac{\partial \ln p}{\partial T} = \frac{H}{R \, T^2} \quad -(7.9)$$

This leaves us with the unknown value of $\frac{d \ln p}{dt}$, and this may be found as follows.

The process of desorption may be considered to be in two phases.

(i) heating (from $T_{a2} - T_{g1}$) -- During this phase the reactor is closed and the total mass of ammonia within the reactor remains constant.

(ii) generation (from $T_{g1} - T_{g2}$) -- During this phase the reactor is linked to the condenser and desorption commences along an isobar.

The total mass of ammonia in the reactor may be defined as the sum of its partial differentials.

$$dm_{tot} = \frac{\partial m_{ads}}{\partial lnp}.dlnp + \frac{\partial m_g}{\partial lnp}.dlnp + \frac{\partial m_{ads}}{\partial T}.dT + \frac{\partial m_g}{\partial T}.dT \qquad - (7.10)$$

differentiating with respect to time gives.

$$\frac{dm_{tot}}{dt} = \frac{\partial m_{ads}}{\partial lnp}.\frac{dlnp}{dt} + \frac{\partial m_g}{\partial lnp}.\frac{dlnp}{dt} + \frac{\partial m_{ads}}{\partial T}.\frac{dT}{dt} + \frac{\partial m_g}{\partial T}.\frac{dT}{dt} \qquad - (7.11)$$

During process (i) the total mass of ammonia within the reactor stays constant and this gives the condition:-

$$\int \frac{dm_{tot}}{dt}.dr = 0 \qquad - (7.12)$$

Applying this condition to equation (7.11) gives;

$$0 = \int (\frac{\partial m_{ads}}{\partial lnp}.\frac{dlnp}{dt} + \frac{\partial m_g}{\partial lnp}.\frac{dlnp}{dt}).dr + \int (\frac{\partial m_{ads}}{\partial T}.\frac{dT}{dt} + \frac{\partial m_g}{\partial T}.\frac{dT}{dt}).dr \qquad - (7.13)$$

Since the pressure is constant throughout the reactor,

$$\frac{dlnp}{dt} = \frac{\int (\frac{\partial m_{ads}}{\partial lnp}.\frac{\partial lnp}{\partial T}.\frac{dT}{dt} - \frac{\partial m_g}{\partial T}.\frac{dT}{dt}).dr}{\int (\frac{\partial m_{ads}}{\partial lnp} + \frac{\partial m_g}{\partial lnp}).dr} \qquad -(7.14)$$

Where $\frac{\partial m_g}{\partial lnp}$ and $\frac{\partial m_g}{\partial T}$ are found from the perfect gas law.

$$\frac{\partial m_g}{\partial lnp} = \frac{p}{R} \frac{V}{T} \quad\text{---(7.15)}$$

and

$$\frac{\partial m_g}{\partial T} = -p \frac{V}{R T^2} \quad\text{---(7.16)}$$

From equation (7.14), it can be seen that in order to calculate the mass of ammonia present in any one location in the reactor, the mass of ammonia present at all remaining locations within the reactor must be taken into account.

Substituting equations (7.14) and (7.5) into equation (7.2) produces an expression for the transient heat transfer through the packed bed medium.

$$(\rho_2 (Cp_2 + Cp_3 x) + m_g Cp_4)\frac{\partial T}{\partial t} = k_2 \left(\frac{1}{r} \frac{\partial}{\partial r}(r \frac{\partial T}{\partial r})\right)$$

$$+ H \left(\frac{\partial m_{ads}}{\partial lnp} \frac{\int(\frac{\partial m_{ads}}{\partial lnp} \cdot \frac{\partial lnp}{\partial T} \cdot \frac{dT}{dt} - \frac{\partial m_g}{\partial T} \cdot \frac{dT}{dt}).dr}{\int(\frac{\partial m_{ads}}{\partial lnp} + \frac{\partial m_g}{\partial lnp}).dr} - \frac{\partial m_{ads}}{\partial lnp} \cdot \frac{\partial lnp}{\partial T} \cdot \frac{dT}{dt} \right) \quad\text{---(7.17)}$$

During phase (ii) desorption takes place along an isobar and the pressure is known.

$$P (t) = constant$$

$$\frac{dlnp}{dt} = 0$$

and equation (7.5) reduces to,

$$\frac{dm_{ads}}{dt} = -\frac{\partial m_{ads}}{\partial lnp} \cdot \frac{\partial lnp}{\partial T} \cdot \frac{dT}{dt} \quad\text{---(7.18)}$$

and the expression for the transient heat transfer through the packed bed becomes.

$$(\rho_2 (Cp_2 + Cp_3 x) + m_g Cp_4)\frac{\partial T}{\partial t} = k_2 \left(\frac{1}{r} \frac{\partial}{\partial r}(r \frac{\partial T}{\partial r})\right) - H \cdot \frac{\partial m_{ads}}{\partial lnp} \cdot \frac{\partial lnp}{\partial T} \cdot \frac{dT}{dt} \quad\text{---(7.19)}$$

The transient heat transfer equations (7.1), (7.17), (7.19) and all relating equations are used in Section 7.2 to produce a one dimensional finite difference scheme to model

dynamic desorption of an ammonia charcoal reactor.

7.2 A Finite Difference Model of an Ammonia Charcoal Reactor,

Finite Difference Spatial Grid.

The reactor is constructed from a stainless steel tube with closed ends and a wall thickness of 1mm. The tube is packed with 208C charcoal and filled with the adsorbate ammonia. The tube is heated via its outer radius by steam or some other suitable constant temperature heat source and is cooled in a similar manner, see fig 7.1.

FIGURE 7.1

Section of Reactor
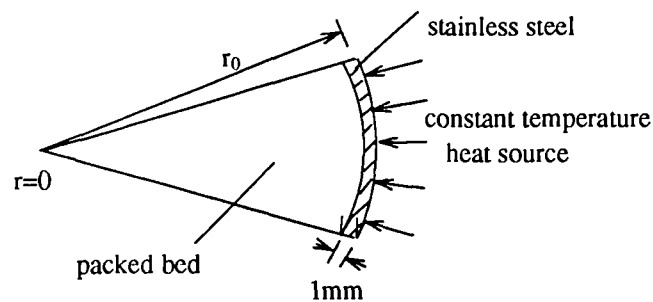
The above reactor is represented by a one dimensional model set in radial coordinates. Each node is equidistant being 1mm apart and the product of the cicumferential and longitudinal increments is set so that it is unity, see fig 7.2.

FIGURE 7.2

Spatial Scheme of Reactor Model
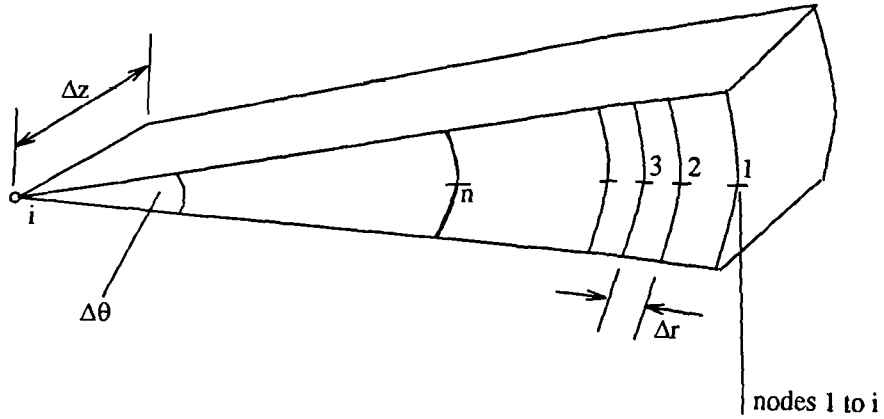
Taking a typical node n in the adsorbent bed, an energy balance may be found in terms of the rate of heat flow to node n from its neighbouring nodes n-1 and n+1, see fig 7.3.

FIGURE 7.3
Heat Flow to Node n
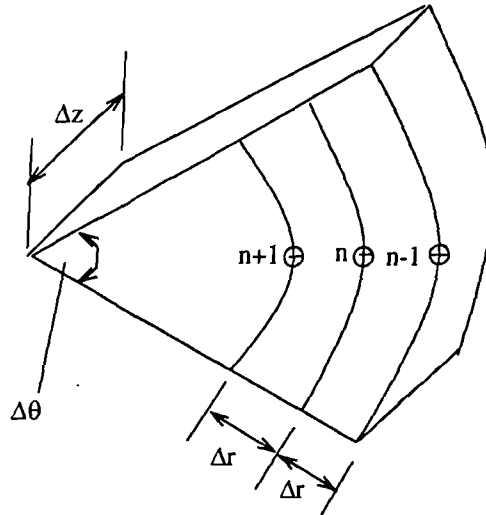
Rate of heat flow from node (n-1) to (n)

$$Q_{n-1,n} = k_2 (r_n + \frac{\Delta r}{2}) \Delta\theta \, \Delta z \, (\frac{T_{n-1} - T_n}{\Delta r}) \qquad — (7.20)$$

Rate of heat flow from node (n+1) to (n)

$$Q_{n+1,n} = k_2 (r_n - \frac{\Delta r}{2}) \Delta\theta \, \Delta z \, (\frac{T_{n+1} - T_n}{\Delta r}) \qquad — (7.21)$$

As already mentioned, the method of solution for the temperature field uses the implicit Crank Nicholson difference scheme in which the space derivatives $\frac{dT}{dr}$ are averaged over the two time levels t and t+Δt. With this in mind and applying equations (7.20) and (7.21) to (7.17), the total heat flow to node n is found from equation (7.22) below.

$$(\rho_2 \Delta\theta \ \Delta z \ r_n \ \Delta r \ (Cp_2 + Cp_3 x_n) + m_{g(n)} Cp_4)(\frac{T'_n - T_n}{\Delta t}) =$$

$$\frac{1}{2}(k_2(r_n + \frac{\Delta r}{2})\Delta\theta.\Delta z. (\frac{T_{n-1} - T_n + T'_{n-1} - T'_n}{\Delta r}) + k_2(r_n - \frac{\Delta r}{2})\Delta\theta.\Delta z. (\frac{T_{n+1} - T_n + T'_{n+1} - T'_n}{\Delta r}))$$

$$+ H_n \ (\frac{\partial m_{ads}}{\partial lnp})_n \frac{\sum\limits_{n=3}^{n=i}((\frac{\partial m_{ads}}{\partial lnp})_n.(\frac{\partial lnp}{\partial T})_n - (\frac{\partial m_g}{\partial T})_n.(\frac{T'_n - T_n}{\Delta t})).\Delta n}{\sum\limits_{n=3}^{n=i}((\frac{\partial m_{ads}}{\partial lnp})_n + (\frac{\partial m_g}{\partial lnp})_n).\Delta n} - H_n(\frac{\partial m_{ads}}{\partial lnp})_n(\frac{\partial lnp}{\partial T})_n(\frac{T'_n - T_n}{\Delta t}) \quad -(7.22)$$

Boundary Conditions

The base case operating temperatures for a refrigerator are taken to be:

$Tg_2 = 150°C = 423$ K

$Ta_2 = Tc = 30°C = 303$ K

$Te = -10°C = 263$ K

and for a heat pump:

$Tg_2 = 250°C = 523$ K

$Ta_2 = Tc = 50°C = 323$ K

$Te = 5°C = 278$ K

At the outer radius of the vessel the temperature is set to Tg_2

$$T_{(1,t)} = Tg_2$$

The centre node i.e when r=0 is treated as a reflected node and so $T_{n+1} = T_{n-1}$. Another method of dealing with this situation is to assume that $T_n = T_{n-1}$. Either assumption suffices for this model.

The initial temperature field is uniform and is set to Ta_2.

$$T_{(r,0)} = Ta_2$$

The initial pressure is calculated from equation (2.9).

$$P_{(0)} = exp\left(\frac{-2823.4}{Te} + 11.749\right)$$

The pressure at which desorption begins is calculated from Tc in a similar manner.

The desorption cycle is assumed to be complete when the average bed temperature has reached 97% of the generating temperature Tg_2.

The maximum time step Δt was found such that the error in pressure calculation tends to less that 0.05% after two minutes of cycle time. This time was found by running the program with a set of time steps ranging from 0.05 to 2 secs. The time step used in each test case is indicated in table 7.1 in Section 7.3.

Method of Solution.

The initial temperature field and pressure are supplied by the cycle operating limits. From this information the initial concentrations and adsorbed phase node masses can be calculated. The new temperature field at time t+Δt is then found by solving the matrix formed from the heat transfer equations (7.20) for each node. Once the new temperature field is known the new system pressure can be found using the following method.

Calculation of new Reactor Pressure.

The pressure at any packed bed node may be expressed by the perfect gas law.

$$p_n = \frac{m_{g(n)} R\ T_{(n,t+\Delta t)}}{V_{(n)}}$$

The total mass of gas in the system is found from summing the mass at each node and since p is constant over the whole reactor, we may write:

$$p = \frac{\sum_{n=3}^{n=i} m_g(n).\Delta n}{\sum_{n=3}^{n=i} \frac{V_n}{R\,T_{(n,t+\Delta t)}}.\Delta n} \qquad —\ (7.23)$$

Since the reactor is closed the sum of the total mass of adsorbed and gaseous ammonia remains constant.

$$\sum_{n=3}^{n=i} m_g{}_{(n,t+\Delta t)} = \sum_{n=3}^{n=i} m_{ads(n,t)} - \sum_{n=3}^{n=i} m_{ads(n,t+\Delta t)} + \sum_{n=3}^{n=i} m_g{}_{(n,t)} \qquad —\ (7.24)$$

Substituting (7.23) into (7.24) gives an implicit equation in the new system pressure $p_{(t+\Delta t)}$, see equation (7.25).

$$p_{(t+\Delta t)} = \frac{\sum_{n=3}^{n=i} m_{ads(n,t)}.\Delta n - \sum_{n=3}^{n=i} m_{ads(n,t+\Delta t)}.\Delta + \sum_{n=3}^{n=i} m_g{}_{(n,t)}.\Delta n}{\sum_{n=3}^{n=i} \frac{V_n}{R\,T_{(n,t+\Delta t)}}.\Delta n} \qquad —\ (7.25)$$

Equation (7.25) is solved using Newton-Raphson iteration.

Once the new system pressure is known, the new concentrations and ammonia node masses are calculated and the first time step is completed.

At the end of every 20 time steps the p-T-x data is saved. The bed pressure, temperature and concentration are defined by equations (7.26)-(7.28) below.

Pressure

$$p = \textit{system pressure} \qquad —\ (7.26)$$

Temperature

$$T = \frac{\sum_{n=3}^{n=i} (\rho_2 V_n (Cp_2 + Cp_3 x_n)).T_{(n)}.\Delta n}{\sum_{n=3}^{n=i} (\rho_2 V_n (Cp_2 + Cp_3 x_n)).\Delta n} \qquad —\ (7.27)$$

Concentration

$$x = \frac{\sum_{n=3}^{n=i} \rho_2 V_n x_n \Delta n}{\sum_{n=3}^{n=i} \rho_2 V_n \Delta n} \qquad - (7.28)$$

The p-T-x data is the used to find the optimum cycle time and power output as outlined in the next sub section.

7.3 Test Programme and Method of Results' Analysis.

The purpose of the test programme outlined in Table 7.1 overleaf is to assess the effect of the different governing parameters on the power performance of the cycle.

The prefix REF and HP in the first column refers to refrigerating and heat pumping cycles respectively. REF A is the base case with the parameters as measured in Section 6, this case is used as a datum to which all other REF cases will be compared.

Variation of Generating Temperature

Test cases REF A - REF C and HP T - HP V varies the upper generating temperature. This parameter is the only one examined for the heat pump since it produces useful information. The other parameters have not been varied in the heat pump cycle since they will only duplicate the results found for the refrigeration cycle.

Variation of the Packing Density and Bed Conductivity

Test cases REF A, REF D - REF F vary the packing density of the bed from a loose fill to a solid. The bulk density and the void ratio ψ are calculated from each other and

TABLE 7.1

Cycle Simulation Test Programme

Test run	Generating Temperature Tg_2 K	Bulk density ρ_2 kg/m^3	Packed Bed conductivity k_2 W/m K	Bed Radius r m	Void Ratio ψ m^3/m^3	Wall to bed heat transfer coefficient h_2 W/m^{2}K
REF A	423	500	0.165	0.021	0.478	50
REF B	393	500	0.165	0.021	0.478	50
REF C	373	500	0.165	0.021	0.478	50
REF D	423	126	0.142	0.021	0.650	50
REF E	423	778	0.255	0.021	0.350	50
REF F	423	1539	0.8625	0.021	0.001	50
REF G	423	1539	0.8625	0.021	0.001	∞
REF H	423	500	0.165	0.021	0.478	1000
REF I	423	500	0.165	0.021	0.478	200
REF J	423	500	0.165	0.021	0.478	100
REF K	423	500	0.165	0.021	0.478	20
REF L	423	500	0.165	0.031	0.478	50
REF M	423	500	0.165	0.026	0.478	50
REF N	423	500	0.165	0.016	0.478	50
REF O	423	500	0.165	0.011	0.478	50
REF P	423	1539	0.8625	0.010	0.001	∞
REF Q	423	1539	0.8625	0.008	0.001	∞
REF R	423	1539	0.8625	0.006	0.001	∞
REF S	423	1539	0.8625	0.004	0.001	∞
HP T	523	500	0.165	0.021	0.478	50
HP U	503	500	0.165	0.021	0.478	50
HP V	473	500	0.165	0.021	0.478	50

For all cycles Tc, Te, and Ta_2 are as stated in the previous section under the heading boundary conditions.

the corresponding bed conductivity is found from figure 6.14 in the previous section. The bed conductivity in the case of the solid adsorbent is taken to be that of the grain conductivity found from the conductivity experiments, (see table 6.3).

Variation of Wall to Bed Heat Transfer Coefficient

If a solid reactor could be manufactured it is sensible to model it without a heat transfer coefficient between the wall and the bed as in test case REF G. Cases REF A, REF H - REF K examine variation of h_2 under base case conditions.

Variation of Bed Radius

Cases REF A, REF L - REF O examine the variation of bed radius or bed thickness.

Simulation of Packed Beds Involving Paths of Enhanced Conductance.

As discussed in Section 6.4 and shown in figure 6.18, it would be highly desirable to construct a reactor from solid charcoal bonded onto metal strip. This would in effect mean that all parts of the solid bed would be close to a high temperature surface. To model this situation exactly it would be necessary to construct a two-dimensional finite difference model. In order to avoid this complication, the two-dimensional case has be approximated to a one-dimensional case by modelling the reactor as a thin rod. Test cases REF P - REF S model a series of thin rods bonded to their containing vessel.

In all cases where the packing density is high or where the bed is solid, it is likely that the rate of desorption will become mass transfer limited and not heat transfer limited.

The balance point between heat or mass transfer limited desorption can only be found experimentally and it will be unique to each charcoal and each packed bed. Since this information is not available to us, it will be assumed that desorption is always heat transfer limited. The assumption is to some extent justified since if a reactor could be manufactured from thin but solid discs of adsorbent which were stacked such that an equal volume void space was left between each disc, then it is likely that desorption would be heat transfer limited.

Analysis of results.

The results of each test run are saved in the form of time, pressure, temperature, concentration data. The data is analyzed on a continuous power output basis. The refrigerating power is calculated from the concentration change once the desorbing pressure has been reached. Assuming that time taken to desorb and adsorb is equal the power output may be found from equation (7.29).

$$P_{ref} = \frac{\rho_2 V_2 \, (x_{(t)} - x_{(des)}) \times h_{fg \, (Tc)}}{2 \times t} \qquad — (7.29)$$

Taking the results from REF A and plotting the continuous power output against the ratio of bed temperature over generating temperature as a percentage, see figure 7.4, it is possible to find the optimum operating conditions for a cycle.

The maximum continuous power output of the cycle is found from the turning point of the curve in figure 7.4. For REF A, the maximum continuous refrigerating power is 4.127 W. This figure is more meaningful if it is expressed in terms of the mass of charcoal in the reactor or in terms of the reactor volume.

$$P_{ref} = 41.27 \frac{W}{kg \; of \; charcoal} \quad OR \quad 20.635 \frac{kW}{m^3 \, of \; reactor}$$

FIGURE 7.4

Refrigerating Power Output. Test Case A.
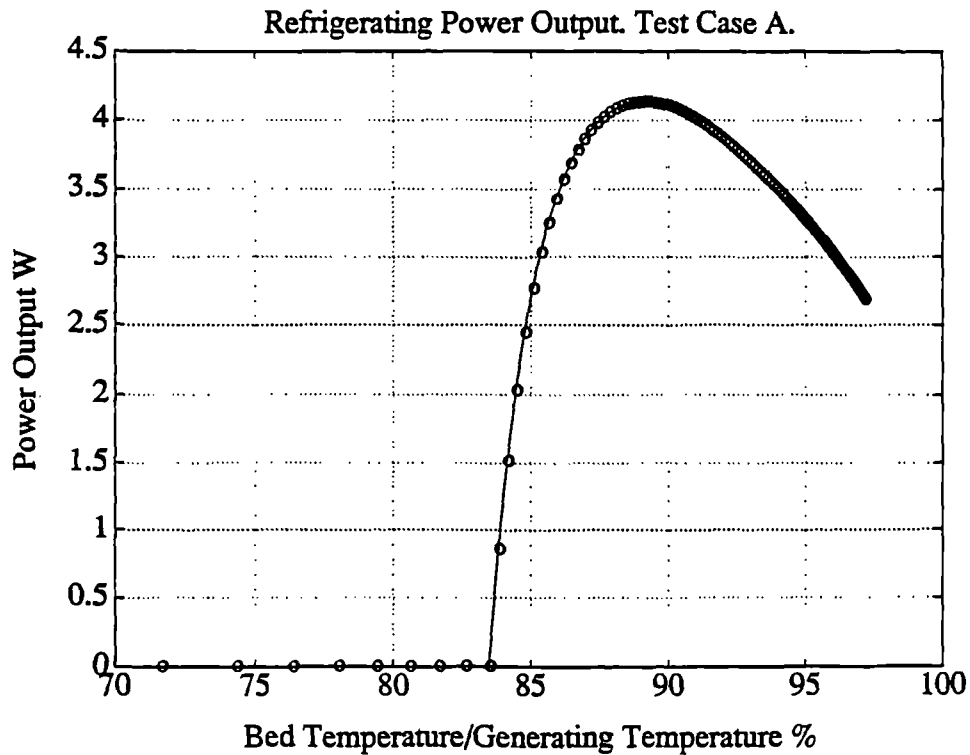
All of the test cases outlined in Table 7.1 are analyzed in this way and the results
are listed in Table 7.3

7.4 Results and Discussion of Cycle Simulations.

The Heat Pipe Effect.

During the heating phase of the desorption cycle, the reactor is closed and the main
method of heat transfer through the packed bed is not that of conduction but of a
phenomenon similar in operation to that of a heat pipe. It is interesting to look at the tem-
perature field of case REF A for the first 8 seconds of heating, see Table 7.2 overleaf.

TABLE 7.2

Temperature Field (Test Case REF A).

node no.	time (s)								
	0	1	2	3	4	5	6	7	8
1	303.0	384.3	409.2	416.9	419.4	420.2	420.5	420.6	420.7
2	303.0	384.0	408.9	416.6	419.1	419.8	420.2	420.3	420.4
3	303.0	304.8	308.7	312.8	316.5	319.8	322.8	325.4	327.8
4	303.0	303.2	303.8	304.7	305.8	307.0	308.3	309.7	311.0
5	303.0	303.1	303.6	304.1	304.6	305.2	305.8	306.4	307.0
6	303.0	303.1	303.6	304.0	304.5	305.0	305.4	305.9	306.3
7	303.0	303.1	303.6	304.0	304.5	304.9	305.4	305.8	306.2
8	303.0	303.1	303.6	304.1	304.5	304.9	305.4	305.8	306.2
9	303.0	303.1	303.6	304.1	304.5	304.9	305.4	305.8	306.2
10	303.0	303.1	303.6	304.1	304.5	304.9	305.4	305.9	306.2
11	303.0	303.1	303.6	304.1	304.5	304.9	305.4	305.9	306.2
12	303.0	303.1	303.6	304.1	304.5	304.9	305.4	305.9	306.2
13	303.0	303.1	303.6	304.1	304.5	304.9	305.4	305.9	306.2
14	303.0	303.1	303.6	304.1	304.5	304.9	305.4	305.9	306.2
15	303.0	303.1	303.6	304.1	304.5	304.9	305.4	305.9	306.2
16	303.0	303.1	303.6	304.1	304.5	304.9	305.4	305.9	306.2
17	303.0	303.1	303.6	304.1	304.5	304.9	305.4	305.9	306.2
18	303.0	303.1	303.6	304.1	304.5	304.9	305.4	305.9	306.2
19	303.0	303.1	303.6	304.1	304.5	304.9	305.4	305.9	306.2
20	303.0	303.1	303.6	304.1	304.5	304.9	305.4	305.9	306.2
21	303.0	303.1	303.6	304.1	304.5	304.9	305.4	305.9	306.2
22	303.0	303.1	303.6	304.1	304.5	304.9	305.4	305.9	306.2
23	303.0	303.1	303.6	304.1	304.5	304.9	305.4	305.9	306.2

node 1 at r=21mm

node 23 at r=0mm

It can be seen that after only 8 seconds the temperature of the centre node has increased by 3.2°C. In the case where there is no mass transfer, the time taken for the centre node to be raised to 3.2°C is 127 seconds. However, the time taken in both cases for the mean bed temperature to reach the stage at which desorption begins is 180 seconds, it would therefore seem that the heat pipe effect makes little or no overall difference to desorption rate. Although the heating time is the same in both cases, there is a very great difference in the temperature profiles of the two beds, and in the case including mass transfer, heat is transferred to the inner nodes at the expense of the outer ones.

Results of Simulation Runs.

Table 7.3 below lists the optimum power outputs and cycle times of test cases REF A - HP V.

where:-

t_1	heating time (s)
t_1	generation time (s)
t_1	total cycle time (s)
P_{ref1}	continuous power output of reactor (W)
P_{ref2}	continuous power output per (W/kg) kg of adsorbent
P_{ref3}	continuous power output per (W/m^3) volume of reactor

Discussion of Results

The results in Table 7.3 are plotted in figures 7.5 to 7.10 overleaf.

Figures 7.5 and 7.6 show the variation of power output of the cycle with generating temperature for a refrigerator and heat pump respectively. It can be seen that in both

TABLE 7.3

Power Output of Adsorption Cycles.

Test Run	time step s	t_1 s	t_2 s	t_3 s	Optimum Tgen K	P_{ref1} W	P_{ref2} W/kg	P_{ref2} kW/m^3
REF A	1	180	420	1200	376	4.127	41.27	20.635
REF B	1	280	620	1800	369	2.076	20.76	10.380
REF C	1	480	920	2800	363	0.858	8.58	4.290
REF D	1	120	200	640	395	2.095	83.10	10.475
REF E	1	180	520	1400	374	5.705	36.67	28.525
REF F	1	300	820	2240	378	8.088	26.00	40.440
REF G	1	60	100	320	370	37.500	121.00	187.500
REF H	1	80	140	370	370	6.871	68.71	34.355
REF I	1	100	200	600	372	6.605	66.03	33.025
REF J	1	120	260	760	371	5.769	57.69	28.846
REF K	1	320	800	2240	368	1.482	14.82	7.410
REF L	1	300	760	2120	375	4.933	21.93	10.960
REF M	1	240	580	1640	376	4.520	28.93	14.464
REF N	1	140	300	880	381	3.316	58.95	29.475
REF O	1	100	180	560	385	2.400	96.02	48.012
REF P	0.5	10	30	80	368	34.460	552.80	850.930
REF Q	0.1	8	22	60	371	27.830	738.20	1136.10
REF R	0.05	5	14	38	372	24.550	1276.0	1963.70
REF S	0.05	3	8	22	379	17.610	2541.0	3913.30
HP T	1	80	280	720	417	15.720	157.20	78.600
HP U	1	120	320	880	416	14.880	148.80	74.400
HP V	1	160	420	1160	412	8.954	89.50	44.767

cases as expected the higher the generating temperature the greater the power output. In the case of the refrigerator, the continuous power output at $T_{g2} = 150°C$ is 20.6 kW/m^3, this would equate to 886 kg of ice production per day per 1 m^3 of reactor.

To get some idea of what this power output means we can compare it to a typical domestic upright refrigerator. The power output of a standard size larder refrigerator is quoted to be in the order of 35W-40W continuous, ref [9]. Assuming the reactor to be about 1 litre in volume, i.e about the same physical size as a compressor, then the power output of an idealized cycle based on the results of test case REF A would be 20.6 W continuous. Taking into account heat losses and the likely difference between adsorption and desorption time, it is felt that this figure would probably need to be at least four times that of REF A for the system to become competitive with a standard vapour compression cycle.

FIGURE 7.5

Variation of Refrigerating Power Output vs. Generating Temperature

FIGURE 7.6

Variation of Heat Pumping Power vs. Generating Temperature
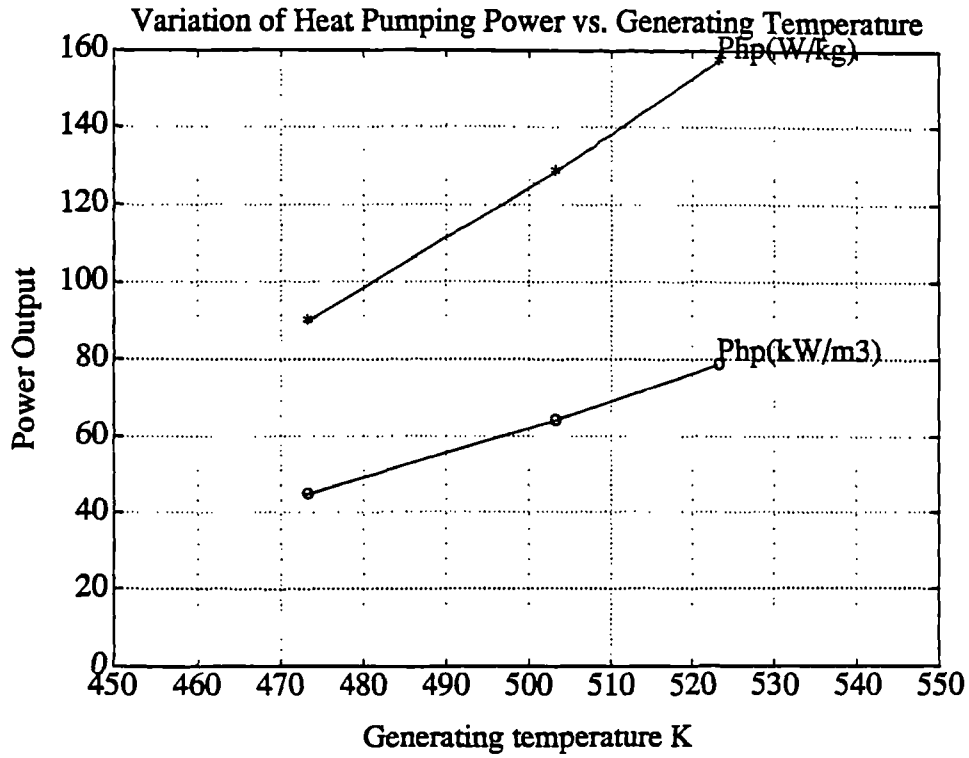

FIGURE 7.7

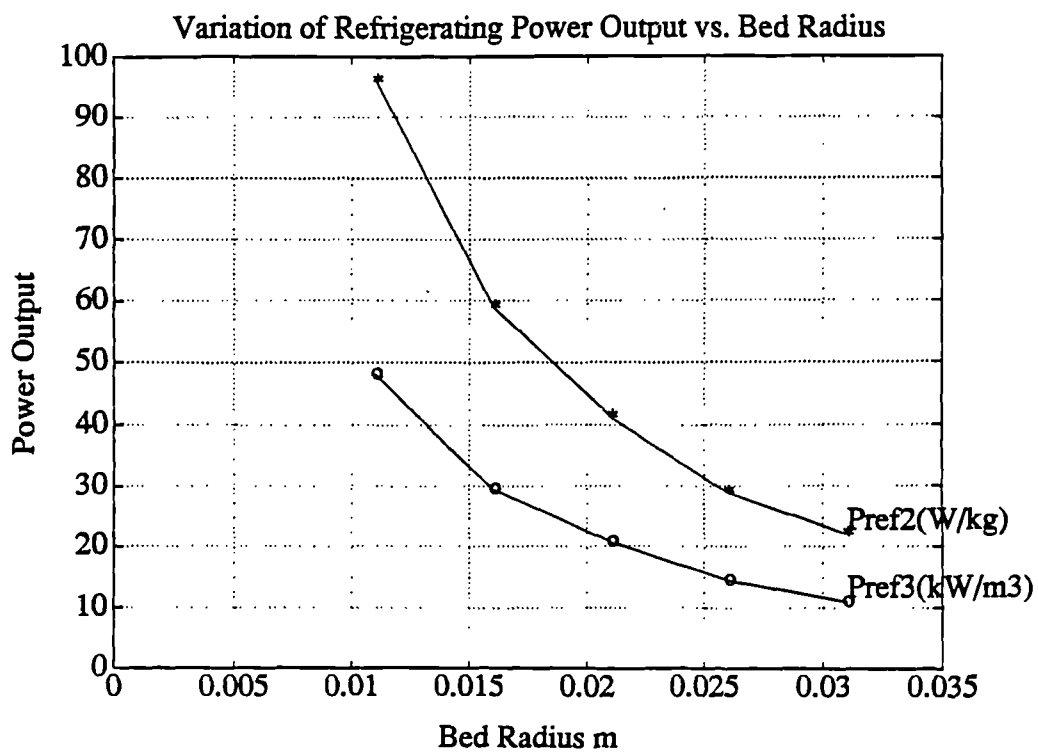Variation of Refrigerating Power Output vs. Bed Radius
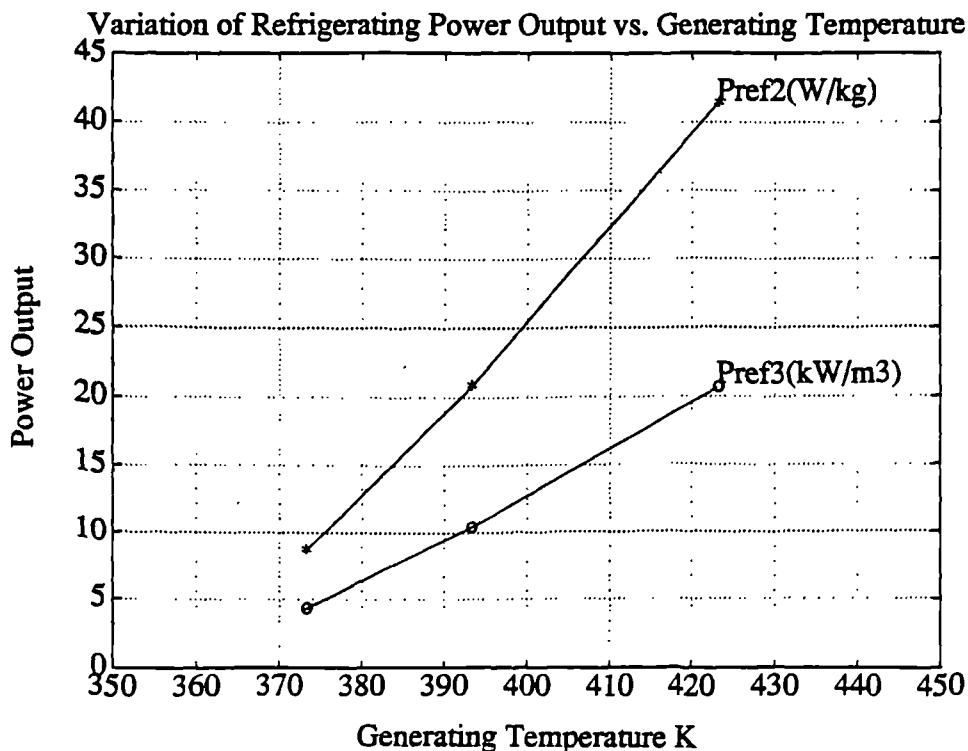
Figure 7.7 on the previous page shows the variation of refrigerating power output with decreasing bed radius. From the graph it is obvious that the smaller the bed radius, the better the power performance and that ideally the reactor should be manufactured with the thinnest beds possible. However, as the bed becomes thinner, the number of beds needed to make a certain reactor volume increases and it may be that the manufacturing costs would become prohibitive. Also, as the bed radius decreases, the COP decreases since proportionally more energy will be lost in the form of sensible heating of the containing vessel.

Reducing the bed radius from 21mm to 11mm increases the power output of the cycle from 20.6 kW/m³ to 48.0 kW/m³. Although this increase is still not enough to make the system comparable to a standard vapour compression cycle, it can clearly be seen that the reactor beds should be made as thin as possible within reason.

Figure 7.8 overleaf shows the variation in power output with packing density. The point at which $\psi=0$ represents the solid case and the data for the three non-solid cases has been generated from the same curve, see figure 6.14, and is valid between the range $0.3 \leq \psi \geq 0.7$. The results are interesting since the power output in W/kg increases as the power output in W/m³ decreases. This may be explained by the fact that in the case of the loose fill bed, $\psi=0.70$, there is a more uniform temperature and concentration in the bed. This being so, the power output per kg of charcoal is high but since there is very little charcoal in the bed in the first place the power output per reactor volume is low.

As the packing becomes more dense the power output increases. Assuming that there are indeed no mass transfer limitations and that the wall to bed heat transfer coefficient is 50 W/m²K as in the base case, the continuous power output of a litre sized solid bed reactor is approximately 40 W.
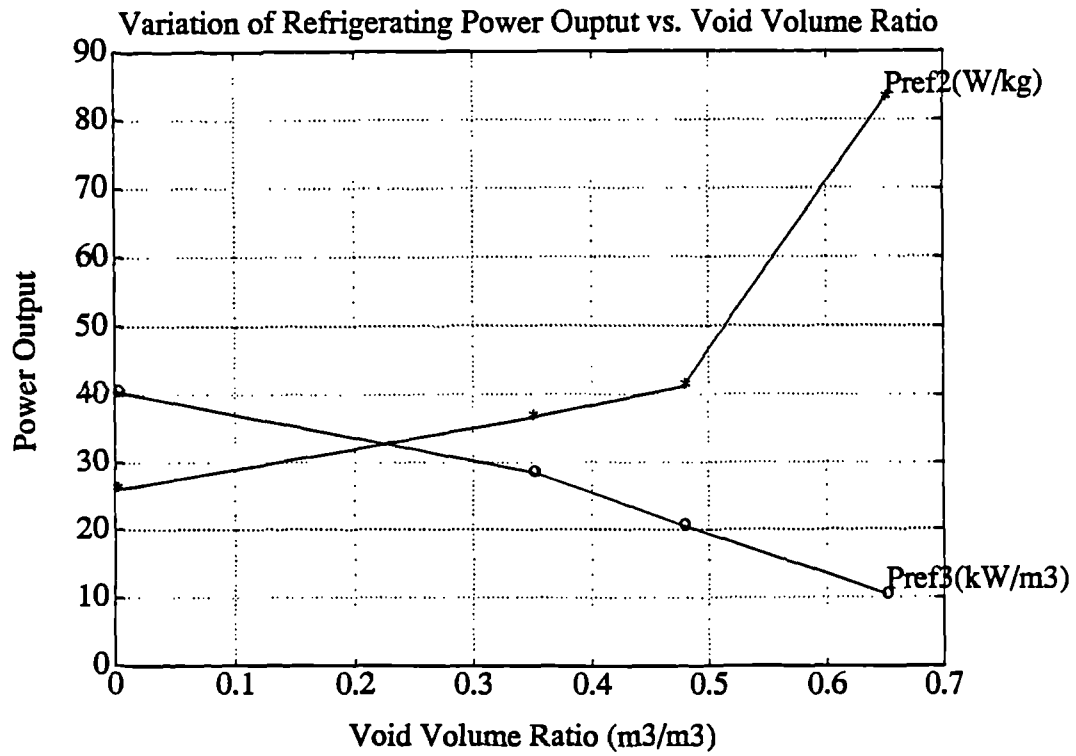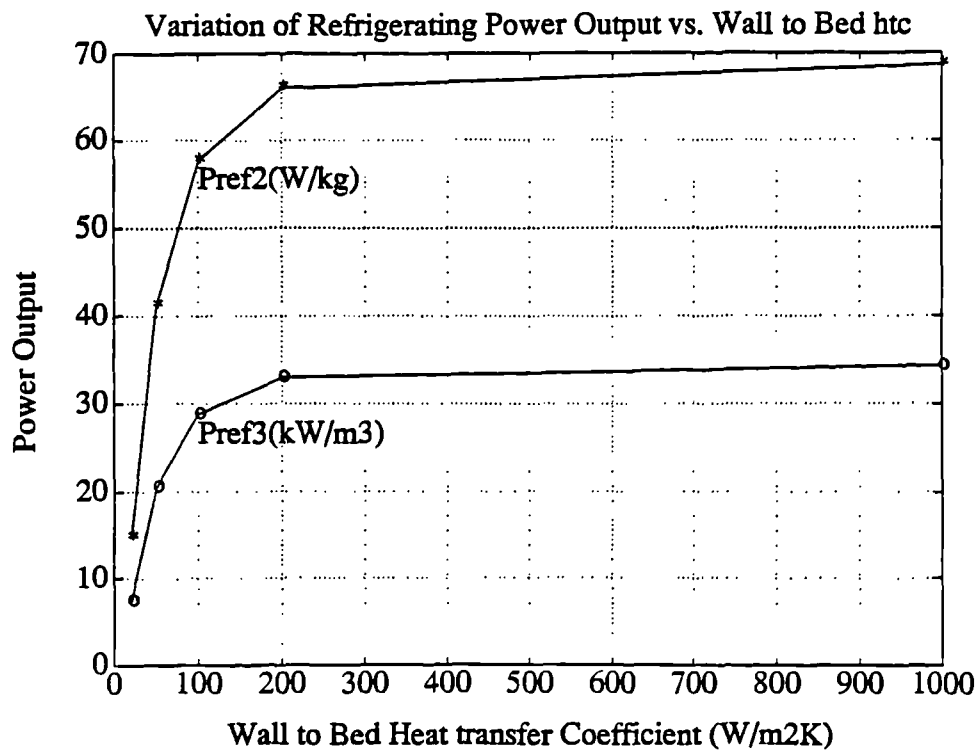
FIGURE 7.8

Variation of Refrigerating Power Ouptut vs. Void Volume Ratio

FIGURE 7.9

Variation of Refrigerating Power Output vs. Wall to Bed htc

Another parameter which has a great effect on the magnitude of the power output of the cycle is the wall to bed heat transfer coefficient, (htc). Figure 7.9 shows the variation of cycle power with the htc ranging from 20 W/m^2K to 1000 W/m^2K with 50 W/m^2K being the base case REF A. This curve is interesting since it shows that the power output continually improves up to a point between 100 $W/m^2K \leq$ htc $\leq 200W/m^2K$, but after this point further increase of the htc does not bring any further benefit. This may be explained by the following theory.

Due to the disturbance of the grain packing at the edge of the bed by the vessel wall, there is gap between the outer grain of the bed and the vessel wall which is filled with gaseous ammonia, see figure 5.15. The thermal resistance of this gap may be equated to a htc as in equation (7.30) below.

$$R = \frac{ln(\frac{r_o}{r_i})}{2\pi L k_g} = \frac{1}{2h_2\pi L r_o} \qquad - (7.30)$$

Where:-

R   Thermal resistance of gap   (K/W)

r_o vessel radius   (m)

$r_o - r_i$ ammonia gap   (m)

L   Axial length of vessel   (m)

k_g Thermal conductivity of ammonia gas   (W/m K)

h_2 Wall to bed htc   (W/m^{2}K)

Rearranging equation (7.30) gives:-

$$ln r_i = ln r_o - \frac{k_g}{h_2 r_o} \qquad - (7.31)$$

Using the conditions for REF A where r_o = 20mm and k_g = 0.02593 W/m K and substituting values for h_2 into equation (7.31) allows us to find the equivalent ammonia gap in each case, see table overleaf.

Wall to Bed htc. h_2(W/m²K)					
	20	50	100	200	1000
r_o–r_i gas gap (mm)	1.26	0.52	0.26	0.13	0.03

It can be seen that the equivalent gas gap is only 1.26 mm in the case when $h_2 = 20$ W/m²K and it would be difficult to make this smaller when packing a coarse grain charcoal. The htc would of course tend to ∞ in the case of the solid charcoal where it is assumed that the bed and vessel could be manufactured in an integral form.

If we consider the thermal resistance due to the heat transfer coefficient R_1 and the thermal resistance of the outer 1 mm of the bed R_2 to be in series, as is the case with the finite difference model, then by equating them we can find the point at which heat transfer becomes limited by the bed conductivity rather than by the wall to bed htc.

$$R_1 = \frac{1}{h_2 r_o 2\pi L} = R_2 = \frac{\ln\frac{(r_o)}{r_i}}{2\pi L k_{BED}} \qquad \text{--- (7.32)}$$

where:-

r_o	outer radius	$= 0.020$ m
r_i	inner radius	$= 0.019$ m
k_{BED}	packed bed conductivity	$= 0.165$ W/m K

Substituting the above values into equation (7.32) gives:-

$$h_2 = 160 \text{W/m}^2\text{K}$$

So when,

$R_1 > R_2$ (i.e $h_2 < 160$ W/m²K) heat transfer is limited by the htc.

and when

$R_1 < R_2$ (i.e $h_2 > 160$ W/m²K) heat transfer is limited by the bed conductivity.

This is borne out by figure 7.9 where increasing the htc to a value above some point between 100 W/m²K and 200 W/m²K does not bring any further improvement to the power output.

Increasing the htc. from the base case to the solid bed case increases the cycle power output from 20 W to 35 W continuous for a litre sized reactor.

From the discussion so far, it can be seen that variation of no one parameter alone can increase the power output to the desired level and it will probably take a combination of these improvements to produce the required effect.

Figure 7.10 overleaf shows the variation of power output with solid beds of different radius where the wall to bed heat transfer coefficient is assumed to be infinitely high. It is assumed that there are no mass transfer limitations although it is envisaged that in the case of the solid bed flow channels would need to be left along which the desorbing gas would travel to reach the condenser. In all solid cases no provision in terms of volume has been made for any gas channels and therefore the values found for the power output per reactor volume will probably be too high. Since the only way to determine to what extent mass transfer does limit the desorption rate is by experiment, no attempt has be made to include it in this model.

Looking at the scale of the power output axis in figure 7.10, it can be seen that power output starts to enter the realms of MW/m³. The effect of making the bed solid and removing h_2 can be found by comparing test cases REF A and REF G. The power output is increased in theses cases from 20.6 kW/m³ to 187.5 kW/m³ which makes the system

FIGURE 7.10

Variation of Refrigerating Power vs. Solid Bed Radius
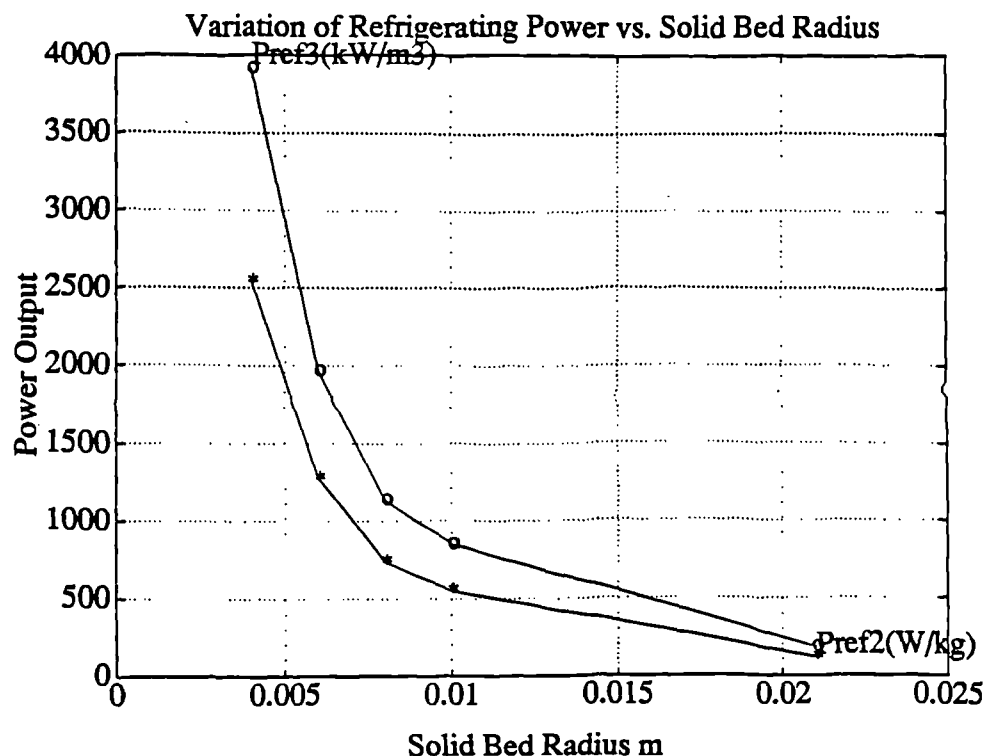
comparable to a standard vapour compression cycle. Even if 50% of the reactor volume needed to be left void for flow channels, this figure is still in range required to make the system viable.

The other points on the curve in figure 7.10 were meant to approximate a large radius two dimensional reactor bed which includes enhanced conductance paths to a small radius one dimensional model. The models have been approximated by assuming that the farthest distance between a hot metal surface and a bed node in the large radius case is equivalent to one dimensional case with bed radius equal to that distance.

The power output values are very high and in the case of an 8 mm solid bed the output per unit volume of reactor is 1.1 MW. These values certainly point the way for further improvement to the cycle, but they would have to be verified by experiment before they could be used in any serious calculation.

7.5 Conclusions

The transient heat transfer mechanisms involved in the adsorption refrigerating or heat pumping cycle have been successfully modelled using a one dimensional finite difference model which is solved using a Crank Nicholson scheme.

The results of cycle simulations show that the continuous power output of an idealized cycle using 208C charcoal and ammonia and operating under standard conditions produces a power output in the order of 20 W continuous per litre volume of reactor. This compares to the power output of a standard vapour compression cycle for a domestic sized larder refrigerator of 40 W continuous.

The effect on power output of varying the generating temperature T_{g2}, the bed radius, the gas void ratio ψ and the wall to bed heat transfer coefficient is examined. The results show that it requires simultaneous optimization of all four of these parameters to produce a cycle power output which makes the adsorption system comparable to a standard system.

The results also show that in the case of small radius solid beds that the power output of the cycle is in the order of MW/m^3 of reactor assuming no mass transfer limitations.

Further experiment needs to be undertaken to determine to what extent mass transfer limits the desorption rate and to investigate the effectiveness of putting flow channels in the reactor as a path for the desorbing gas to reach to condenser.

The cycle simulations show that the only reactor which has a power output high enough to make the system feasible is that of a small radius solid reactor or a large radius solid reactor which incorporated path of enhanced conductance. It is recommended that further work should include the manufacture of a solid reactor which is integral with its containing vessel.

References

1. Barrer R M

"Zeolites and Clay Minerals as Sorbents and Molecular Sieves." Academic Press, New York 1978

2. Ruthven D M, Lee Lapkeung

"Kinetics of Nonisothermal Sorption System with Bed Diffusion Control" AICh E Journal. Vol 27. No 4. 1981. pp 654-663

3. Rajnak P, Ilavsky J

"Mathematical and Experimantal Modelling of Adsorption in Fixed Beds. I.Mathematical Model Development and Numerical Investigation of Non Isothermal Solute Adsorption." Adsorption Science and Technology. Vol 3. 1986. pp 233-244

4. Sun L M, Meunier F, Mischler B

"Etude des Distributions de Temperature et de Concentration à l'interieur d'un Grain Spherique d'adsorbant Solide Soumis a un Echelon de Pression de Vapeur Adsorbable." International Journal of Heat and Mass Transfer. Vol 29. 1986. pp 1393-1406

5. Udell Kent S

"Heat Transfer in Porous Media Considering Phase Change and Capillarity - The Heat pipe Effect" International Journal of Heat and Mass Transfer. Vol 28. No 2. 1985. pp 485-495

6. Shelton S V, Wepfer W J, Miles D J

"External Fluid Heating of a Porous Bed" Chemical Engineering Communications. Vol 71. 1988. pp 39-52.

7. Aittomaki A, Harkonen M

"Modelling of Zeolite/Methanol Adsorption Heat Pump Process." Heat Recovery Systems and CHP. Vol 5. 1988. pp 475-482

8. Guilleminot JJ, Meunier F, Pakleza J

"Heat and Mass Transfer in a Non-Isothermal Fixed Bed Solid Adsorbent Reactor. A Uniform Pressure - Non-uniform Temperature Case." International Journal of Heat and Mass Transfer. Vol 30. 1987. pp 1595-1606

9. Dosset D

"Future Influences on Energy Consumption in Household Refrigerators" Energy Management. AUG 1989. pp23-30

8. OVERALL CONCLUSIONS AND RECOMMENDATIONS FOR FURTHER WORK.

Conclusions

This work has studied and evaluated the three areas in which there is potential for improvement to the ammonia-charcoal adsorption cycle, these are :-

(i) cycle thermodynamics

(ii) ammonia-charcoal porosity characteristics

(iii) heat transfer properties of an ammonia-charcoal packed granular bed.

In order to make an ammonia charcoal adsorption cycle economically viable we must reduce both the capital cost of the plant and the running cost. The running cost is lowered by having as high a COP or COA as possible. The capital cost is lowered either by increasing the useful energy per cycle or by reducing the cycle time. The first of these is achieved by improving the adsorbent porosity characteristics and the second by improving the heat transfer through the adsorbent bed.

As discussed in Section 2, the COP or COA may be increased either by improving the charcoal porosity characteristics or by using more advanced thermodynamic cycles. Through the use of models it was found that varying the charcoal porosity between realistic limits only produced an increase of $\approx 50\%$ in the COP and an increase of $\approx 10\%$ in the COA. Far greater gains were made by the use of multiple bed cycles. Looking at a cycle operating within the temperature limits set in Section 7 reveals the the COP ,may be improved by $\approx 90\%$ by using a dual bed cycle and by $\approx 250\%$ using an infinitely regenerative cycle. Similarly, the COA can be increased by $\approx 25\%$ by using a dual bed

cycle and by ≈ 110 % by using an infinitely regenerative cycle. Unfortunately, increasing the number of beds will have the effect of increasing the capital cost of the system and the importance of a high COP or COA will depend upon the cost of the supply energy.

As we have already mentioned, the capital cost of the system may be lowered by improving the charcoal porosity characteristics. This has been dealt with in Section 3 where the charcoal has been assessed in terms of a figure of merit. The figure of merit corresponds to the amount of useful energy obtained from one adsorption cycle and it was found that the two charcoals AX21 and AX31 offered an improvement of about 100% over the base case charcoal 208C. This means that a reactor using AX21 or AX31 would only need to be half the size of a reactor using 208C and this would reduce capital cost considerably. The cost of these charcoals however is four times that of 208C and it would be decision of the designer which charcoal to use for a certain system.

The set of experiments involving surface modifications to charcoals was found to be very difficult to analyze due to the non-uniform nature of the starting material, overall it did not appear to be very effective.

Finally the capital costs may be lowered by increasing the thermal conductivity of the reactor, thus reducing the cycle time and increasing the power output. The lower the cycle time the smaller the size of reactor required. In order to find the cycle time it was first necessary to find the thermal conductivity of an ammonia charcoal packed granular bed and to model it. The thermal conductivity was measured using the apparatus described in Section 5 and was modelled using the Zehner- Bauer model modified to include the adsorbed phase, see Section 4. It was found that an average value of 0.165 W/m K could be used with reasonable accuracy to represent the thermal conductivity of an ammonia charcoal packed bed over its concentration range.

The cycle time and power output of a reactor operating under idealized conditions was found by using a dynamic finite difference model of a desorbing reactor outlined in

Section 7. The results showed that in order to increase the power output of the cycle to a reasonable level a number of improvements have to be made. Ideally, the reactor bed should be constructed from solid charcoal pieces with as small a radius as is feasible and which are integral with the container wall thus eliminating any thermal resistance between the container wall and the bed. If such a charcoal bed could be manufactured, the power output (per m^3) of the cycle could be increased from the base case value of 20 kW/m^3 to 187 kW/m^3 in the case of a 21mm radius bed. If the radius of a solid bed is reduced further, the power output starts increase to the order of MW/m^3.

As a final conclusion, it can be said that although there is scope for improving the COP or COA of the cycle, it is achieved at the expense of raising the capital cost of the system. By far the greatest gains to be had in terms of reducing capital cost are from improvements to the heat transfer through the reactor bed.

Recommendations for Further Work.

The research undertaken by the author into the areas of cycle thermodynamics, charcoal porosity and heat transfer characteristics, has shown that by far the area which holds the greatest scope for improvement is the heat transfer properties of the adsorber. Therefore, it is recommended that future work should be guided by the aim of improving the power output of the cycle.

Following on from this work, research is continuing at Warwick University into the design and build of a rapid cycling ammonia charcoal adsorption unit containing solid charcoal beds. This research will include an investigation into the possible mass transfer limitations of a solid reactor and should tackle the problems of enhanced paths of con- ductance and interfacing between the bed and the containing vessel wall.

In addition, research is also being carried out into a novel adsorption cycle which uses forced convection to overcome the heat transfer problem.

Both rapid cycling machines and forced convection machines are conceptual and both offer advantages and disadvantages. It is hoped that both types of machines will be built and evaluated at this university in the near future.

APPENDICES

Appendix 2a

Troutons Rule.

The differential form of the Clausius-Clapeyron equation exists as:-

$$\frac{d(\ln p)}{dT} = -\frac{Le}{R} T^2$$

If the latent heat of vapourization (Le) is assumed to be independent of temperature then:-

$$\ln p_2 - \ln p_1 = \frac{Le}{R} \left(\frac{1}{T_1} - \frac{1}{T_2}\right)$$

If the end state 1 is the boiling temperature of the substance at one atmosphere then:-

$$\ln p_2 = \frac{Le}{R} \left(\frac{1}{T_b} - \frac{1}{T_2}\right)$$

The empirically derived equation known as Trouton's Law states that for all substances the ratio of the latent heat to the boiling point at one atmosphere is a constant.

$$\frac{Le}{T_b} = k = 22$$

Substituting this into the previous equation gives,

$$\ln p = \frac{k}{R} \left(1 - \frac{T_b}{T_2}\right)$$

As $-1/T_2 \to \infty$ $\ln p \to k/R$

This indicates that the isosteres will all meet at a single point and when represented on a ln p -1/T diagram would look as shown below
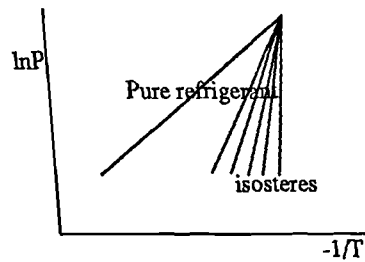
Appendix 2b.

Measurement of the Specific Heat of Charcoal 208C.

The specific heat of 208C charcoal was measured at NPL using a scanning differential calorimeter. Curve fitting to the graph below produces the straight line equation

$$Cp_c = 0.175 + 2.245 \times 10^{-3} T$$
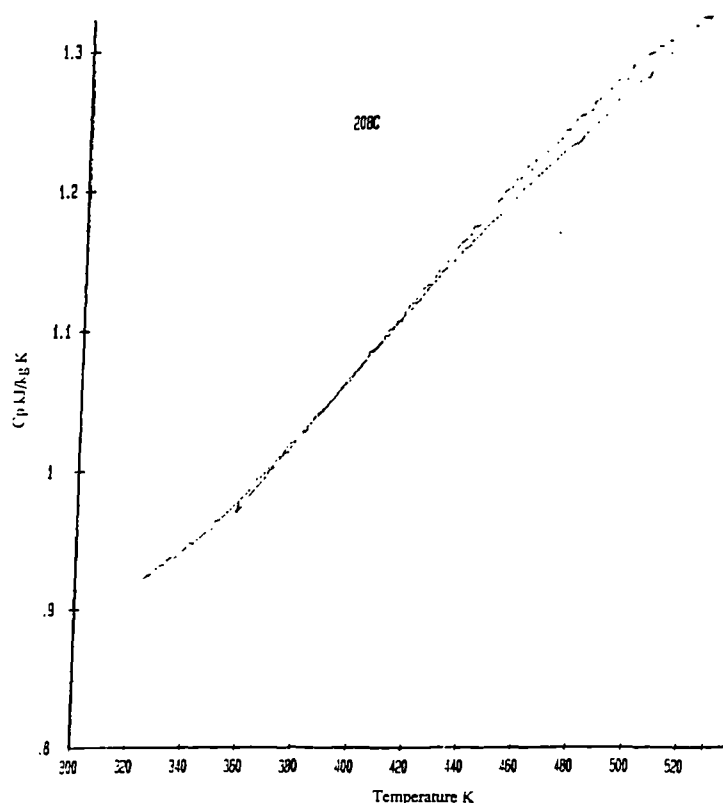
Appendix 2c.

Derivation of the Clausius Clapeyron Equation.

Consider a liquid in equilibrium with its vapour at a pressure p and temperature T. If some of the liquid is vapourized reversibly at T then the change of free energy of the system is zero since it is in equilibrium. Let G_1 and G_2 be the free energies of one mole of liquid and one mole of vapour respectively. Then

$$G_1 = G_2 \quad —(i)$$

If the temperature is raised to T+ΔT, then the pressure will increase to p+Δp in order to

preserve equilibrium. The free energies of the species will now be

$$G_1 + dG_1 = G_2 + dG_2 \quad —(ii)$$

Combining (i) and (ii) gives

$$dG_1 = dG_2$$

Now

$$G_1 = U_1 + p_1\, dV_1 - T_1\, dS_1$$

or

$$dG_1 = dU_1 + p_1\, dV_1 + V_1\, dp_1 - T_1\, dS_1 - S_1\, dT_1$$

for a reversible process

$$dU_1 + dw_1 = dq_1 = T_1\, dS_1$$

$$dU_1 = T_1\, dS_1 - dw_1 = T_1\, dS_1 - p_1\, dV_1$$

So, it follows that

$$dG_1 = V_1\, dp_1 - S_1\, dT_1$$

$$dG_2 = V_2\, dp_2 - S_2\, dT_2$$

Hence at equilibrium

$$V_1\, dp_1 - S_1\, dT_1 = V_2\, dp_2 - S_2\, dT_2$$

Since the liquid and vapour are at the same temperature

$$T = T_1 = T_2 \text{ and } p = p_1 = p_2$$

Hence

$$V_1\, dp - S_1\, dT = V_2\, dp - S_2\, dT$$

$$(V_1 - V_2)\, dp = (S_1 - S_2)\, dT$$

$$\frac{dp}{dT} = \frac{S_1 - S_2}{V_1 - V_2}$$

Now

$$S_1 - S_2 = \frac{Le}{T}$$

therefore:-

$$\frac{dp}{dT} = \frac{Le}{T(V_1 - V_2)}$$

If the temperature of the substance is not near the critical point then the volume of the gaseous phase can be considered to be very much larger than the volume of the liquid phase and the above equation approximates to

$$\frac{dP}{dT} = \frac{Le}{T} V_2$$

And if the vapour phase behaves as a perfect gas then

$$V_2 = R \frac{T}{p}$$

$$\frac{dp}{p\, dT} = \frac{dT}{R\, T^2} Le$$
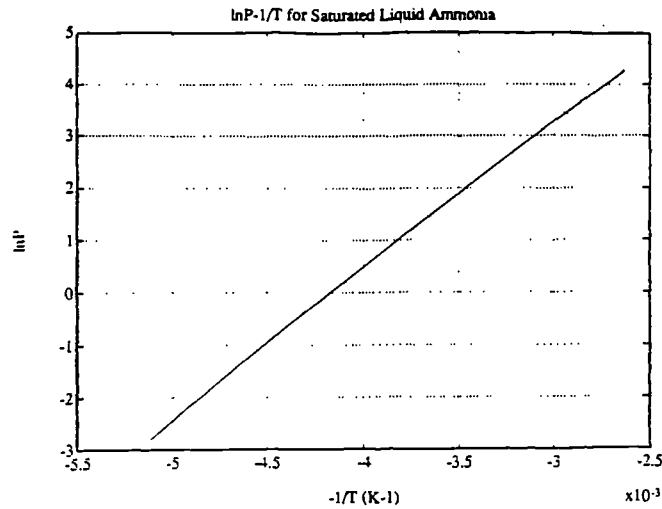
But

$$\frac{d}{dp}(\ln p) = \frac{1}{p}$$

And

$$d\ln p = \frac{dT}{RT^2} Le$$

If the latent heat is constant with respect to T, then on integrating the above equation we obtain

$$\ln \frac{p_2}{p_1} = \frac{Le}{R} \left(\frac{1}{T_1} - \frac{1}{T_2} \right)$$

Appendix 2d.

Relationship between ln P-1/T for Saturated Liquid Ammonia.

lnP-1/T for Saturated Liquid Ammonia

Curve fitting to the graph above [38] produces the straight line fit

$$\ln P = -2823.4/T_{sat} + 11.749$$

Appendix 2e.

Specific heat at Constant Pressure of Ammonia Gas.

The graph below shows values of specific heat of ammonia gas [39,40]. For processes taking place at the condensing pressure the average value of $Cp_{ag(T)} = 2.8$ kJ/kg K. For processes taking place at Pe an average value of 2.5 kJ/kg K is used.

Specific Heat at Constant Pressure for Ammonia Gas.

30Bar Ref**

10Bar Ref**

5Bar Ref**

1Bar Ref*

1Bar Ref**
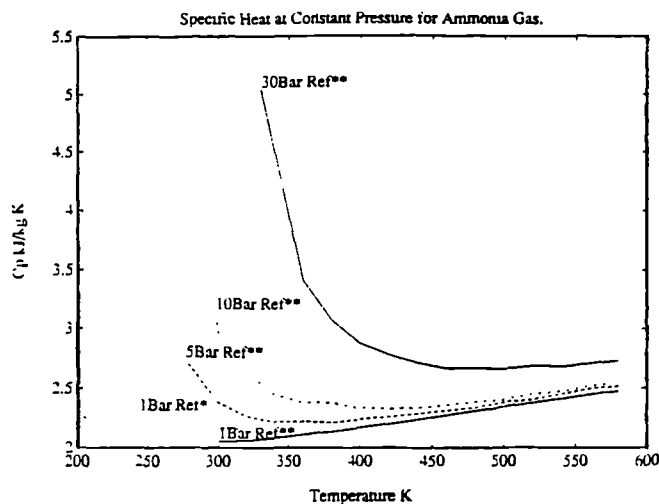
**--[39]

*--[40]

Appendix 2f.

Specific Heat at Constant Pressure of Saturated Liquid Ammonia.

Data taken from reference source [41] is approximated to the straight line fit.

$$Cvf_{(T)} = -4.1 \times 10^{-3} + 4.083$$

Specific Heat at Constant Volume of Saturated Liquid Ammonia
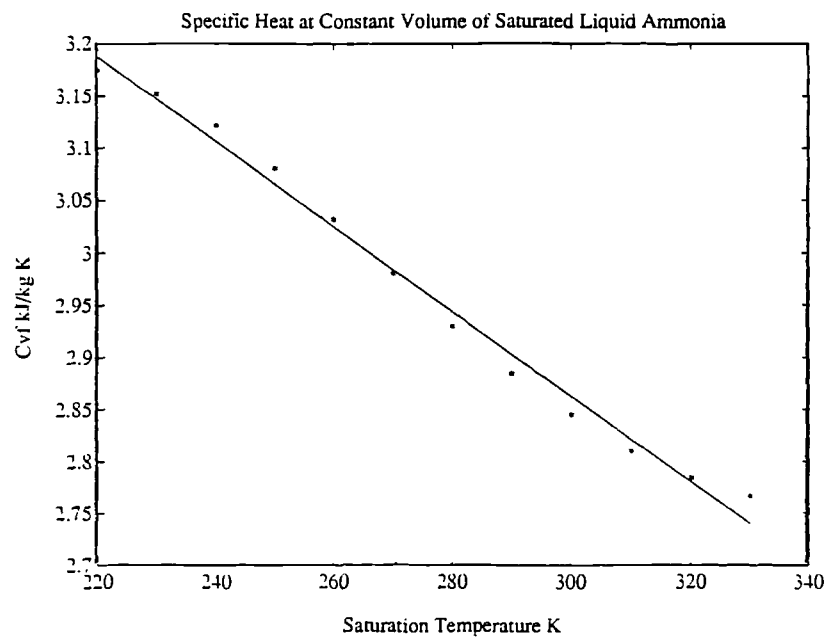
Appendix 3a

Derivation of the Modified D-R Equation.

Equation (3.6) in Section 3.2 shows the DR equation in terms of the system and adsorbate saturation pressures, p and p_{sat} respectively.

If we look at the lnp vs. 1/T plot shown below, it can be seen that these pressures may alternatively be represanted as temperatures.
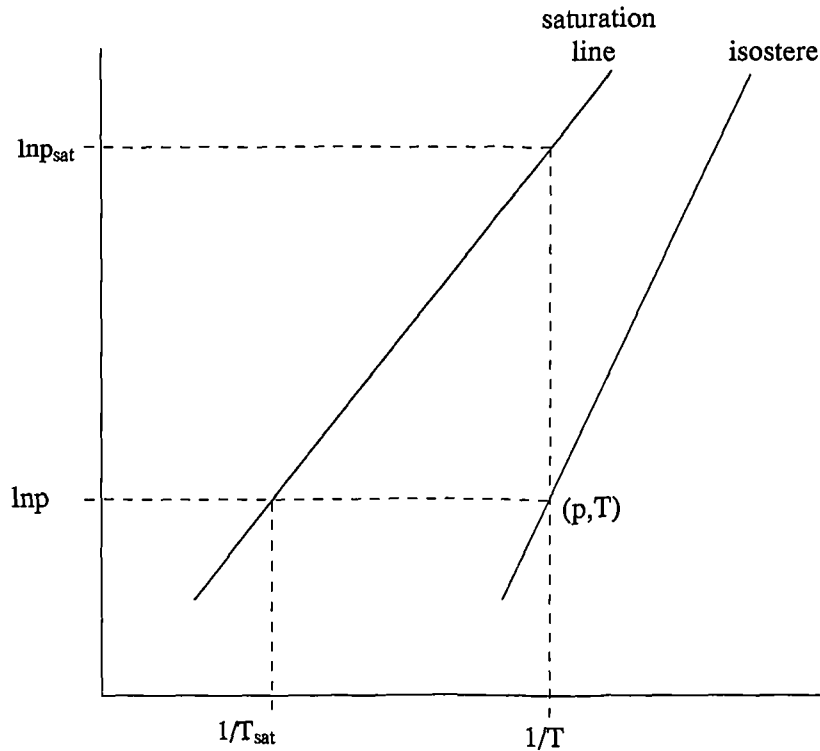
If the system pressure and temperature are p and T, then moving across an isobar to the the saturation line shows that

$$\ln p = A - \frac{C}{T_{sat}}$$

and moving along an isotherm to the saturation curve shows that

$$\ln p_{sat} = A - \frac{C}{T}$$

Substituting these equations for p and p_{sat} into equation (3.6) will lead to the final form of the D-R equation (3.8).

Appendix 4a

Radiant Heat Transfer Between Two Parallel Grey Plates.

If radiative heat exchange occurs between two parallel grey plates, some of the radiation impinging on the surface is absorbed and some of it is reflected, see diagram below.
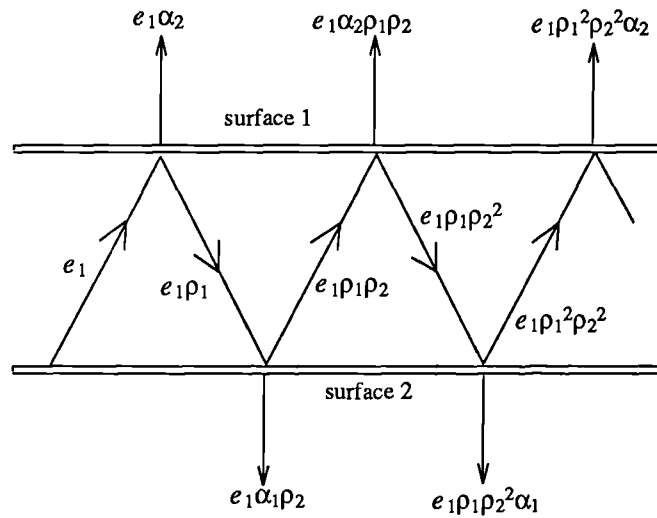
Radiant Heat Exchange Between Two Parallel plates [13]

where:-

α absorptivity

ρ reflectivity

e_1 incident energy

$_1$ $_2$ subscripts surface 1,2

The heat flow which leaves surface 1 per unit area is given by:-

$$q_{12} = (1 - \alpha_1\rho_2 - \alpha_1\rho_2\rho_2^2 - \alpha_1\rho_2^2\rho_2^3)e_1$$

$$= [1 - \alpha_1\rho_2(1 + \rho_1\rho_2 + \rho_1^2\rho_2^2)]e_1$$

The sum of the series in the parentheses is :-

$$\frac{1}{1 - \rho_1\rho_2}$$

therefore

$$q_{12} = (1 - \frac{\alpha \rho_2}{1 - \rho_1 \rho_2}) e_1$$

Replacing the absorptivities and reflectivities by the emissivities of the two surfaces gives:-

$$q_{12} = [1 - \varepsilon_1 \frac{(1 - \varepsilon_2)}{\varepsilon_1 + \varepsilon_2 - \varepsilon_1 \varepsilon_2}] e_1 = [\frac{\varepsilon_2}{\varepsilon_1 + \varepsilon_2 - \varepsilon_1 \varepsilon_2}] e_1$$

Surface 2 emits radiation of emissive power e_2. The amount $\alpha_1 e_2$ is absorbed by surface 1. The total radiation given off by surface 2 which is absorbed by surface 1 after successive reflections is :-

$$q_{21} = \alpha_1 (1 + \rho_1 \rho_2 + \rho_1^2 \rho_2^2 + \ldots \ldots) e_2$$

Summing the series and introducing the emissivity as before gives

$$q_{21} = [\frac{\varepsilon_1}{\varepsilon_1 + \varepsilon_2 - \varepsilon_1 \varepsilon_2}] e_2$$

The net heat flow which leaves surface 1 during radiant heat exchange is

$$q = q_{12} - q_{21} = \frac{\varepsilon_2 e_1 - \varepsilon_1 e_2}{\varepsilon_1 + \varepsilon_2 - \varepsilon_1 \varepsilon_2}$$

The radiant emission from surfaces 1 & 2 respectively is given by :-

$$e_1 = \varepsilon_1 \, Cs \times 10^8 \, T_1^4$$

$$e_2 = \varepsilon_2 \, Cs \times 10^8 \, T_2^4$$

therefore

$$q = \frac{Cs \times 10^8}{\frac{1}{\varepsilon_1} + \frac{1}{\varepsilon_2} - 1} (T_1^4 - T_2^4)$$

In our case $\varepsilon_1 = \varepsilon_2$, so

$$q = \frac{Cs \times 10^8}{\frac{2}{\varepsilon} - 1} (T_1^4 - T_2^4)$$

Heat conducted per unit area q is also equal to

$$q = \frac{\lambda_R (T_1 - T_2)}{x_R}$$

Substituting this into the previous equation and expanding the brackets gives

$$\lambda_R = \frac{Cs \times 10^8 \, x_R}{\frac{2}{\varepsilon} - 1} \frac{(T_1{}^2 + T_2{}^2)(T_1 + T_2)(T_1 - T_2)}{(T_1 - T_2)}$$

if $T_1 - T_2$ is small then $T_1 \approx T_2$ and

$$\lambda_R = \frac{Cs \times 10^8 x_R}{\frac{2}{\varepsilon} - 1} (2T^2) \, (2T)$$

$$\frac{\lambda_R}{\lambda} = \frac{0.04 \, Cs}{(\frac{2}{\varepsilon} - 1)\lambda} (\frac{T}{100})^3 \, x_R \qquad - (4.13)\text{Chap4.1}$$

Appendix 4b

Derivation of Knudsen Effect Conductivity λ_D.

When the space in which a molecule is moving becomes comparable to the characteristic dimension of the heat transfer surfaces, it can no longer be assumed that the temperature of the gas immediately next to the surface is at the same temperature as the surface.

Consider two parallel infinite plates. Normal heat transfer through the gas produces a linear temperature profile. In cases where $\sigma > L$ there appears to be a temperature jump at the wall, see fig below.
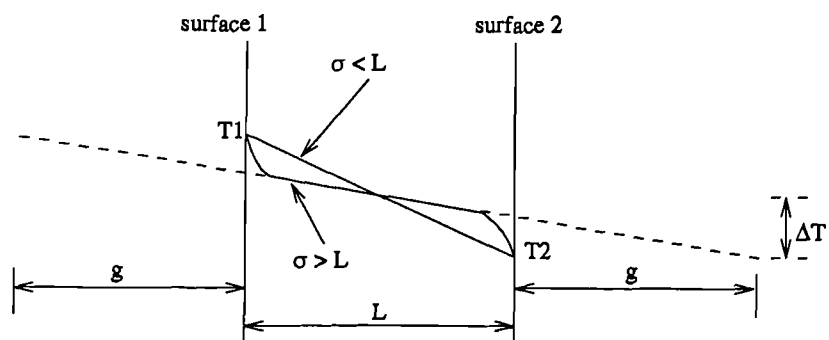
Extrapolating the straight portion of the curve $\sigma > L$ back to the wall surface produces a temperature jump of ΔT.

$$\frac{q}{A} = \frac{\lambda\,(T_1 - T_2)}{g + L + g} = \frac{\lambda\,\Delta T}{g} \qquad —(b\,1)$$

The temperature jump at the wall will depend on the type of gas and the surface material and finish, and is defined by the accommodation coefficient γ where:-

$$\gamma = \frac{E_i - E_r}{E_i - E_w}$$

E Energy

i - incident   :   r - reflected   :   w - wall

The value of γ must be determined experimentally.

Using the statistical thermodynamics from ref [15] it was found that

$$g = (\frac{2 - \gamma}{\gamma})\,\sigma$$

Equation (b1) may also be expressed in terms of the Knudsen conductivity :-

$$\frac{q}{A} = \frac{\lambda\,(T_1 - T_2)}{L + 2g} = \lambda_D\,\frac{(T_1 - T_2)}{L}$$

therefore

$$\frac{\lambda}{\lambda_D} = \frac{L + 2g}{L}$$

$$= \frac{L + 2(\frac{2 - \gamma}{\gamma})\sigma}{L}$$

$$\frac{\lambda}{\lambda_D} = 1 + 2\frac{\sigma}{L}(\frac{2}{\gamma} - 1) \qquad — (4.14)\text{Chap4.1}$$

where :-

$L = s$ if λ_D is based on the pore depth

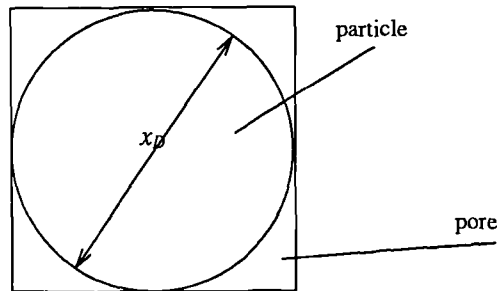$L = x_D$ if λ_D is based on the characteristic dimension of the particle.

Appendix 4c

The approximation of the ratio pore depth to particle diameter [10].

The cross sectional of the pore F_p shown in the diagram below may be approximated by the equation

$$F_p = [1 - \sqrt{1 - \psi}]x_D{}^2$$

Making the assumption that the pore depth s is statistically equal in all three dimensions then :-

$$s = x_D \sqrt{1 - \sqrt{1 - \psi}}$$

If the porosity is not too small, then the above equation can be simplified to :-

$$s = \psi x_D$$

$$\frac{s}{x_D} = \psi \qquad \text{— (4.18)}$$

Appendix 4d.

Derivation of λ'.

λ' is the equivalent fluid conductivity in the mixed bed region due to radiation and gas conduction with pressure effect.

Equivalent Radiation Conductivity

The equation for radiation between two parallel grey plates may be used but with a correction for area due to the non-parallel nature of the particle surfaces. The diagram below shows a section of the mixed phase region of the unit cell.

Annular Element
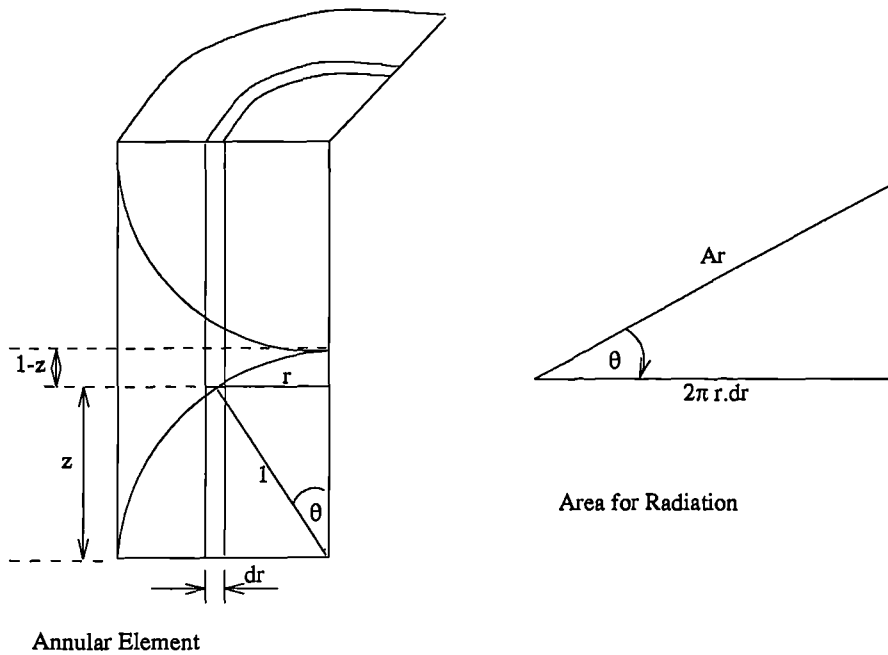
Area for Radiation

Taking the small annular element shown for the area for conduction A_c,

$$A_c = 2\pi r.dr$$

Also,

$$\cos\theta = z$$

The area for radiation A_r

$$A_r = \frac{2\pi r.dr}{Cos\theta} = \frac{2\pi r.dr}{z}$$

Equating the radiation and conduction equations gives

$$(T_1 - T_2)\frac{A_c}{1-z}\lambda_{R2} = A_r \frac{Cs \times 10^8}{(\frac{2}{\epsilon}-1)}(T_1^4 - T_2^4)$$

$$\frac{2\pi r.dr}{1-z}\lambda_{R2} = \frac{2\pi r.dr}{z}\frac{0.04\,Cs}{(\frac{2}{\epsilon}-1)}(\frac{T}{100})^3$$

$$\lambda_{R2} = \frac{1-z}{z}\frac{0.04\,Cs}{(\frac{2}{\epsilon}-1)}(\frac{T}{100})^3$$

$$\frac{\lambda_{R2}}{\lambda} = \frac{\lambda_R}{\lambda}\frac{1-z}{z}$$

Equivalent gas conductivity:

$$\frac{\lambda}{\lambda_{D2}} = 1 + \frac{2\sigma}{1-z}(\frac{2-\gamma}{\gamma}) = \frac{\frac{\lambda}{\lambda_D}-1}{(1-z)} + 1$$

Now

$$\lambda' = \lambda_R + \lambda_D$$

which gives:-

$$\frac{\lambda'}{\lambda} = \frac{\lambda_R}{\lambda}(\frac{1-z}{z}) + \frac{1}{1 + \frac{(\frac{\lambda}{\lambda_D}-1)}{1-z}} \qquad \text{— (4.27)}$$

Appendix 4e

Derivation of Equation (4.28)

$$r^2 + \frac{z^2}{(B-(B-1)z)^2} = 1 \qquad \text{— (4.4)}$$

let

$$W = \frac{z^2}{(B -(B-1)z)^2}$$

$$\frac{dW}{dz} = \frac{z^2.2(B-1)}{(B-(B-1)z)^3} + \frac{2z}{(B-(B-1)z)^2}$$

$$\frac{dr}{dW} = \frac{-1}{2}[1-W]^{\frac{-1}{2}}$$

$$\frac{dr}{dz} = \frac{-1}{2}\Big[1 - \frac{z^2}{(B-(B-1)z)^2}\Big]^{\frac{-1}{2}} \Big(\frac{z^2.2(B-1)}{(B-(B-1)z)^3} + \frac{2z}{(B-(B-1)z)^2}\Big)$$

$$\frac{dr}{dz} = \frac{-1}{r}\Big(\frac{z^2(B-1)+z(B-(B-1)z)}{(B-(B-1)z)^3}\Big)$$

$$r.dr = \frac{-Bz}{(B-(B-1)z)^3}.dz \qquad - (4.28)$$

Appendix 4f

Derivation of Integral Equation (4.29)

$$\frac{\lambda_{so**}}{\lambda} = \frac{1}{(1-z)\frac{\lambda}{\lambda'} + \frac{\lambda}{\lambda_s}(z)} \qquad - (4.26a)$$

$$\frac{\lambda}{\lambda'} = \frac{z(\frac{\lambda}{\lambda_D}-z)}{(1-z)z + (1-z)(\frac{\lambda}{\lambda_D}-z)\frac{\lambda_R}{\lambda}}$$

$$\frac{\lambda_{so**}}{\lambda} = \frac{1}{\frac{(1-z)z(\frac{\lambda}{\lambda_D}-z)}{(1-z)z+(1-z)(\frac{\lambda}{\lambda_D}-z)\frac{\lambda_R}{\lambda}} + z\frac{\lambda}{\lambda_s}}$$

$$= \frac{\lambda_s(z + (\frac{\lambda}{\lambda_D}-z)\frac{\lambda_R}{\lambda})}{\lambda_s z(\frac{\lambda}{\lambda_D}-z) + z\lambda(z + (\frac{\lambda}{\lambda_D}-z)\frac{\lambda_R}{\lambda})}$$

$$= \frac{z(\lambda_s - \lambda_s\frac{\lambda_R}{\lambda}) + \lambda_s\frac{\lambda_R}{\lambda}\frac{\lambda}{\lambda_D}}{z^2(\lambda - \lambda\frac{\lambda_R}{\lambda} - \lambda_s) + z(\lambda_s(\frac{\lambda}{\lambda_D}-1) + \lambda_s + \lambda\frac{\lambda_R}{\lambda} + \frac{\lambda_R}{\lambda}\lambda(\frac{\lambda}{\lambda_D}-1))}$$

dividing top and bottom by λ_s gives:-

$$\frac{\lambda_{so^{**}}}{\lambda} = \frac{z(1 - \frac{\lambda_R}{\lambda}) + \frac{\lambda_R}{\lambda}\frac{\lambda}{\lambda_D}}{z^2(\frac{\lambda}{\lambda_s} - \frac{\lambda}{\lambda_s}\frac{\lambda_R}{\lambda} - 1) + z(1 + \frac{\lambda_R}{\lambda}\frac{\lambda}{\lambda_s})\frac{\lambda}{\lambda_D}}$$

and

$$\frac{\lambda_{so^{**}}}{\lambda}r.dr = \frac{-\left(z(1 - \frac{\lambda_R}{\lambda}) + (\frac{\lambda_R}{\lambda}\frac{\lambda}{\lambda_D})\right)B}{\left(z(\frac{\lambda}{\lambda_s} - \frac{\lambda_R}{\lambda}\frac{\lambda}{\lambda_s} - 1) + (1 + \frac{\lambda_R}{\lambda}\frac{\lambda}{\lambda_s})\frac{\lambda}{\lambda_D}\right)(B - (B-1)z)^3}.dz$$

Appendix 4g

Integrating Equation (4.29)

Following on from equation (4.30) we may write :-

$$z(1 - \frac{\lambda_R}{\lambda}) + \frac{\lambda_R}{\lambda}\frac{\lambda}{\lambda_D} = S(B - (B-1)z)^3 + T(z(\frac{\lambda}{\lambda_s} - \frac{\lambda}{\lambda_s}\frac{\lambda_R}{\lambda} - 1) + N) +$$

$$U(z(\frac{\lambda}{\lambda_s} - \frac{\lambda}{\lambda_s}\frac{\lambda_R}{\lambda} - 1) + N)(B - (B-1)z) + V(z(\frac{\lambda}{\lambda_s} - \frac{\lambda}{\lambda_s}\frac{\lambda_R}{\lambda} - 1) + N)(B - (B-1)z)^2 \qquad —(g0)$$

when z = 0 the above equation (g0) becomes

$$\frac{\lambda_R}{\lambda}\frac{\lambda}{\lambda_D} = SB^3 + TN + UNB + VNB^2 \qquad —(g1)$$

when $z = \frac{B}{B-1}$ equation (g0) becomes

$$\frac{B}{(B-1)}(1 - \frac{\lambda_R}{\lambda}) + \frac{\lambda_R}{\lambda}\frac{\lambda}{\lambda_D} = T(\frac{B}{B-1}(\frac{\lambda}{\lambda_s} - \frac{\lambda_R}{\lambda}\frac{\lambda}{\lambda_D} - 1) + N) \qquad —(g2)$$

when $z = \dfrac{-N}{\frac{\lambda}{\lambda_s} - \frac{\lambda}{\lambda_s}\frac{\lambda_R}{\lambda} - 1}$ equation (g0) becomes

$$\frac{-N(1-\frac{\lambda_R}{\lambda})}{\frac{\lambda}{\lambda_s} - \frac{\lambda}{\lambda_s}\frac{\lambda_R}{\lambda} - 1} + \frac{\lambda_R}{\lambda}\frac{\lambda}{\lambda_D} = S\left(B + \frac{(B-1)N}{\frac{\lambda}{\lambda_s} - \frac{\lambda}{\lambda_s}\frac{\lambda_R}{\lambda} - 1}\right)^3 \quad -(g\,3)$$

when z = 1 equation (g0) becomes

$$1 + (\frac{\lambda}{\lambda_D} - 1)\frac{\lambda_R}{\lambda} = S + (T + U + V)(\frac{\lambda}{\lambda_s} - \frac{\lambda}{\lambda_s}\frac{\lambda_R}{\lambda} - 1 + N) \quad -(g\,4)$$

Also

$$\frac{\lambda}{\lambda_s} - \frac{\lambda}{\lambda_s}\frac{\lambda_R}{\lambda} - 1 = \frac{M - NB}{B}$$

Taking equation (g2) first, expanding brackets and substituting M & N into the equation gives

$$B + (\frac{\lambda}{\lambda_D} - 1)\frac{\lambda_R}{\lambda}B - \frac{\lambda_R}{\lambda} - \frac{\lambda}{\lambda_s}\frac{\lambda_R}{\lambda} = T(M - N)$$

$$\frac{\lambda_s}{\lambda}\left(1 - (N - M) - (B-1)(\frac{\lambda}{\lambda_D} - 1)\right) = T(M - N)$$

$$T = \frac{\frac{\lambda_s}{\lambda}\left(1 - (N - M) - (B - 1)(\frac{\lambda}{\lambda_D} - 1)\right)}{M - N}$$

Similarly with equation (g3)

$$\frac{-NB}{M - BN}(1 - \frac{\lambda_R}{\lambda}) + \frac{\lambda_R}{\lambda}\frac{\lambda}{\lambda_D} = S\left(B + (B - 1)\frac{NB}{M - BN}\right)^3$$

$$\frac{\lambda_R}{\lambda}\left(M\frac{\lambda}{\lambda_D} - BN(\frac{\lambda}{\lambda_D} - 1) - BN\right) = \frac{SB^3(M - N)^3}{(M - BN)^2}$$

$$S = \frac{\frac{\lambda}{\lambda_D}(M - BN)^2}{B^2(M - N)^3}$$

Substituting S & T into (g1) and (g2) gives :-

$$\frac{\lambda_R}{\lambda}\frac{\lambda}{\lambda_D} = \frac{\frac{\lambda}{\lambda_D}(M - BN)^2 B}{(N - M)^3} + N\frac{\lambda_s}{\lambda}\frac{\left(1 - (N - M) - (B - 1)(\frac{\lambda}{\lambda_D} - 1)\right)}{M - N} + UNB + VNB^2$$

Similarly with equation (g4)

$$1 + (\frac{\lambda}{\lambda_D} - 1)\frac{\lambda_R}{\lambda} = \frac{\frac{\lambda}{\lambda_D}(M - BN)^2}{B^2(N - M)^3} + M\frac{\lambda_s}{\lambda}\frac{(1 - (N - M) - (B - 1)(\frac{\lambda}{\lambda_D} - 1))}{B(M - N)} + \frac{UM}{B} + \frac{VM}{B}$$

Making the substitutions of

$$A = M - BN$$

$$C = N - M$$

$$D = \frac{\lambda_s}{\lambda}(1 - (N - M) - (B - 1)(\frac{\lambda}{\lambda_D} - 1))$$

$$F = \frac{\lambda}{\lambda_D}$$

The above two equations become respectively :-

$$\frac{\lambda_R}{\lambda}F = \frac{FA^2B}{C^3} - \frac{ND}{C} + UNB + VNB^2 \quad —(g5)$$

and

$$1 + (\frac{\lambda}{\lambda_D} - 1)\frac{\lambda_R}{\lambda} = \frac{FA^2}{C^3B^3} - \frac{MD}{BC} + \frac{UM}{B} + \frac{VM}{B} \quad —(g6)$$

Substitution and rearranging equation (g5) gives

$$1 = \frac{A^2}{C^2} + UC(1 + \frac{\lambda_R}{\lambda}\frac{\lambda}{\lambda_s}) + VBC(1 + \frac{\lambda_R}{\lambda}\frac{\lambda}{\lambda_s}) \quad —(g7)$$

Similarly with equation (g6) :-

$$B^2N = A^2\frac{N}{C} + UMBC(1 + \frac{\lambda_R}{\lambda}\frac{\lambda}{\lambda_s}) + VMBC(1 + \frac{\lambda_R}{\lambda}\frac{\lambda}{\lambda_s})$$

Eliminating V from the above equations and rearranging gives,

$$U = -\frac{(\frac{\lambda}{\lambda_D})(B - 1)}{C^2}$$

Substituting the value for U back into equation (g7) and rearranging gives,

$$V = \frac{\frac{\lambda}{\lambda_D}(B - 1)(M - BN)}{BC^3}$$

The integral (4.29) becomes ;

$$\frac{\lambda_{so^*}}{\lambda} = -2B \int\limits_{z=1}^{z=0} \left(\frac{S}{z\left(\frac{\lambda}{\lambda_s} - \frac{\lambda_R}{\lambda}\frac{\lambda}{\lambda_s} - 1\right) + \left(1 + \frac{\lambda_R}{\lambda}\frac{\lambda}{\lambda_s}\right)\frac{\lambda}{\lambda_D}} + \frac{T}{(B - (B-1)z)^3} \right.$$

$$\left. + \frac{U}{(B - (B-1)z)^2} + \frac{V}{(B - (B-1)z)} \right) .dz \quad —(29)$$

All of these are standard integrals and may be found in ref [14]. Integration and substitution of U,V,S & T will lead to equations (4.11) and (4.12).

Appendix 5a
Pressure Vessel Stress Calculations

All stress formulae for the different pressure vessel components are taken from Young [7]. Data for the design strength of the material is taken from BS3605 [8] which gives 0.2% proof stress for stainless steels at elevated temperatures. At 200°C, 0.2% proof stress for stainless steel 316 this equals 133 MPa.

The calculations for the design of each of the seven pressure vessel components is based on a working pressure of 30 bar. For components 1 and 2 the tube is only available from the supplier in certain wall thicknesses and so these are checked to ensure that the maximum design stress is not exceeded. For components 3-6 , the minimum material thickness is found such that the design stress of 65 $\frac{NM}{m^2}$ is not exceeded.

Part 1 Outer Tube

Outer diameter	165.1 mm
Available wall thickness	6.25 mm
tolerance on wall thickness	$\pm 30 \times 10^{-3}$"
tolerance on wall thickness	$\pm 10\%$
minimum possible wall thickness	5.635 mm

$$\sigma_{hoop} = \frac{P \times r}{t}$$

where:-

σ_{hoop}	hoop stress	Pa
σ_{tens}	tensile stress	pa
P	pressure in vessel	Pa
r	tube radius	m
t	wall thickness	m

$$\sigma_{hoop} = \frac{30 \times 10^5 \times 0.08255}{5.625 \times 10^{-3}} = 44.0 \frac{MN}{m^2}$$

$$\sigma_{tens} = 22.0 \frac{MN}{m^2}$$

Maximum design stress= 1/2 of 0.1% proof stress = 65 $\frac{MN}{m^2}$.
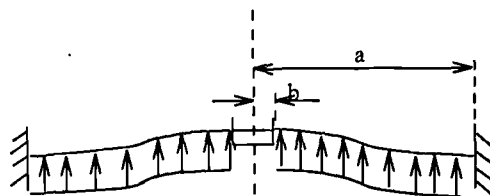
Part 2 Inner Tube

outer diameter	50.8 mm
wall thickness	4.76 mm
minimum wall thickness	4.284 mm

$$\sigma_{hoop} = \frac{30 \times 10^5 \times 25.4 \times 10^{-3}}{0.004284} = 17.8 \frac{MN}{m^2}$$

$$\sigma_{tens} = 8.9 \frac{MN}{m^2}$$

Part 6 Large End Plate   Ref[7] pg 406

a	radius to bolt holes	120 mm
b	radius pipe fitting	7.5 mm
M_{rb}	bending moment at b	3771 Nm
M_{ra}	bending moment at a	3727 Nm

σ_b stress at point b

$$\sigma_b = \frac{6 \times 3771}{t^2}$$

Maximum design stress = 65 MPa, which implies that $t \geq 18.6$ mm.

Part 5 Flange   Ref [7] pg 402
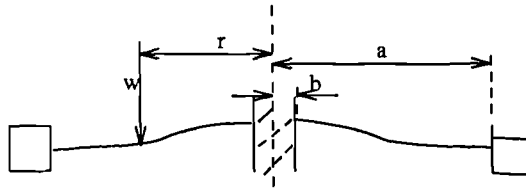
a	radius of plate	145 mm
b	radius outer wall of vessel	82.55 mm
r	radius to bolt holes	120 mm
w	load from bolts	125 kN/m
M_b	bending moment at a	3450 Nm

$$\sigma_b = \frac{6 \times 3450}{t^2} = 65 \text{ MPa}$$

Maximum design stress = 65 MPa, which implies that $t \geq 17.8$ mm.
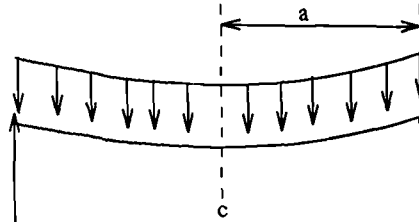
Part 4   Annulus Plate ref [7] pg 406

a	outer radius of inner tube	25.4 mm
b	inner radius of outer tube	76.3 mm
M_{rb}	bending moment at b	1425 Nm
M_{ra}	bending moment at a	1809 Nm
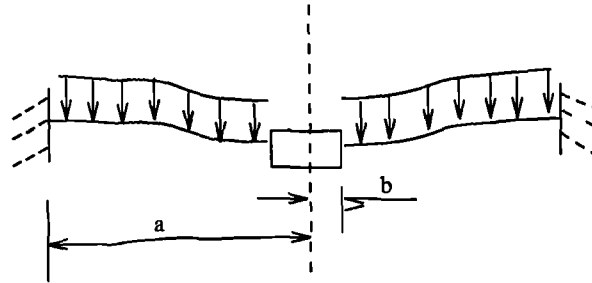
$$\sigma_{ra} = \frac{6 \times 1809}{t^2} = 65 \text{ MPa}$$

Maximum design stress = 65 MPa, which implies that t ≥ 12.9 mm.

Part 3   Small End Plate   Ref [7] pg 429

a	inner radius inner tube	20.6 mm
M_c	bending moment at c	152 Nm

$$\sigma_c = \frac{6 \times 152}{t^2} = 65 \text{ MPa}$$

Maximum design stress = 65 MPa, which implies that t ≥ 3.7 mm.

Appendix 5b

Finite Difference Model of Bed Conductivity

Two dimensional cylindrical steady state conduction with no internal heat generation may be expressed by the partial differential equation below.

$$\frac{\partial^2 T}{\partial r^2} + \frac{1}{r}\frac{\partial T}{\partial r} + \frac{1}{r^2}\frac{\partial^2 T}{\partial \theta^2} = 0$$

This however may be transformed by introducing a new variable ξ such that,

$$\xi = \ln r$$

Substituting ξ into the original equation gives,

$$\frac{\partial^2 T}{\partial \xi^2} = \frac{\partial^2 T}{\partial \theta^2} = 0$$

which is identical to the equation generated by a two dimensional cartesian coordinate system and may be handled in the same way.

The bed is modelled using a two dimensional rectangular grid consisting of 120×22 square nodes. The node size is found from the equation below :-
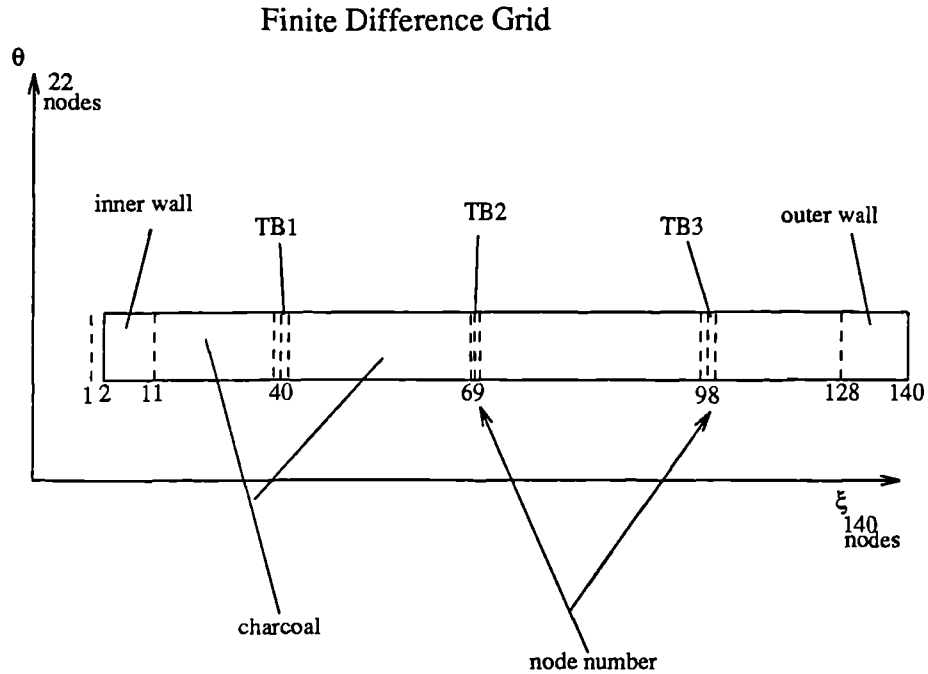
$$\delta r = \frac{1}{2}\sqrt{CSA}$$

where:-

δr = radial node size

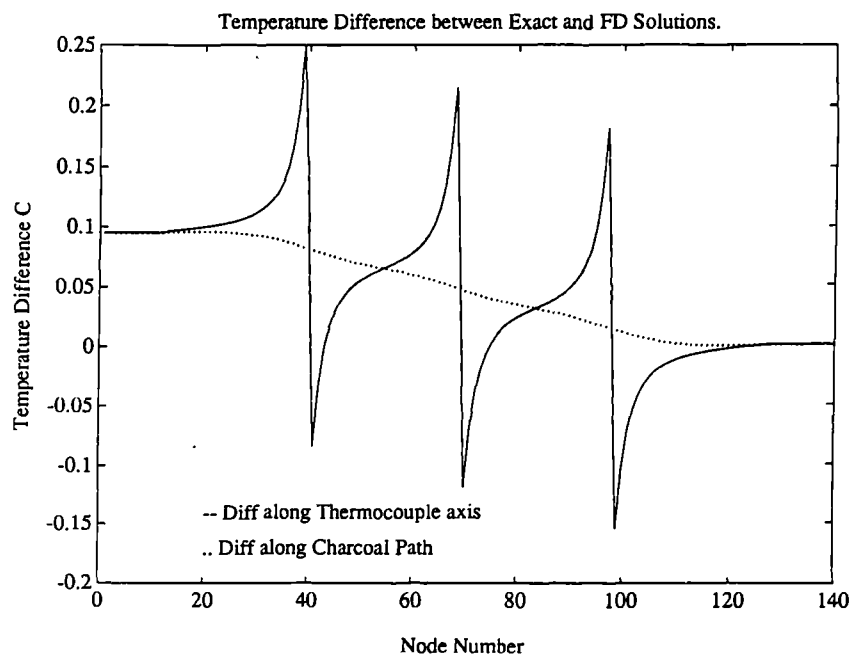CSA = cross sectional area of probe = $\pi \times 0.5^2 = 0.785$ mm^2

The grid used is shown overleaf.

Finite Difference Grid

The finite difference program is run until the solution has converged to within 5×10^{-6}. When the finite difference solution and the exact solution of a bed with no thermocouples were compared, it was found that the error between the two is totally random and is less than 0.001°C. The graph below shows the profiles of the temperature differences between,

solid line- {thermocouple axis (node $\theta = 1$)} minus {exact solution no thermocouples}

dotted line- {charcoal path (node $\theta = 22$)} minus {exact soution no thermocouples}

Temperature Difference between Exact and FD Solutions.

-- Diff along Thermocouple axis

.. Diff along Charcoal Path

Node Number

It can be seen that the error in the temperature measurement in the bed between the walls of the vessel due to the presence of the thermocouples is ± 0.045°C. Since the accuracy of temperature measurement via the interface is only ±0.1 °C it is concluded that the thermocouples do not affect the results as long as they are spaced by 12 mm or more.

Appendix 5c

Pressure Transducer Calibration

The Druck PDCR 0-30 bar strain gauge pressure transducer was calibrated using a dead weight tester. The results form the straight line graph below.

Pressure Transducer Calibration Curve
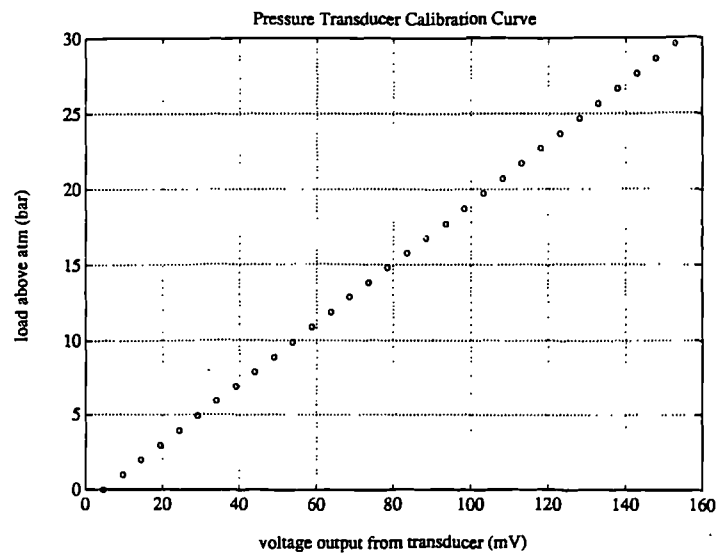
The atmospheric pressure Pa = 769.55 mm = 1.027 bar

The equation of the straight line was found to be :-

$$P = 0.1985 \times mV + 0.1116$$

Appendix 5d

Ammonia Reservoir Design Calculations

The reservoir is designed to hold 1.6 litres of saturated liquid ammonia which is 25% of the weight of the charcoal packed in the pressure vessel. This amount is the difference between the maximum and minimum concentration. The vessel consists of a cylinder 200 mm long with 12 × 30 mm tappings in to the wall thickness at either end, two end plates which are fixed by bolts onto the end plates, and two o'-ring seals.

Again the components are designed to work with a maximum stress of 65 MPa.

End Plates Ref[7] pg 406

Diagram as Part 4 in Appendix 5a.

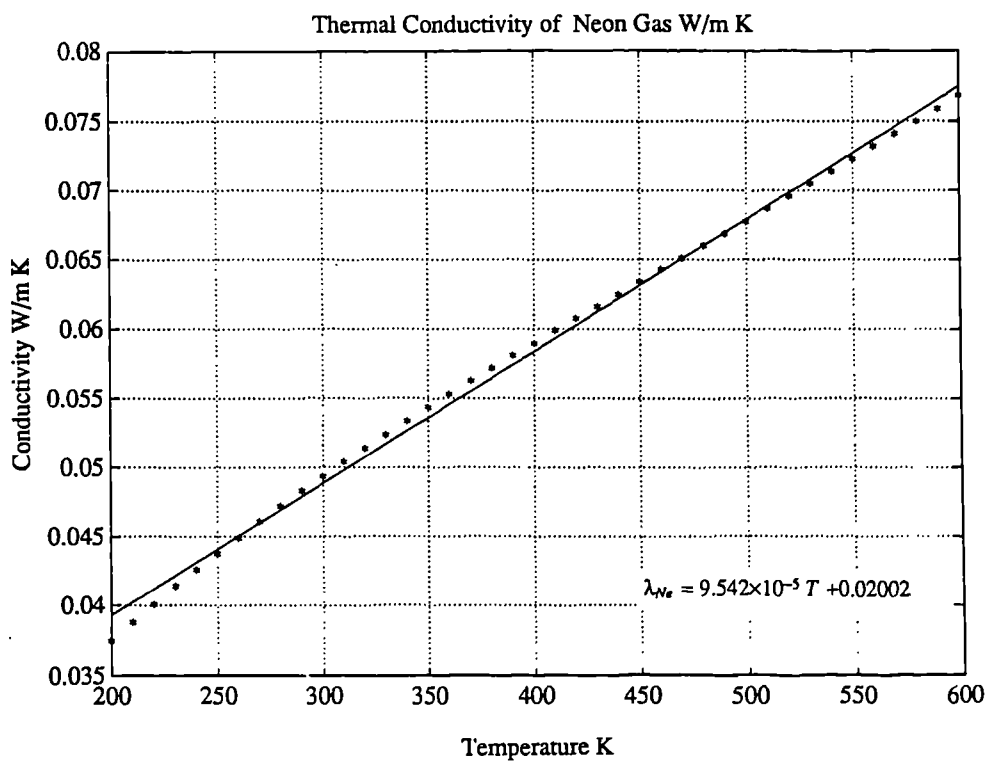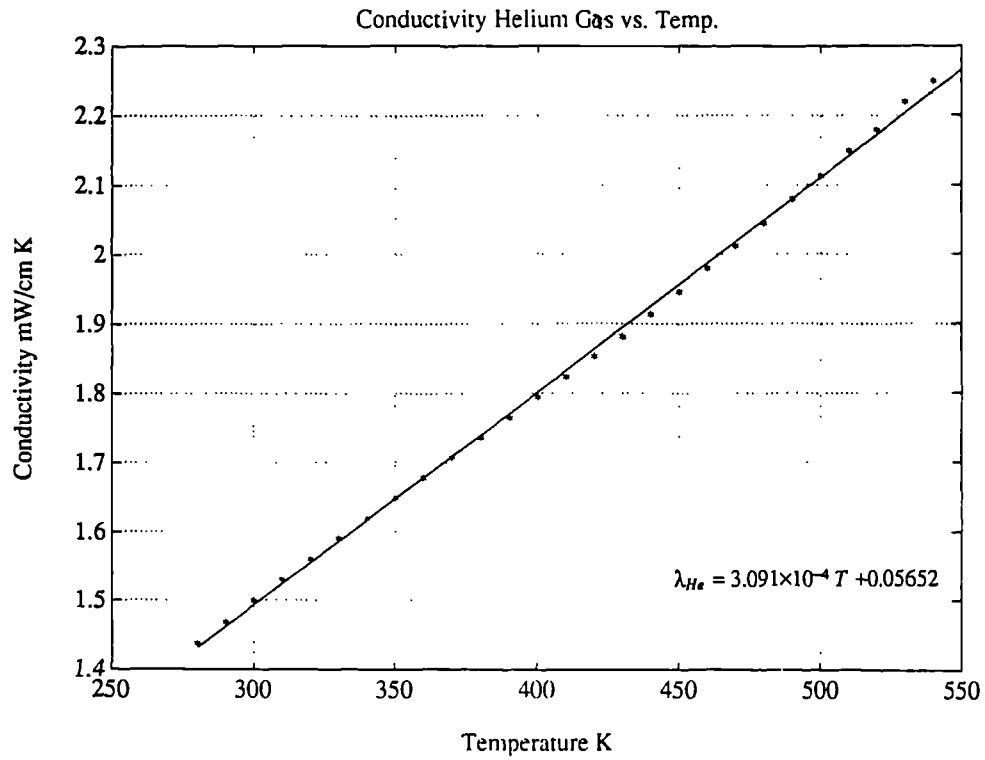|		
a	radius to bolt holes	67.5 mm
b	radius of pipe fitting	7.5 mm
M_{rb}	bending moment at b	1730 Nm
σ_b	bending moment at b	

$$\sigma_b = \frac{6 \times 1730}{t^2}$$
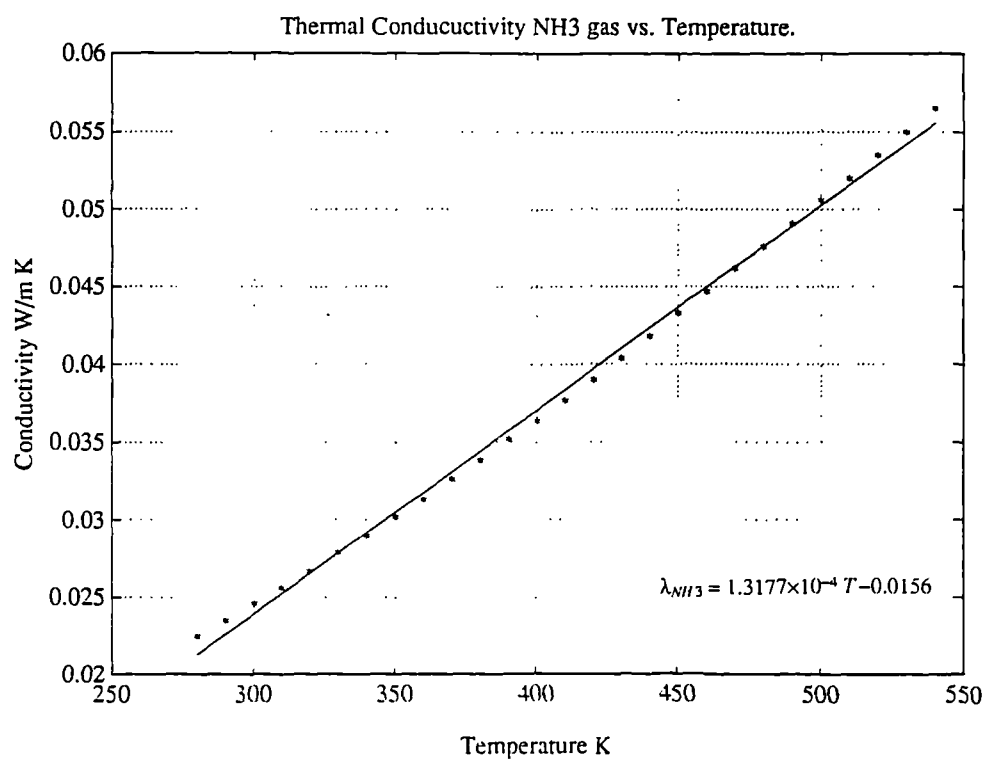
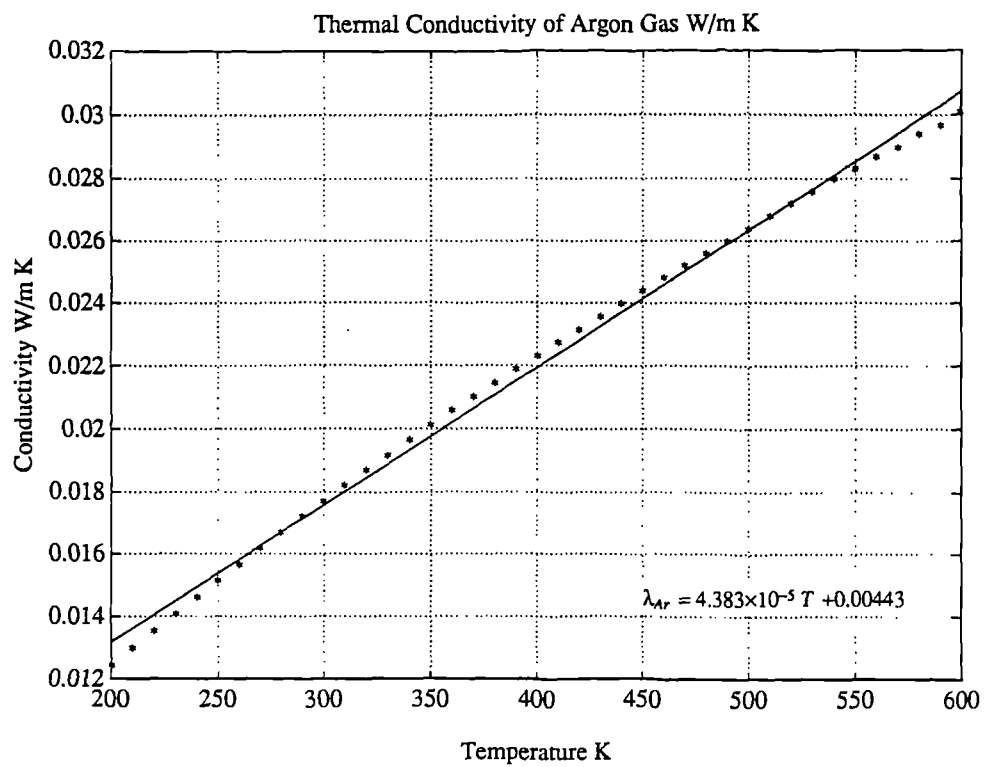which implies that t ≥ 12 mm

Cylinder

The wall thickness of the cylinder is predetermined by the tapping diameter giving stresses of σ_{hoop} = 12 MPa and σ_{tens} = 6 MPa.

Appendix 6a

Plots of Gas Conductivity vs. Temperature

Conductivity Helium Gas vs. Temp.

$$\lambda_{He} = 3.091 \times 10^{-4}\, T + 0.05652$$

Thermal Conductivity of Neon Gas W/m K

$$\lambda_{Ne} = 9.542 \times 10^{-5}\, T + 0.02002$$

Plots of Gas Conductivity vs. Temperature

Thermal Conductivity of Argon Gas W/m K

$\lambda_{Ar} = 4.383 \times 10^{-5}\ T + 0.00443$

Temperature K

Thermal Conducuctivity NH3 gas vs. Temperature.

$\lambda_{NH3} = 1.3177 \times 10^{-4}\ T - 0.0156$

Temperature K

Appendix 6b

Derivation Of Equation (6.27).

With reference to figure 6.7, the bed porosity ψ of the unit cell can be written as ,

$$\psi = 1 - \frac{V_{SM}}{V_z}\sqrt{1-\psi}$$

where

V_{SM} = volume of particle model.

V_z = volume of cylinder into which particle fits.

Rearranging the above equation in ψ gives,

$$\psi = 1 - (\frac{V_{SM}}{V_z})^2$$

The ratio $(\frac{V_{SM}}{V_z})$ can be calculated, using a volume integral, from the equation below defining the particle geometry.

$$r^2 + \frac{z^2}{(B-(B-1)z)^2} = 1$$

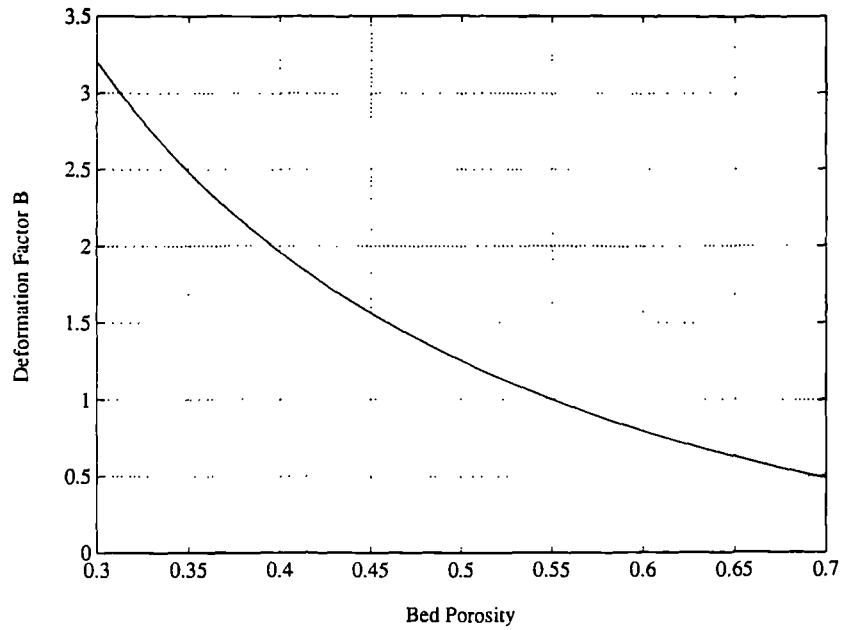Inserting this into the equation in ψ gives,

$$\psi = 1 - \frac{B}{(B-1)^3}(3 - 4B + B^2\, 2\ln B)$$

This equation can be approximated to

$$B = 1.25(\frac{1-\psi}{\psi})^{10/9} \qquad —(i)$$

Plotting a graph of ψ against B reveals the curve shown overleaf.

Plot of Bed Porosity vs. Deformation Factor

In our case the bed porosity was measured to be 0.478. Substituting this into equation (i) produces a value for B of 1.3785. From the ZB minimization program using experimental data, B was found to be 1.3764. These two values are in very good agreement and it may be assumed that the approximation of equation (i) is valid for modelling purposes.